Liquid Crystals Confined in Millimetre-Sized Rectangular Shapes Towards Sensing Applications



Abigail Bond

Department of Physics and Astronomy

University of Leeds

Submitted in accordance with the requirements for the degree of

Doctor of Philosophy

February 2026

The candidate confirms that the work submitted is their own, except where work which has formed part of jointly authored publications has been included. The candidate's contribution and the other authors to this work has been explicitly indicated below. The candidate confirms that appropriate credit has been given within the thesis where reference has been made to the work of others.

Some information in Chapters 2 - 4 and the Appendix (Chapter A) is from [1]. This is the case most in Chapter 4. Reference [1]: A. Bond, T. Moorhouse, S.A. Peyman, H.F. Gleeson (2025). The behaviour of nematic liquid crystals in chemically patterned millimetre-sized rectangular surfaces. *Liquid Crystals*. pp 1-15. https://doi.org/10.1080/02678292.2025.2489426
The method to chemically pattern the surfaces was created by Thomas Moorhouse. All other experimental work in the paper, including fabrication of the surfaces, was completed by Abigail Bond. Supervision on both the experimental work and writing of the paper was completed by Helen F. Gleeson and Sally A. Peyman.

In Chapter 3, the wavelengths of light used in photolithography were measured by Thomas Moorhouse.

In Chapter 7, the thermogravimetric analysis data was taken by Thomas Raistrick.

In Chapter 8, the estimated biphasic region of the nematic to isotropic phase transition for FNLC-919 is based off of differential scanning calorimetry data by Diana Nikolova.

This copy has been supplied on the understanding that it is copyright material and that no quotation from the thesis may be published without proper acknowledgement.

The right of Abigail Bond to be identified as Author of this work has been asserted by Abigail Bond in accordance with the Copyright, Designs and Patents Act 1988.

Publications

A. Bond, T. Moorhouse, S.A. Peyman, H.F. Gleeson (2025). The behaviour of nematic liquid crystals in chemically patterned millimetre-sized rectangular surfaces. *Liquid Crystals*. pp 1-15. https://doi.org/10.1080/02678292.2025.2489426

Conferences

Talks

International Liquid Crystal Conference (ILCC) 2024,
Rio de Janiero, Brazil

The British Liquid Crystal Society (BLCS) annual meeting 2025,
Birmingham, UK

Postgraduate Symposium 2025,
Leeds, UK

Conference on Research and Innovations in Science and Technology of Materials (CRISTMAS), 2023.
Attended online. Recorded talk with poster.

Posters

19th International Conference on Ferroelectric Liquid Crystals (ICFLC), 2025
Leeds, UK

ILCC 2024,
Rio de Janiero, Brazil

Bragg Exchange 2024, 2025
Leeds, UK

Bragg PhD Colloquium 2023, 2025
Leeds, UK

CRISTMAS, 2023
Attended online.

Stoner Colloquium, 2023
Leeds, UK

BLCS Meeting for Early-Stage Researchers, 2023,
Birmingham, UK

Prizes and Bursaries

PhD Funding	Engineering and Physical Sciences Research Council of Great Britain
Prizes	Poster prize at CRISTMAS, 2023.
Bursaries	**Awarded to attend ILCC 2024:** The Soft Matter Physics group at University of Leeds conference fund The BLCS bursary for PhD students Institute of Physics Research Student Conference Fund Registration fee waiver **Awarded to attend ICFLC 2024:** The Soft Matter Physics group at University of Leeds conference fund

This thesis is dedicated to my fiancé, family and friends, and to myself who kept going when the going got tough.

Acknowledgements

I would like to express my immense gratitude to my supervisor, Prof. Helen Gleeson. It has been a joy to learn from your depth of knowledge both in Physics and in life. Another big thank you goes out to Dr. Daniel Baker, the Soft Matter Physics Group Experimental Officer, for all that you do for us. Your helpful and easy to talk to persona has made this PhD less stressful. I would also like to thank Dr. Sally Peyman for helping me through the last ∼8 years, first as my tutor as an undergraduate and now as my supervisor. Thank you also to Prof. Stephen Evans for your wise supervision. I would also like to thank Kathryn, for supporting me throughout my whole time at the University of Leeds.

To my fiancé, Thomas, thank you for encouraging me outside of my comfort zone to achieve things such as flying to Rio de Janeiro for a conference, or this PhD itself. And thank you for standing by me in the difficult moments. I would not be here without my parents either, who gave me an interest in STEM, encouraged me through hard times and let me know that I am capable of anything. And to my big sister, who is making us all proud (and Peach the dog of course!). I cannot forget my (soon to be) in-laws who have provided a lovely and supportive second home for me. I love you all.

One of the best parts about a PhD is the friendship built up with those around you. There are so many people in the Soft Matter Physics and Molecular Nanoscale Physics groups at Leeds who I have formed a strong bond with over these last three and a half years. I would like to give my thanks for all of the fun conversations, and insightful scientific

conversations, and hope we can continue to have more! Thank you to Sandra Sanni, my desk mate who made long days in the office that bit nicer. And thank you to Diana Nikolova, who has taken this journey with me since undergraduate. Thank you to Thomas Moorhouse who trained me and gave me confidence on many techniques early on in my PhD. And last but not least, thank you to Stuart Berrow, Emily Cooper, Thomas Raistrick, and Jordan Hobbs for all your amazing support as postdocs.

Abstract

The confinement behaviours of liquid crystals (LC) in chemically patterned, rectangular, millimetre-sized geometries with a free air/LC interface are presented in this thesis. Motivating this work is the development of an LC-based sensing device that does not require expensive polarised light imaging to detect analytes, is easily scalable for industrial purposes, is reusable for sustainability and has a reasonable shelf-life.

Initial work includes a derivation of a non-LC specific model to describe the height across the width of the confined LC. The model predicts maximum heights of the confined LCs throughout the thesis to be between approximately 20 - 420μm, and is validated using polarised imaging of the confinement of the nematic liquid crystal (NLC), E7. The identification of the confinement aspect ratios that have the most potential for sensing applications through confinement of the well known E7 is also completed, where a 6 x 6mm square is concluded to be most preferable of the aspect ratios tested. Therefore, it is the confinement size used throughout the rest of this thesis.

Another NLC with different physical properties to E7, MLC 7023, is then confined in the 6 x 6mm squares. Unlike the homeotropic anchoring (perpendicular to the interface) at the air/NLC interface for E7, it has been indicated in previous literature that the anchoring at the air/NLC interface for MLC 7023 is non-homeotropic. The 84° tilt angle at the air/NLC interface measured in this work suggests that using MLC 7023 broadens the range of analytes that can be detected by the system, with a suspected transition from tilted to homeotropic

or planar (parallel to the air/NLC interface) on addition of an analyte. This is hoped to result in a greater optical contrast between the anchoring transitions on addition of an analyte under polarised imaging than for E7. MLC 7023 is summarised as preferable for sensing devices from the improved filling quality compared to E7 into the confinement. Additionally, the measured height of the confined NLC across the width fits well to the non-LC specific model to a greater height of approximately 125μm for MLC 7023 versus 50μm for E7.

With a motivation to improve the efficiency of the fabrication process, 6 x 6mm squares are then patterned onto surfaces fabricated with an equivalent method to the surfaces used throughout the thesis, but with the step to rub the alignment layer removed. The non-rubbed surfaces are filled with E7 and MLC 7023, with the resulting polarised images concluded as more difficult to evaluate for the non-rubbed surfaces compared to the rubbed.

Subsequently, it is quantified that the patterned substrates are reusable for at least 6 repeats with confined E7 without significant degradation, *via* rinsing the 'old' NLC off of the surface with isopropanol. It is also concluded for both E7 and MLC 7023 that the confined samples have a shelf-life of at least 14 days, with the E7 samples being resistant to changes upon heating and cooling.

A final investigation utilised a ferroelectric nematic liquid crystal (FNLC), FNLC-919, to give a novel introduction to the confinement behaviours in a 6 x 6mm chemically patterned square. The nematic phase behaved in a similar way to the E7 and MLC 7023 confined NLCs, with the height behaviour and variation of the effective birefringence in the nematic phase discussed for FNLC-919. However the two additional phases associated with FNLC-919, namely the N_x and the ferroelectric nematic phase, N_f, show interesting textures due to properties such as the polar nature of FNLCs. For example, an unexpected shrinkage along the rubbing axis is observed on cooling the

smallest confined FNLC-919 sample, predominantly observed over the N_x phase (whose properties are debated in the literature). Another observation for the confined FNLC-919 systems is the ejected FNLC from the corners of the confinement, as is attributed to a competition between charges and surface tension. In the N_f phase, the FNLC textures under polarised imaging are discussed and compared to relevant literature, with the main observation being domains of twisted FNLC throughout the FNLC height.

The research discussed throughout this thesis can be used to predict behaviours of confined NLC over any width with the non-LC specific model. This, alongside the discussion of confinement behaviours for different LCs, can inform in both the planning of further research in the area and industrialisation of the system as a sensing device.

Abbreviations

LC	Liquid crystal
POM	Polarised optical microscopy
NLC	Nematic liquid crystal
FNLC	Ferroelectric nematic liquid crystal
$\mathbf{n}$	Director
φ	Average tilt angle
Cr	Crystal phase
N	Nematic phase
I	Isotropic phase
n_e	Extraordinary refractive index
n_o	Ordinary refractive index
Δn	Birefringence
Γ	Retardation
f_{total}	Total free energy
f_{field}	Field component of free energy
$f_{elastic}$	Elastic component of free energy
$f_{surface}$	Surface component of free energy
K_1	Splay elastic constant
K_2	Twist elastic constant
K_3	Bend elastic constant
s	Defect strength
$\mathbf{P}$	Polarisation vector
N_f	Ferroelectric nematic phase
N_x	Debated nematic phase
LN	Lithium niobate
λ	Wavelength
n_{av}	Average refractive index
θ	Contact angle
PVA	Poly(vinyl alcohol)
Semi-droplet	Name for the confined LC in this thesis
SDS	Sodium dodecyl sulphate
BSA	Bovine serum albumin
UV	Ultraviolet

IPA	Isopropanol
DI	Deionised water
RT	Room temperature
Silane	1H,1H,2H,2H-Perfluorooctyltrichlorosilane 97%
ζ	Angle between incident polarised light and optic axis
I_0	Intensity into polariser and birefringent sample system
I	Intensity out of polariser and birefringent sample system
ϕ	Director angle through semi-droplet height
ϕ_{max}	Maximum director angle
Δn_{eff}	Effective birefringence
h	Height
$\frac{z}{h}$	Dimensionless semi-droplet height
m	Number of pink birefringent fringes
ρ	Density
HAN	Hybrid aligned nematic
2d	Semi-droplet width
L_c	Capillary length
γ	NLC/air interfacial tension
g	Gravitational acceleration
L	Length
h(x)	Height variation along semi-droplet width
A	Semi-droplet cross-sectional area
V	LC dispense volume
ϵ	$\frac{A}{d^2}$
r	Circle radius
h(0)	Maximum height
θ_I	Interface angle
α	$\left[1-\left(\frac{x\sin(\theta_I)}{d}\right)^2\right]^{\frac{1}{2}}$
$T_{N\rightarrow I}$	Temperature at start of N - I biphasic region
T_{NI}	Temperature at end of N - I biphasic region
$\Delta T_{N\rightarrow I}$	Difference in $T_{N\rightarrow I}$ after change in MLC 7023 semi-droplet
ΔT_{NI}	Difference in T_{NI} after change in MLC 7023 semi-droplet
$T_{I\rightarrow N}$	Start of I - N phase transition
$T_{N\text{-}N_x}$	N - N_x phase transition
$T_{N_x\text{-}N_f}$	N_x - N_f phase transition

Contents

Dedication iv

Acknowledgement vi

Abstract viii

Abbreviations xi

Contents xiii

List of Figures xix

1 Introduction 1

1.1 Introduction 1

1.2 Roadmap 2

2 Background 5

2.1 Introduction 5

2.2 Nematic Liquid Crystals 6

2.2.1 Nematic Phase Geometries and Order Parameter 6

2.2.2 Birefringence 7

2.2.3 Director Fields 8

2.3 Ferroelectric Nematic Liquid Crystals 11

2.4 Liquid Crystals Confined in Rectangular-like Shapes 14

2.5 Liquid Crystal- and Polarised Optical Microscopy-Based Sensing . . . 17
2.5.1 Sensing Mechanism and Geometries . . . 17
2.5.2 Liquid Crystal Droplet Stability . . . 18
2.5.3 LC-based Sensor Sensitivities . . . 19
2.6 Summary . . . 20

3 Experimental Methods and Materials 21
3.1 Introduction . . . 21
3.2 Surface Patterning . . . 22
3.2.1 Patterning Method Overview . . . 22
3.2.2 Glass Cleaning . . . 23
3.2.3 Spin Coating . . . 23
3.2.4 Mechanical Rubbing . . . 25
3.2.5 Photolithography . . . 25
3.2.6 Silane Deposition . . . 28
3.3 Polarised Light Imaging . . . 29
3.3.1 Bespoke Imaging System and Key Principles of Polarised Light Imaging . . . 30
3.3.2 Retardation Colours and Full Wave Plate . . . 33
3.3.3 Defect Characterisation . . . 34
3.3.4 Identification of Twist . . . 37
3.3.5 Semi-Droplet Height . . . 37
Effective Birefringence . . . 37
Semi-Droplet Height Measurement . . . 40
3.4 Liquid Crystal Materials . . . 42
3.4.1 NLC Density Measurements . . . 42
3.5 Thermogravimetric Analysis . . . 44
3.6 Summary . . . 44

4 E7 Confined in Chemically Patterned Rectangles 45
4.1 Introduction . . . 45
4.2 Experimental Methods . . . 46
4.2.1 Patterned Surface Fabrication . . . 46

4.2.2 NLC Deposition . . . 46
4.2.3 Measurement of semi-droplet height . . . 47
4.3 Geometric Modelling of the Semi-Droplets . . . 48
4.4 Results and Discussion . . . 53
4.4.1 Semi-Droplet Height . . . 53
4.4.2 Defect Formation in E7 Semi-Droplets . . . 62
4.5 Further Investigations on 6mm Square Confinements . . . 64
4.5.1 E7 Semi-Droplet Interface Angle . . . 64
4.5.2 E7 Semi-Droplet Director Fields under Varied Polarisation Conditions . . . 67
4.5.3 Filling Quality Observations . . . 70
Effect of Experience . . . 70
Other Filling Features . . . 71
Spherical Cap Assumption . . . 72
4.6 Summary . . . 73

5 MLC 7023 Confined in Chemically Patterned Squares 77
5.1 Introduction . . . 77
5.2 Experimental Methods . . . 78
5.2.1 Patterned Surface Fabrication . . . 78
5.2.2 NLC Deposition . . . 78
5.3 Results and Discussion . . . 79
5.3.1 MLC 7023 Semi-Droplet Height . . . 79
5.3.2 MLC 7023 Semi-Droplet Interface Angle . . . 86
5.3.3 Defect Formation in MLC 7023 Semi-Droplets . . . 89
5.3.4 MLC 7023 Semi-Droplet Director Fields under Varied Polarisation Conditions . . . 91
5.4 Summary . . . 96

6 Confinement of Liquid Crystals on Non-Rubbed Chemically Patterned Squares 99
6.1 Introduction . . . 99
6.2 Experimental Methods . . . 100
6.2.1 Patterned Surface Fabrication . . . 100

6.2.2 NLC Deposition . . . 100
6.3 Results and Discussion . . . 101
6.3.1 Semi-Droplet Height . . . 101
6.3.2 Semi-Droplet Director Fields under Varied Polarisation Conditions . . . 107
6.4 Summary . . . 113

7 Reusability of Chemically Patterned Surfaces and Shelf Life of Confined Semi-Droplets 115
7.1 Introduction . . . 115
7.2 Experimental Methods . . . 116
7.2.1 Sample Preparation . . . 116
7.2.2 NLC Deposition . . . 116
7.2.3 Phase Transition Measurements . . . 117
Patterned Surface Reusability . . . 117
Shelf-life of E7 Semi-Droplets . . . 118
Shelf-life of MLC 7023 Semi-Droplets . . . 118
7.3 Results and Discussion . . . 119
7.3.1 Patterned Surface Reusability . . . 119
7.3.2 Shelf Life of E7 Semi-Droplets . . . 121
7.3.3 Shelf Life of MLC 7023 Semi-Droplets . . . 122
7.4 Summary . . . 127

8 FNLC-919 Confined in Chemically Patterned Squares 131
8.1 Introduction . . . 131
8.2 Experimental Methods . . . 132
8.2.1 Patterned Surface Fabrication . . . 132
8.2.2 FNLC Deposition . . . 132
8.2.3 Measurement of Phase Behaviour . . . 133
8.3 Results and Discussion . . . 133
8.3.1 Phase Transitions . . . 133
Isotropic-to-Nematic Phase Transition . . . 135
Nematic to Nematic ‘x’ Phase Transition . . . 139
Nematic ‘x’ to Ferroelectric Nematic Phase Transition . . . 143

8.3.2 Small Semi-Droplet Behaviour in the N Phase and the Effective Birefringence . . . 148
8.3.3 Instabilities at Semi-droplet Corners . . . 150
8.3.4 Semi-Droplet Shrinkage and Growth . . . 152
8.3.5 N_f Phase Director Field After Cooling . . . 155
8.4 Summary . . . 164

9 Conclusions and Further Work 167
9.1 Conclusions . . . 167
9.2 Further Work . . . 170

A Supplementary Information 175
A.1 Appendix for Chapter 3 . . . 175
A.1.1 Bespoke Photomask . . . 175
A.1.2 Code to Align Images for Figures . . . 176
A.2 Appendix for Chapter 4 . . . 177
A.2.1 Contact Angle . . . 177
A.2.2 Additional Polarised Images . . . 178
A.2.3 Code to Fit to Measured Heights . . . 180
A.2.4 Additional Crossed Polariser Rotation . . . 181
A.3 Appendix for Chapter 5 . . . 183
A.3.1 Additional Polarised Images . . . 183
A.3.2 Code for Tilt Angle . . . 184
A.3.3 Effective Birefringence . . . 185
A.3.4 Additional Crossed Polariser Rotations . . . 186
A.4 Appendix for Chapter 6 . . . 188
A.4.1 Additional Crossed Polarisers Rotation . . . 188
A.5 Appendix for Chapter 7 . . . 190
A.5.1 E7 Semi-Droplet Heating . . . 190
A.5.2 MLC 7023 'Misting' Investigations . . . 191
A.6 Appendix for Chapter 8 . . . 193
A.6.1 Transition Temperatures . . . 193
A.6.2 Semi-Droplet Movies . . . 194
A.6.3 Effective Birefringence . . . 194

A.6.4 E7 Semi-Droplet 195
A.7 Appendix for Chapter 9 196
A.7.1 Polymer Stabilisation 196

References **214**

List of Figures

2.1 *a*: An optical indicatrix of the average values of an aligned sample of the nematic phase. n_o and n_e represent the ordinary and extraordinary refractive indices, respectively, and the symmetric director is demonstrated by $\boldsymbol{n}$ = -$\boldsymbol{n}$. *b:* Schematic of an aligned nematic phase sample. Not to scale. *a, b redrawn/adapted from information in references such as [2] and [3, 4], respectively.* . . . 6

2.2 Schematic of the principle of birefringence. When linearly polarised light (Polarisation A) enters a birefringent material, perpendicular light components are slowed by different amounts corresponding to n_e and n_o. The components leave the material with a path difference, Γ, and vectorially add, resulting in a changed polarisation of the light (Polarisation B). In this schematic, n_o is arbitrarily into the plane of the paper and experienced by the light component arbitrarily drawn in red, and n_e is perpendicular to this and drawn arbitrarily in blue. The apparent discontinuity of the wave on exiting the sample in this schematic is not a real feature, and is as a result of forming a clear description. Not to scale. *Based off of information in references such as [5].* 8

2.3 Schematics of the three key elastic constants of liquid crystals including splay (K_1), twist (K_2) and bend (K_3). Not to scale. *Redrawn/ adapted from references such as [4, 6].* 9

2.4 Schematics of *a-c:* the common anchoring used in LCs. *a:* Non-rubbed planar. *b:* Rubbed planar with the director along the rubbing direction. A pretilt from parallel to the surface is sometimes observed. *c:* Homeotropic alignment, with the molecules perpendicular to the anchoring surface. *d:* The commonly used LC 'cell' for NLC investigations. Not to scale. *a-c, and d redrawn/adapted from information in references such as [4, 7] and [3, 8], respectively.* 10

2.5 Schematics of commonly seen defects in LC director fields with strengths, s, of $\pm$ 1 or $\pm\frac{1}{2}$. Not to scale. *Redrawn/adapted from [9].* 11

2.6 Schematic of ferroelectric nematic liquid crystals. The director is non-symmetric, $\boldsymbol{n} \neq$ -$\boldsymbol{n}$. The dipoles are largely aligned, with the polarity vector, $\boldsymbol{P}$, aligned with the director. Not to scale. *Adapted from information in references such as [10, 11].* 12

2.7 Schematics of observations from FNLC-919 confinements in the N_f phase. *a:* The approximate 180°twist of a director seen in an antiparallel planar rubbed FNLC-919 cell. *b:* In free surface samples, a director rotating around a central defect (marked in blue) has previously been observed. Not to scale. *c:* Best fits of a hexagonally-confined free surface sample of FNLC-919 across a width cross-section, demonstrating a lowered region in the centre. *a,b,c redrawn/adapted from information in [12] and [13, 14] and [14], respectively.* 14

2.8 Diagram to indicate the contact angle, θ, height, width and radius of the confined LC in the work by Bao *et al.*, modelled as a circle. The solid line denotes the outer border of the confined LC. *Based off of information from [15].* 16

2.9 Schematic of an exemplar mechanism for LC-droplet based sensing. The droplet is in the bipolar director field configuration before addition of an analyte causes a conversion of the director field to radial, which can be detected *via* POM. The blue circles highlight defects in the director field and the green shapes demonstrate the analytes. Not to scale. *Redrawn/ adapted from references such as [6, 16, 17].* 18

3.1 Schematic *a*: side and *b:* top view of chemically patterned rectangles, with the LC confined between a hydrophobic monolayer and sitting on a planar rubbed polyimide alignment layer. Whilst it is impractical to draw the schematic to scale, the approximate expected layer thicknesses are labelled to show that the hydrophobic layer is significantly less thick than the LC. *Approximate expected thicknesses based off of information from: LC[1], silane[18], SE130[19]. Left image adapted from [1].* 22

3.2 Key steps to spin coat a thin film onto a substrate using a static deposition method. *a:* The liquid is deposited onto the surface and spread to the key areas using a pipette tip or by adding more liquid. *b:* The rotation of the stage is started, removing excess liquid. *c:* The film is baked. Not to scale. *Redrawn/adapted from information in references such as [1, 20, 21].* 23

3.3 Schematic of mechanical rubbing. The substrates are stabilised with a vacuum, and the stage is passed linearly under a rotating cloth roller. Not to scale. *Image adapted from [1].* 25

3.4 Schematics of the key steps in photolithography to pattern rectangles onto the substrates. *a:* The photo resist is spin coated on top of the alignment layer. *b:* The desired rectangle from the photomask is aligned with the rubbing axes of the substrate before *c:* exposure to UV light. *d:* The substrate is agitated in developer and DI water. *e:* The resulting surface after photolithography is exposed to further UV. Not to scale. *c adapted from [1]. Information on photolithography can be read at references such as [22].* . . 26

3.5 *a:* Bespoke photomask design, created to define the rectangular confinement shapes of the surface patterning. *b:* Zoomed area of a commonly used region of the photomask containing the 6 x 6mm square, with the large arrow denoting the rubbing direction and the numbers referring to the rectangles. Two rectangles in this area of the photomask are difficult to resolve in this image due to their small size and are therefore circled. 27

3.6 Chemical structure of 1H,1H,2H,2H-Perfluorooctyltrichlorosilane, 'silane'. *Redrawn/adapted from [23].* 28

3.7 Schematics of the key steps to coat the patterned surfaces with silane. *a:* The substrates are placed in an oven prior to transfer to the dessicator. *b:* A droplet of silane in placed in the dessicator with the substrates, before nitrogen gas is passed through the dessicator and then taken down to a vacuum. *c:* The substrate is agitated in IPA and DI. Not to scale. *Relevant information for a-c, with b adapted from, references [18, 24].* 29

3.8 *a*: Real image showing the main components of the bespoke imaging system designed to take high-quality large field of view images in a range of polarisation conditions. The polarisers and beamsplitter can be moved into and out of the light path. *b*: A schematic of the components required to take cross polarised images of LC samples in transmission and reflection mode. *Image adapted from supplementary information in [1].* 31

3.9 Schematic to describe the transmission of light through a birefringent sample sandwiched by crossed polarisers. Unpolarised light will be polarised in the direction of the polariser axis. This direction will have an angle, ζ, to the optic axis. The value of ζ will determine if the polarised light experiences birefringent effects through the sample (see Section 2.2.2). Only the light aligned with the analyser axis leaves the system. The colours for the polarisers, sample and light arrows are chosen arbitrarily. Not to scale. *Redrawn/adapted based off diagrams and/or information in references such as [5, 25].* 32

3.10 *a:* Schematic of the retardation colours observed in approximately the first two orders of a Michel-Lévy chart. *bii:* Between crossed polarisers, first order magenta is observed for a full waveplate added into polarised imaging apparatus with no birefringent sample. If the waveplate axis is added *bi:* perpendicular to the director of a birefringent sample, the retardation colour will decrease with respect to the first order magenta. If the waveplate axis is added *biii:* parallel to the director, the retardation will increase with respect to the first order magenta. The arrows show the axes of the polarisers, the director of the birefringent samples and the axis of the waveplate. The colours of the samples and polarisers are arbitrary in this figure. *Approximate retardations in Figure a are read from Michel-Lévy chart at [26]. b redrawn/adapted from information in references such as [25].* 33

3.11 Schematic of the method to evaluate of the sign and strength, s, of LC defects. *ai,bi*: Under crossed polarisers there are four dark brushes suggesting a defect with a strength of $\pm$ 1. *aii,bii*: When the crossed polarisers are rotated at the same rate clockwise, the dark brushes for the $s = +1$ defect will also rotate clockwise, and will rotate anti-clockwise for the s = -1 defect. Not to scale. *c:* Rotation of crossed polarisers through 0°to 45°of an NLC semi-droplet. The yellow circle represents the origin of the potential strength = +1 defect, and the orange lines represent the dark brushes. The scale bars are 2mm. P and A show the relative directions of the polariser and analyser, respectively. The sample in *c* does not have a rubbed alignment layer as is the main focus of Chapter 6, however the dark brushes are clear. *a,b redrawn/adapted from [9].* 35

3.12 *a:* Schematic of twist, a common observation in FNLC samples. *b:* To identify this twist, images on a consistent sample area (represented schematically here) are taken with the analyser rotated to a slightly uncrossed position relative to the polariser in both directions (*i* or *iii*). A and B refer to regions A and B in *a*. If there is an optical difference between the two conditions, there is twist in differing directions. P and A show the relative directions of the polariser and analyser, respectively. Not to scale. *a and b adapted/redrawn from information in [12] and [12, 27], respectively.* 38

3.13 General shape of the director field throughout the dimensionless height, $\frac{z}{h}$, for an NLC semi-droplet, from a pretilt at the substrate surface of $\phi = 2°$, to a maximum tilt angle, ϕ_{max}, at the air/NLC interface. *Image adapted from [1].* 39

3.14 Plots through the dimensionless height of the E7 semi-droplet, $\frac{z}{h}$, of *a:* director angle, ϕ, *b:* extraordinary refractive index, n_e, and *c:* $n_e(\frac{z}{h}) - n_o$, where n_o is the ordinary refractive index. *Image adapted from supplementary information in [1].* 40

3.15 *a*: Top view polarised light image of NLC confined in a chemically patterned 6 x 6mm square. The value of m represents the number of pink birefringent fringes counting from the semi-droplet edge. White lines show the cross-section along which the centre-to-centre distances of the fringes have been measured for the height variation. P, A and R show the relative directions of the polariser, analyser and rubbing, respectively. The scale bar is 2mm. *b*: Plot of the centre-to-centre distances of the pink birefringent fringes along the horizontal line in *a* with their corresponding measured heights. *Image adapted from [1].* 41

3.16 Density variation of *a:* E7 and *b:* MLC 7023 near room temperature. 43

4.1 Schematic of the hybrid-aligned nematic director of E7 semi-droplets through the dimensionless height of the semi-droplet, $\frac{z}{h}$, from a pretilt of $\sim 2°$at the patterned surface, to homeotropic at the air/NLC interface. Not to scale. *Figure adapted from [1].* 48

4.2 Schematics used in the derivation of Equation 4.6 to describe the cross-section of a confined NLC semi-droplet. *a:* A non-shifted circle (blue) is shifted by the radius of the circle, r, minus the semi-droplet maximum height, $h(0)$ (red). y is replaced by the change in height, $h(x)$, along the x - axis, with the shaded region denoting a confined liquid crystal semi-droplet cross-section, bounded by $x^2 + (h(x) - r + h(0))^2 = r^2$, $h(x) \geq 0$, and -$d \leq x \leq d$. The distance $2d$ is the length of the minor chord of the circle, and the width of the semi-droplet. *b:* Diagram of the key geometric model parameters used to describe the cross-section of an NLC 'semi-droplet' confined in a rectangular geometry where the shaded area is the cross-sectional area of the semi-droplet, A, and the interface angle is at the edge of the confinement, θ_{I}. The height of the semi-droplets in this work are of the order of 10-500µm, and the radius of the circle is of the order of 10-100mm. *Figure b is published in [1].* 51

4.3 Polarised light imaging of varying NLC 'semi-droplet' volumes confined in 6mm squares on chemically patterned surfaces with a rubbed alignment layer on a solid substrate and an NLC/air interface. Maximum heights measured using pink birefringent fringes are compared to those predicted from calculation of the semi-droplet cross-sectional area ($V = AL$), leading to predictions of ϵ (Equation 4.2), interface angle (Equation 4.7) and finally, height (Equation 4.6). White lines show the cross-sections along which the centre-to-centre distances of the fringes have been measured to deduce the height variations across the semi-droplet width and length. The rubbing direction is at 45°to the crossed polarisers, with arrows marked P, A and R to show the relative directions of the polariser, analyser and rubbing respectively. The scale bars are 2mm. The cropping of the images was varied to ensure that the field of view required to capture all the information (e.g any overflowing LC) is retained while maximising the image visibility. *Figure published in [1].* 54

4.4 Polarised light images of varying NLC 'semi-droplet' volumes confined in rectangles of dimensions *a-d:* 11 x 11mm; *e-h:* 16 x 13mm, on patterned surfaces with a rubbed alignment layer on a solid substrate and a NLC/air interface. Maximum heights measured using pink birefringent fringes are compared to those predicted from calculation of the semi-droplet cross-sectional area ($V = AL$), leading to predictions of ϵ (Equation 4.2), interface angle (Equation 4.7) and finally, height (Equation 4.6). White lines show the cross-sections along which the centre-to-centre distances of the fringes have been measured to deduce the height variation across the semi-droplet width and length. P, A and R show the relative directions of the polariser, analyser and rubbing respectively. The scale bars are 3mm. Extra domains other are sometimes seen when the confinement is overfilled, as circled in *d* as an example. The cropping of the images was varied to ensure that the field of view required to capture all the information (e.g any overflowing liquid crystal) is retained while maximising the image visibility. *Figure adapted from [1].* 55

4.5 Polarised light images of varying NLC 'semi-droplet' volumes confined in rectangles with dimensions of 20 x 10mm, on patterned surfaces with a rubbed alignment layer on a solid substrate and a NLC/air interface. Maximum heights measured using pink birefringent fringes are compared to those predicted from calculation of the semi-droplet cross-sectional area ($V = AL$), leading to predictions of ϵ (Equation 4.2), interface angle (Equation 4.7) and finally, height (Equation 4.6). White lines show the cross-sections along which the centre-to-centre distances of the fringes have been measured to deduce the height variation across the semi-droplet width and length. Blue lines show the width and length measured to approximate the true surface area of NLC. P, A and R show the relative directions of the polariser, analyser and rubbing respectively. The scale bars are 3mm. The cropping of the images was varied to ensure that the field of view required to capture all the information (e.g any overflowing liquid crystal) is retained while maximising the image visibility. *Figure adapted from [1].* 56

4.6 Comparison of measured and predicted maximum heights for four different confinement dimensions: *red triangles:* 6 x 6mm, *green squares:* 11 x 11mm, *blue diamonds:* 16 x 13mm, *gold circles:* 20 x 10mm *a*: Maximum height predicted from the models (closed data points), vs. the height measured using the number of birefringent fringes (open data points). A black line of the expected $y = \frac{3}{2}x$ (Equation 4.2) is added to further validate the models. *b*: Fractional difference between the measured and predicted maximum heights assuming no deviation from the expected d and L values (*closed data points*). For a selection of samples with less good agreement between the measured and predicted heights, heights are calculated using the same models, but with a measured d and L to reflect the true NLC area (*open data points*). The corresponding polarised light images where this comparison is completed are marked on the figure. $\frac{V}{2dL}$ is calculated using the known d and L, allowing for a clear comparison. The dashed line at *fractional difference* = 0 is for ease of analysis. *Figure adapted from [1].* . . 57

4.7 Height variation using the centre-to-centre distances of pink birefringent fringes across NLC semi-droplet widths for three NLC dispense volumes, V, and four confinement sizes: *a:* 6 x 6mm with V = 0.5µL (red), 1µL (green), 1.8µL (blue). *b:* 11 x 11mm with V = 5µL (red), 10µL (green), 11µL (blue). (c) 16 x 13mm with V = 5µL (red), 9µL (green), 10µL (blue). (d) 20 x 10mm with V = 5µL (red), 7µL (green), 9µL (blue). The data is fitted to both Equation 4.6 (*black line*), or Equation 4.2 (*circles*). A dashed line is included at $x = 0$, as well as solid lines at the expected edges of the confinement shapes. *Figure published in [1].* 59

4.8 Height variation using the centre-to-centre distances of pink birefringent fringes across NLC semi-droplet lengths for three NLC dispense volumes, V, and four confinement sizes: *a:* 6 x 6mm with $V = 0.5\mu$L (red), 1μL (green), 1.8μL (blue). *b:* 11 x 11mm with $V = 5\mu$L (red), 10μL (green), 11μL (blue). *c:* 16 x 13mm with $V = 5\mu$L (red), 9μL (green), 10μL (blue). *d:* 20 x 10mm with $V = 5\mu$L (red), 7μL (green), 9μL (blue). A dashed line is included at $y = 0$, as well as solid lines at the expected edges of the confinement shapes. *Figure published in [1].* 60

4.9 Schematic to demonstrate the likely origin of disclination lines in semi-droplets near their centre ($x \sim 0$), and the potential anchoring breaking near the confinement edges ($x \sim \pm d$). Not to scale. . . . 63

4.10 Two key properties identified through different methods of the E7 semi-droplets confined in 6mm squares. *a:* The predicted interface angle, θ_{I}, is derived from either calculating $V = AL$, estimating ϵ (Equation 4.2), and finally Equation 4.7 (blue), or measured from linear fits of the first few data points on the left-hand side of the height variation plots in Figure 4.7 using the small angle approximation ($\tan(\theta_{\mathrm{I}}) \approx \theta_{\mathrm{I}}$ for small θ_{I}) (red). *b:* The maximum height is derived from the θ_{I} in *a* using Equation 4.6. The measured heights from the birefringent fringes are also included (green). . . 66

4.11 Rotation of crossed polarisers through 0°(i) - 45°(v) with respect to the rubbing direction of an E7 semi-droplets with predicted heights: *a,b:* 21μm and *c:* 208μm. The yellow dashed lines indicate the position of the two dark brushes evidencing a potential strength $= +\frac{1}{2}$ defect. P, A, and R show the relative directions of the polariser, analyser and rubbing, respectively. The scale bars are 2mm. The * indicates where the imaging exposure was known to be adjusted to preserve the quality of the images. 68

4.12 Polarised images of E7 semi-droplets with predicted heights: *a:* 21µm and *b:* 208µm. A lambda plate is added *i:* perpendicular or *ii:* parallel to the rubbing direction. P, A, R, WP show the relative directions of the polariser, analyser, rubbing and lambda waveplate, respectively. The scale bars are 2mm. 69
4.13 Polarised image of a second E7 semi-droplet confined in a 6mm square with a predicted height of 380µm to check the filling quality. P, A and R show the relative directions of the polariser, analyser and rubbing, respectively. The scale bar is 2mm. 70
4.14 Small additional features outside of the confinement, as circled in yellow. *a:* The semi-droplet with predicted height = 125µm (Figure 4.3d) demonstrates a string-like effect from the corner. *b:* The semi-droplet with predicted height = 330µm (Figure 4.3g) demonstrates a small droplet of liquid crystal outside the right-hand edge. *c:* The semi-droplet with predicted height = 380µm (Figure 4.3h) demonstrates a region with low birefringence colours near its bottom right corner. P, A, and R show the relative directions of the polariser, analyser and rubbing, respectively. The scale bars are 2mm. 72
4.15 Schematic diagram of semi-droplets modelled as a spherical cap with a radius, d, maximum height, $h(0)$, and a LC volume, V, denoted by the orange shaded area. Not to scale. 73

5.1 Polarised light imaging of varying MLC 7023 semi-droplet volumes confined in 6mm chemically patterned squares. Maximum heights measured using pink birefringent fringes are compared to the those predicted from calculation of the semi-droplet cross-sectional area ($V = AL$), leading to predictions of ϵ (Equation 4.2), interface angle (Equation 4.7) and finally, height (Equation 4.6). White lines shows the cross-sections along which the centre-to-centre distances of the fringes have been measured to deduce the height variations across the semi-droplet width and length. P,A and R show the relative directions of the polariser, analyser and rubbing, respectively. The scale bars are 2mm. The cropping of the images was varied to ensure that the field of view required to capture all the information (e.g. any overflowing liquid crystal) is retained while maximising the image visibility. 80

5.2 Spread of Δn_{eff} with MLC 7023 semi-droplet predicted height, with a dashed line at the average $\Delta n_{\text{eff}} = 0.036$. 81

5.3 Schematic of the MLC 7023 semi-droplet director through the dimensionless height of the semi-droplet, $\frac{z}{h}$, from an approximately planar tilt angle ($\phi = 2°$) at the patterned surface, to a maximum tilt angle $\phi_{\text{max}} = 84°$at the air/NLC interface. Not to scale. *Figure adapted from [1].* 83

5.4 Height variation using the centre-to-centre distances of pink birefringent fringes for MLC 7023 semi-droplets confined in 6 x 6mm squares across the *a:* widths. The data is fitted to both Equation 4.6 (*black line*), or Equation 4.2 (*circles*). *b:* The centre-to-centre distances of the fringes along the lengths. Four different volumes are demonstrated including: $V = 0.5\mu$L (red), $V = 1\mu$L (light green), 1.8µL (light blue), $V = 3\mu$L (magenta), $V = 5\mu$L (brown). A dashed line is included at $x,y = 0$, as well as solid lines at the expected edges of the confinement shapes. 85

5.5 Two key properties identified through different methods of the MLC 7023 semi-droplets confined in 6mm squares. *a:* The predicted interface angle, θ_I, is derived from either calculating $V = AL$, estimating ϵ (Equation 4.2), and finally Equation 4.7 (blue), or measured from linear fits of the first few data points on the left-hand side of the height variation plots in Figure 5.4a using the small angle approximation ($\tan(\theta_I) \approx \theta_I$ for small θ_I) (red). These data points are also calculated for the larger semi-droplets without the small angle approximation (magenta). *b:* The maximum height is calculated from the θ_I in *a* using Equation 4.6. The measured heights from the birefringent fringes are also included (green). . . 87

5.6 Plot of the radius with dispense volume of the MLC 7023 semi-droplets based on the simple geometric circle on which they are modelled (see Figure 4.2b). The values presented here correspond to those that would be seen for E7 as they are from the same, non LC-specific predictive model. 88

5.7 The tilt angle at the air/NLC interface for MLC 7023 semi-droplets, $\phi_{max} = 84°$, can in theory either cause a *a:* continuous or *b:* discontinuous region of the director field, dependent on the direction of the tilt. The tilts may not be exactly opposite as in *b*. Not to scale. *Aspects of the figures adapted from [1].* 91

5.8 Rotation of crossed polarisers through 0°(i) - 45°(v) with respect to the rubbing direction of MLC 7023 semi-droplets with predicted heights: *a:* 21µm, *b:* 208µm, *c:* 380µm. The yellow circles indicate examples of potential origins of possible strength = $\pm\frac{1}{2}$ defects. P, A and R show the relative directions of the polariser, analyser and rubbing direction, respectively. The scale bars are 2mm. The * indicates where the imaging exposure was known to be adjusted to preserve the quality of the images. 92

5.9 Polarised images with crossed polarisers aligned with the rubbing direction to demonstrate the low birefringence colour features (circled in yellow) in 'tall' MLC 7023 semi-droplets with predicted heights: *a:* 208µm and *b:* 330µm. P, A and R show the relative directions of the polariser, anaylser and rubbing, respectively. The scale bars are 2mm. 94

5.10 Polarised images of MLC 7023 semi-droplets with predicted heights = *a:* 21µm and *b:* 208µm. A lambda plate is *i:* not added or added *ii:* perpendicular or *iii:* parallel to the rubbing direction. P, A, R and WP show the relative directions of the polariser, analyser, rubbing direction, and lambda waveplate, respectively. The scale bars are 2mm. 95

6.1 Polarised light imaging of varying E7 semi-droplet volumes confined in 6mm squares on chemically patterned surfaces without rubbing of the polyimide alignment layer. Maximum heights measured using pink birefringent fringes are compared to those predicted from calculation of the semi-droplet cross-sectional area ($V = AL$), leading to predictions of ϵ (Equation 4.2), interface angle (Equation 4.7) and finally, height (Equation 4.6). White lines show the cross-sections along which the centre-to-centre distances of the fringes have been measured to deduce the height variations across the semi-droplet width and length. P and A show the relative directions of the polariser and analyser, respectively. The scale bars are 2mm. The cropping of the images was varied to ensure that the field of view required to capture all information (e.g. any overflowing liquid crystal) is retained while maximising image visibility. The blue circle in *c* is an e.g of the least uniform region of the semi-droplets, generally near the semi-droplet centre. 102

6.2 Polarised light imaging of varying MLC 7023 semi-droplet volumes confined in 6mm squares on chemically patterned surfaces without rubbing of the polyimide alignment layer. Maximum heights measured using pink birefringent fringes are compared to those predicted from calculation of the semi-droplet cross-sectional area ($V = AL$), leading to predictions of ϵ (Equation 4.2), interface angle (Equation 4.7) and finally, height (Equation 4.6). White lines show the cross-sections along which the centre-to-centre distances of the fringes have been measured to deduce the height variations across the semi-droplet width and length. P and A show the relative directions of the polariser and analyser, respectively. The scale bars are 2mm. The cropping of the images was varied to ensure that the field of view required to capture all information (e.g. any overflowing liquid crystal) is retained while maximising image visibility. The four regions denoted by disclination lines is shown in *e*. The green circles in *e*-*i* are exemplar regions of low birefringence colours near the tall semi-droplet centres. 103

6.3 Height variation using the centre-to-centre distances of pink birefringent fringes across the widths of *a:* E7 and *b:* MLC 7023 semi-droplets confined in a 6 x 6mm square. The data is fitted to both Equation 4.6 (*black line*), or Equation 4.2 (*circles*). Three NLC dispense volumes are used with $V = 0.5\mu$L (red), 1µL (green), 1.8µL (blue), 3µL (magenta). A dashed line is included at $x = 0$, as well as solid lines at the expected edges of the confinement shapes. 106

6.4 Height variation using the centre-to-centre distances of pink birefringent fringes across the lengths of *a:* E7 and *b:* MLC 7023 semi-droplets confined in a 6 x 6mm square. Three NLC dispense volumes are used with $V = 0.5\mu$L (red), 1µL (green), 1.8µL (blue), 3µL (magenta). A dashed line is included at $y = 0$, as well as solid lines at the expected edges of the confinement shapes. 107

6.5 Rotation of crossed polarisers through 0°- 45°with respect to the horizontal/vertical axes of E7 semi-droplets with predicted heights: *a:* 21µm, *b:* 42µm, *c:* 420µm. P and A show the relative directions of the polariser and analyser, respectively. The scale bars are 2mm. The dashed lines in *ai,v* provide a guide to the shape of the potential strength = +1 defect, with the yellow lines demonstrating the dark brushes and the yellow circle in *aii* representing the origin of the potential strength = +1 defect. The green circles in *bi* represent the origins of potential strength = $\pm \frac{1}{2}$ defects. . . . 108

6.6 Rotation of crossed polarisers through 0°- 45°with respect to the horizontal of MLC 7023 semi-droplets with predicted heights: *a:* 21µm, *b:* 42µm, *c:* 380µm, *d:* 420µm. P and A show the relative directions of the polariser and analyser, respectively. The scale bars are 2mm. The yellow circles in *ai,bi* represent the origins of the potential strength = +1 defect. 109

6.7 *a,b:* E7 or *c-e:* MLC 7023 semi-droplets with predicted heights *a,c,d:* 21µm, *b,e:* 208µm, with a lambda plate added along the length axis of the semi-droplet, at 45°to the crossed polarisers. Director representations are imposed onto the inset image for *a* to demonstrate what the waveplate implies about the director field near the corner of the semi-droplet (not to scale). The inset for *b* is to increase the clarity of the birefringent colours at the semi-droplet corner. P, A and WP to show the relative directions of the polariser, analyser and lambda waveplate, respectively. The scale bars are 2mm. 111

6.8 Schematic summary of the director at the *a:* substrate surfaces and *b:* air/ NLC interfaces based on the information from Chapters 4 - 5. *a:* In the rubbed samples, the director is expected to align approximately along the rubbing direction, marked with a blue arrow. *aii:* In the non-rubbed samples, waveplate data suggests the director is parallel to the confinement edges. *bi,ci*: If the director rotation is in the same direction, there will be no discontinuity, however *bii,biii:* there is potential for a discontinuity if the rotation is in opposite directions. It is clear that the non-rubbed samples have more degeneracy than the rubbed samples. Not to scale. *Some aspects of the figures adapted from [1].* 112

7.1 Polarised images of E7 semi-droplets with predicted height = 208µm. The 'old' NLC is rinsed off of the surface with IPA before refilling the same surface with E7, completing the temperature cycle in Table 4.1 and imaging, with this process repeated seven times. P,A, and R show the relative directions of the polariser, analyser and rubbing, respectively. The scale bars are 2mm. 120

7.2 $T_{N\rightarrow I}$ (red) and T_{NI} (blue) upon heating E7 semi-droplets with predicted height = 208µm on six reuses of one chemically patterned 6 x 6mm square. The solid lines indicate the average $T_{N\rightarrow I}$ and T_{NI}, with the dashed lines ± three error bars. 120

7.3 $T_{N\rightarrow I}$ (red) and T_{NI} (blue) upon heating of a single E7 semi-droplet with predicted height = 208µm over 14 days and six temperature cycles. The solid lines indicate the average $T_{N\rightarrow I}$ and T_{NI}, with the dashed lines ± three error bars. 121

7.4 Measurements of $T_{N\rightarrow I}$ (red) and T_{NI} (blue) on heating to quantify the shelf life of MLC 7023 semi-droplets. *a:* A single semi-droplet with predicted height = 208µm, experiencing either the temperature cycle in Table 7.1(1a) (Day 0) or in Table 7.1(1b) (Day 1). *b:* MLC 7023 after experiencing the temperature cycle in Table 7.1(2a) as semi-droplets with predicted height = 420µm, and subsequently pipetted into untreated cover slips. The measurements are from MLC 7023 in untreated cover slips. The solid lines indicate the average $T_{N\rightarrow I}$ and T_{NI}, with the dashed lines ± three error bars. 123

8.1 Transition temperatures on cooling for $T_{I\rightarrow N}$ (blue), $T_{N\text{-}N_x}$ (green) and $T_{N_x\text{-}N_f}$ (red) for the small, medium and large FNLC-919 semi-droplets measured in reflection (R) or transmission (T) imaging modes. The expected values from Merck are labelled with grey solid horizontal lines. 134

8.2 Cooling over the I - N phase transition of the small FNLC-919 semi-droplet in *a*: reflection and *b*: transmission mode polarised images. The potential centre of a possible strength = ± 1 defect is indicated in orange (*biv*). P, A and R show the relative directions of the polariser, analyser and rubbing, respectively. The reflection scale bars are 2mm, and for transmission are 0.5mm. 136

8.3 *a,c,e:* Reflection and *b,d,f:* transmission mode polarised images of the *a,b:* small, *c,d:* medium and *e,f:* large FNLC-919 semi-droplets at two temperatures in the N phase on cooling, *i:* a few degrees after $T_{I \rightarrow N}$ and *ii:* near the N - N_x transition. The blue arrows highlight some disclination lines (*ai,cii,eii*), the orange circle presents the origin of four dark brushes (*bi*), the yellow dashed line demonstrates an inner square (*ci,ei*), the purple dashes denote the edges of bright brushes (*dii,fii*), the green circles are low birefringence colour examples (*dii,fii*), the purple arrows indicate examples of brush-like textures (*dii,fii*), and the red arrow is an example of another brush-like texture (*eii*). P, A and R show the relative directions of the polariser, analyser and rubbing, respectively. The reflection scale bars are 2mm, and for transmission are 0.5mm. 137

8.4 *a:* Reflection and *b:* transmission mode polarised images across the N - N_x phase transition on cooling for the small FNLC-919 semi-droplet. Blue lines show the approximate direction of the line textures (*ai,aii*) and purple lines indicate the edges of dark brushes (*biii*). P, A and R show the relative direction of the polariser, analyser and rubbing, respectively. The scale bars are 2mm for reflection, and for transmission are 0.5mm. *c:* Suggested splay stripe structure. Not to scale. *c based from [28, 29].* Note: The textures in *a* are difficult to resolve, even after contrast enhancement. 140

8.5 *a,c*: Reflection and *b,d*: transmission mode polarised images across the N - N_x phase transition for the *a,b*: medium and *c,d:* large FNLC-919 semi-droplets. The green circles highlight exemplar regions of low birefringence colour (*bi,di*), the blue circles highlight a small dark region (*bii,biii*), and the purple dashes indicate bright and dark fringes (*b,d*). P, A and R show the relative directions of the polariser, analyser and rubbing, respectively. The scale bars are 2mm for reflection, and for transmission are 0.5mm. 142

8.6 *a:* Reflection and *b:* transmission mode polarised images of the small FNLC-919 semi-droplet across the N_x - N_f phase transition. The blue and yellow dashes highlight the directions of the textures. P, A and R show the relative directions of the polariser, analyser and rubbing, respectively. The scale bars are 2mm for reflection, and for transmission are 0.5mm. Note: Especially in *a*, the textures are difficult to resolve due to contrast limitations. 144

8.7 Transmission mode images of the small FNLC-919 semi-droplets a few °C *a:* before and *b:* after the N_x - N_f phase transition to highlight the approximately 10x difference in the stripe texture periodicity. P, A and R show the relative directions of the polariser, analyser and rubbing, respectively. The scale bars are 0.5mm. . . 145

8.8 Transmission mode images of the *a:* medium and *b:* large FNLC-919 semi-droplets across the N_x - N_f phase transition. A dark spot is circled in blue (*ai-iv*), green represents disclination lines (*avix,bvi*), red highlights the outer borders of two very subtle, potential dark brushes suggesting a possible strength = $\pm \frac{1}{2}$ defect (*av,axi*), and yellow is a guide to the texture directions. P, A and R show the relative directions of the polariser, analyser and rubbing, respectively. The scale bars are 0.5mm. 147

8.9 Variation of Δn_{eff} with temperature on cooling across the N phase of the small FNLC-919 semi-droplet. 148

8.10 Schematic of the hybrid-aligned ferroelectric nematic director of FNLC semi-droplets through the dimensionless height of the semi-droplet, $\frac{z}{h}$, from planar at the patterned surface, to homeotropic at the air/FNLC interface in the N phase. *Figure adapted from [1].* 150

8.11 *ai:* Reflection mode image of the small FNLC-919 semi-droplet at 51.2°C on heating. The scale bar is 2mm. *aii* The same region at 51°C on cooling. The scale bar is 1mm. *b:* Transmission mode image after the second temperature cycle of the large FNLC-919 semi-droplet. The scale bar is 1mm. The instability features are highlighted by the yellow circles. P, A and R show the relative directions of the polariser, analyser and rubbing, respectively. . . 151

8.12 Reflection mode polarised images of the shrinkage behaviour of small FNLC-919 semi-droplets for *a:* rubbed and *c,d:* non-rubbed surfaces. *b:* Plot of the shrinkage with temperature along the axis marked in white in *a*, normalised to the width at 50°C. For the non-rubbed semi-droplet, images are presented on *c:* heating and *d:* cooling. The orange circle indicates the impurity on the sample (*ci*), the green circle highlights the shrinkage forming an instability (*cii*), and the blue arrow shows the 'shadow' remaining near the end of the temperature cycle (*diii*). P, A and R show the relative directions of the polariser, analyser and rubbing, respectively. The scale bars are 2mm. 153

8.13 Transmission mode polarised images of the small semi-droplet after the *a:* first and *b:* second temperature cycles. The annotations in *ai* demonstrate features of the director field: *yellow*: large domain aligning approximately perpendicular to the rubbing axis, *purple*: domains aligning approximately parallel to the rubbing axis, *orange*: dark point, *red*: triangular end points of domains, *blue*: small textures approximately parallel to the rubbing axis, *green*: brush-like textures. P, A and R show the relative directions of the polariser, analyser and rubbing, respectively. The scale bars are 2mm. 156

8.14 Description of twist in FNLC systems. *a:* Reproduction of Figure 8.13a to highlight the domains perpendicular to the rubbing axis. The scale bar is 2mm in *ai* and 1mm in *aii*. *b:* π-twist of the director throughout the height of an FNLC sample observed for domain-like structures in the literature that lie perpendicular to the rubbing axis. *c:* The sharper domain structures observed in some works that demonstrate twist. (*cii, ciii*). P, A and R demonstrate the relative directions of the polariser, analyser and rubbing, respectively. Not to scale. *b,c redrawn and/or adapted from information in [12].* 157

8.15 Transmission mode images of a second and third small FNLC-919 semi-droplet on *a:* rubbed or *b:* non rubbed surfaces. The analyser is untwisted with respect to crossed with a second polariser in *aii,aiii,bi,biii*, with different optical regions observed in the different conditions as circled in yellow as an example. P, A and R show the relative directions of the polariser, analyser and rubbing, respectively. The scale bars on *i* are 2mm, and on *ii,iii* are 0.5mm. 158

8.16 Schematics of different twist angles. *a:* A twist angle of 360°would be less energetically favourable than a 180°due to the added director distortion. *bi:* If the twist angle is 90°or 270°, and the directors rotate in opposite directions, the director (and hence polarisations, see Section 2.3) will be opposite to each other, with the domain wall director rotating in one of the ways as shown in *bii*. *bi and bii redrawn/ adapted from information in [11, 30, 31] and [30, 31], respectively.* 160

8.17 Highlighted regions of the *ai:* reproduced Figure 8.13a. *aii:* Reproduced Figure 8.13b for reference. P, A and R show the relative directions of the polariser, analyser and rubbing, respectively. The scale bar is 2mm. *b:* At the end of the perpendicular domains there are triangular points, likely approximately 180°twist regions. *c:* The domains that align approximately parallel to the rubbing axis could be from a β°twist angle. *d:* Dark regions are observed at the combination of the domain lines. *e:* Textures parallel to the rubbing axis. *f*: Brush-like textures parallel to the rubbing axis at the edge and perpendicular to it at the top of the semi-droplet. Schematics not to scale. The scale bars are 1mm. *b,c as well as d schematics redrawn and/or adapted from information in [12, 30] and [30]([31]), respectively.* 162

8.18 Transmission mode polarised images of the *a*: medium and *b*: large FNLC-919 semi-droplets after the second temperature cycle. The red dashed lines show an approximate shape of the domain structures. P, A, and R show the relative directions of the polariser, analyser and rubbing, respectively. The scale bars are 2mm. . . . 164

A.1 Annotated options for the code written to efficiently align images measured under increasing height. The user saves the images as the corresponding temperature and includes them in a list in the code. The code inserts the images, aligns them, and labels them. This could easily be adapted for use in, for example, increasing voltage. The whole code is not included here. 176

A.2 Droplet of E7 on homogeneous SE130 polyimide or silane to measure the contact angle. *Images included in DOI of [1].* 177

A.3 Varying NLC 'semi-droplet' volumes confined in 11 x 11 mm squares on chemically patterned surfaces with a rubbed alignment layer on a solid substrate and an NLC/air interface. Maximum heights measured using pink birefringent fringes are compared to those predicted heights from the presented models from calculation of the semi-droplet cross-sectional area ($V = AL$), leading to predictions of ϵ (Equation 4.2), interface angle (Equation 4.7) and finally, height (Equation 4.6). The rubbing direction is at 45°to the crossed polarisers, with arrows marked P, A and R to show the relative directions of the polariser, analyser and rubbing respectively. The scale bars are 3mm. (*): Only rubbing axis known, but number of fringes counted to measure the height if clear fringes are present. The cropping of the images was varied to ensure that the field of view required to capture all the information (e.g any overflowing liquid crystal) is retained while maximising the image visibility. *Image adapted from supplementary information in [1].* . 178

A.4 Varying NLC 'semi-droplet' volumes confined in rectangles of *a-d:* 16 x 13mm; *e,f* 20 x 10mm, on chemically patterned surfaces with a rubbed alignment layer on a solid substrate and an NLC/air interface. Maximum heights measured using pink birefringent fringes are compared to those predicted heights from the presented models from calculation of the semi-droplet cross-sectional area ($V = AL$), leading to predictions of ϵ (Equation 4.2), interface angle (Equation 4.7) and finally, height (Equation 4.6). The rubbing direction is at 45°to the crossed polarisers, with arrows marked P, A and R to show the relative directions of the polariser, analyser and rubbing respectively. The scale bars are 3mm. (*): Only rubbing axis known, but number of fringes counted to measure the height if clear fringes are present. The cropping of the images was varied to ensure that the field of view required to capture all the information (e.g any overflowing liquid crystal) is retained while maximising the image visibility. *Image adapted from supplementary information in [1].* 179

A.5 Annotated code to fit the measured height across the semi-droplet cross-section widths. 180

A.6 Rotation of crossed polarisers through 0°- 45°with respect to the rubbing direction of E7 semi-droplets with predicted heights: *a:* 42µm, *b:* 75µm, *c:* 125µm, *d:* 208µm. P, A and R show the relative directions of the polariser, analyser and rubbing direction, respectively. The scale bars are 2mm. The * indicates where the imaging exposure was known to be adjusted to preserve the quality of the images. 181

A.7 Rotation of crossed polarisers through 0°- 45°with respect to the rubbing direction of E7 semi-droplets with predicted heights: *a:* 290µm, *b:* 330µm, *c:* 380µm, *d:* 420µm. P, A and R show the relative directions of the polariser, analyser and rubbing direction, respectively. The scale bars are 2mm. The * indicates where the imaging exposure was known to be adjusted to preserve the quality of the images. 182

A.8 Polarised light imaging of varying MLC 7023 semi-droplet volumes confined in 6mm chemically patterned squares with a rubbed alignment layer on a solid substrate and an air/NLC interface. Maximum heights measured using pink birefringent fringes are compared to the those predicted from calculation of the semi-droplet cross-sectional area ($V = AL$), leading to predictions of ϵ (Equation 4.2), interface angle (Equation 4.7) and finally, height (Equation 4.6). P, A and R show the relative directions of the polariser, analyser and rubbing, respectively. The scale bars are 2mm. The cropping of the images was varied to ensure that the field of view required to capture all the information (e.g. any overflowing liquid crystal) is retained while maximising the image visibility). 183

A.9 Annotated code to calculate the air/NLC interface tilt angle of the MLC 7023 semi-droplets, based on a comparison of Δn_{eff} calculated for 10000 air/NLC angles with the expected $\Delta n_{\text{eff}} = 0.036$. 184

A.10 Plots through the dimensionless height of the MLC 7023 semi-droplet, $\frac{z}{h}$, of *a:* director angle, ϕ, *b:* extraordinary refractive index, n_{e}, and *c:* $n_{\text{e}}(\frac{z}{h}) - n_{\text{o}}$, where n_{o} is the ordinary refractive index. *Image adapted from supplementary information in [1].* . . . 185

A.11 Rotation of crossed polarisers through 0°- 45°with respect to the rubbing direction of MLC 7023 semi-droplets with predicted heights: *a:* 42µm, *b:* 75µm, *c:* 125µm, *d:* 290µm, *e:* 330µm, *f:* 420µm. P, A and R show the relative directions of the polariser, analyser and rubbing direction, respectively. The scale bars are 2mm. The * indicates where the imaging exposure was known to be adjusted to preserve the quality of the images. The yellow circles in *c,d,f* indicate examples of potential origins of possible strength $= \pm\frac{1}{2}$ defects. 186

A.12 Rotation of crossed polarisers through 0°- 45°with respect to the rubbing direction of a MLC 7023 semi-droplet with a predicted height = 208µm. P, A and R show the relative directions of the polariser, analyser and rubbing direction, respectively. The scale bars are 2mm. The yellow circles indicate examples of potential origins of possible strength = $\pm\frac{1}{2}$ defects. 187

A.13 Rotation of crossed polarisers through 0°- 45°with respect to the rubbing direction of E7 semi-droplets with predicted heights: *a:* 75µm, *b:* 125µm, *c:* 208µm, *d:* 290µm, *e:* 330µm, *f:* 380µm. P and R show the relative directions of the polariser and analyser, respectively. The scale bars are 2mm. The yellow circle in *a* represents the origin of the potential strength = +1 defect. The green circles in *c* represent the origins of possible strength = $\pm\ \frac{1}{2}$ defects. 188

A.14 Rotation of crossed polarisers through 0°- 45°with respect to the rubbing direction of MLC 7023 semi-droplets with predicted heights: *a:* 75µm, *b:* 125µm, *c:* 208µm, *d:* 290µm, *e:* 330µm. P and R show the relative directions of the polariser and analyser, respectively. The scale bars are 2mm. The yellow circles in *a,b* represent the origins of the possible strength = +1 defect. 189

A.15 Polarised images of a single E7 semi-droplet with predicted height = 208µm for three heating and cooling cycles, imaged at 60°C on heating. P and A show the relative positions of the polariser and analyser, respectively. The scale bars are 0.5mm. 190

A.16 Images of a hot plate heated to 100°C at 10°Cmin^{-1}. The hot plate was cleaned with IPA and a shape was drawn onto the window prior to heating with *a:* no sample, *b:* three chemically patterned surfaces or a *c:* MLC 7023 sample with a free surface, on the hot plate. The images in *c* shown most sign of additional blurriness, with an example circled in yellow. The scale bars are 0.5mm. The movement of the image drawn onto the window is a result of the exact positioning of the window over the imaging hole in the hot plate. Imaged with no polarisers. Improvement of this investigation to further understand the effect of the 'misting' is saved for future work. 191
A.17 Thermogravimetric analysis of MLC 7023 between 30°C and 100°C, normalised to the mass at 30°C. The heating rate was 10°Cmin^{-1}. There is a minimal change over this temperature range of 0.8%. *Data taken by Thomas Raistrick.* 192
A.18 Plots through the dimensionless height of the FNLC-919 semi-droplet, $\frac{z}{h}$, of *a:* director angle, ϕ, *b:* extraordinary refractive index, n_e, and *c:* $n_e(\frac{z}{h}) - n_o$, where n_o is the ordinary refractive index. *Image adapted from supplementary information in [1].* . . . 194
A.19 Polarised image of an E7 semi-droplet with predicted height = 208µm to qualitatively evaluate the reusability of the patterned surfaces after use with FNLC-919. P, A and R show the relative directions of the polariser, analyser and rubbing, respectively. The scale bar is 2mm. 195
A.20 Polymer network in a 16 x 13mm rectangle with a free surface. A sample of E7 was polymer stabilised before the E7 was washed out of the network with IPA. Further details are beyond the scope of this thesis, and are left for future work. P, A and R show the relative direction of the polariser, analyser and rubbing, respectively. 196

Chapter 1

Introduction

1.1 Introduction

Liquid crystals (LC) are utilised for a growing number of applications in everyday life, from the very common liquid crystal display, e.g.[32, 33, 34, 35, 36], to developing technologies such as augmented and virtual reality devices, e.g.[37, 38, 39, 40, 41]. One exciting use is LC-based sensing devices, e.g.[16, 42, 43, 44, 45], utilising the long-range orientational order and liquid properties of LCs, resulting in a sensitive and rapid detection of analytes[46]. A common geometry for such sensing devices is LC droplets with the method of detection often a clear optical contrast of images taken under polarised optical microscopy (POM) pre- and post-analyte addition. This is the detection mechanism that is the focus of discussion throughout this thesis.

A key issue with the droplet geometry is that micron sized droplets are colloidal systems that tend to coalesce and therefore do not have a long shelf-life as was a main investigative goal in many works such as the thesis by A. Parry[47]. Therefore, a different structure is suggested in this work in which LC is confined on a solid patterned surface with a free air/LC interface. The confinement behaviours in rectangles on the order of millimetres in size for two nematic LCs (NLC) will be used to identify suitable parameter spaces for future sensing devices such as the

confinement size, the dispense volume of NLC into the confinements, and the clarity of the director field pre- analyte addition. The reusability and shelf-life of the surfaces will be discussed in relation to sustainablity and stability as sensing devices. An interesting extension is the deposition of the relatively new ferroelectric nematic liquid crystal material from Merck, FNLC-919, into the confinements.

1.2 Roadmap

In the next chapter, Chapter 2, fundamental LC concepts underpinning the data presented in later chapters are introduced. This consists of the main properties of NLCs and FNLCs, an introduction to literature related to LCs confined in rectangular shapes, and an outline of literature on LC-based sensing using polarised imaging as the detection method.

The main experimental methods and materials used throughout the thesis are introduced in Chapter 3, including most prominently a description of the method to fabricate the patterned surfaces to confine LCs, as well as polarised light imaging as this is the most commonly used characterisation technique in this work. The key properties of the LCs used are also summarised.

Chapter 4[1] is the first results chapter and develops the analytic methods used throughout the thesis. Four different rectangular confinement sizes are fabricated and various confined NLC E7 heights are created within these rectangles, towards optimisation of the device configuration for future sensing devices. The well-documented E7 is chosen to allow for a focus on the geometric effects without the added complications of unknown material properties. A 6 x 6mm square is identified as that with the greatest potential for successful sensing devices of those investigated in this chapter, hence is the size focused on for the rest of the thesis. A non-LC specific model is derived to predict the height and shape of a confined LC cross-section, and validated by comparison to the confined LC height measured from polarised imaging.

[1] A significant portion of Chapter 4 is published in [1].

In Chapter 5 the same experimental methods from Chapter 4 are used, but for the NLC MLC 7023 that, when compared to E7, has a similar density but much lower surface tension[48] and birefringence[1][49]. The key reason for this choice of NLC is that literature indicates that the average orientation of the molecules at air/NLC interface is different to E7[15, 48] and could therefore allow for a greater contrast in polarised imaging for a larger range of analytes in sensing applications.

Chapter 6 again uses the same methods as Chapters 4 and 5 as well as using both E7 and MLC 7023, but instead of the chemically patterned surfaces used in Chapters 4 and 5 that have a rubbed alignment layer, the surfaces used in this chapter are fabricated without the rubbing step. The motivation is the potentially simplified surface patterning method if the suitability of the director field pre- analyte addition for sensing devices is comparable or better than the rubbed surfaces.

The patterned surfaces discussed in Chapters 4 - 6 are reused for multiple measurements, hence the reusability of the surfaces is quantitatively validated in Chapter 7. Experiments to test the shelf-life of E7 and MLC 7023 confined on the patterned surfaces are also presented.

Although a proof-of-concept of the system as a sensing device is worthwhile future work, a more novel investigative route was chosen for Chapter 8. Three different confined LC heights of the recently introduced ferroelectric nematic liquid crystal from Merck, FNLC-919, are confined in squares fabricated using the same methods as in the previous chapters. As the specific properties of FNLC-919 are less documented than E7 and MLC 7023, this investigation has a greater focus on understanding the system rather than towards sensing applications.

Finally, Chapter 9 provides a summary of the key results obtained throughout the thesis as well as recommended future work.

[1]Data sheets from Merck.

Chapter 2

Background

Please note a small portion of this chapter is published in A. Bond *et al.* (2025). The behaviour of nematic liquid crystals in chemically patterned millimetre-sized rectangular surfaces. *Liquid Crystals*. pp 1-15. https://doi.org/10.1080/02678292.2025.2489426[1]. Figures that have been taken or adapted from [1] are marked in the relevant captions.

2.1 Introduction

There are excellent textbooks that describe liquid crystal physics and optics in depth such as the 'Handbook of Liquid Crystals'[50], 'Introduction to Liquid Crystals: Chemistry and Physics'[51], 'Fundamentals of Liquid Crystal Devices'[52], 'Optics'[53], and 'Polarized Light in Liquid Crystals and Polymers'[54], to name a few. The following background as well as methods and materials chapters (Chapters 2 and 3, respectively) focus on the key information required to understand the data presented throughout this thesis. In this chapter, the background behind nematic and ferroelectric nematic liquid crystals (NLCs and FNLCs, respectively) will be introduced, followed by an outline of background literature for both the confinement of LCs in rectangular confinements and LC-based sensing examples.

2.2 Nematic Liquid Crystals

2.2.1 Nematic Phase Geometries and Order Parameter

Liquid crystalline phases lie between solids and liquids[3] with a key property being the director, $\boldsymbol{n}$, that describes the average direction of the liquid crystal's composite molecules[4]. For the rod-like molecules that make up calamitic NLCs, this director is symmetric as denoted by $\text{-}\boldsymbol{n} = \text{-}\boldsymbol{n}$ in Figure 2.1. The molecules often have an instantaneous angle, φ, (with the average along the director) from parallel to the director with a measure of the quality of this alignment given by the order parameter,

$$\text{Order parameter} = \langle \frac{3}{2}\cos^2(\varphi) - 1 \rangle. \tag{2.1}$$

The $\langle\rangle$ brackets indicate an average over the LC sample. For an order parameter

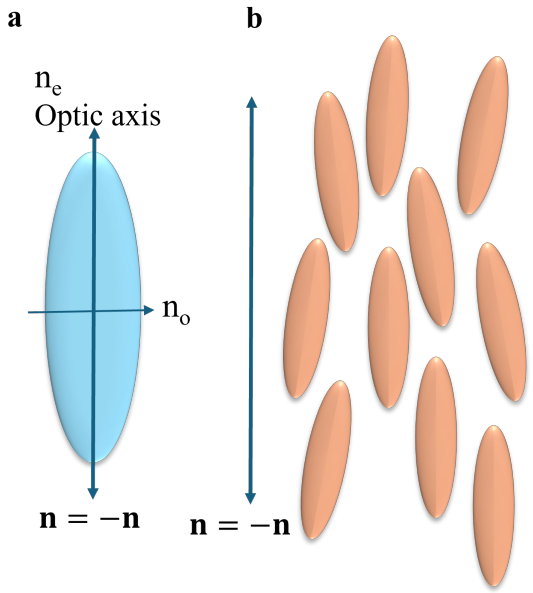

Figure 2.1: *a*: An optical indicatrix of the average values of an aligned sample of the nematic phase. n_o and n_e represent the ordinary and extraordinary refractive indices, respectively, and the symmetric director is demonstrated by $\boldsymbol{n} = \text{-}\boldsymbol{n}$. *b:* Schematic of an aligned nematic phase sample. Not to scale. *a, b redrawn/adapted from information in references such as [2] and [3, 4], respectively.*

of 0 the LC is completely randomly oriented, and for an order parameter of 1 there is perfect alignment with a φ of 0°[3].

An important property of NLCs is their phase behaviour with increasing temperature from crystalline, Cr, into the nematic, N, phase and finally into the isotropic, I, phase[55],

$$\text{Cr} \longleftrightarrow \text{N} \longleftrightarrow \text{I}.$$

The most relevant phase change for this thesis is the first order[56] nematic-to-isotropic transition, with a general change in order parameter from 0 in the I phase, to 0.4 - 0.7 in the N phase[55]. When E7 is taken as an example, as it is a commonly used NLC throughout this thesis, at the nematic-to-isotropic temperature the order parameter is approximately 0.3 before increasing to approximately 0.73 at 0.8 times the transition temperature[57].

Aligned nematic phase samples have two main perpendicular axes corresponding to an ordinary or extraordinary refractive index, n_{o} or n_{e}, respectively[2, 58], with the optic axis denoting the axis along which light propagating through the liquid crystal will not experience birefringent effects[2] (see Section 2.2.2). In the nematic phase there is long range orientational order that makes them suitable for sensing devices[46].

2.2.2 Birefringence

Birefringence, Δn, is important in the characterisation of NLC samples *via* polarised light imaging, a method that will be described in depth in Section 3.3. The principle of birefringence is described schematically in Figure 2.2 and can be calculated by[5],

$$\Delta n = n_{\text{e}} - n_{\text{o}}. \tag{2.2}$$

If linearly polarised light enters a birefringent sample at an angle not parallel to the optic axis[2], perpendicular light components will by slowed an amount corresponding to n_{e} or n_{o}. After traversing the sample, the light components will

be shifted with a path length, Γ, relative to each other and the vectorial addition of these components could result in a different polarisation of light compared to the original linear polarisation[5]. Another name for $\Gamma = \Delta n \cdot height$ is the retardation[25] and will be discussed further in Section 3.3.2.

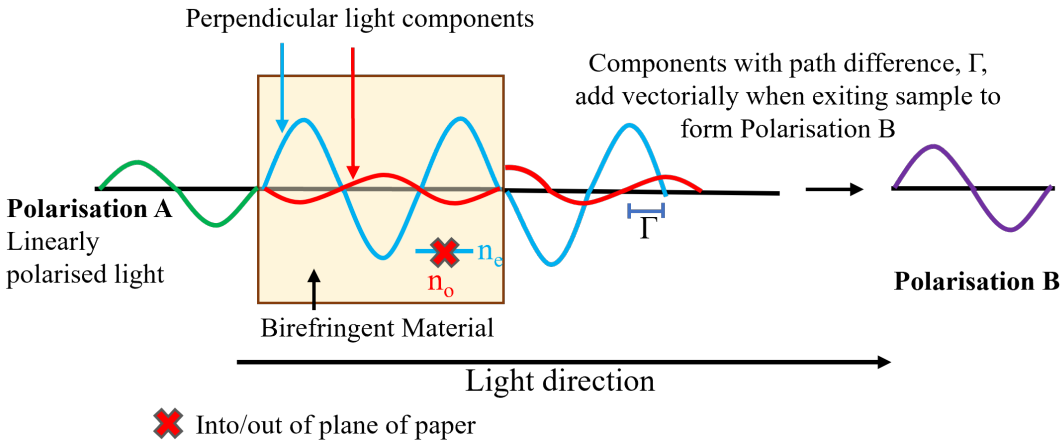

Figure 2.2: Schematic of the principle of birefringence. When linearly polarised light (Polarisation A) enters a birefringent material, perpendicular light components are slowed by different amounts corresponding to n_e and n_o. The components leave the material with a path difference, Γ, and vectorially add, resulting in a changed polarisation of the light (Polarisation B). In this schematic, n_o is arbitrarily into the plane of the paper and experienced by the light component arbitrarily drawn in red, and n_e is perpendicular to this and drawn arbitrarily in blue. The apparent discontinuity of the wave on exiting the sample in this schematic is not a real feature, and is as a result of forming a clear description. Not to scale. *Based off of information in references such as [5].*

2.2.3 Director Fields

Throughout this thesis, the term 'director field' refers to the orientation of the director throughout the confined LCs. Director fields of NLCs will form in such a way as to minimise the free energy of the system, f_{total},

$$f_{\text{total}} = f_{\text{field}} + f_{\text{elastic}} + f_{\text{surface}}, \tag{2.3}$$

as summarised by Yang[59] for LC droplets. There is no electric or magnetic field applied to the semi-droplets in this work, therefore the f_{field} term is not considered. The f_{surface} and f_{elastic} terms are interpreted and described here in a suitable manner for the confined LC in the current work.

The energy density of the elastic components of an NLC[60], is given by the Frank-Oseen energy equation[61, 62],

$$f_{\text{elastic}} = \frac{1}{2}K_1(\nabla \cdot \boldsymbol{n})^2 + \frac{1}{2}K_2(\boldsymbol{n} \cdot \nabla \times \boldsymbol{n})^2 + \frac{1}{2}K_3(\boldsymbol{n} \times \nabla \times \boldsymbol{n})^2, \tag{2.4}$$

based on the director, $\boldsymbol{n}$, and three elastic constants named splay, K_1, twist, K_2 and bend, K_3[4, 6]. A schematic representation of the elastic constants is given in Figure 2.3.

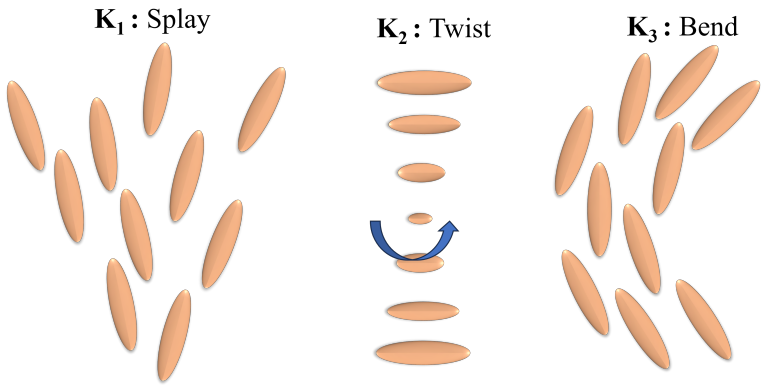

Figure 2.3: Schematics of the three key elastic constants of liquid crystals including splay (K_1), twist (K_2) and bend (K_3). Not to scale. *Redrawn/ adapted from references such as [4, 6].*

For the f_{surface} term, it is important to note that the director field alignment is related to the anchoring conditions[63]. For example, often an alignment layer is formed by rubbing a polyimide to give the NLC director a preferred direction. The most important anchoring conditions for this thesis are non-rubbed planar, rubbed planar and homeotropic as demonstrated in Figures 2.4a-c, respectively. The molecules on average lie parallel to the plane of the substrate, in the substrate plane along one preferred direction, or perpendicular to the sub-

strate plane, respectively. The nomenclature of homogeneous and planar are often interchanged[7]. For tilted anchoring, the angle of the molecules lies on average somewhere between parallel and perpendicular to the substrate plane. Some polyimides can induce a pretilt[4], in which the director is not parallel to the plane of the substrate[7] as shown in Figure 2.4b.

It is well known that the effect of the anchoring decreases until approximately 100µm from a bounding surface in NLCs. This is an important factor throughout this thesis as the height of the confined LCs varies between approximately 20 - 420µm.

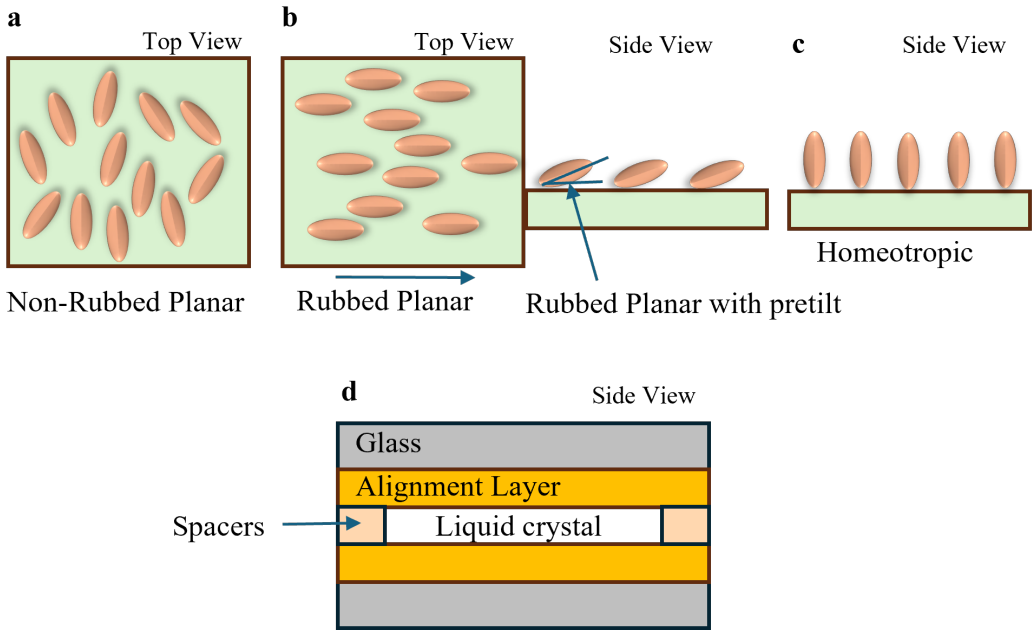

Figure 2.4: Schematics of *a-c:* the common anchoring used in LCs. *a:* Non-rubbed planar. *b:* Rubbed planar with the director along the rubbing direction. A pretilt from parallel to the surface is sometimes observed. *c:* Homeotropic alignment, with the molecules perpendicular to the anchoring surface. *d:* The commonly used LC 'cell' for NLC investigations. Not to scale. *a-c, and d redrawn/adapted from information in references such as [4, 7] and [3, 8], respectively.*

Another important consideration is the geometry of the confining region, with reviews of the effect given in references such as [64, 65]. The most common is

confinement of NLC between two glass surfaces filled by capillary action of the LC, using some material to form the cell thickness as presented in Figure 2.4d. A discussion of relevant literature for LCs confined in rectangles is given in Section 2.4. Geometries commonly used for LC-based sensing are introduced in Section 2.5.1, where the LC is often interfaced with a fluid or air[16] to allow diffusion of analytes towards the LC surface.

Defects are locations where there are discontinuities in the director and can be read about in more depth in references such as[6, 9, 66]. Figure 2.5 provides schematics of the four defects relevant to this thesis, i.e. those with strengths of $\pm$ 1 or $\pm \frac{1}{2}$. The methods to characterise the strength, s, using polarised imaging will be discussed in Section 3.3.3. There are other defects as discussed in e.g [9], including those with strengths of $\pm\frac{3}{2}$ and ± 2, that are beyond the scope of this thesis.

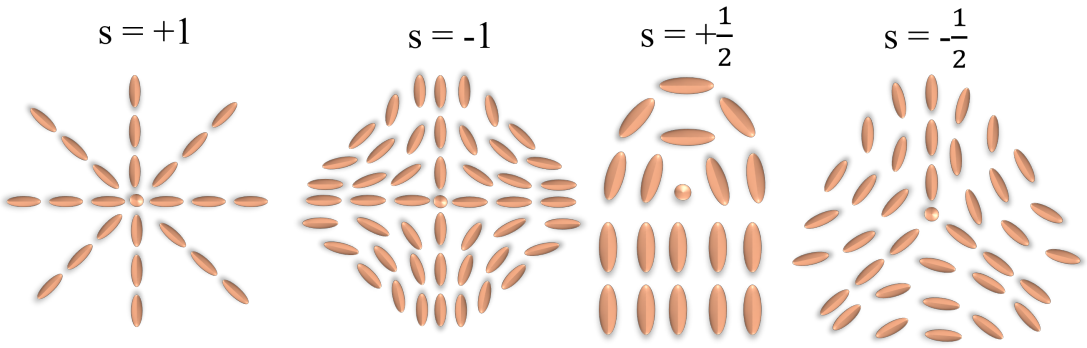

Figure 2.5: Schematics of commonly seen defects in LC director fields with strengths, s, of $\pm$ 1 or $\pm\frac{1}{2}$. Not to scale. *Redrawn/adapted from [9].*

2.3 Ferroelectric Nematic Liquid Crystals

Ferroelectric nematic liquid crystals (FNLCs) are an exciting type of LC predicted 100 years ago by Born[67], with the first experimental examples published in 2017 by Mandle *et al.*[68, 69] and Nishikawa *et al.*[70], most notably for the FNLCs RM734 and DIO, respectively. FNLCs have polar symmetry, with Chen *et al.* first experimentally demonstrating Born's predicted structure, the ferroelectric

nematic, N_f, showing that the polarity vector, $\boldsymbol{P}$, aligns with the director [11, 67]. Unlike for NLCs, the N_f phase director is not symmetric, as denoted by $\boldsymbol{n} \neq \text{-}\boldsymbol{n}$, with research on FNLCs summarised in reviews such as that by Lavrentovich *et al.*[71], Sebastián *et al.*[72], and Liao *et al.*[10]. A schematic of FNLCs is shown in Figure 2.6.

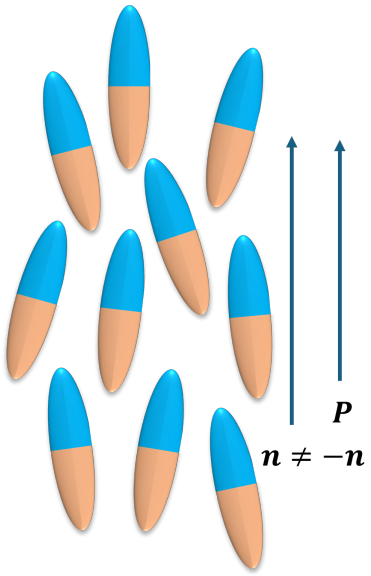

Figure 2.6: Schematic of ferroelectric nematic liquid crystals. The director is non-symmetric, $\boldsymbol{n} \neq \text{-}\boldsymbol{n}$. The dipoles are largely aligned, with the polarity vector, $\boldsymbol{P}$, aligned with the director. Not to scale. *Adapted from information in references such as [10, 11].*

The Merck material FNLC-919 is investigated in this thesis, with the first paper on this system published by Yu *et al.*[12] in 2023 confirming the expected phase progression of,

$$\text{Cr} \leftrightarrow \text{N}_\text{f} \leftrightarrow \text{N}_\text{x} \leftrightarrow \text{N} \leftrightarrow \text{I}$$

where Cr, N and I represent the crystal, nematic and isotropic phases as described in Section 2.2.1. N_x is another nematic phase, the exact properties of which are under debate by the liquid crystal community and the phase been previously labelled for different FNLCs as the e.g. M_2[70], N_x[73, 74], N_s[72, 75] or SmZ_a[76,

77] phase.

A brief introduction to some published research on the confinement behaviours of FNLCs is presented here, with a discussion comparing the experimental results from this thesis with relevant literature given in Chapter 8. For example, when FNLC-919 cells are formed with the rubbing directions parallel to each other, a good uniformity of the N_f phase is observed[12, 14]. In an antiparallel cell, there are twisted domains where the director rotates throughout the FNLC sample height[12, 78]. In Yu *et al.*[12] a twist of approximately 180° is described, as shown schematically in Figure 2.7a. The method to identify this twist will be described in Section 3.3.4.

Perera *et al.*[14] discuss FNLC-919 in a hexagonal confinement of 200µm in width and 20µm in confinement height, identifying a director field centered around a central defect in the N_f, previously discussed for a free surface RM 734 droplet by Mathé *et al.*[13] and shown schematically in Figure 2.7b. Interestingly, for the FNLC-919[14] in the N_f phase there is a lowered region in the centre with a width of approximately 100µm, with the best fits replotted in Figure 2.7c. For the examples presented here for FNLC-919 confinements[12, 14, 78, 79], the thicknesses are $\lesssim$ 20µm, which is generally smaller than the confined LC heights in this work between approximately 20 - 420µm.

For RM 734, four different anchoring conditions are presented by Caimi *et al.*[80], including two rubbed surfaces of silane and teflon, and two unrubbed including Fluorolink® and hydroxylated glass. Kumari *et al.*[27] discuss the alignment DIO on rubbed polyimide with top FNLC-interface conditions including polystyrene, glycerin and air. Another investigation of DIO on glycerin with a free air/FNLC interface is demonstrated by Kumari *et al.*[81]. A significant portion of the sessile FNLC droplets in the literature are placed on or near the ferroelectric material, lithium niobate (LN) e.g.[82, 83, 84, 85, 86, 87] instead of the glass, e.g.[13, 88], that is used in this thesis. A recent review can be found at [89].

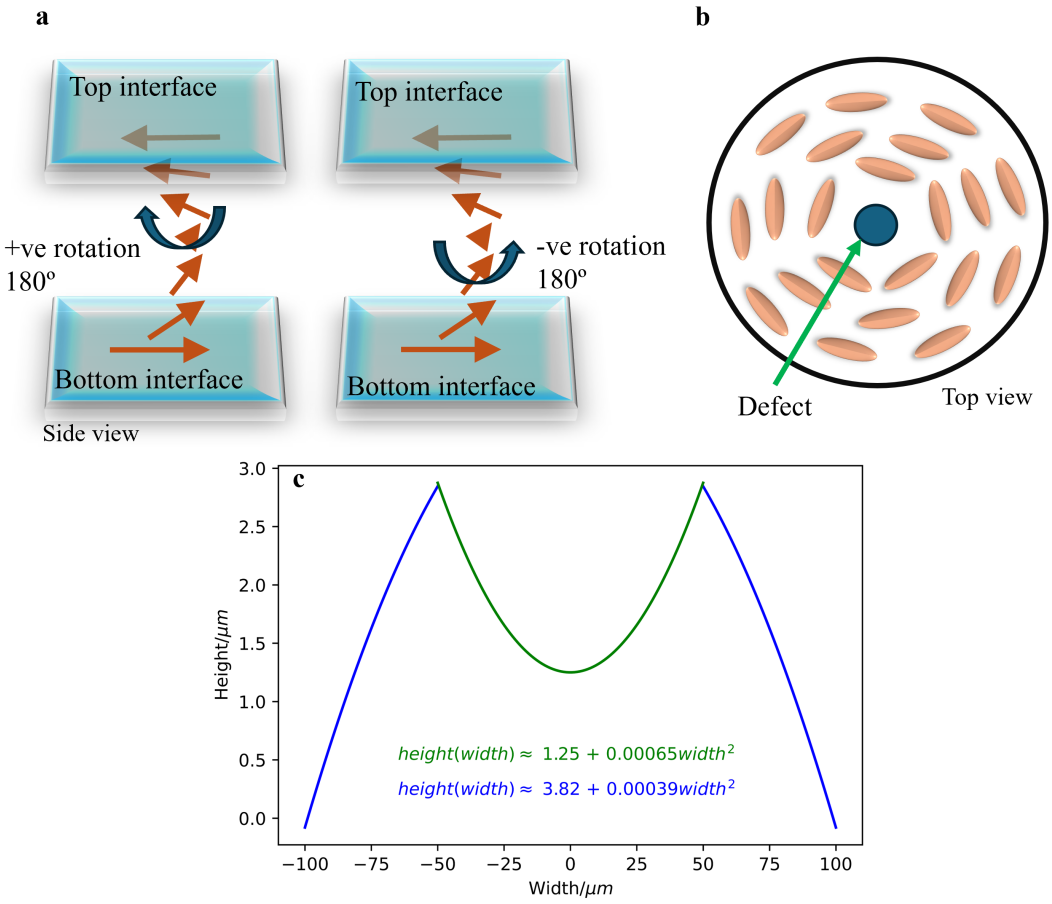

Figure 2.7: Schematics of observations from FNLC-919 confinements in the N_f phase. *a:* The approximate 180° twist of a director seen in an antiparallel planar rubbed FNLC-919 cell. *b:* In free surface samples, a director rotating around a central defect (marked in blue) has previously been observed. Not to scale. *c:* Best fits of a hexagonally-confined free surface sample of FNLC-919 across a width cross-section, demonstrating a lowered region in the centre. *a,b,c redrawn/adapted from information in [12] and [13, 14] and [14], respectively.*

2.4 Liquid Crystals Confined in Rectangular-like Shapes

It is well researched that the behaviour of LCs is strongly dependent on the anchoring conditions, confinement shape, and elastic constants as was discussed in Section 2.2.3. In this work, three different LCs with varied physical properties are

confined within rectangles with a range of aspect ratios. The research topic of LC confined in rectangular-like shapes is broad, therefore there is ample theoretical and experimental literature that could be included, e.g.[1, 15, 90, 91, 92, 93, 94, 95, 96, 97, 98, 99, 100, 101, 102]. A focus is given to the papers by Bao *et al.*[15] in 2021 and Cousins *et al.*[100] in 2023 as these form the basis for Chapter 4, hence the basis for the rest of this thesis.

Bao *et al.*[15] discuss stripes (rectangles with a low width : length ratio) with widths between 10 and 30µm, fabricated with the key steps of using a direct-write laser to pattern the surfaces, cleaning the surfaces with O_2 plasma, and deposition of a self-assembled monolayer, with no specific alignment layer on the LC confinement area. They present an equation for the maximum height of the confined NLC related to the number of interference fringes imaged in reflection mode (a mode that will be discussed in Section 3.3.1),

$$height = \frac{fringes \cdot wavelength}{2n_{\text{av}}},$$

where the wavelength is that of the imaging light and n_{av} is the average refractive index. This method is not suitable for the much taller confined LCs in this thesis as the fringes cannot be clearly viewed. Additionally, the angle of the LC at the confinement edge, labelled the contact angle, θ, in Bao *et al.*, is generally not large enough in this thesis to be measured directly without large uncertainties. Therefore, direct use of another equation highlighted by Bao *et al.*,

$$\sin(\theta) = \frac{width}{2 \cdot radius},$$

is not practical here. The radius is that which the confined LC would take if the cross section of the confined LC was continued into a full circle, as indicated in Figure 2.8. These reasons are part of the motivation for forming a non-LC specific model for the height of the confined LC as will be described in Section 4.3.

Bao *et al.*[15] present the height, contact angle and resultant director field for stripes with widths of 30µm as is summarised in Table 2.1 for E7 and MLC

7023. For E7, an 'escaped radial' configuration is observed, which is comprised of a alternating pattern of defects with strengths of ± 1 (see Section 2.2.3). The director configuration for MLC 7023 is less clear. The heights of the stripes in Table 2.1 are approximately one or two orders of magnitude smaller than those presented in this thesis, and the widths are of the order of µms in their work compared to millimetres in this work.

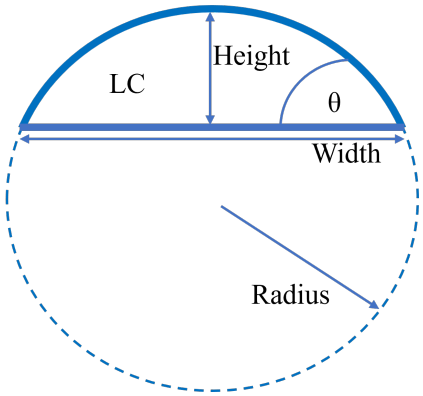

Figure 2.8: Diagram to indicate the contact angle, θ, height, width and radius of the confined LC in the work by Bao *et al.*, modelled as a circle. The solid line denotes the outer border of the confined LC. *Based off of information from [15].*

LC	**Height** µm	**Contact Angle** °	**Director Field**
E7	1.22	9.3	'escaped radial'
MLC 7023	2.04 or 2.02	15.5 or 15.4	∼'escaped radial' or 'twisted planar escaped' or 'planar escaped'

Table 2.1: Summary of properties of LCs confined in stripes with a width of 30µm. *Data from Bao* et al.[15].

Cousins *et al.*[100] utilise rubbed poly(vinyl alcohol) (PVA) as an alignment layer, with confinement created from Teflon surrounding a rectangular shape. The size of the stripes is of a greater order of magnitude to that in Bao *et al.*[15] with a width : length of 1.2 : 60mm. Cousins *et al.* record two situations of approximately 1µL and 3µL 5CB (NLC) dispense volumes into their confinement

area and present a model to describe the height variation across the width of the confined NLC, which is discussed in relation to a derived equation in Chapter 4.

The key extensions to these excellent works are that the height behaviour is measured across the entire confined LC in this thesis compared to at the edges in Cousins *et al.*[100] and the experimental confinements have greater widths than in the papers[15, 100]. Different confinement aspect ratios with a more balanced ratio of width : length than either paper[15, 100] are experimentally investigated here.

2.5 Liquid Crystal- and Polarised Optical Microscopy-Based Sensing

2.5.1 Sensing Mechanism and Geometries

The mechanism targeted in this thesis for LC-based sensing[43] consists of an analyte interacting with an LC surface and causing a local change in the director field. This in turn creates a rapid change in the director field across the whole LC due to the long range orientational order and liquid-like properties of LCs[46]. A commonly used method to detect these changes is to observe an optical change in the director field imaged under polarised optical microscopy (POM)[16]. The LC-droplet geometry is most similar to the samples in this thesis, with the confined LC within the rectangles labelled as 'semi-droplets'. Therefore, the sensing mechanism using LC-droplets is presented schematically in Figure 2.9, for the example of changing from a bipolar to radial director configuration which can be recorded *via* POM[16].

Examples of LC-droplet, POM-based sensing from the literature are discussed in the following sections. Zhan *et al.*[16] present an excellent review into other geometries of LC-based sensors in the literature such as LC-solid or LC-aqueous. More recent reviews are available from, for example, Tang *et al.*[103] and Sil *et al.*[104]. With the shift of all technologies towards artificial intelligence, an

artificial intelligence aspect has emerged for LC-based sensing, as reviewed by Chattha *et al.*[105].

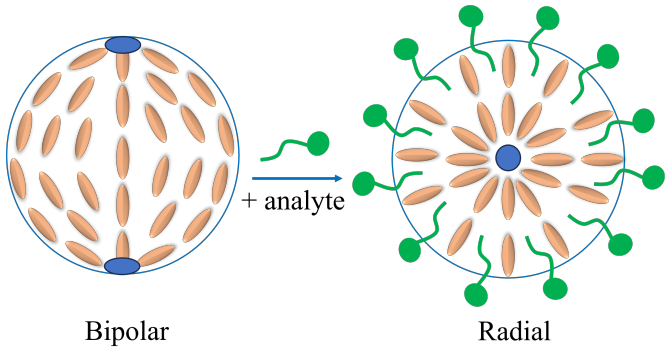

Figure 2.9: Schematic of an exemplar mechanism for LC-droplet based sensing. The droplet is in the bipolar director field configuration before addition of an analyte causes a conversion of the director field to radial, which can be detected *via* POM. The blue circles highlight defects in the director field and the green shapes demonstrate the analytes. Not to scale. *Redrawn/ adapted from references such as [6, 16, 17].*

2.5.2 Liquid Crystal Droplet Stability

The continued improvement of methods to stabilise LC droplets is identified to be of importance in the thesis by A. Parry[47], therefore exemplar methods presented in the literature to do so are presented here, with a focus on POM methods of detection.

Work by Aery *et al.*[17] use proteins from potatoes to stabilise LC-droplets and provide results on sensing sodium dodecyl sulphate (SDS), as well as the effect of using a microgel from that protein. Pickering stabilisation[106] is concluded as the explanation for the microgel having more stability, with a solution lasting for at least a month[17]. Some other examples of stabilisation using the pickering method are presented by Piñeres-Quiñones *et al.*[107] where droplets last for upwards of three months, and by Aery *et al.*[108] being stable for at least a week.

Hydrogels have been used to stabilise droplets, such as the work by Zhang et al[109] using polyacrylamide for the hydrogel with samples lasting for at least four

months. Su *et al.*[110] use a chitosan network for stability, detecting methanol and ethanol using the reflection properties of cholesteric LCs. The sensitivity does not vary largely within a period of thirteen days.

Ma *et al.*[111] present microfluidically fabricated LC droplets with graphene oxide to be stable for at least 10 days.

Whilst this is not an extensive list of the methods previously utilised to stabilise LC-droplets it provides an indication of the range of shelf-lives demonstrated in the literature, a property that is investigated for the semi-droplets in Chapter 7.

2.5.3 LC-based Sensor Sensitivities

An example from the literature that demonstrates the importance of the choice of hydrogel to improve the sensitivity (often called a detection limit) of LC droplet based sensing is by Deng *et al.*[112]. They describe the detection limits for sodium tetradecyl sulphate ($SC_{14}S$), alkyl tetradecyltrimethylammonium bromide ($C_{14}TAB$), cholic acid (CA), and deoxycholic acid (DCA). 5CB droplets are stabilised in hydrogels, with the added functionalisation of $C_{14}TAB$ for the detection of CA and DCA. The detection limits for $SC_{14}S$, $C_{14}TAB$, CA and DCA for an agarose hydrogel are ∼180μM, ∼4μM, 5μM, and 40μM, respectively. The detection limits for $SC_{14}S$, $C_{14}TAB$, CA and DCA for an chitosan hydrogel are ∼8μM, ∼40μM, 2μM, and 10μM, respectively[112].

The work by Aery *et al.*[17] is insightful as it highlights improved detection limit when a microgel of a potato protein is used for droplet stabilisation, compared to just the protein itself. Detection limits of 11.7 and 16.8μM versus 3.2 and 4.3 μm of SDS are reported for the non-microgel and microgel samples, respectively[17]. A droplet with a changing surfactant in the system is demonstrated by Aery *et al.*[108] to change the detection limit. For systems utilising SDS and DTAB (dodecyltrimethylammonium bromide), the detection limits are 155.0μg/mL and 484.1μg/mL for BSA, respectively[108]. Doping LC droplets, such as using 4'-pentyl-biphenyl-4-carboxylic acid, has been presented as having a detection limit of 178μg/mL for penicillin G[113].

Although the specific adaptions to the devices discussed here such integrating a hydrogel, functionalising the semi-droplets or doping the LC could improve the sensitivity, the work in this thesis is more fundamental and therefore similar investigations are suitable as future work. It is hoped that the millimetre sized confinements will create changes in the director field pre- and post- analyte addition on a large enough scale to detect without the need for complicated and expensive polarised microscopy. Additionally, this system may be easier to scale for industrial purposes than microfluidics.

2.6 Summary

This chapter has introduced the key concepts required to describe the results in the next sections of the thesis. The main properties of NLCs including the phase behaviour, birefringence, and director field properties were introduced, as well as a brief description of FNLC material confinements. Background literature relevant to confining LC in rectangles were discussed, as well as a brief discussion of previous LC droplet- and POM- based sensing literature. The next chapter will describe the main experimental methods and associated materials used throughout the thesis.

Chapter 3

Experimental Methods and Materials

Please note some of this chapter is published in: A. Bond *et al.* (2025). The behaviour of nematic liquid crystals in chemically patterned millimetre-sized rectangular surfaces. *Liquid Crystals*. pp 1-15. https://doi.org/10.1080/02678292.2025.2489426[1]. Figures that have been taken or adapted from [1] are marked in the relevant captions.

The method for surface patterning was originally created by Thomas Moorhouse. The photomask for photolithography was designed by Abigail Bond.

3.1 Introduction

In this chapter, key experimental methods used throughout this thesis will be introduced including, most importantly, the fabrication of the chemically patterned surfaces and the polarised imaging theory used to characterise the samples. The materials used are included within the relevant method's description, with the key properties of the LCs used throughout the thesis summarised at the end of this chapter.

3.2 Surface Patterning

3.2.1 Patterning Method Overview

To create the chemically patterned surface shown schematically in Figure 3.1, glass microscope slides were cut to size and cleaned in an ultrasonication bath[114, 115]. The glass was placed under ultraviolet (UV)/ozone[116] for a minimum of 5 minutes, before a polyimide alignment layer was deposited *via* spin coating and mechanically rubbed. Photo resist was then spin coated onto the surface in preparation for photolithography to pattern the rectangles with a bespoke photomask. After development from the photolithography, the samples were exposed to the same UV wavelengths as photolithography with no photomask. A hydrophobic 'monolayer' was then deposited onto the samples, following which the substrates were agitated at least once each in isopropanol (IPA) and deionised water (DI). The majority of the fabrication was completed in a clean room to reduce the likelihood of contaminants on the sample surface. Sections 3.2.2 - 3.2.6 describe the key steps of this process in more depth.

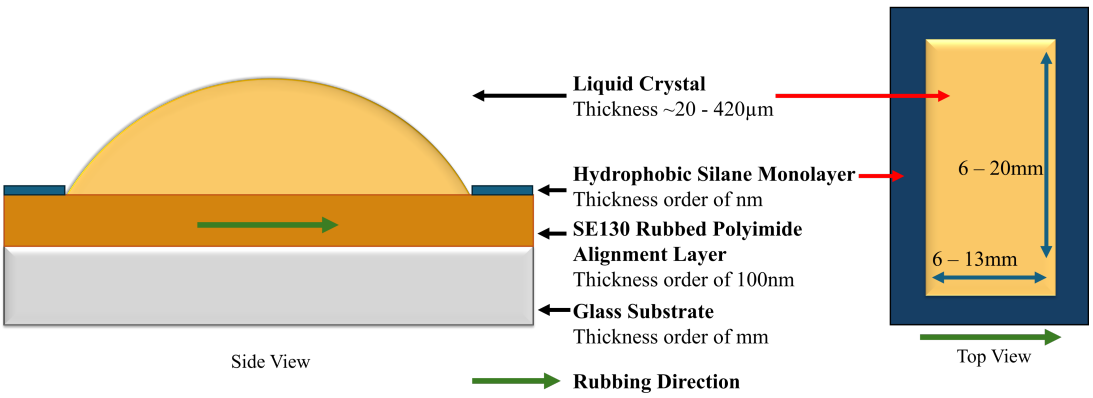

Figure 3.1: Schematic *a*: side and *b:* top view of chemically patterned rectangles, with the LC confined between a hydrophobic monolayer and sitting on a planar rubbed polyimide alignment layer. Whilst it is impractical to draw the schematic to scale, the approximate expected layer thicknesses are labelled to show that the hydrophobic layer is significantly less thick than the LC. *Approximate expected thicknesses based off of information from: LC[1], silane[18], SE130[19]. Left image adapted from [1].*

3.2.2 Glass Cleaning

The glass was cleaned in an ultrasonication bath using the following settings of time, solvent, and heat, respectively: 15 minutes in approximately 10:1 DI:Decon-90 at 40°C; 10 minutes in DI with no active heating repeated twice, and 30 minutes in acetone with no active heating.

3.2.3 Spin Coating

Spin coating is a method by which thin films can be formed through deposition of a liquid onto a substrate and rapid rotation of the substrate on a vacuum stage, with the excess drips flung off the substrate during rotation[20] as shown schematically in Figure 3.2. Whilst inspection of specific parameters for the liquids dispensed is beyond the scope of this thesis, it is worth noting that from a simple perspective, there is an inverse square relation between the height of the film and the rotation speed of the stage[21],

$$thickness \propto \frac{1}{\sqrt{rotation\ speed}}. \tag{3.1}$$

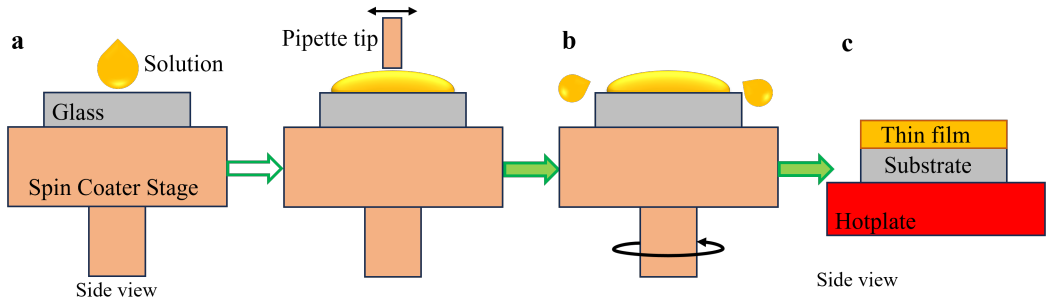

Figure 3.2: Key steps to spin coat a thin film onto a substrate using a static deposition method. *a:* The liquid is deposited onto the surface and spread to the key areas using a pipette tip or by adding more liquid. *b:* The rotation of the stage is started, removing excess liquid. *c:* The film is baked. Not to scale. *Redrawn/adapted from information in references such as [1, 20, 21].*

The two liquids deposited to form the chemically patterned surfaces were the

planar polyimide, SE130, used as an alignment layer from Nissan Chemical Industries, Ltd., with an approximately 2°[1] pretilt, and the photo resist for photolithography (see Section 3.2.5) from Shipley Microposit® S1813®. The spin coating parameters are summarised in Table 3.1.

Solution	**Step**	**Acceleration** rpm^2	**Speed** rpm	**Time** s	**Temperature** °C
SE130	Spin step 1	200	500	2	RT
	Spin step 2	500	5000	60	RT
	Drying[i]	N/A	N/A	60	80
	Curing[i]	N/A	N/A	1800	200
S1813	Spin step 1	200	500	2	RT
	Spin step 2	500	4000	40	RT
	Softbake[ii]	N/A	N/A	60	115

Table 3.1: Spin coating parameters for the thin films deposited to fabricate the patterned surfaces. RT stands for room temperature. i: Based on drying and curing parameters in data sheet for 'Alignment Coatings for LCDs-SUNEVER Series'-1/2 (Nissan Chemical Industries, Ltd). ii: Based on softbake parameter given in data sheet for Microposit® S1800® Series Photo Resists (Shipley).

The liquid can be deposited dynamically or statically, where the stage holding the sample is either already rotating during deposition or the solution is placed onto the substrate before rotation is started[21]. In this work, the latter method was used to ensure that the important areas of the substrates are properly covered, as shown in Figure 3.2a. This was accomplished by either using a pipette tip to spread the SE130 (Figure 3.2a), or by using more photo resist as contacting the surface could have interfered with the direction rubbed into the alignment layer (see Section 3.2.4). The final step involves the substrate being heated to bake the films[20] (Figure 3.2c).

An important consideration for spin coated thin films is that there may be inconsistencies of the coating at the substrate edges[21]. In this work, the rectangles were patterned close to the centre of the substrate where there should be higher quality coverage.

[1]Nissan Chemical Industries Ltd. Data sheet for 'Alignment Coatings for LCDs-SUNEVER Series'-1/2

3.2.4 Mechanical Rubbing

After the spin coating steps for SE130 planar polyimide (Table 3.1), this film was mechanically rubbed to provide a preferred director direction (as well as a pretilt, see Section 2.2.3). The key principle is that if the LC were not to align with the grooves and/or organised polymer chains set by the rubbing, there would be an undesirable energy cost[4].

In this work, the substrates were held onto a vacuum stage that was linearly translated whilst a rotating cloth roller stayed in one position for four passes under the roller as demonstrated in Figure 3.3. The pretilt of SE130 is approximately 2° hence is not likely to have a significant impact on the imaged director fields.

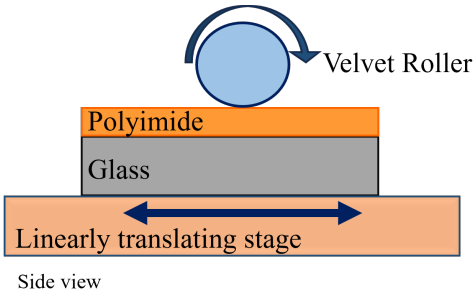

Figure 3.3: Schematic of mechanical rubbing. The substrates are stabilised with a vacuum, and the stage is passed linearly under a rotating cloth roller. Not to scale. *Image adapted from [1].*

3.2.5 Photolithography

Photolithography allows for the rectangular confinement areas to be precisely patterned onto the surfaces as is schematically summarised in Figure 3.4. Further information on the process can be read in textbooks such as [22]. Firstly the photo resist, Microposit® S1813®, was spin coated on top of the rubbed polyimide surface using the parameters given in Table 3.1 (Figure 3.4a). A photomask was contacted against the substrate surface with the desired rectangle aligned appropriately with the rubbing direction (Figure 3.4b). The system was subsequently exposed to UV light with wavelengths of 365.8nm, 405.0nm, and 436.7nm for

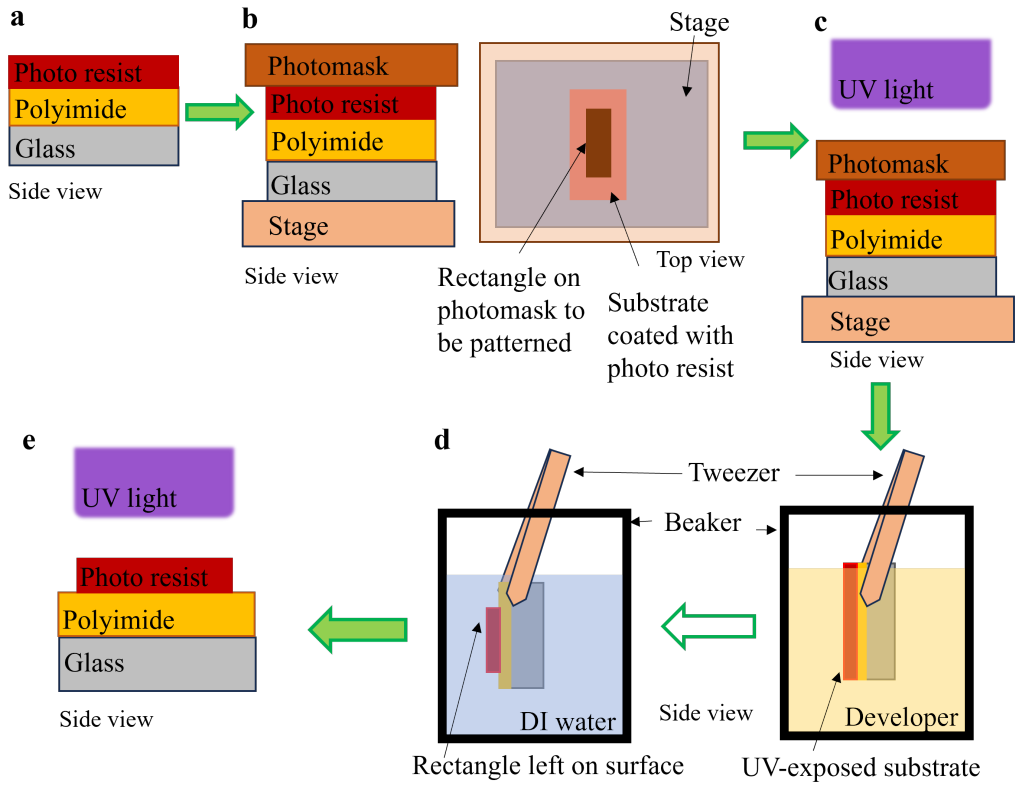

Figure 3.4: Schematics of the key steps in photolithography to pattern rectangles onto the substrates. *a:* The photo resist is spin coated on top of the alignment layer. *b:* The desired rectangle from the photomask is aligned with the rubbing axes of the substrate before *c:* exposure to UV light. *d:* The substrate is agitated in developer and DI water. *e:* The resulting surface after photolithography is exposed to further UV. Not to scale. *c adapted from [1]. Information on photolithography can be read at references such as [22].*

25s[1], with the ideal wavelength for this photo resist quoted as 436nm[2] (Figure 3.4c). S1813 is a positive photo resist meaning that the area exposed to the UV light becomes more soluble[22], hence on agitation of the substrate at least once for 30s in the Microposit® MF® CD-26 developer from Shipley[3] (Figure 3.4d), the area protected by the photomask remained. The substrates were then agitated at least once in DI water for 30s, with the resulting surface in Figure 3.4e

[1]Wavelengths measured by Thomas Moorhouse.
[2]Data sheet for Microposit® S1800® Series Photo Resists (Shipley).
[3]Data sheet for Microposit® MF® CD-26 Developer (Shipley).

having the remaining photo resist in the shape of the rectangle. This surface was exposed to another 25s of UV light (Figure 3.4e) to loosen the photo resist so that it can be removed easier at the end of the fabrication, as will be explained in Section 3.2.6.

The photomask shown in Figure 3.5a was designed specifically for this research, with a wide range of shapes to prevent limitations in future research. In the zoomed example section in Figure 3.5b there are four 'rectangles', however two of them are almost too small to resolve in this image and therefore are circled. This area is chosen as an example since it shows the commonly used 6 x 6mm square. There are labels near each rectangle to identify the size and rubbing direction post - fabrication, with further information on the photomask available in Section A.1.1.

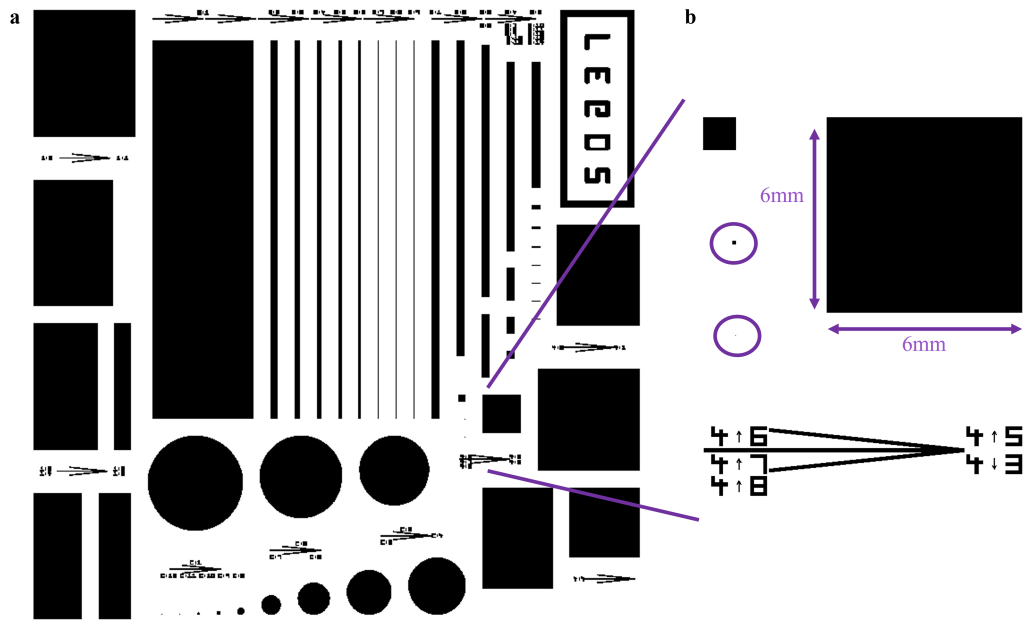

Figure 3.5: *a:* Bespoke photomask design, created to define the rectangular confinement shapes of the surface patterning. *b:* Zoomed area of a commonly used region of the photomask containing the 6 x 6mm square, with the large arrow denoting the rubbing direction and the numbers referring to the rectangles. Two rectangles in this area of the photomask are difficult to resolve in this image due to their small size and are therefore circled.

3.2.6 Silane Deposition

The hydrophobic layer surrounding the rectangular confinement shape (see Figure 3.1) was 1H,1H,2H,2H-Perfluorooctyltrichlorosilane 97% (silane) from Thermo Scientific, with the structure shown in Figure 3.6. Some examples of this material being used for hydrophobicity can be found at[117, 118, 119]. The process used in this thesis to deposit the silane as shown in Figures 3.7a-c is based on the processes described by Amalathas and Alkaisi[24] as well as Munief *et al.*[18]. Although the height of the silane layer has not been directly measured in this thesis, it is named as a monolayer since the similar method has been shown to provide layers of that height order[18].

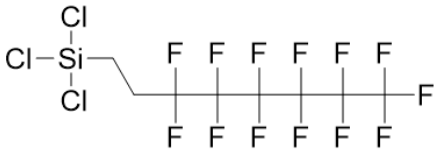

Figure 3.6: Chemical structure of 1H,1H,2H,2H-Perfluorooctyltrichlorosilane, 'silane'. *Redrawn/adapted from [23].*

Water in the system is non-ideal when forming the coatings[18], therefore moisture was removed from the substrates[24] by placement in an oven at 100°C for a minimum of 15 minutes prior to transfer into a dessicator (Figure 3.7a). A droplet of silane was added onto a glass cover slip in the dessicator with the substrates and the lid was replaced. Munief *et al.*[18] use a nitrogen atmosphere around the dessicator since the inert gas can reduce negative impacts on how reactive the silanes are. Nitrogen gas was passed over the samples in the current work. The dessicator was then taken down to a vacuum, again reducing the amount of water in the system[18]. The system was left for approximately 1hr at room temperature (Figure 3.7b), compared to 1hr or 2hrs at 20°C or room temperature for [18] and [24], respectively. The droplet of silane placed in the sealed dessicator under vacuum formed a vapour, which landed on top of the substrates[18, 24]. To complete the surface fabrication, the resulting surface was agitated in IPA followed by DI at least once each for 30s (Figure 3.7d), removing the remaining photoresist and resulting in the structure in Figure 3.1.

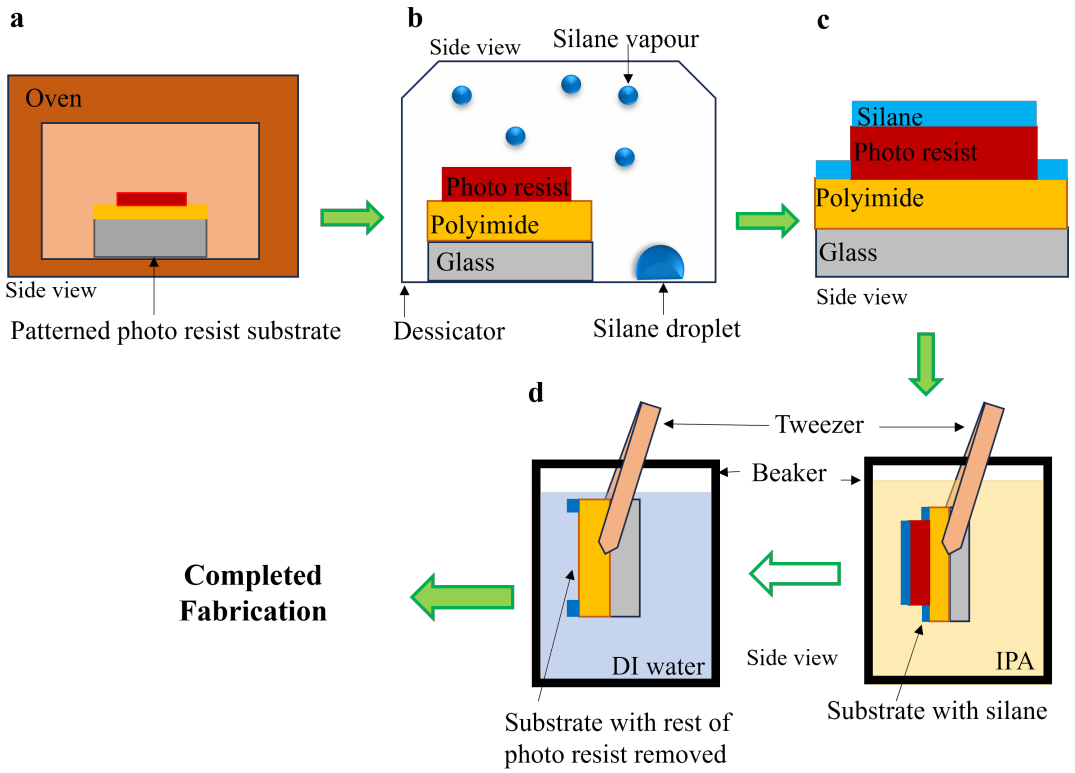

Figure 3.7: Schematics of the key steps to coat the patterned surfaces with silane. *a:* The substrates are placed in an oven prior to transfer to the dessicator. *b:* A droplet of silane in placed in the dessicator with the substrates, before nitrogen gas is passed through the dessicator and then taken down to a vacuum. *c:* The substrate is agitated in IPA and DI. Not to scale. *Relevant information for a-c, with b adapted from, references [18, 24].*

3.3 Polarised Light Imaging

The main method of characterisation throughout this thesis is polarised light imaging, named as such since the imaging system used in this work is not a conventional commercial polarising microscope, although the system used operates with the same principles. Therefore, a specific focus is given in this section to the mechanisms behind polarised light imaging including the bespoke imaging system created for this project, the significance of birefringent colours, how to identify defects and twist in LC samples, as well as how to use polarised imaging to measure semi-droplet height.

3.3.1 Bespoke Imaging System and Key Principles of Polarised Light Imaging

Preliminary work with the chemically patterned millimetre sized rectangles highlighted that use of conventional polarising microscopes (which can be read about at references such as [25]) would not be practical to image across the whole confinement area as they have a maximum field of view of approximately 2mm. Additionally, a 1x magnification objective lens with threading suitable for a commercial microscope was found to be too long, and would only fit well with the polariser removed. Therefore, to allow for high quality polarised light images, a bespoke imaging system was designed and built as shown in Figure 3.8a. The system can be used in a combination of polarisation conditions including one polariser, two polarisers or no polarisers. The actual field of view is set by the size of the stage with the additional consideration of the beam splitter in reflection mode.

The bespoke imaging device has a similar configuration to conventional polarising microscopes[25] as shown schematically in Figure 3.8b. In 'Transmission' mode, two linear polarisers in rotation mounts are placed with their polarising axes at 90° to each other (crossed) on either side of an LC sample, sat on a stage that can rotate. The polariser below the stage is often called the polariser and the one above called the analyser. A camera images the LC textures. 'Reflection' mode, as is also shown in Figure 3.8a, is less commonly used in this thesis and consists of the light source and first polariser at a right angle to the stage, with use of a beamsplitter to direct the light onto the stage.

The camera in the bespoke system is from Ximea[120] with a resolution of 5Mpixels and images in colour, allowing for high quality images. When using the camera with a 2/3" sensor, the combination of lenses that provides the greatest field of view of those found at [121] is a 6.5x zoom lens, 0.67x extension tube, and a 0.25x attachment. A field of view between 14.66mm - 93.62mm is in theory possible with this lens configuration, which is ample for the samples imaged throughout this thesis. Whilst the stage can move up and down on a runner, the more precise control for focusing on samples originates from an adjuster on the lens set-up.

Diffusers were added into the threading for the light sources to disperse the light evenly.

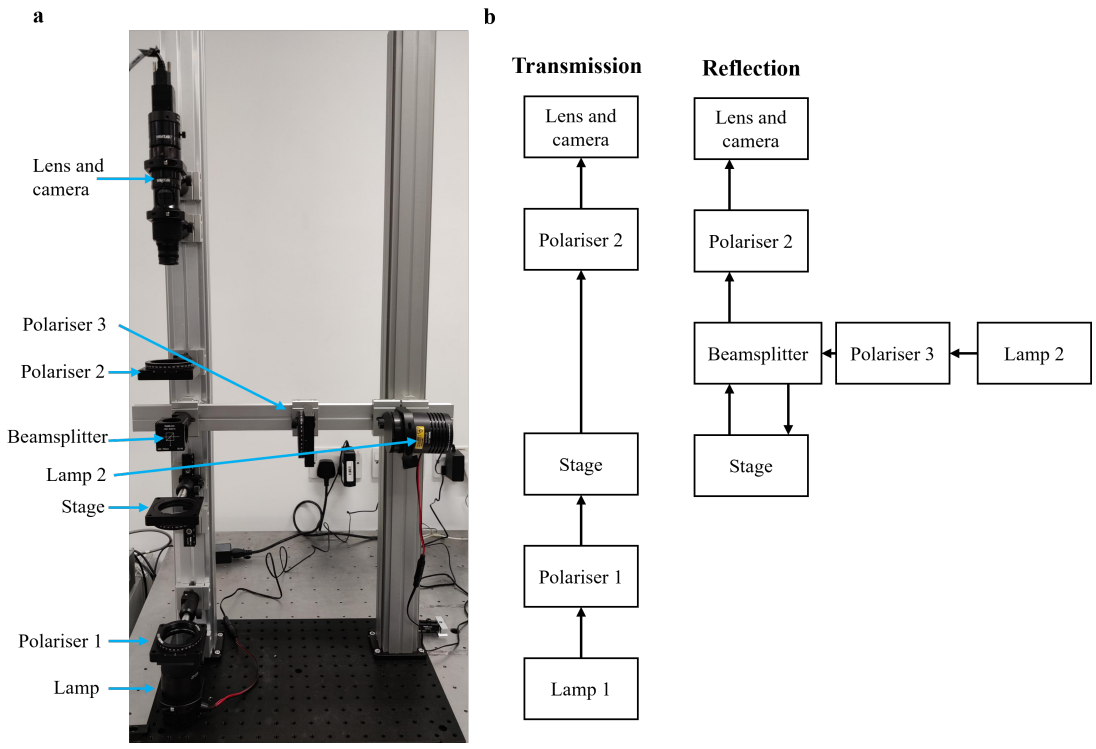

Figure 3.8: *a*: Real image showing the main components of the bespoke imaging system designed to take high-quality large field of view images in a range of polarisation conditions. The polarisers and beamsplitter can be moved into and out of the light path. *b*: A schematic of the components required to take cross polarised images of LC samples in transmission and reflection mode. *Image adapted from supplementary information in [1].*

Generally, polarised imaging involves white light, linearly polarised by the first polariser and entering the sample at some angle, ζ, to the optic axis. Dependent on ζ, the light may undergo birefringent effects as previously described in Section 2.2.2. The light that exits the microscope is only that which aligns with the analyser axis, as drawn schematically in Figure 3.9. This can be described mathematically when considering the light intensity out of the microscope, I, versus

from the lamp, I_0[25],

$$I = \frac{I_0}{2} sin^2(2\zeta) sin^2\left(\frac{\pi \cdot \Delta n(\lambda) \cdot height}{\lambda}\right), \tag{3.2}$$

where λ is a specific wavelength, corresponding to a birefringence, $\Delta n(\lambda)$. The height is often named the sample thickness, however it has been changed here as the confined LC semi-droplets throughout this thesis are referred to in terms of their heights. It is clear to see from Equation 3.2[25] that at $\zeta = 45°$, $\sin(2\zeta) = 1$, therefore the observed birefringent effect is the largest. At $\zeta = 0°$ or $90°$ the sample will appear dark.

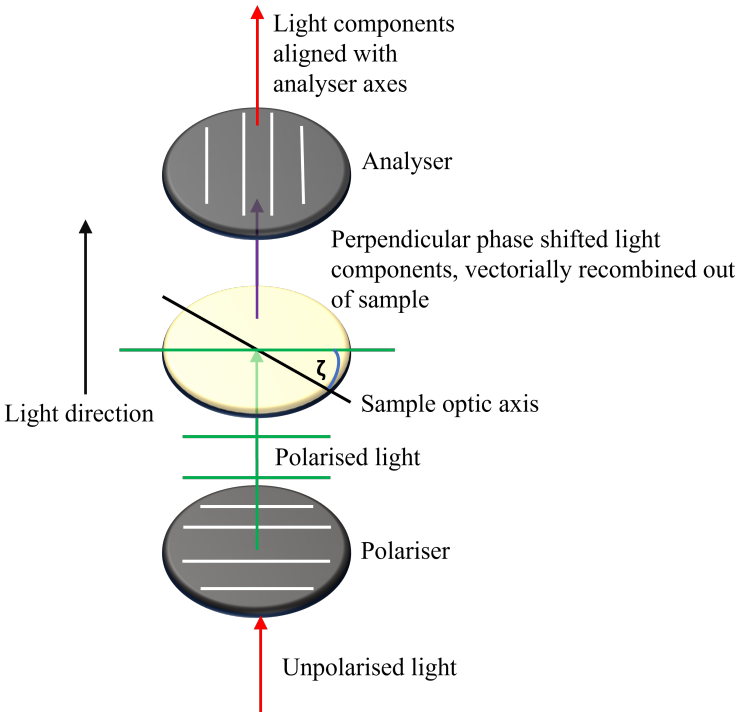

Figure 3.9: Schematic to describe the transmission of light through a birefringent sample sandwiched by crossed polarisers. Unpolarised light will be polarised in the direction of the polariser axis. This direction will have an angle, ζ, to the optic axis. The value of ζ will determine if the polarised light experiences birefringent effects through the sample (see Section 2.2.2). Only the light aligned with the analyser axis leaves the system. The colours for the polarisers, sample and light arrows are chosen arbitrarily. Not to scale. *Redrawn/adapted based off diagrams and/or information in references such as [5, 25].*

3.3.2 Retardation Colours and Full Wave Plate

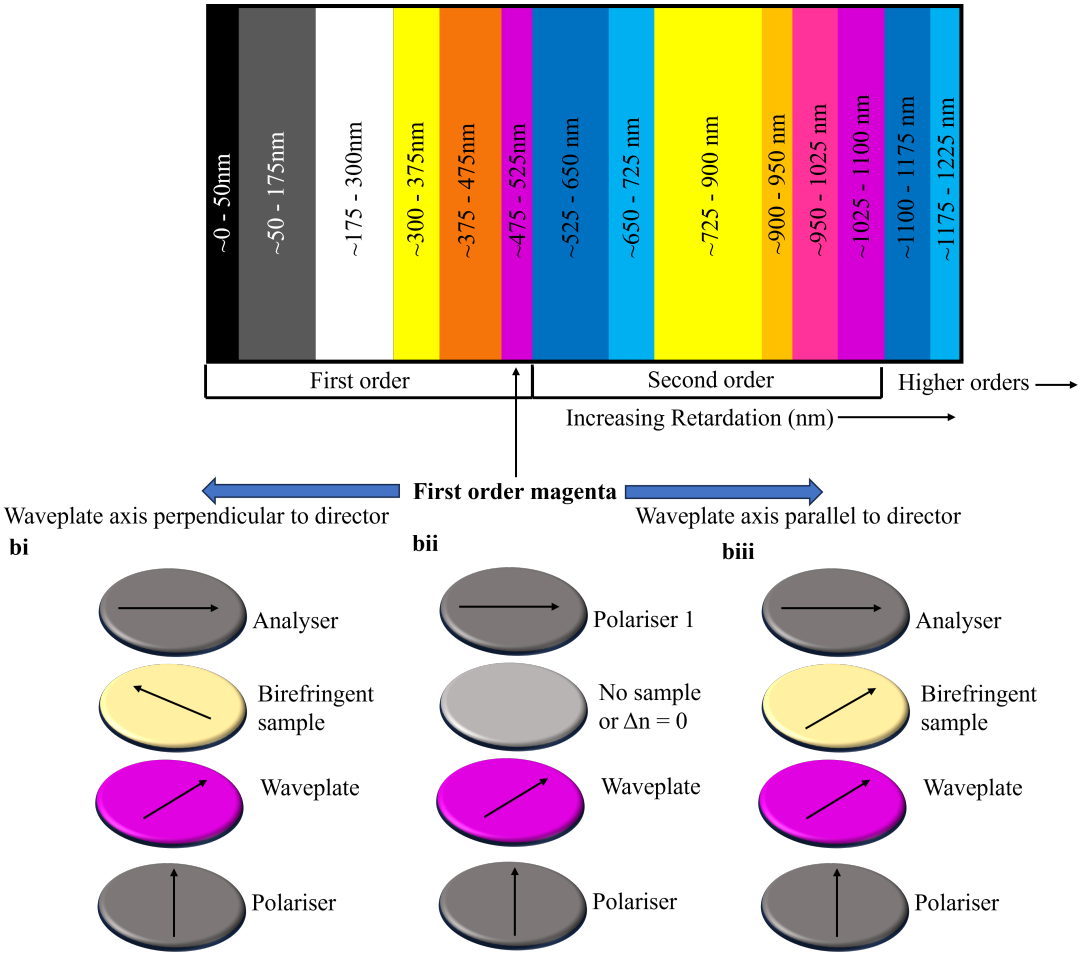

Figure 3.10: *a:* Schematic of the retardation colours observed in approximately the first two orders of a Michel-Lévy chart. *bii:* Between crossed polarisers, first order magenta is observed for a full waveplate added into polarised imaging apparatus with no birefringent sample. If the waveplate axis is added *bi:* perpendicular to the director of a birefringent sample, the retardation colour will decrease with respect to the first order magenta. If the waveplate axis is added *biii:* parallel to the director, the retardation will increase with respect to the first order magenta. The arrows show the axes of the polarisers, the director of the birefringent samples and the axis of the waveplate. The colours of the samples and polarisers are arbitrary in this figure. *Approximate retardations in Figure a are read from Michel-Lévy chart at [26]. b redrawn/adapted from information in references such as [25].*

Retardation, Γ[25],

$$\Gamma = \Delta n \cdot height, \tag{3.3}$$

is set by the path length shift between the two light components on exiting a birefringent sample[5] (see Section 2.2.2). The three terms in Equation 3.3 are related using the Michel-Lévy chart, an example of which is given by Sørensen[26]. Representations of the colours observed under polarised imaging corresponding to retardation values are marked in the schematic version of a Michel-Lévy chart in Figure 3.10a, up to an approximate retardation of 1225nm. Retardation colour is often non-trivial to identify accurately as similar colours occur in multiple orders upon increasing retardation along the chart[25, 26].

As discussed in Section 2.5, the director field of the semi-droplets is important when considering them for use as sensing devices. A method to further analyse the director field is to add a full wave plate into the imaging system's light path[25], in this case between the first polariser and the stage. If there were no birefringent sample on the stage, a first order magenta colour would be observed[25] as highlighted in Figure 3.10bii. When the axis of the lambda plate is perpendicular with the director, the retardation in the system decreases and hence the retardation colour decreases relative to the magenta. When added parallel to the director, the retardation increases relative to the magenta[25], as is summarised in Figure 3.10b.

3.3.3 Defect Characterisation

The four defects used throughout this thesis were shown in Figure 2.5 including those with strengths, s, of $\pm$ 1 or $\pm$ $\frac{1}{2}$[6, 9, 66]. Figures 3.11a,b schematically represent the identification of defects with strengths of +1 and -1, respectively, and Figure 3.11c demonstrates polarised images of an NLC semi-droplet confined within a 6 x 6mm square as an example of the type of images that are observed throughout the thesis. The method to characterise the defects is explained by Lydon *et al.*[9], and summarised here. Highlighted in Figure 3.11 are the dark brushes (marked in orange in c) which represent where the director is aligned with the axis of one of the crossed polarisers and therefore there is no observed

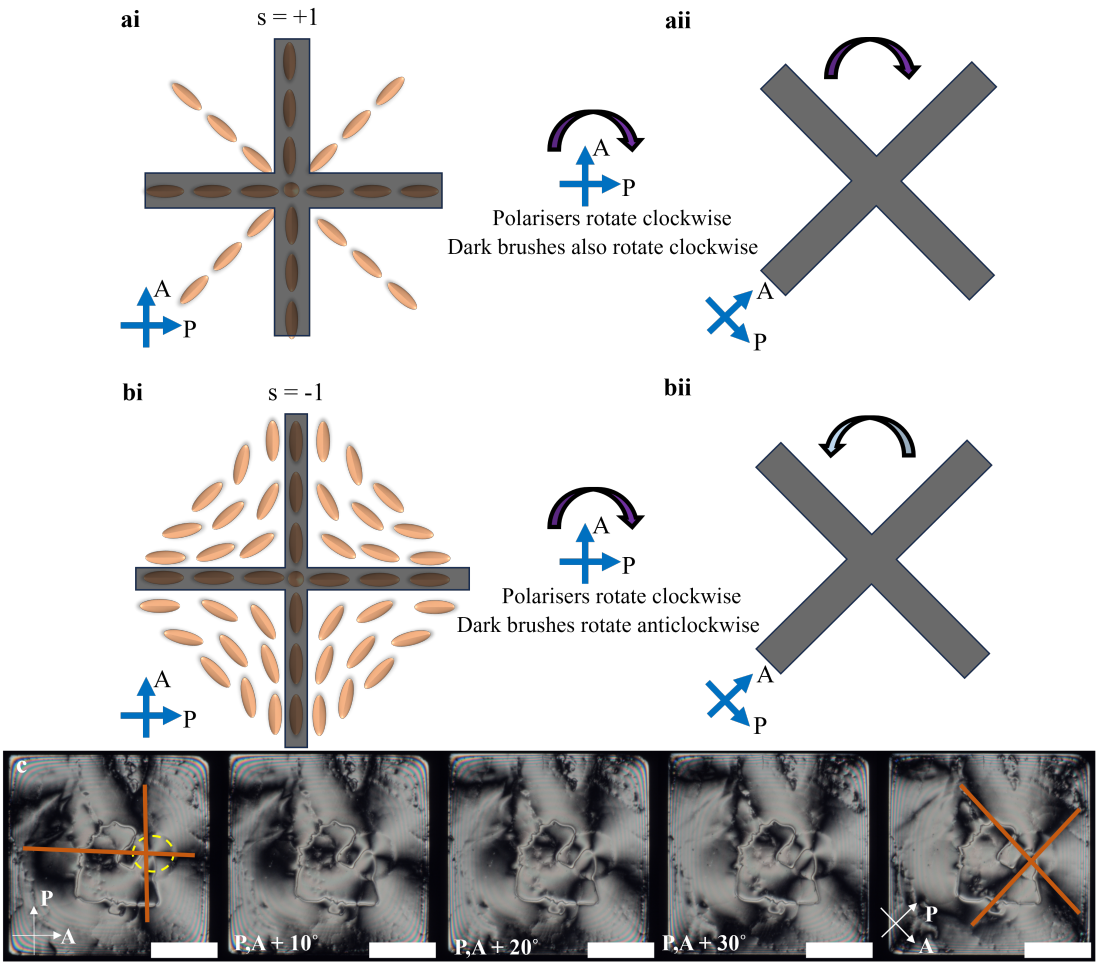

Figure 3.11: Schematic of the method to evaluate of the sign and strength, s, of LC defects. *ai,bi*: Under crossed polarisers there are four dark brushes suggesting a defect with a strength of $\pm$ 1. *aii,bii*: When the crossed polarisers are rotated at the same rate clockwise, the dark brushes for the $s = +1$ defect will also rotate clockwise, and will rotate anti-clockwise for the s = -1 defect. Not to scale. *c:* Rotation of crossed polarisers through 0° to 45° of an NLC semi-droplet. The yellow circle represents the origin of the potential strength = +1 defect, and the orange lines represent the dark brushes. The scale bars are 2mm. P and A show the relative directions of the polariser and analyser, respectively. The sample in *c* does not have a rubbed alignment layer as is the main focus of Chapter 6, however the dark brushes are clear. *a,b redrawn/adapted from [9].*

birefringence (see Section 3.3.1). Whether the defect has a value of 1 or $\frac{1}{2}$ is quantified by the number of dark brushes divided by four, therefore all of the examples in Figure 3.11 have a strength of $\pm$ 1. The $\pm$ is evaluated by rotating the crossed polarisers at the same rate and direction as each other, with a stationary sample. If the rotation of the brushes is in the same direction as the polarisers the sign is positive, otherwise the sign is negative[9].

This process for identification was completed in this thesis by rotation of the crossed polarisers in clockwise steps of 5° or 10° from the crossed polarisers parallel and perpendicular to the horizontal axis, to 45° from parallel and perpendicular (see Equation 3.2). This can be seen in the example in Figure 3.11c for a potential defect with a strength of +1. There is not a significant change in transmission in this example since the alignment layer is not rubbed (as is the focus of Chapter 6), however it very clearly shows the four dark brushes.

There are multiple potential descriptors of the dark regions (e.g. 3.11c) observed in these rotations including, but not necessarily limited to, defects as described above, or a defect free director field with rotating dark regions as previously seen for smaller square confinements in Tsakonas *et al.*[122]. In their[122] work, E7 is confined in 12µm thick, 20 - 80µm length and width squares patterned using SU8 photo resist within an LC cell (similar to Figure 2.4d). For their non-rubbed samples, director fields with alignment parallel to the walls close to the edges, similar to the non-rubbed surfaces in Chapter 6, and alignment in the centre of the LC sample along either a diagonal or the vertical axis is observed. The deductions about the director field are asserted through rotation of crossed polarisers over 90°. However, defects are observed only at some corners *via* modelling of the system as a 1µm square[122].

It is not possible to directly compare that work[122] with the semi-droplet director fields due to the significantly larger confinement sizes; semi-droplet heights; the free surface; the rubbing of the samples, and the central disclination lines observed in the current work (see e.g. the circle disclination in Figure 3.11c). Whilst the explanation focused on throughout this thesis is that the dark brushes may be

due to defects, the consideration that they may indeed be more closely related to the artefacts observed by Tsakonas *et al.*[122] should not be forgotten.

In order to efficiently make high quality figures with well-aligned images such as in Figure 3.11c, a code was written that allows a user to input the the names of the images they wish to align, decide how many columns they wish to align the images with and save the aligned images. This is particularly useful for measurements with increasing temperature, where the temperature can also be labelled on each image. An example of the code is given in Figure A.1.

3.3.4 Identification of Twist

Twist domains have been identified for FNLC-919 samples, e.g.[12, 78], and are often observed in other ferroelectric nematic liquid crystal (FNLC) investigations e.g.[27, 80, 123, 124, 125]. Focusing on the example for FNLC-919 cells with antiparallel rubbed surfaces by Yu *et al.*[12], twisted regions with a right or left twist of approximately 180° are observed in 4.2µm and 10.2µm cell gaps, with Figure 2.7 adapted here for clarity in Figure 3.12a. Demonstrated for their[12] e.g. 2.9µm cell, under crossed polarisers the twist is not observed. However, when the analyser is uncrossed with respect to the polariser, the two regions with opposing twist will display different colours due to different rotations of the incident polarised light[12]. This is drawn schematically in Figure 3.12b for two regions labelled A and B.

3.3.5 Semi-Droplet Height

Effective Birefringence

For NLC semi-droplets in the nematic (N) phase, it is assumed that there is a director angle, $\phi = 2°$, pretilt from the substrate surface from the SE130 alignment layer that linearly rotates through the dimensionless height, $\frac{z}{h}$, to a maximum angle close to 90°, $\phi_{\max}$, at the air/NLC interface. z is the distance in the vertical direction and h is the height of the semi-droplet. This is drawn

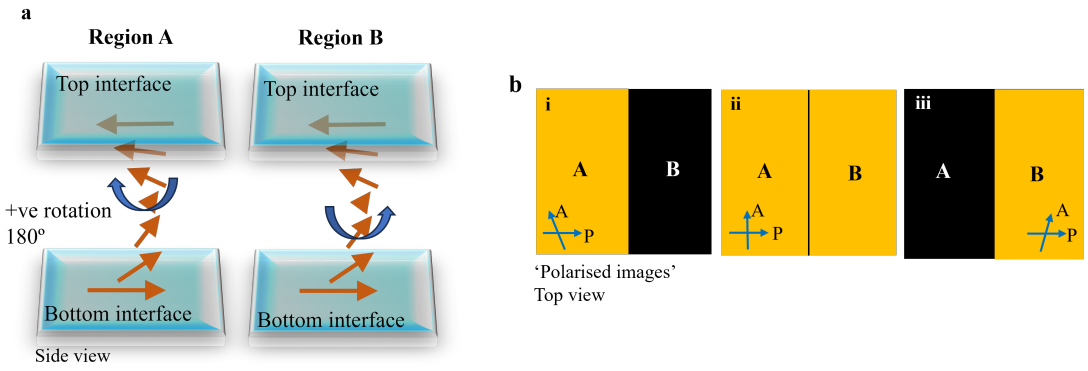

Figure 3.12: *a:* Schematic of twist, a common observation in FNLC samples. *b:* To identify this twist, images on a consistent sample area (represented schematically here) are taken with the analyser rotated to a slightly uncrossed position relative to the polariser in both directions (*i* or *iii*). A and B refer to regions A and B in *a*. If there is an optical difference between the two conditions, there is twist in differing directions. P and A show the relative directions of the polariser and analyser, respectively. Not to scale. *a and b adapted/redrawn from information in [12] and [12, 27], respectively.*

schematically in Figure 3.13 and is written generally in degrees as,

$$\phi\left(\frac{z}{h}\right) = (\phi_{\max} - 2^\circ)\frac{z}{h} + 2^\circ. \tag{3.4}$$

The 2° pretilt is not included for FNLC-919 as pretilts can be energetically unfavourable for FNLCs (as highlighted by references such as [27, 31, 124]), and is therefore given as,

$$\phi\left(\frac{z}{h}\right) = 90^\circ\frac{z}{h}, \tag{3.5}$$

assuming a homeotropic ($\phi_{\max} = 90^\circ$) air/FNLC-919 interface in the N phase[14].

Whilst the assumptions of planar anchoring at the rubbed polyimide surface for the NLCs are generally accepted, evidence supporting the assumption for FNLC-919 in the N phase is given by works such as [14, 79], where FNLC-919 in cells with parallel rubbing directions form a relatively uniform director field in the N phase. Similarly, the anchoring at the air/LC has been quoted, with example references given, as homeotropic for E7[15, 48] as well as planar[48] and/or tilted[15] for MLC 7023.

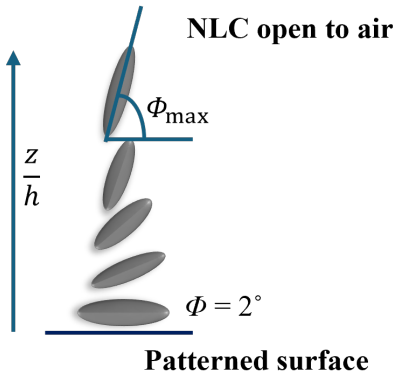

Figure 3.13: General shape of the director field throughout the dimensionless height, $\frac{z}{h}$, for an NLC semi-droplet, from a pretilt at the substrate surface of ϕ = 2° , to a maximum tilt angle, $\phi_{\max}$, at the air/NLC interface. *Image adapted from [1].*

To calculate the effective birefringence, Δn_{eff}, based off of the director field variation, the variation of n_e throughout the height, $n_e\left(\frac{z}{h}\right)$, is calculated using $\phi\left(\frac{z}{h}\right)$ from Equations 3.4 and 3.5,

$$n_e\left(\frac{z}{h}\right) = \frac{n_e n_o}{\left[n_e^2 sin^2\left(\phi\left(\frac{z}{h}\right)\right) + n_o^2 cos^2\left(\phi\left(\frac{z}{h}\right)\right)\right]^{\frac{1}{2}}}. \tag{3.6}$$

Δn_{eff} is then calculated by an integral over the whole dimensionless height,

$$\Delta n_{\text{eff}} = \int_0^1 \left(n_e\left(\frac{z}{h}\right) - n_o\right) d\left(\frac{z}{h}\right). \tag{3.7}$$

A very similar description is given on pages 202 - 204 in [126] for $n_e = 1.7$, $n_o = 1.5$ and $\Delta n_{\text{eff}} = 0.0953$. This is in good agreement with the calculation here for E7, with $n_e = 1.73$ and $n_o = 1.52$[49] resulting in $\Delta n_{\text{eff}} = 0.1$, as an example. Figure 3.14 demonstrates how the quantities in Equations 3.4, 3.6, and 3.7 vary with $\frac{z}{h}$ between 0 and 1 for E7. The specific versions of Equation 3.4 for E7 and MLC 7023 and the resulting effective birefringence calculations are provided in Chapters 4 and 5, respectively.

A point of note when calculating Δn_{eff} was introduced in Section 2.2.3, wherein NLCs are typically well-aligned up to approximately 100µm from anchoring con-

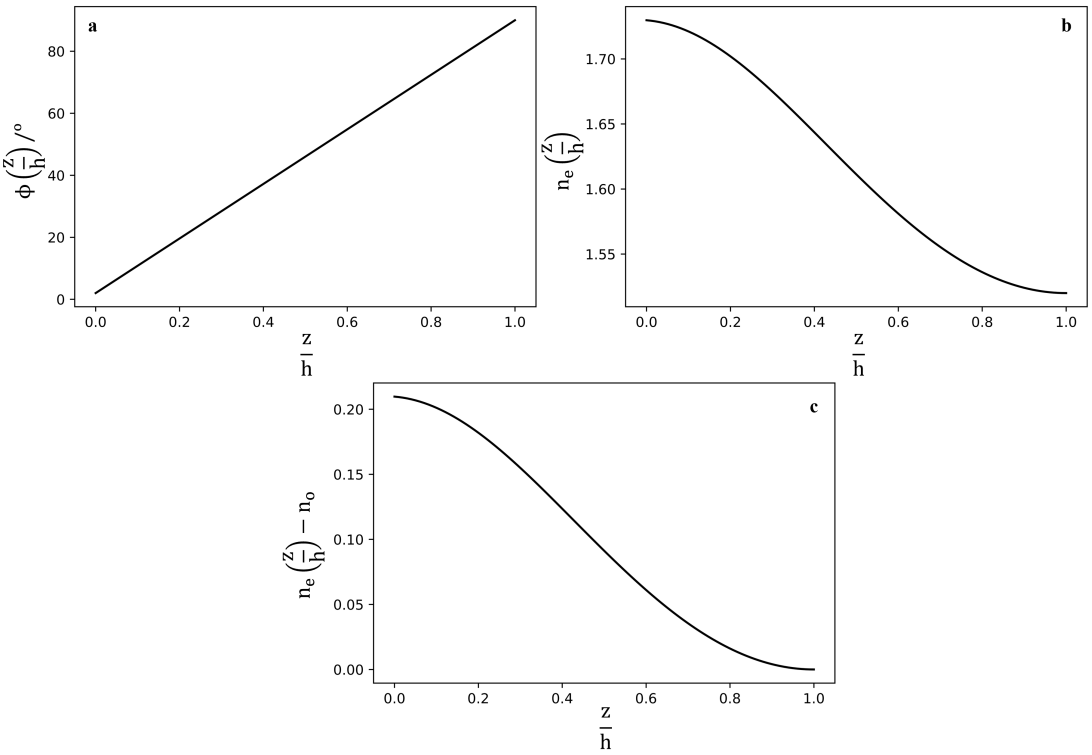

Figure 3.14: Plots through the dimensionless height of the E7 semi-droplet, $\frac{z}{h}$, of *a:* director angle, ϕ, *b:* extraordinary refractive index, n_e, and *c:* $n_e(\frac{z}{h}) - n_o$, where n_o is the ordinary refractive index. *Image adapted from supplementary information in [1].*

ditions. Therefore, for the taller semi-droplets there may be some disorder in the centre of the confined NLC which would make the assumed director fields less accurate and therefore have some effect on Δn_{eff}.

Semi-Droplet Height Measurement

If the perpendicular components of light through a birefringent sample (see Section 2.2.2) have a retardation of an integer multiple of wavelengths,

$$\Gamma = \Delta n_{\text{eff}} \cdot height = m\lambda,$$

then,

$$height = \frac{m\lambda}{\Delta n_{\text{eff}}}, \tag{3.8}$$

where $m \in \mathbb{Z}$, where Equation 3.8 is the full waveplate condition. Waveplates

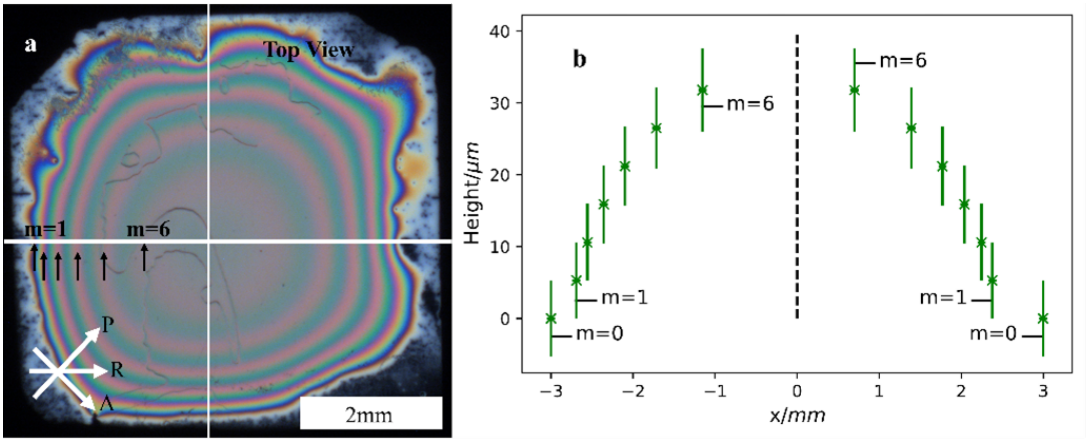

Figure 3.15: *a*: Top view polarised light image of NLC confined in a chemically patterned 6 x 6mm square. The value of m represents the number of pink birefringent fringes counting from the semi-droplet edge. White lines show the cross-section along which the centre-to-centre distances of the fringes have been measured for the height variation. P, A and R show the relative directions of the polariser, analyser and rubbing, respectively. The scale bar is 2mm. *b*: Plot of the centre-to-centre distances of the pink birefringent fringes along the horizontal line in *a* with their corresponding measured heights. *Image adapted from [1].*

can be read about in references such as [5]. The wavelength of linearly polarised white light that agrees with the condition in Equation 3.8 will not have a rotated polarisation out of the birefringent sample and is therefore perpendicular to the analyser axis, hence none of that wavelength is transmitted[5]. In this thesis, it is taken that a green wavelength matches this condition, with $\lambda = 0.53 \pm 0.04\mu$m assumed. Since the apparatus in Figure 3.8a utilises white light, if only the red and blue components of the light are left, then a 'pink' colour is observed. Therefore, the number of pink fringes, m, are counted from $m = 1$ at the semi-droplet edge. Figure 3.15a presents an exemplar image of an NLC semi-droplet imaged with the rubbing direction at 45° to the crossed polarisers. From substitution of $m = 6$ into Equation 3.8, the maximum measured height is 32μm. The corresponding height cross-section shown in Figure 3.15b is highlighted with a white horizontal line in Figure 3.15a.

3.4 Liquid Crystal Materials

A summary of the main properties of the LCs used throughout this thesis is given in Table 3.2 as given in the literature. E7 is from Synthon, with MLC 7023 and FNLC-919 from Merck.

Liquid Crystal	$\mathbf{n_e}$	$\mathbf{n_o}$	$\mathbf{\Delta n}$	**N-I** °C	**Surface Tension** $Nm^{-1}{\cdot}10^{-3}$	**Air/LC Interface**
E7	1.73[i]	1.52[i]	0.21	60[ii]	24.2[iii]	H[iii,iv]
MLC 7023	1.53[v]	1.46[v]	0.07	79.5[v]	'low'[iii]	P[iii] or P/T[iv]
FNLC-919	1.71[vi]	1.48[vi]	0.25	80[v]	∼3[vii]	P[viii]

Table 3.2: Main relevant properties of the LCs used throughout this thesis. N-I is the nematic to isotropic phase transition temperature. For the air/LC interface, H refers to homeotropic, P to planar, and T to tilted. i: [49]. ii: [127]. iii: [48]. iv: [15]. v: Merck data. vi: Read from Figure 9 in [128] at approximately 0.53µm. vii: [129]. viii: [14].

The first publication investigating the Merck FNLC (see Section 2.3), FNLC-919, was by Yu *et al.*[12] in 2023, with an expected phase progression of,

$$\mathrm{Cr} \xleftrightarrow{8^{\circ}\mathrm{C}} \mathrm{N_f} \xleftrightarrow{32^{\circ}\mathrm{C}} \mathrm{N_x} \xleftrightarrow{44^{\circ}\mathrm{C}} \mathrm{N} \xleftrightarrow{80^{\circ}\mathrm{C}} \mathrm{I}.$$

3.4.1 NLC Density Measurements

To measure the density of the NLCs, a density meter from Anton Parr was utilised. The tube was cleaned with IPA and pumped out twice with this cleaning repeated twice before approximately 1mL of the NLC was deposited into it. The instrumentation uses Equation 3.9,

$$\rho = A \cdot Q^2 \cdot f_1 - B \cdot f_2, \tag{3.9}$$

where

$$Q = \frac{Tube\ period}{Reference\ period},$$

i.e. the period of oscillation of the tube filled with the NLC versus a reference period. ρ is the density, with A and B constants, and f_1 and f_2 correctional

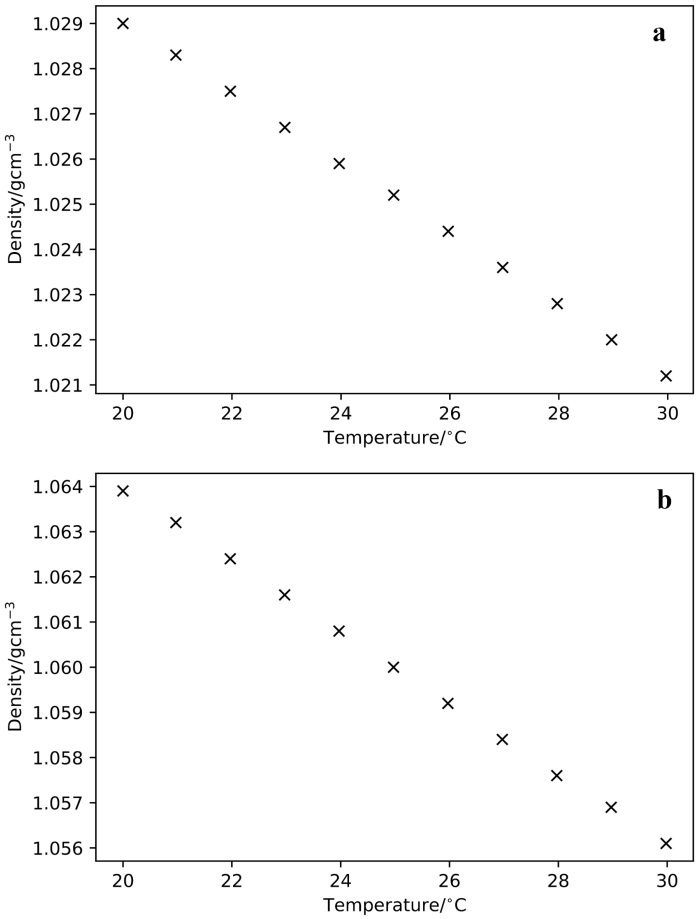

Figure 3.16: Density variation of *a:* E7 and *b:* MLC 7023 near room temperature.

components. Whilst an in-depth description of the instrumentation is beyond the scope of this thesis, further information can be read at references such as [130, 131].

In this work, the densities of E7 and MLC 7023 were measured every 1°C between 20 - 30°C as the majority of the data presented in this thesis were imaged at room temperature. As can be deduced from Figures 3.16a,b for E7 and MLC 7023, respectively, to 1d.p both NLCs have densities of 1gcm^{-3} with a minimal variation of approximately 8 x 10^{-3}gcm^{-3} over the temperature range. This is of a similar magnitude to data presented by Parton-Barr *et al.*[131] for the density variation of 5CB (NLC) the N phase ($\sim$ 25 - 35°C) of approximately 11 x 10^{-3}gcm^{-3}.

3.5 Thermogravimetric Analysis

Thermogravimetric analysis (TGA[1]) is briefly used in Chapter 7. A pan was filled with MLC 7023 and the change in mass with increasing temperature was measured. Whilst an in-depth description of TGA is out of the scope of this thesis, more can be read at references such as [132].

3.6 Summary

This chapter has provided an in-depth description of the methods used to fabricate the chemically patterned surfaces, as well as the background to polarised imaging as this is the most commonly used characterisation technique throughout this thesis. Some specific information on the LCs used throughout the thesis was introduced. In Chapters 4 - 8, the results using these methods and materials will be presented and discussed.

[1]Data taken by Thomas Raistrick.

Chapter 4

E7 Confined in Chemically Patterned Rectangles

Please note a significant portion of this chapter is published in A. Bond *et al.* (2025). The behaviour of nematic liquid crystals in chemically patterned millimetre-sized rectangular surfaces. pp 1-15. *Liquid Crystals*. https://doi.org/10.1080/02678292.2025.2489426[1]. Figures that have been taken or adapted from [1] are marked in the relevant captions.

4.1 Introduction

This chapter presents an investigation of the nematic liquid crystal (NLC) E7 confined in chemically patterned rectangles with aspect ratios between 0.5 - 1, widths between 6 - 13mm, lengths between 6 - 20mm and the height of the confined NLC semi-droplets between approximately 20 - 420µm. These configurations are discussed in relation to their potential use in future sensing devices. The confinement dimensions to contain NLC are important for the resultant liquid crystal director field within the confinement (see Section 2.2.3), as is clear from the papers that form the basis of the following work, i.e those by Bao *et al.*[15] and Cousins *et al*[100]. The confinement dimensions are over a greater

range and of a greater size than has previously been seen in the literature (see Section 2.4), hence the choice of the well known NLC E7.

The heights of the semi-droplets were measured using polarised light imaging to count a discrete number of pink birefringent fringes, which is then used with the full-wave condition for imaging of birefringent materials as explained in Section 3.3.5. A non-LC specific, simple geometric model with the key parameter of the interface angle at the edge of a semi-droplet cross-section is derived and compared to the model deduced by Cousins *et al.*[100] which has a focus on the area of the confined LC cross-section. Combining the models allows the semi-droplet's predicted height to be calculated. For a smaller parameter space for a chosen confinement dimension, further investigations are completed to both compare methods of calculation of the interface angle, as well as to discuss the effects of rotating crossed polarisers with respect to the rubbing axis and addition of a waveplate (see Sections 3.3.2 and 3.3.3).

4.2 Experimental Methods

4.2.1 Patterned Surface Fabrication

The chemically patterned surfaces were fabricated using the method described in Section 3.2 to produce rectangles with dimensions of 6 x 6mm, 11 x 11mm, 16 x 13mm, and 10 x 20mm. The liquid crystal was confined within a hydrophobic monolayer denoting these shapes, and sat atop a rubbed alignment layer.

4.2.2 NLC Deposition

A vial containing the E7 NLC was placed alongside the chemically patterned substrate on a hot plate above the N - I (nematic to isotropic) phase transition temperature, before the NLC was pipetted using specifically measured volumes onto the confinement areas of the substrate. The NLC was spread to the confinement edges using directional compressed air or gentle tilting as required, before removing the sample from the heat. The sample was then exposed to a tempera-

ture cycle as detailed in Table 4.1 to remove any air bubbles before imaging with the bespoke imaging device (see Section 3.3.1).

Step No.	**Rate**/ °C min^{-1}	**End Temperature**/ °C	**Hold Time**/ min
1	5	55	0
2	0.5	65	0
3	2	70	10
4	2	65	0
5	0.5	55	0
6*	5	<< I-N Transition	<120

Table 4.1: Temperature cycle for E7 semi-droplets on chemically patterned rectangles. *This cooling rate is faster than the hot stage can complete and the sample is removed from the hot stage well below the isotropic - nematic (I-N) phase transition temperature.

The surfaces were used multiple times and between each new dispense of NLC, the 'old' NLC was removed from the surface with isopropanol (IPA), before drying with compressed air and/or evaporation on a hot plate.

4.2.3 Measurement of semi-droplet height

As was described in Section 3.3.5 the effective birefringence, Δn_{eff}, was calculated for E7 by assuming a hybrid-aligned nematic (HAN) director field through the dimensionless height, $\frac{z}{h}$, of the semi-droplet, i.e. from an approximately planar anchoring at the substrate surface (with a $\sim 2°$ pretilt[1]) to a homeotropic air/NLC interface, as demonstrated in Figure 4.1.

This orientation is described in degrees by,

$$\phi\left(\frac{z}{h}\right) = 88°\frac{z}{h} + 2°, \tag{4.1}$$

which, when substituted into Equations 3.6 and 3.7 (for $n_{\text{e}}(\frac{z}{h})$ and Δn_{eff}, respectively) calculates $\Delta n_{\text{eff}} = 0.1$, using $n_{\text{e}} = 1.73$ and $n_{\text{o}} = 1.52$[49]. The variations of

[1]Nissan Chemical Industries Ltd. Data sheet for 'Alignment Coatings for LCDs-SUNEVER Series'-1/2

these three properties throughout the dimensionless height are included in Figure 3.14. When Δn_{eff} is substituted into Equation 3.8, $h = \frac{m\lambda}{\Delta n_{\text{eff}}}$, with the number of pink birefringent fringes observed under polarised imaging, m, the height is measured. The HAN assumption is a good approximation across the majority of the cross-section for the semi-droplets as the semi-droplet heights are approximately three orders of magnitude smaller than the radius of the circle they are modelled on as will be seen in Section 4.3, with a height near the very edge of the semi-droplet where the assumed HAN will break down.

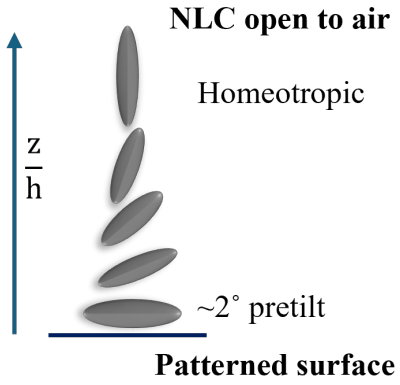

Figure 4.1: Schematic of the hybrid-aligned nematic director of E7 semi-droplets through the dimensionless height of the semi-droplet, $\frac{z}{h}$, from a pretilt of $\sim 2^{\circ}$ at the patterned surface, to homeotropic at the air/NLC interface. Not to scale. *Figure adapted from [1].*

4.3 Geometric Modelling of the Semi-Droplets

A large amount of work on modelling of semi-droplets of NLCs has been undertaken by Cousins *et al.*[100] who presented an in-depth theoretical description of a specific case of general equations described in an earlier paper[133] on confined NLC within a rectangular geometry with a solid aligning surface and open air/NLC interface, assuming the NLC is static and can be treated as 2D. Cousins *et al.*[100] pinned this NLC semi-droplet at the edges, assumed it to be a thin semi-droplet with symmetry about the central axis and allowed for the assumption that the effects of gravity on the semi-droplet were negligible by ensuring

that the semi-droplet half-width, d, is much smaller than the capillary length, L_C, i.e. $d << L_C = (\frac{\gamma}{\rho g})^{\frac{1}{2}}$ [134], where γ is the NLC/air interfacial tension, ρ is the NLC density and g is the gravitational acceleration. For their experimental semi-droplet, Cousins *et al.*[100] filled a $2d$ = 1.2mm, and length, L = 60mm confinement area with approximately 1µL or 3µL of the NLC 5CB. Their confinement was formed using a rubbed alignment layer of poly(vinyl alcohol) (PVA) surrounded by Teflon. They experimentally validated Equation 4.2 as the height variation at the very edge of their experimental semi-droplet (x = 400 - 600µm), assuming the material was isotropic, static and with a well-defined edge-pinning position,

$$h(x) = \frac{3\epsilon(d^2 - x^2)}{4d} = \frac{3V(d^2 - x^2)}{4d^3 L}. \tag{4.2}$$

In Equation 4.2, $h(x)$ is the height variation across the semi-droplet's x – axis, A is the cross-sectional area, L is the length and V is the NLC volume of the semi-droplets. $\epsilon = \frac{A}{d^2}$ and it is assumed that $\epsilon \ll 1$, implying the semi-droplet is thin.

It is assumed in the current work that the cross-sectional area of the semi-droplet is constant along the confined length and therefore can be determined from the volume of NLC, known from the dispensing conditions to be between 0.5 - 30µL, i.e $V = AL$. In such case, it is simple to see in Equation 4.2 that the NLC maximum height should vary linearly with V. This is useful as the key experimental parameters in this work are the rectangle's size and the dispense volume of the NLC.

The work by Cousins et al.[100] is extremely detailed, theoretically describing the confined NLC semi-droplets in relation to important NLC properties such as the elastic energy of the director field, different possible director field orientations, and anchoring strength. However, in this work a simple geometric model that describes the height variation across the width of the semi-droplet is presented, with a focus on experimental parameters. Like Cousins *et al.*'s semi-droplet isotropic model (Equation 4.2), the model in the current work does not consider gravity and is static. In addition, in this current chapter it is expected that ϵ is between approximately 0.007 – 0.2, therefore largely matching the assumptions used in

Equation 4.2. The model presented is not LC-specific, further simplifying the description of the semi-droplet and making it broadly applicable. In this work, the half-width is between 3 – 6.5mm which is somewhat greater than the capillary length for the NLC E7, $L_c \sim 1.55$mm (calculated using $\gamma = 24.2$ x 10^{-3} Nm^{-1}[48], $\rho = 1.025 gcm^{-3}$ and $g = 9.81$ ms^{-2}). This contrasts to the assumption in Cousins *et al.*[100] where $d << L_c$, therefore can be used as a comparison to see where the assumption of negligible gravitational contributions breaks down. The ρ is an average over the values in Figure 3.16a.

To form the simple geometric model, it is assumed that the base of the semi-droplets (with width $2d$) are chords of a circle and the height is therefore described by the minor arc of the minor segment of a circle with radius, r. The derivation begins with the equation to describe a circle shifted in the negative y-axis by (r - $h(0)$), where $h(0)$ is the maximum height and $y = h(x)$, i.e. the height variation along the x - axis,

$$x^2 + (y + r - h(0))^2 = r^2. \tag{4.3}$$

Figure 4.2a demonstrates the unshifted (blue) and shifted (red) circles, with their corresponding equations. The region bound under this shifted curve bound by $h(x) \geq 0$ and -$d \leq x \leq d$ is assumed to be the cross-section of the semi-droplet, as is demonstrated by the shaded region in Figure 4.2a. The diagram is not to scale, as the maximum height is approximately 10^3 times smaller than the radius, hence the shaded region is expanded for clarity.

The maximum height is derived from this Equation 4.3 by substitution of the boundary conditions that at $x = \pm$ d, $h(x) = 0$,

$$h(0) = r \pm \sqrt{r^2 - d^2}, \tag{4.4}$$

where the -ve solution is chosen in the choice of $\pm$, otherwise $h(0)$ is orders of magnitude larger than the measured semi-droplet heights. i.e. as r >> d and r >> $h(0)$, $\sqrt{r^2 - d^2}$ >> $h(0)$. By substitution of Equation 4.4 and rearrangement of Equation 4.3 to solve for h(x),

$$h(x) = \pm\sqrt{r^2 - x^2} - \sqrt{r^2 - d^2}. \tag{4.5}$$

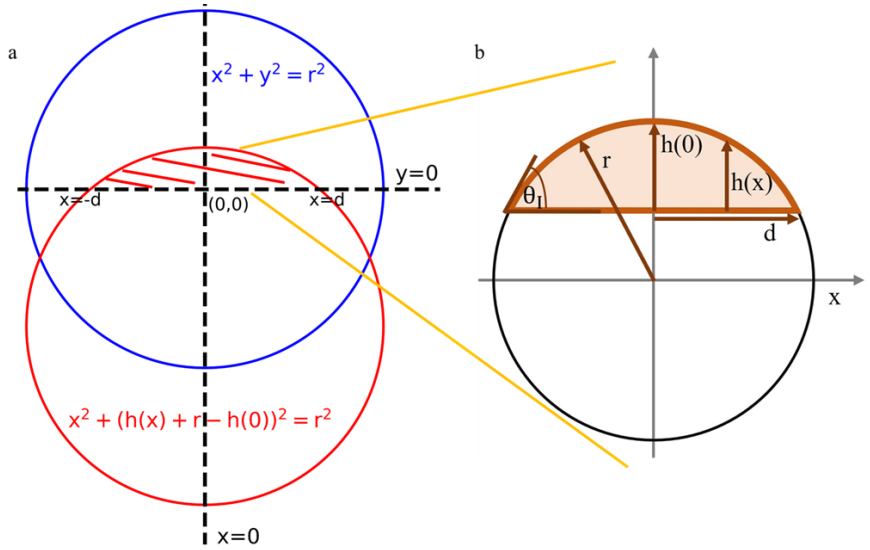

Figure 4.2: Schematics used in the derivation of Equation 4.6 to describe the cross-section of a confined NLC semi-droplet. *a:* A non-shifted circle (blue) is shifted by the radius of the circle, r, minus the semi-droplet maximum height, $h(0)$ (red). y is replaced by the change in height, $h(x)$, along the x - axis, with the shaded region denoting a confined liquid crystal semi-droplet cross-section, bounded by $x^2+(h(x)-r+h(0))^2=r^2$, $h(x)\geq 0$, and -$d \leq x \leq d$. The distance $2d$ is the length of the minor chord of the circle, and the width of the semi-droplet. *b:* Diagram of the key geometric model parameters used to describe the cross-section of an NLC 'semi-droplet' confined in a rectangular geometry where the shaded area is the cross-sectional area of the semi-droplet, A, and the interface angle is at the edge of the confinement, θ_{I}. The height of the semi-droplets in this work are of the order of 10-500µm, and the radius of the circle is of the order of 10-100mm. *Figure b is published in [1].*

For this equation to be physical with a *height* ≥ 0, the +ve root must be chosen. After substitution into Equation 4.5 with the simple geometric equation $r = \frac{d}{\sin(\theta_{\mathrm{I}})}$, where θ_{I} is the interface angle, then Equation 4.6 is reached,

$$h(x) = d\left(\frac{\alpha}{\sin(\theta_{\mathrm{I}})} - \frac{1}{\tan(\theta_{\mathrm{I}})}\right), \tag{4.6}$$

where,

$$\alpha = \left[1 - \left(\frac{x\sin(\theta_{\mathrm{I}})}{d}\right)^2\right]^{\frac{1}{2}}.$$

It is worth noting that the angle that the NLC makes with the surface at $x = \pm d$, θ_{I}, is not the same as the contact angle of NLC on the polyimide surface since the NLC cannot spread freely due to the confinement shown in Figure 3.1. To show this, a droplet of E7 was placed onto homogeneous SE130 or silane coated onto glass. On the former the droplet spread to a very thin layer, whereas on the silane the droplet shape was retained with a contact angle of 70° ± 2°, with the images shown in Figure A.2. Figure 4.2b demonstrates the key parameters used to model the semi-droplet cross-section in detail.

Equating the simple geometric model, Equation 4.6, with Cousins *et al.*'s[100] isotropic semi-droplet model, Equation 4.2, at $x = 0$ provides Equation 4.7,

$$\theta_{\mathrm{I}} = 2\mathrm{cot}^{-1}\left(\frac{4}{3\epsilon}\right). \tag{4.7}$$

Section 4.4.1 demonstrates that the models are equivalent and therefore allows for a simple method to predict the interface angle, which itself a powerful tool to predict other properties of the semi-droplet, as Equation 4.2 describes the semi-droplet height in terms of its cross-sectional area, whereas Equation 4.6 describes the height in terms of θ_{I}. The known properties of the NLC semi-droplets as formed are V, d and L, meaning A can be calculated (assuming uniform filling) using $V = AL$. This in turn can be used with d to predict ϵ with Equation 4.2, which can then be used with Equation 4.7 to predict θ_{I}. This method to predict θ_{I} is necessary as it would be impractical to measure some of the smaller interface angles. When θ_{I} is substituted into Equation 4.6 at $x = 0$, the maximum semi–droplet height is predicted, or with substitution into Equation 4.6, $h(x)$ can be predicted.

Although it is not discussed in-depth in this current work, the interface angle could alternatively be used with the simple geometric equation, $r = \frac{d}{\sin(\theta_{\mathrm{I}})}$ to predict the radius of the circle shown in Figure 4.2b.

Summarising, the model given by Cousins *et al.*[100] for a thin semi-droplet that is symmetric about $x = 0$, for an isotropic material within a well-defined con-

finement area is compared to the geometric model derived here (with the same assumptions), which was created as a simpler approach to describe the shape of the semi-droplets. However, unlike in Cousins *et al.* where $d \ll L_c$, in this work $d > L_c$. Experimentally, the height across the whole semi-droplet width is measured and considered with respect to whether the model breaks down due to the comparable sizes of the half-width and capillary length. Equation 4.2 can be used in conjunction with Equation 4.6 to provide a simple route for predicting θ_I, which is a valuable property to allow many other properties of the semi-droplets to be predicted.

4.4 Results and Discussion

4.4.1 Semi-Droplet Height

Figure 4.3 shows polarised light images of samples with varying NLC semi-droplet heights, produced by dispensing different volumes of material into the 6mm square confinement size. Examples of 11mm square, 16 x 13mm rectangular and 20 x 10mm rectangular confinements, also with varying semi-droplet heights are given in Figures 4.4, 4.5, A.3 and A.4.

Figures 4.3a–d, 4.4a-c,e-g, 4.5, A.3a,b and A.4a,b show clear birefringent fringes that allow for measurements of the height across the semi-droplets as described in Section 3.3.5. ϵ, the interface angle and the maximum height can all be predicted from the dispensed volume of NLC and geometric equations, as was described in Section 4.3. Figure 4.6 compares the experimentally measured height with the predicted height for these semi-droplets, removing geometric effects by scaling the volume of dispensed NLC by the surface area of each confinement size, $(\frac{V}{2dL})$. Figure 4.6a shows that the heights predicted using the model are in good agreement with the experimental data, i.e. within three error bars (Figure 4.5d), two error bars (Figures 4.3a,c, 4.4b, 4.5a-c) or, as is the case for the majority of the samples, within one error bar, across the different confinement dimensions and NLC volumes. It is expected that the data should fall on a straight line with gradient $\frac{3}{2}$ (Equation 4.2), and this is also shown in the figure. Therefore, it

NLC Volume, V/µL	0.5 ± 0.01	1 ± 0.01	1.8 ± 0.01
Measured height, h/µm	32 ± 6	42 ± 6	58 ± 7
Predicted height, h/µm	21 ± 1	42 ± 2	75 ± 3
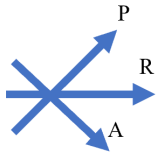	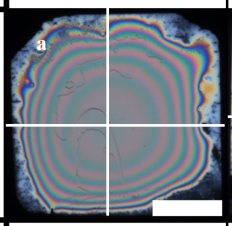	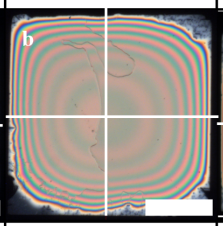	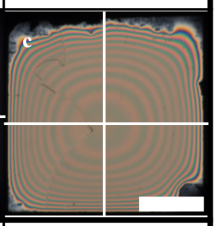
NLC Volume, V/µL	3 ± 0.01	5 ± 0.01	7 ± 0.01
Measured height, h/µm	110 ± 10	-	-
Predicted height, h/µm	125 ± 6	208 ± 9	290 ± 10
	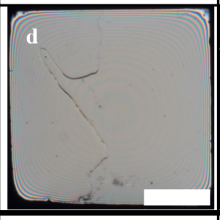	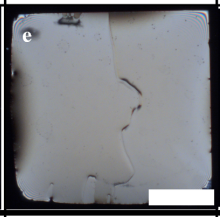	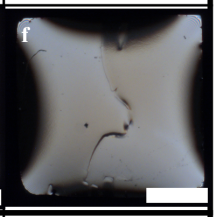
NLC Volume, V/µL	8 ± 0.01	9 ± 0.01	10 ± 0.1
Predicted height, h/µm	330 ± 10	380 ± 20	420 ± 20
	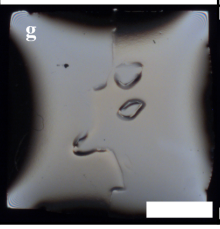	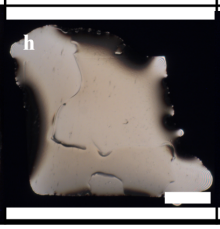	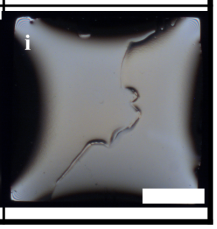

Figure 4.3: Polarised light imaging of varying NLC 'semi-droplet' volumes confined in 6mm squares on chemically patterned surfaces with a rubbed alignment layer on a solid substrate and an NLC/air interface. Maximum heights measured using pink birefringent fringes are compared to those predicted from calculation of the semi-droplet cross-sectional area ($V = AL$), leading to predictions of ϵ (Equation 4.2), interface angle (Equation 4.7) and finally, height (Equation 4.6). White lines show the cross-sections along which the centre-to-centre distances of the fringes have been measured to deduce the height variations across the semi-droplet width and length. The rubbing direction is at 45° to the crossed polarisers, with arrows marked P, A and R to show the relative directions of the polariser, analyser and rubbing respectively. The scale bars are 2mm. The cropping of the images was varied to ensure that the field of view required to capture all the information (e.g any overflowing LC) is retained while maximising the image visibility. *Figure published in [1].*

NLC Volume, V/µL	5 ± 0.01	10 ± 0.1	11 ± 0.1	30 ± 0.1
Measured height, h/µm	53 ± 7	101 ± 9	130 ± 10	-
Predicted height, h/µm	62 ± 2	124 ± 4	136 ± 5	370 ± 10
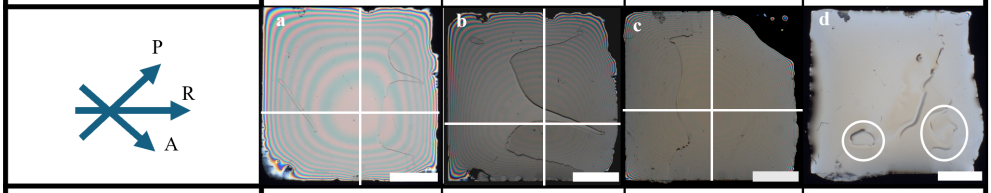				
NLC Volume, V/µL	5 ± 0.01	9 ± 0.01	10 ± 0.1	30 ± 0.1
Measured height, h/µm	37 ± 6	74 ± 8	69 ± 7	-
Predicted height, h/µm	36 ± 2	65 ± 2	72 ± 3	216 ± 8
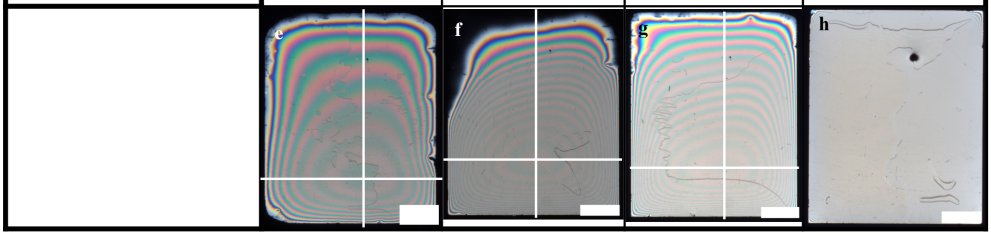				

Figure 4.4: Polarised light images of varying NLC 'semi-droplet' volumes confined in rectangles of dimensions *a-d:* 11 x 11mm; *e-h:* 16 x 13mm, on patterned surfaces with a rubbed alignment layer on a solid substrate and a NLC/air interface. Maximum heights measured using pink birefringent fringes are compared to those predicted from calculation of the semi-droplet cross-sectional area ($V = AL$), leading to predictions of ϵ (Equation 4.2), interface angle (Equation 4.7) and finally, height (Equation 4.6). White lines show the cross-sections along which the centre-to-centre distances of the fringes have been measured to deduce the height variation across the semi-droplet width and length. P, A and R show the relative directions of the polariser, analyser and rubbing respectively. The scale bars are 3mm. Extra domains other are sometimes seen when the confinement is overfilled, as circled in *d* as an example. The cropping of the images was varied to ensure that the field of view required to capture all the information (e.g any overflowing liquid crystal) is retained while maximising the image visibility. *Figure adapted from [1].*

can be concluded that the simple model can be used to predict the height of the semi-droplet from the dispense volume reasonably well.

Figure 4.6b shows the fractional difference, Equation 4.8, between the experimentally measured maximum height of the semi-droplets and those predicted from

the models,

$$Fractional\ difference = \frac{h\ measured - h\ predicted}{h\ measured}. \tag{4.8}$$

Considering this fractional difference, despite the good agreement in the height information (Figure 4.6a), there remain some systematic differences, especially for some of the larger rectangles used highlighted in Figure 4.6b, that need to be accounted for.

NLC Volume, V/µL	5 ± 0.01	7 ± 0.01	7.5 ± 0.01	9 ± 0.01
Measured height, h/µm	48 ± 6	74 ± 8	74 ± 8	101 ± 9
Predicted height, h/µm	38 ± 2	53 ± 3	56 ± 3	68 ± 5

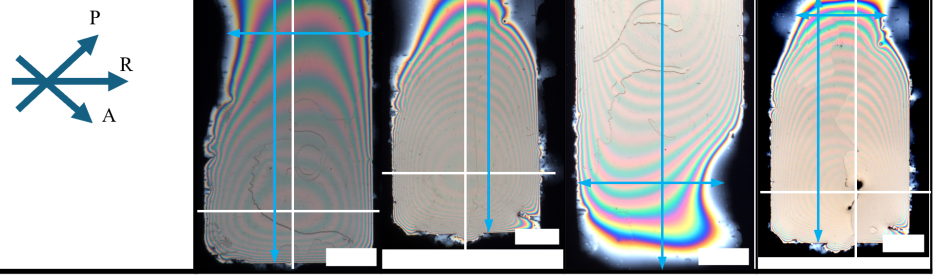

Figure 4.5: Polarised light images of varying NLC 'semi-droplet' volumes confined in rectangles with dimensions of 20 x 10mm, on patterned surfaces with a rubbed alignment layer on a solid substrate and a NLC/air interface. Maximum heights measured using pink birefringent fringes are compared to those predicted from calculation of the semi-droplet cross-sectional area ($V = AL$), leading to predictions of ϵ (Equation 4.2), interface angle (Equation 4.7) and finally, height (Equation 4.6). White lines show the cross-sections along which the centre-to-centre distances of the fringes have been measured to deduce the height variation across the semi-droplet width and length. Blue lines show the width and length measured to approximate the true surface area of NLC. P, A and R show the relative directions of the polariser, analyser and rubbing respectively. The scale bars are 3mm. The cropping of the images was varied to ensure that the field of view required to capture all the information (e.g any overflowing liquid crystal) is retained while maximising the image visibility. *Figure adapted from [1].*

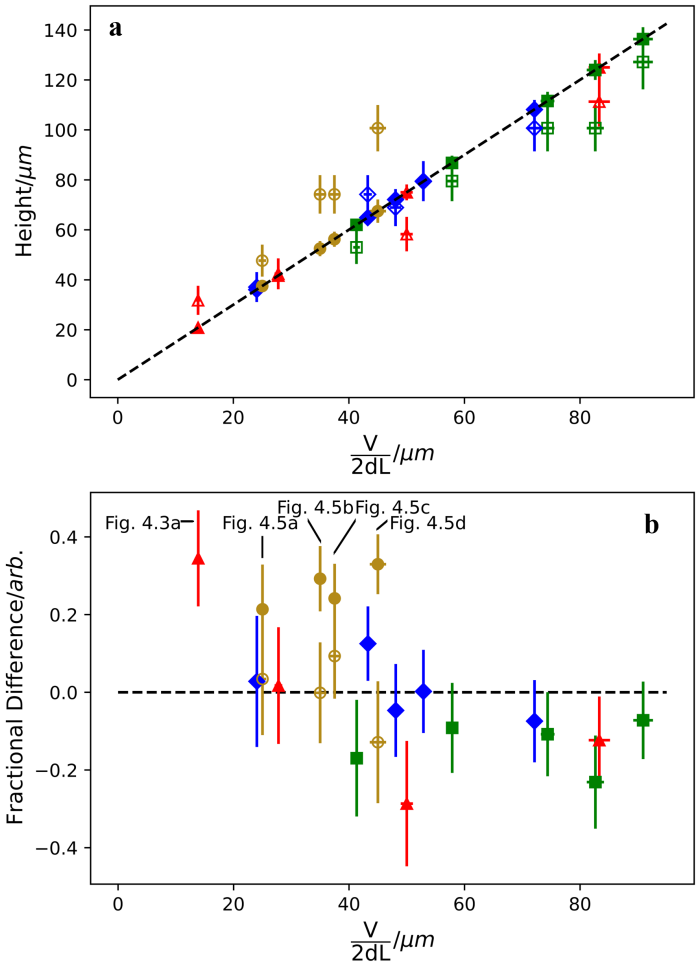

Figure 4.6: Comparison of measured and predicted maximum heights for four different confinement dimensions: *red triangles:* 6 x 6mm, *green squares:* 11 x 11mm, *blue diamonds:* 16 x 13mm, *gold circles:* 20 x 10mm *a*: Maximum height predicted from the models (closed data points), vs. the height measured using the number of birefringent fringes (open data points). A black line of the expected $y = \frac{3}{2}x$ (Equation 4.2) is added to further validate the models. *b*: Fractional difference between the measured and predicted maximum heights assuming no deviation from the expected d and L values (*closed data points*). For a selection of samples with less good agreement between the measured and predicted heights, heights are calculated using the same models, but with a measured d and L to reflect the true NLC area (*open data points*). The corresponding polarised light images where this comparison is completed are marked on the figure. $\frac{V}{2dL}$ is calculated using the known d and L, allowing for a clear comparison. The dashed line at *fractional difference* = 0 is for ease of analysis. *Figure adapted from [1].*

One possibility for this discrepancy is that some samples are underfilled (e.g. Figure 4.3a), and some are overfilled (e.g. Figure 4.3h) and in such cases, assuming that d and L are accurately known is somewhat questionable. The blue lines on Figure 4.5 for 20 x 10mm confinement sizes show where the size of d and L was measured directly to obtain a more accurate NLC coverage surface area within the rectangle. These four samples were chosen because, as a confinement size group of samples, they have the worst agreement in general between the measured and predicted maximum heights, where Figures 4.5a-c agree within two error bars, and Figure 4.5d agrees within three error bars. Samples 4.5a-d are marked in Figure 4.6b. The maximum height was predicted in the same way using the models (i.e. estimating A from $V = AL$, then predicting ϵ, followed by θ_{I} and finally height at $x = 0$), but with the measured d and L values, and compared to the fractional difference for the heights assuming known d and L values (Figure 4.6b). In all cases, using the measured d and L values moves the points for these four samples closer to the *fractional difference* $= 0$ dashed line.

A second possible reason for the discrepancies in the measured and predicted heights is that the assumption that the semi-droplet cross-sectional area is a minor segment of a circle (see section 4.3) is incorrect. Figure 4.7 directly compares the measured and predicted heights across the semi-droplets for three relatively small heights (predicted heights between 21 - 136μm) for each of the four confinement dimensions. Equations 4.2 and 4.6 are fitted to the measured heights, where the cross-sectional area and interface angle, respectively, are allowed to vary. An example of this code can be found in Figure A.5. It can be seen that the models are indistinguishable for this parameter space and that there is an excellent fit for the semi-droplets with the smallest heights, but that the actual shapes of the semi-droplets deviate from the model as the height increases. In particular for the semi-droplet profiles with greater heights, the centres are flatter and there is more curvature at the edges. It can be suggested that this distortion can be attributed to the effect of gravity as neither model includes gravitational terms, and the height is much smaller than the width in all cases, so it is to be expected that the middle region will be relatively flattened.

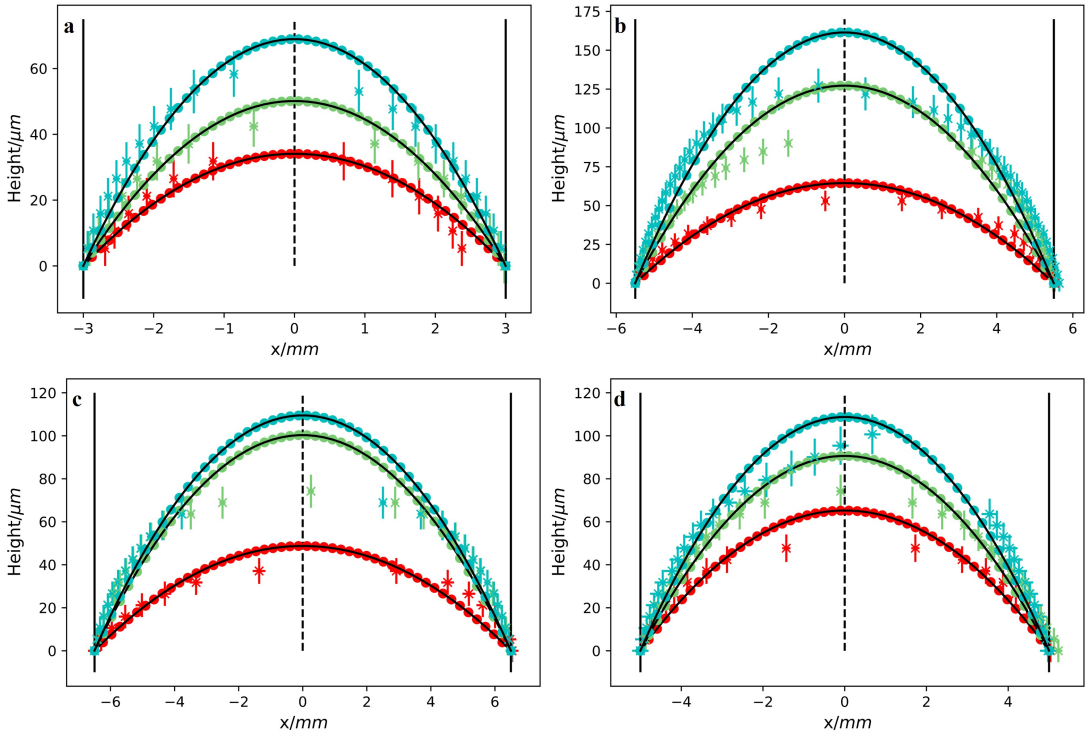

Figure 4.7: Height variation using the centre-to-centre distances of pink birefringent fringes across NLC semi-droplet widths for three NLC dispense volumes, V, and four confinement sizes: *a:* 6 x 6mm with $V = 0.5\mu$L (red), 1μL (green), 1.8μL (blue). *b:* 11 x 11mm with $V = 5\mu$L (red), 10μL (green), 11μL (blue). (c) 16 x 13mm with $V = 5\mu$L (red), 9μL (green), 10μL (blue). (d) 20 x 10mm with $V = 5\mu$L (red), 7μL (green), 9μL (blue). The data is fitted to both Equation 4.6 (*black line*), or Equation 4.2 (*circles*). A dashed line is included at $x = 0$, as well as solid lines at the expected edges of the confinement shapes. *Figure published in [1].*

Ensuring that the geometry is smaller than the capillary length allows us to make the assumption that gravitational effects can be neglected; for E7, L_c is approximately 1.55mm as demonstrated in Section 4.3. In this work $d > L_c$, i.e $\frac{d}{L_c} \sim 1.9$ for the 6mm square confinements; $\frac{d}{L_c} \sim 3.2$ for the 20 x 10mm rectangles; $\frac{d}{L_c} \sim 3.5$ for the 11mm squares, and $\frac{d}{L_c} \sim 4.2$ for the 16 x 13mm rectangles, i.e. this important constraint is relaxed in the expectation that the semi-droplets will be more readily visible without the need for a microscope. Qualitatively for heights $\lesssim 50\mu$m, the fits of the models to the data in Figure 4.7 agree well,

regardless of the ratio of the semi-droplet half-width to the capillary length.

Figure 4.8, like Figure 4.7, compares the measured and predicted heights of the semi-droplets along their lengths (y - axis) instead of width. A common feature in the measured heights for Figures 4.7 and 4.8 is their asymmetry, as shown relative to the dashed lines at x,$y = 0$. As no special effort was made to ensure the stage of the imaging system was perfectly flat, there was probably a tilt of a few degrees in the x- and y - axes, which would explain this asymmetry, but does not have a significant or adverse effect on the semi-droplets. When the semi-

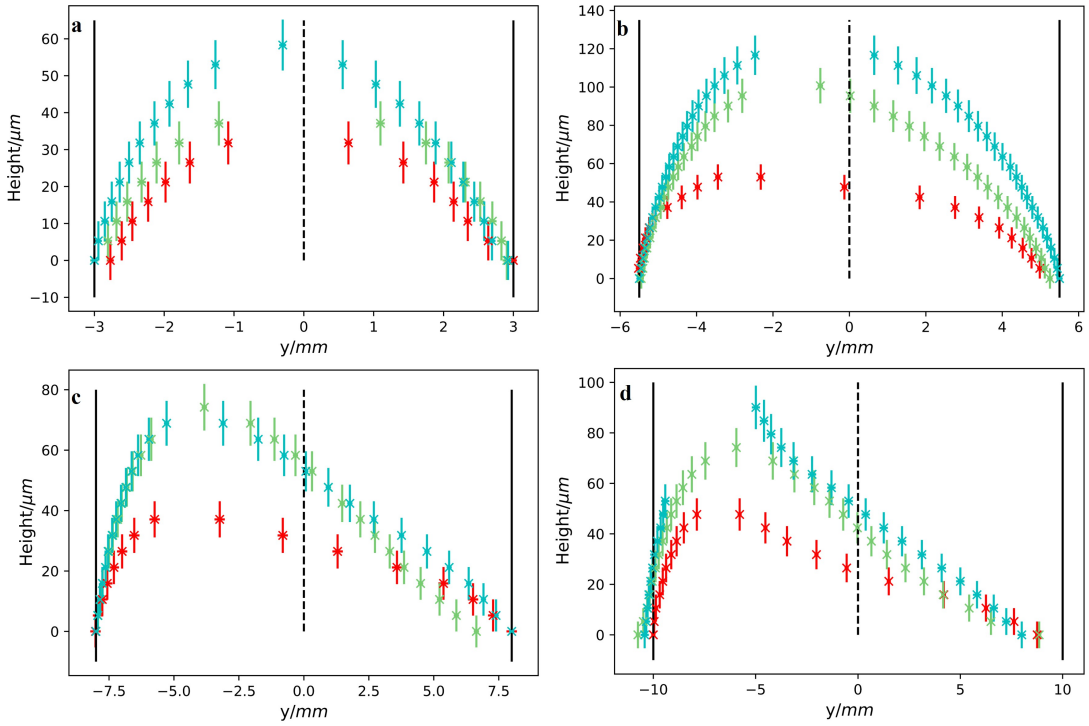

Figure 4.8: Height variation using the centre-to-centre distances of pink birefringent fringes across NLC semi-droplet lengths for three NLC dispense volumes, V, and four confinement sizes: *a:* 6 x 6mm with $V = 0.5\mu$L (red), 1μL (green), 1.8μL (blue). *b:* 11 x 11mm with $V = 5\mu$L (red), 10μL (green), 11μL (blue). *c:* 16 x 13mm with $V = 5\mu$L (red), 9μL (green), 10μL (blue). *d:* 20 x 10mm with $V = 5\mu$L (red), 7μL (green), 9μL (blue). A dashed line is included at $y = 0$, as well as solid lines at the expected edges of the confinement shapes. *Figure published in [1].*

droplets are imaged, they are in a steady state. The asymmetry is most clearly seen both along the width and length for the predicted height of 68µm for the 20 x 10mm samples (Figures 4.7d and 4.8d, with the polarised light image in Figure 4.5d). Along the length for the rectangles, there is a clear increase of asymmetry for the rectangles as compared to the squares, with the 6mm square generally the most symmetric. It is to be expected that a more asymmetric flow of the NLC is possible in the lower aspect ratio rectangles; the squares have an aspect ratio of 1, whereas the rectangles have aspect ratios of approximately 0.8 for the 16 x 13mm and 0.5 for the 20 x 10mm rectangles. It is also to be expected that the shape is less symmetric along the length of the rectangular samples, especially in the longest samples (20 x 10mm), as the increased length will allow for gravity to have a larger effect on the symmetry of the semi-droplet. It is worth noting also the ratio $\frac{L}{L_c} \geq \frac{d}{L_c}$.

A potential reason that the height profiles in Figures 4.7 and 4.8 are asymmetric on one side of the $x,y = 0$ lines relates to the direction they were imaged on the stage relative to their rubbing direction, hence the direction of the possible stage tilt experienced. The one-sided asymmetry is unlikely to be significantly related to the surface fabrication as the samples in e.g. Figure 4.5 are completed with the same reused surface.

Another consideration when using the pink fringes to plot the semi-droplet cross-sectional shapes is the assumption that the height (thus the fringe number, m, see Figure 3.15) increases towards the centre of the semi-droplet. It would be non-trivial to identify if the fringes instead indicated a dip in the semi-droplet profile, similar to the confined ferroelectric nematic liquid crystal in Figure 2.7c. However, the excellent agreement of the measured heights with the predicted heights and the expected $height = \frac{3}{2}\frac{V}{2dL}$ (see Equation 4.2) in Figure 4.6a implies that the assumption of increasing height towards the semi-droplet centre is valid.

The solid black lines at the edge of the plots indicate the expected values for $x = \pm d$ (Figure 4.7) or $y = \pm\frac{L}{2}$ (Figure 4.8) and allow us to consider the quality of filling of the semi-droplet within the confinements. All the samples presented in Figure 4.7 demonstrate a good agreement with these lines, except for those

with predicted heights of 136µm for the 11mm square confinement, and 53µm for the 20 x 10mm rectangle confinement (Figures 4.7b,d, with the polarised light images in Figures 4.4c and 4.5b, respectively). In the x – axis, they are overfilled by 0.15 ± 0.08mm and 0.2 ± 0.1mm, respectively, hence there are only slight differences with the measured and expected sample edge, indicating that there is overall good filling along the width of the confinement. For Figure 4.8, the 20 x 10mm size confinements (Figure 4.8d) are the only examples given with significant under- or overfilling. For Figure 4.5a (predicted height of 38µm) this corresponds to an underfill at the top of the confinement (positive x - axis in Figure 4.8) of 1.2 ± 0.1mm; for Figure 4.5b (predicted height of 53µm), there is an overfill at the bottom of the confinement (negative x - axis in Figure 4.8) of 0.8 ± 0.1mm, and an underfill at the top of 1.1 ± 0.1mm, and for Figure 4.5d (predicted height of 68µm) the overfill at the bottom is 0.4 ± 0.2mm and the underfill at the top is 2.0 ± 0.2mm. Therefore, this size can be ruled out as a choice for useful sensing devices in the future. In general, for the other confinement sizes (Figures 4.8a-c) however, there is good filling along the length.

4.4.2 Defect Formation in E7 Semi-Droplets

A key consideration of use of this system as a sensor is how clear and reproducible the director fields are before addition of the analyte. A common feature of NLC confined on a stripe surface seen in the literature is a central disclination line. For example, in Bao *et al.*[15], a central disclination is described by an 'escaped radial' director field, characterised by alternating defects of strength of ± 1. Cousins *et al.*[100] describe the central disclination line observed in their work in terms of a discontinuous angle of the NLC director. A similar feature is seen in each of the polarised light images in Figures 4.3 - 4.5, A.3 and A.4, i.e. a disclination line, or line of defects that runs approximately perpendicular to the rubbing direction. Figure 4.9 schematically describes the likely origin of these disclination, due to rotations of the director in opposite directions throughout the semi-droplet height. The disclination line is most consistent in the 6mm square and is straightest in the sample with a V of 7µL (predicted height of 290µm, Figure 4.3f) sample,

although samples such as that with a V of 5µL in a 6mm square (predicted height of 208µm, Figure 4.3e) have a similar level of quality.

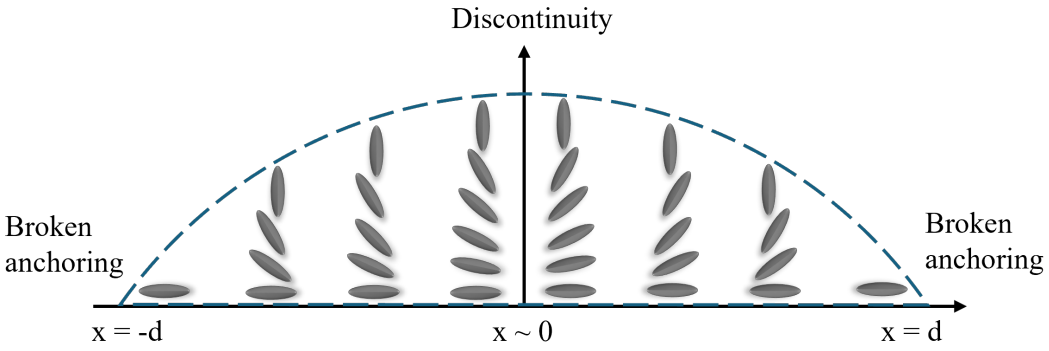

Figure 4.9: Schematic to demonstrate the likely origin of disclination lines in semi-droplets near their centre ($x \sim 0$), and the potential anchoring breaking near the confinement edges ($x \sim \pm d$). Not to scale.

Also demonstrated in Figure 4.9 is regions near $x = \pm d$ where there is likely to be anchoring breaking. Such an effect is observed in Cousins *et al.*[100], where their experimentally pinned ridge approaches planar at the confinement edge.

As already discussed, the square confinement shapes (Figures 4.8a,b) have a generally more symmetric filling than the rectangles (Figures 4.8c,d). Examples from Figures 4.3 - 4.5, A.3 and A.4 demonstrate however that there is a balance to be found for the NLC dispense volume so as not to overfill (e.g. Figure 4.3h) or underfill (e.g. Figure 4.3a) the samples. Significant overfilling could impact the quality of the director field significantly, e.g. Figure 4.4d (with a predicted height of 370µm) has extra domains other than the central disclination line. This could also relate to the fact that the effect of an anchoring surface only lasts until approximately 100µm into the NLC (see Section 2.2.3). This would imply that the region in the centre of the taller semi-droplets is no longer HAN (see Section 4.2.3). As the 6mm square confinement was identified as having the straightest central disclination line in general, it should be the focus for identifying the correct volume of the semi-droplet. i.e., qualitatively V between 3 - 5µL corresponding to predicted heights of 125 - 208µm (Figure 4.3d-e) offers a uniform fill

including to the corners of the confinement, but without overfilling it, suggesting a good choice of parameter space to continue development for sensors.

These key points, i.e. how straight the central defect is, as well as the quality and symmetry of the filling implies that the 6mm square with V between approximately 3 - 7µL is the most suitable for future sensor development. There are clear benefits to this finding, in that less LC will need to be used to fill the sample than would be needed in a larger confinement size or a higher dispense volume, however a balance must be found between usage of material and sensitivity of the sample. For example, whilst Bao *et al.*[15] present a sample with a straighter central disclination line, the width of their stripes was of the order of µm instead of mm as in this work, hence may well be less sensitive to gaseous stimuli due to less surface area available to interact with stimuli, and would likely have to be viewed using a microscope.

4.5 Further Investigations on 6mm Square Confinements

As discussed in Section 4.4.2, the 6mm square is the most ideal of the confinement sizes investigated for potential future sensing devices. Therefore, it is beneficial to complete further analyses of the system including probing the interface angle, polarised imaging with a rotation of crossed polarisers with respect to the rubbing direction, and an added full waveplate. The semi-droplet with a predicted height of 125µm (Figure 4.3d) is included in these discussions as it is the limit of measurement for the pink birefringent fringes across the x - axis, for the heights experimentally investigated.

4.5.1 E7 Semi-Droplet Interface Angle

As was mentioned in Section 4.3, the interface angle is a powerful parameter as it can allow many other semi-droplet parameters to be predicted including maximum height and height variation along the semi-droplet width (Equation 4.6), as well as the radius of the circle on which the semi-droplets are modelled

(Figure 4.2b). The validity of θ_I predicted from the models, (i.e. using $V = AL$ to deduce the cross-sectional area, followed by Equation 4.2 to predict ϵ, and Equation 4.7 to predict θ_I) is discussed in this section for the V = 0.5 - 3μL semi-droplet samples (Figures 4.3a-d), using Figure 4.10. The predicted θ_I values are shown in Figure 4.10a in blue, and are compared to measurements of θ_I made by applying a linear fit to the first few data points on the left of Figure 4.7a in red. All the interface angles presented are less than 6.5° which highlights one aspect of why the models presented simplify the prediction of the interface angle and hence the prediction of the height variation across the semi-droplet. i.e., this angle would be difficult to measure directly accurately using contact angle apparatus.

The measured interface angle is always greater than the predicted interface angle, as would be expected from examination of the experimental data and models in Figure 4.7a. There are two contributions to this observation. Firstly, the predicted values of θ_I, having only the uncertainties in V, d and L which are small, is likely to be quite accurate, whereas the measurement relies only on a few data points, and the linear fit is only an approximation of the shape. The only values of θ_I that agree within three error bars or better is for the sample with a V of 1.8μL.

To determine whether the interface angle deduced from measurement or the model is better at predicting the semi-droplet height, Figure 4.10b also compares calculations (blue and red, corresponding with the θ_I from Figure 4.10a) with the measured heights from Figures 4.3a-d (green). None of the interface angles predicted from the two methods agree within three error bars or less for the 1.8μL sample. For the sample with a V of 0.5μL, the predicted height from the measured interface angle is closer to the measured height than the predicted height from the predicted interface angle, i.e. in agreement within one and two error bars, respectively. However, the inverse is seen for the taller samples which agree with the measured height within one error bar for the predicted interface angle for samples with V of 1μL and 3μL, compared to within two and greater than three error bars from the height using the measured interface angle, respectively.

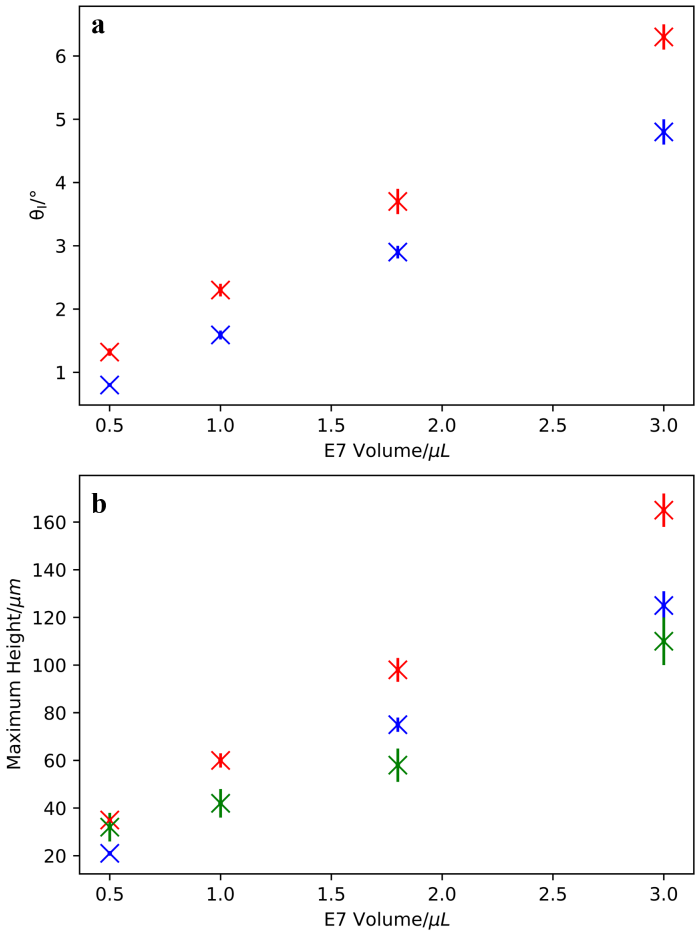

Figure 4.10: Two key properties identified through different methods of the E7 semi-droplets confined in 6mm squares. *a:* The predicted interface angle, θ_{I}, is derived from either calculating $V = AL$, estimating ϵ (Equation 4.2), and finally Equation 4.7 (blue), or measured from linear fits of the first few data points on the left-hand side of the height variation plots in Figure 4.7 using the small angle approximation ($\tan(\theta_{\mathrm{I}}) \approx \theta_{\mathrm{I}}$ for small θ_{I}) (red). *b:* The maximum height is derived from the θ_{I} in *a* using Equation 4.6. The measured heights from the birefringent fringes are also included (green).

For a V of 1.8µL, the agreement from the predicted interface angle agrees with the measured height within two error bars compared to greater than three error bars for the measured interface angle.

The radius of the circle used to model the semi-droplets (Figure 4.2b) can be

calculated using the predicted interface angle with $r = \frac{d}{\sin(\theta_I)}$ to be between 220 - 36mm for V of 0.5 - 3µL, respectively. The fact that the radius is approximately three orders of magnitude larger than the heights further validates the use of the HAN director field (Figure 4.1) that was assumed in this work to describe the director throughout the NLC semi-droplet height.

4.5.2 E7 Semi-Droplet Director Fields under Varied Polarisation Conditions

Figure 4.11a demonstrates the rotation of crossed polarisers between 0° and 45° with respect to the rubbing direction for a semi-droplet with a predicted height of 21µm (Figure 4.3a). Figure 4.11ai shows the 'dark' state (with crossed polarisers aligned to the rubbing axis) which, when paired with the 'bright' state in Figure 4.11av (where the crossed polarisers are at 45° to the rubbing axis) implies that there is relatively good alignment of the director with the rubbing axis from the expected dark to brighter transition between these angles (see Equation 3.2). A similar effect is seen in Figure 4.11bi which has both measured and predicted heights of 21 ± 6µm and 21 ± 6µm, respectively. These height values are in better agreement than was seen for the sample in Figure 4.3a, likely due to the fact that there is better filling to the full 6mm square, therefore the d and L assumed in the predictive model are more accurate. In Figure 4.11bi, the 'dark' state is not completely black, which is expected otherwise it would imply that the director was planar throughout the whole height and the disclination line would not be seen, e.g. like is seen for a planar aligned LC cell. At the beginning of the rotation of the crossed polarisers for these two samples until approximately 20 - 30° from the rubbing direction, the domains on either side of the central disclination line are distinguishable by a difference in brightness, however this becomes homogeneous for the rest of the rotation. This suggests a very slightly different director orientation on either side of the line, as would be expected.

As it was identified that E7 semi-droplets with predicted heights of 125 - 208µm are most suitable for future sensing investigations out of the device configurations discussed in this work, a semi-droplet with a predicted height of 208µm is

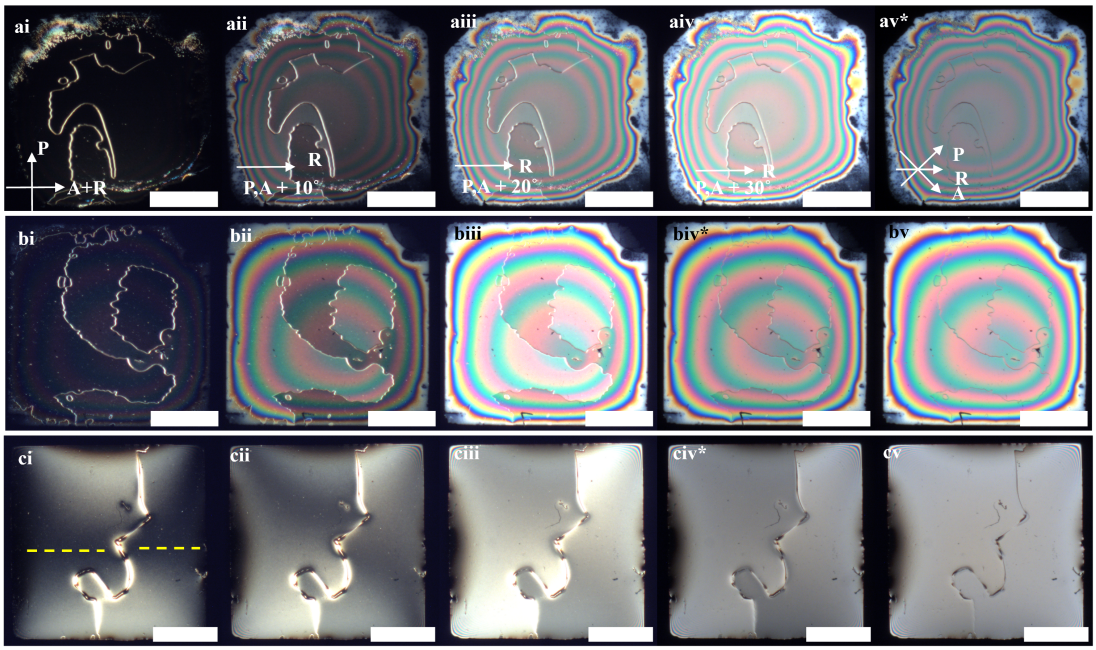

Figure 4.11: Rotation of crossed polarisers through 0° (*i*) - 45° (*v*) with respect to the rubbing direction of an E7 semi-droplets with predicted heights: *a,b:* 21µm and *c:* 208µm. The yellow dashed lines indicate the position of the two dark brushes evidencing a potential strength $= +\frac{1}{2}$ defect. P, A, and R show the relative directions of the polariser, analyser and rubbing, respectively. The scale bars are 2mm. The * indicates where the imaging exposure was known to be adjusted to preserve the quality of the images.

presented in Figure 4.11c to show the effect of the rotation of crossed polarisers. Unlike for Figure 4.11ai, the semi-droplet is not mostly dark in the 'dark' state (Figure 4.11ci), which is likely a cause of a decreased effect of the anchoring at the substrate and air/NLC interfaces for the taller semi-droplet, as there is more liquid crystal between these bounding surfaces. As previously discussed in Section 2.2.3, LC in the bulk only has good alignment from anchoring conditions until approximately 100µm. The semi-droplet has homogeneous brightness in the 'bright' state, Figure 4.11cv, similar to Figures 4.11av,bv. Whilst there are likely other defects along the central disclination line, the most obvious potential defect (see Section 3.3.3) is a strength $= +\frac{1}{2}$ defect, identified by the two dark brushes that rotate in the same direction as the crossed polarisers and highlighted in yellow dashed lines in Figure 4.11c. Equivalent rotations of crossed polarisers for

E7 semi-droplets are presented in Figures A.6 and A.7 for the samples in Figure 4.3. These demonstrate that, except for in the case of the semi-droplets with a predicted height of 21µm (Figures 4.11a,b), the main visible potential defect is strength $= +\frac{1}{2}$.

A slight modification was made to the bespoke imaging system (see Section 3.3.1) to allow a lambda plate (see Section 3.3.2) to be added in-between the first polariser and the stage in transmission mode. Figures 4.12ai,aii show the waveplate axis perpendicular or parallel to the rubbing axis, respectively, for the semi-droplet with a predicted height of 21µm and demonstrate that the director at the edges of the confinement are parallel to the rubbing axis, from a decrease in the retardation towards orange when the waveplate is perpendicular, and an increase towards blue when it is parallel. In Figure 4.12aii it appears as though the retardation continuously increases towards the centre of the droplet, as would

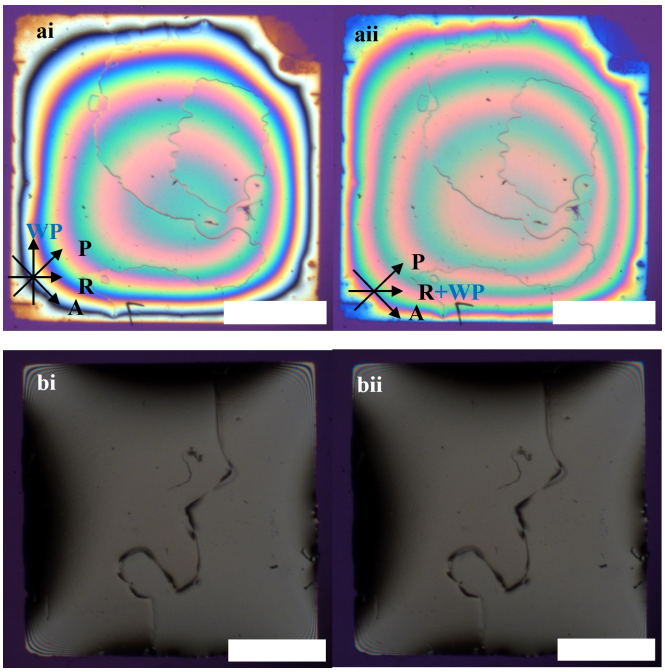

Figure 4.12: Polarised images of E7 semi-droplets with predicted heights: *a:* 21µm and *b:* 208µm. A lambda plate is added *i:* perpendicular or *ii:* parallel to the rubbing direction. P, A, R, WP show the relative directions of the polariser, analyser, rubbing and lambda waveplate, respectively. The scale bars are 2mm.

be expected for the increasing height. However, Figure 4.12ai suggests that there may be a discontinuity before the black fringe, potentially the bright line near the confinement edges in Figure 4.11bi, as the orange border would not support a continuous increase in retardation towards the black fringe. To consider a semi-droplet within the range of predicted heights of 125 - 208µm, Figure 4.12b demonstrates the equivalent images for the predicted height of 208µm, showing a similar shift in retardation colour for the first few birefringent fringes.

4.5.3 Filling Quality Observations

Effect of Experience

To verify that the quality of filling was dependant largely on the NLC dispense volume instead of improving experience of the researcher in filling the confinements, three E7 semi-droplet heights (predicted heights of 21µm, 208µm, 380µm) in 6mm squares were remeasured, as shown in Figures 4.11b,c and Figure 4.13, respectively.

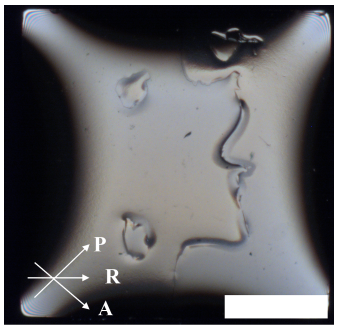

Figure 4.13: Polarised image of a second E7 semi-droplet confined in a 6mm square with a predicted height of 380µm to check the filling quality. P, A and R show the relative directions of the polariser, analyser and rubbing, respectively. The scale bar is 2mm.

For the semi-droplet with a predicted height of 21µm, there is a slight improvement in the filling quality between Figure 4.3a and Figure 4.11b, however there is still imperfect filling near the edges and corners of the confinement, implying that a V of 0.5µL is still too little E7 for high quality confinement.

For the semi-droplet with a predicted height of 208µm, Figure 4.11c shows a slightly better filling than Figure 4.3e, especially in the corners, indicating that the experience in filling the confinement will have at least a small effect on the director field of the semi-droplet as expected. However, the disclination line is slightly more central in Figure 4.3e than Figure 4.11c.

The semi-droplet with a predicted height of 380µm as shown in Figure 4.3h is an overfilled sample, however in Figure 4.13 the confinement is not obviously overfilled which again implies a different level of experience affects the quality of filling of the samples. These observations lend further validation to the conclusion that V between approximately 3 - 7µL (predicted heights of 125 - 290µm) as most ideal for potential sensing devices, as this range should be the most lenient on less experienced persons filling the samples if this system were to be industrialised.

Other Filling Features

Some extra features that evidence the filling quality of the samples seen outside the 6mm confinement square are circled in yellow in Figure 4.14. Figure 4.14a demonstrates a string-like texture with birefringence from the corner of the semi-droplet with a predicted height of 125µm. This is reminiscent of the branched textures that are seen in ferroelectric nematic liquid crystals when on a ferroelectric surface, as a competition between electrostatic forces vs. surface tension[82], as will be discussed in Section 8.3.3. Although nematic liquid crystals are not polar, a small instantaneous charge combined with the unfavourable surface tension at the corner could cause rare occurrences of a similar effect.

Figure 4.14b demonstrates a small birefringent droplet to the right-hand side of the 6 x 6mm confinement of the semi-droplet with a predicted height of 330µm. This is likely from the deposition of the liquid crystal, if a small quantity did not dispense with the rest of the droplet. However, the droplet is clearly small compared to the volume of the whole semi-droplet.

Figure 4.14c is the most dramatic extra feature, shown for the semi-droplet with a predicted height of 380µm. The region of birefringent material near the corner

was likely previously connected to the clear overflow seen. The low birefringence colours imply that this region is not very tall ($\Gamma = \Delta n \cdot height$, see Section 3.3.2) and therefore is minimal compared to the volume of the semi-droplet bulk.

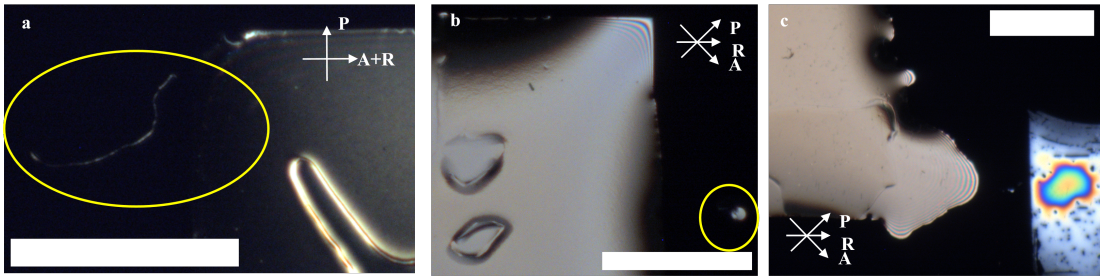

Figure 4.14: Small additional features outside of the confinement, as circled in yellow. *a:* The semi-droplet with predicted height = 125µm (Figure 4.3d) demonstrates a string-like effect from the corner. *b:* The semi-droplet with predicted height = 330µm (Figure 4.3g) demonstrates a small droplet of liquid crystal outside the right-hand edge. *c:* The semi-droplet with predicted height = 380µm (Figure 4.3h) demonstrates a region with low birefringence colours near its bottom right corner. P, A, and R show the relative directions of the polariser, analyser and rubbing, respectively. The scale bars are 2mm.

Spherical Cap Assumption

The assumed arc of a circle shape for the semi-droplet (see Section 4.3) was chosen due to the length of the semi-droplet confinement being greater than the width in two out of the four cases, hence the assumption $V = AL$ is likely more valid. However it may be suitable to model the square semi-droplets as spherical caps with the well-known Equation 4.9[1],

$$V = \frac{1}{6}\pi h(0)(3d^2 + h(0)^2), \tag{4.9}$$

as sketched in Figure 4.15. d is the radius of the spherical cap, V is the NLC volume and $h(0)$ is the maximum height.

To evaluate this, parameters for the 6 x 6mm and 11 x 11mm semi-droplets in Figures 4.3d and 4.4a that qualitatively have relatively high quality filling

[1]Further information can be found at e.g. Wolfram Mathworld.

(with predicted heights from the circle arc assumption of 125µm and 62µm, respectively) are substituted into Equation 4.9. In both cases, the spherical cap approximation is significantly worse at predicting the maximum height, resulting in predicted heights of 212µm and 105µm for measured heights of 110µm and 53µm, respectively. A discussion of the semi-droplet shape in relation to the capillary length (surface tension and gravitational effects) was included in Section 4.4.1. As the arc of a circle assumption is non-LC specific, it is assumed that the surface tension is dominant over the elastic torque from the NLC's elastic constants (see Section 2.2.3).

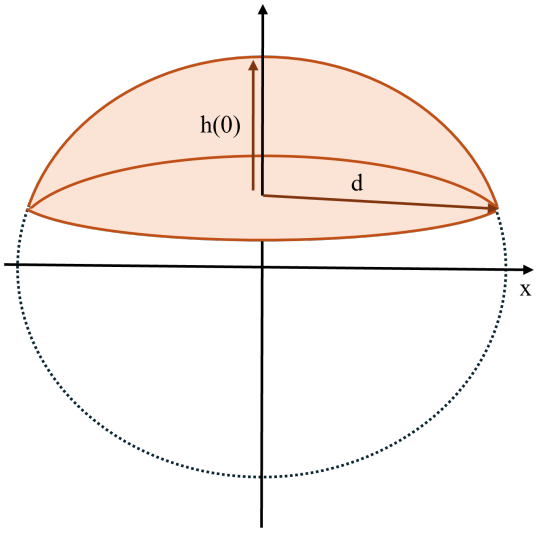

Figure 4.15: Schematic diagram of semi-droplets modelled as a spherical cap with a radius, d, maximum height, $h(0)$, and a LC volume, V, denoted by the orange shaded area. Not to scale.

4.6 Summary

Here, a novel chemical patterning method has been used to create rectangles with accurately known dimensions on a surface to confine NLC, forming relatively large NLC semi-droplets. These all have a well-defined hybrid alignment due to one rubbed planar surface (solid substrate) and one homeotropic surface (NLC/air). The fabricated rectangles cover a wide dimensional range with widths between 6

- 13mm; lengths between 6 - 20mm, and aspect ratios between 0.5 - 1, therefore the well-known E7 NLC was used to make the findings clearer. The confined NLC semi-droplets had a range of heights between approximately 20 - 420µm. This work has therefore investigated a significant range of variables, allowing a better understanding of the limiting factors in the parameter spaces in context of a future sensing device.

A simple model to describe the height of the NLC across the rectangle was derived and compared to an existing, more detailed model. The two models had a similar experimental and theoretical geometry, however the model in this work is calculated using the interface angle, while the existing model utilises the cross-sectional area. Therefore, a combination of the two models allows for the cross-sectional area (estimated using the volume of the semi-droplet and assuming that the cross-sectional area is constant along its length) to give a prediction of the interface angle. This in turn can be used to predict the height variation across the semi-droplet, as well as the maximum height. These predictions were found to be in excellent agreement with experimentally measured semi-droplet heights, found from the birefringent fringes of the NLC polarised light images, lending validation to the model. The height variation was deduced across the whole semi-droplet width, whereas Cousins *et al.*[100] evaluated this at the semi-droplet edge. Systematic differences such as the effect of under- or over-filling the confinements and the potential effect of gravity were discussed. It was shown that the height of the NLC in semi-droplets is both more symmetric in the width- rather than length- direction, and that the squares, particularly the 6mm square, were most symmetric. The model was found to agree well with measurements for heights $\lesssim 50\mu m$, even though the dimensions exceeded the capillary length of the NLC, $\frac{d}{L_c} > 1$, irrespective of the value of the ratio $\frac{d}{L_c} \sim 1.9 - 4.2$.

The 6mm square was seen to exhibit a more well-defined, straight, and central defect line (a feature commonly seen in NLC semi-droplets) than the 11mm square or rectangular confinements. The study has also shown that there must be enough NLC to fill the sample, but not so much to overfill it or to cause a decrease in the quality of the director field by causing extra domains to form in the semi-

droplet. Of the samples investigated, the square with V approximately between 3 - 7µL-filled 6mm squares, corresponding to predicted heights between 125 - 290µm, demonstrated the best director field of those presented for simplicity and reproducibility as a sensor. Combined with the good symmetry as previously discussed, the 6mm square is suggested to be a good parameter space for future sensing work.

Rotation of crossed polarisers with respect to the rubbing direction for semi-droplets confined in 6mm squares demonstrates that, except for the predicted height of 21µm semi-droplets which have domains of different brightness on rotation, the main visible defect (if that is the origin of the dark brushes) is strength $= +\frac{1}{2}$. For the semi-droplets confined in the 6mm squares, addition of a lambda plate into the imaging system allowed for identification of the director orientation at the edges as parallel to the rubbing direction for the predicted height of 21µm semi-droplet. These are all beneficial investigations to further understand the director field, as would be useful pre-analyte addition in sensing devices.

The use of the well-known E7 NLC allowed exploration of a wide range of geometries. However, in all cases the anchoring at the air/NLC interface was homeotropic, which is not necessarily an ideal geometry for interactions with certain analytes, such as those that homeotropically align an LC on contact (see Section 2.5.1). Therefore, the next chapter considers a different NLC that is not homeotropic at the air/NLC interface, and therefore may provide a better system for sensing applications.

Chapter 5

MLC 7023 Confined in Chemically Patterned Squares

5.1 Introduction

In the previous chapter, E7 nematic liquid crystal (NLC) semi-droplets were confined in millimetre-sized chemically patterned rectangles and analysed for their maximum height and the variation in height across the semi-droplet width and length, using both the full wave equation for polarised imaging and a simple, non-LC specific predictive height model. The measured heights and model agreed well within three error bars or better for the maximum height, with agreement across the width cross-section for semi-droplets with heights $\lesssim 50\mu m$. It was qualitatively discussed that a 6mm square confinement filled with a V of approximately 3 - 7μL NLC (predicted height $\sim$ 125 - 290μm) would likely be the most ideal of those investigated for future sensing devices. Therefore, further investigations on semi-droplets within 6mm squares were used to discuss the accuracy of different methods to calculate the interface angle[1]; identify the main defects seen on polariser rotation, and present further information on the director field from addition of a lambda plate.

Whilst the systems in Chapter 4 presented features that could be suitable for

future sensing devices, E7 semi-droplets would likely not be ideal to detect homeotropically-aligning analytes due to the already homeotropic air/NLC interface. i.e., there may not be a significant contrast between the director field pre- and post-analyte addition. Therefore, this chapter discusses the NLC MLC 7023 as the anchoring at the air/NLC interface is non-homeotropic[15, 48].

Device parameters are again investigated over MLC 7023 dispense volumes, V, between 0.5 - 10µL (predicted heights of 21 - 420µm) in 6mm squares fabricated using the same method as the surfaces discussed in Chapter 4. The predicted maximum height from the non-LC specific model discussed in the previous chapter is used in conjunction with the number of pink birefringent fringes from polarised imaging and the full wave equation to calculate the effective birefringence for the MLC 7023 semi-droplets. This is subsequently used to determine the director field throughout the semi-droplet height with a specific focus on the anchoring at the air/NLC interface. The effects of the much lower MLC 7023 birefringence and surface tension compared to E7 (see Section 3.4) on the filling quality of the squares is discussed. Again, the interface angle calculations, key defects identified on rotation of crossed polarisers, and information of the director field using a lambda plate are presented, with a discussion of the most suitable parameters of those investigated for potential MLC 7023-based sensing devices.

5.2 Experimental Methods

5.2.1 Patterned Surface Fabrication

The chemically patterned surfaces were fabricated using the methods described in Section 3.2 to produce 6 x 6mm squares. The MLC 7023 was confined within a hydrophobic monolayer denoting this shape, and sat atop a rubbed alignment layer.

5.2.2 NLC Deposition

The MLC 7023 semi-droplets were filled onto the substrates at room temperature and spread to the confinement edges using directional compressed air or gentle

tilting as required. The confined MLC 7023 experienced a temperature cycle as shown in Table 5.1.

Step No.	**Rate**/ °C min^{-1}	**End Temperature**/ °C	**Hold Time**/ min
1	5	75	0
2	0.5	85	0
3	2	90	10
4	2	85	0
5	0.5	75	0
6*	5	<< I-N Transition	<120

Table 5.1: Temperature cycle for MLC 7023 semi-droplets on chemically patterned rectangles. *This cooling rate is faster than the hot stage can complete and the sample is removed from the hot stage well below the isotropic - nematic (I-N) phase transition.

The surfaces were used multiple times, and between each new dispense of NLC, the 'old' NLC was removed from the surface with isopropanol (IPA) before drying with compressed air and/or evaporation on a hot plate. Polarised imaging was completed using the bespoke imaging device (Section 3.3.1).

5.3 Results and Discussion

5.3.1 MLC 7023 Semi-Droplet Height

MLC 7023 semi-droplets confined in 6mm chemically patterned squares with predicted heights of 21 - 420µm are shown in Figure 5.1, with the crossed polarisers at 45° to the rubbing direction. Four other semi-droplets with predicted heights of 63 - 250µm are presented in Figure A.8, but are not included in the following discussions to allow a direct comparison with the E7 samples in Chapter 4. The extra data is used to improve the number of data points in the calculation of Δn_{eff}, as will be described in the next paragraph. The predicted heights are again deduced from the model described in the previous chapter starting from $V = AL$, followed by prediction of ϵ (Equation 4.2) and finally using Equations 4.7 and 4.6, the results of which match the predicted heights for E7 as the model is not LC-specific.

NLC Volume, V/µL	0.5 ± 0.01	1 ± 0.01	1.8 ± 0.01
Measured height, h/µm	10 ± 10	40 ± 20	70 ± 20
Predicted height, h/µm	21 ± 1	42 ± 2	75 ± 3
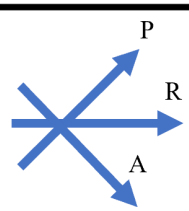	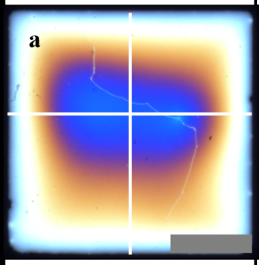	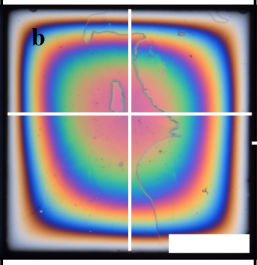	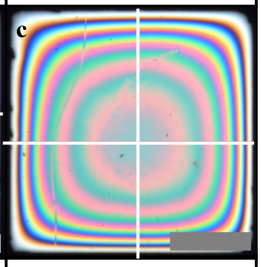
NLC Volume, V/µL	3 ± 0.01	5 ± 0.01	7 ± 0.01
Measured height, h/µm	150 ± 20	210 ± 30	-
Predicted height, h/µm	125 ± 5	208 ± 9	290 ± 10
	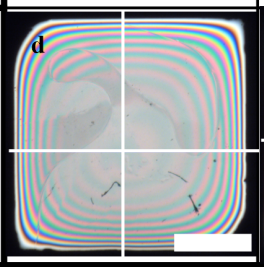	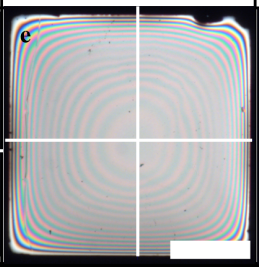	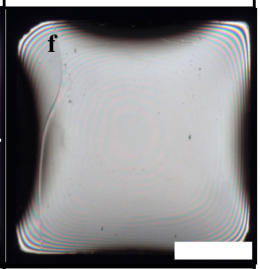
NLC Volume, V/µL	8 ± 0.01	9 ± 0.01	10 ± 0.01
Predicted height, h/µm	330 ± 10	380 ± 20	420 ± 20
	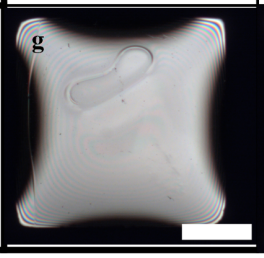	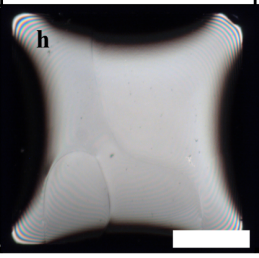	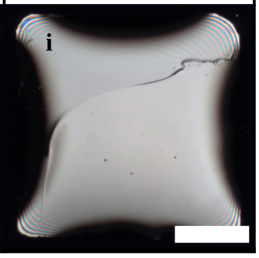

Figure 5.1: Polarised light imaging of varying MLC 7023 semi-droplet volumes confined in 6mm chemically patterned squares. Maximum heights measured using pink birefringent fringes are compared to the those predicted from calculation of the semi-droplet cross-sectional area ($V = AL$), leading to predictions of ϵ (Equation 4.2), interface angle (Equation 4.7) and finally, height (Equation 4.6). White lines shows the cross-sections along which the centre-to-centre distances of the fringes have been measured to deduce the height variations across the semi-droplet width and length. P,A and R show the relative directions of the polariser, analyser and rubbing, respectively. The scale bars are 2mm. The cropping of the images was varied to ensure that the field of view required to capture all the information (e.g. any overflowing liquid crystal) is retained while maximising the image visibility.

The measurement of MLC 7023 semi-droplet heights is more difficult than for E7 as the anchoring of MLC 7023 at an air/NLC interface is quoted as either planar[48] or 'planar/tilted'[15], but it is unclear to what extent the director is tilted at the air/NLC interface. Therefore, it is less trivial to model the director field throughout the height of the semi-droplet, hence it is also difficult to calculate Δn_{eff} for substitution into the full wave equation, $h = \frac{m\lambda}{\Delta n_{\text{eff}}}$. It is assumed in this work, as was the case for E7, that MLC 7023 is planar at the substrate surface rubbed alignment layer. Instead of assuming a model throughout the height to calculate Δn_{eff}, the full-wave equation is used with the number of birefringent fringes on the polarised images in Figures 5.1a-e and A.8 to calculate a value of Δn_{eff} for each sample, with a resulting average $\Delta n_{\text{eff}} = 0.036 \pm 0.004$.

The spread of Δn_{eff} with predicted height is shown in Figure 5.2 with the blue dashed line at $\Delta n_{\text{eff}} = 0.036$, lending validation to this method of calculation as the values agree within one error bar to this dashed line (or very close to one error bar in the case of the semi-droplet with a predicted height of 125µm case). Interestingly, Δn_{eff} for the smallest semi-droplet height (predicted height of 21µm) is smaller than for the others, which could relate to the ratio of the anchoring at the substrate surface vs. air/NLC interface being most prominent

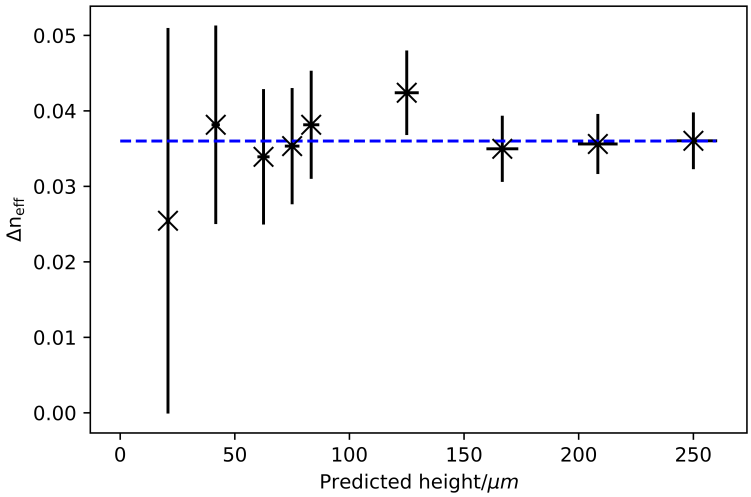

Figure 5.2: Spread of Δn_{eff} with MLC 7023 semi-droplet predicted height, with a dashed line at the average $\Delta n_{\text{eff}} = 0.036$.

as there is less 'bulk' LC in-between these anchoring surfaces. However, due to the large error bar of this data point, it could be simply related to the single measurable data point, i.e. $m = 1$. There is a convergence to the $\Delta n_{\text{eff}} = 0.036$ line in the last three data points on Figure 5.2 (predicted heights of 167 - 250µm).

For Figure 5.1, the measured and predicted heights agree within one error bar as is expected from the calculation method of Δn_{eff}. The uncertainty is greater for these samples than seen generally for E7 in Chapter 4 (Figure 4.3) which is likely from the uncertainty in Δn_{eff} for MLC 7023 from averaging.

Greater heights can be measured using the pink birefringent fringes for MLC 7023 than for E7 with the highest predicted heights with measurable fringes at 208µm and 125µm, respectively. This difference is caused by the varied Δn for MLC 7023 and E7 of $\Delta n = 0.07$[1] and 0.21[49], respectively (see Section 3.4), hence for MLC 7023 there are fewer fringes per height as described by the full-wave equation (Equation 3.8). Whilst post-imaging contrast editing aids in the measurement and a higher resolution may provide a slight improvement, part of the limitation in the measurement originates from the dark edges in the taller semi-droplets for predicted heights $\geq$ 208µm and 290µm for E7 and MLC 7023, respectively. Potentially, a significant increase in the brightness may allow these outer edges to be resolved, however it is likely to still be unclear. This dark region is unlikely to be related to a dark retardation colour except at the very edges of the semi-droplets, assuming that the approximately black colour is seen for $\Gamma \lesssim 50$nm as observed on a Michel-Lévy chart (see Section 3.3.2). Through substitution of Δn_{eff} values of 0.036 or 0.1[1] and a Γ of 0.05µm into $\Gamma = height \cdot \Delta n_{\text{eff}}$, it is estimated that the black retardation should end at a height of approximately 1.4µm or 0.5µm for the MLC 7023 or E7 semi-droplets, respectively. This is less than 0.7% of the heights for MLC 7023 semi-droplets of $\geq$ 208µm and 290µm, respectively, therefore is not likely to account for the widths of the dark regions. The dark regions could relate to the director fields observed by Tsakonas *et al.*[122] (see Section 3.3.3).

[1] Merck data

To calculate the tilt angle from $\phi = 2°$ at the substrate (from the polyimide pretilt[1]) to a maximum angle at the air/NLC interface, ϕ_{max}, as discussed in Section 3.3.5 and shown in Figure 5.3, code was developed as presented in Figure A.9). The code iterates over $2° \leq \phi_{max} \leq 90°$ in 10000 steps with a resolution of approximately 0.009°, i.e. much lower than reasonable experimental errors. The NLC director is symmetric, $\boldsymbol{n}$ = -$\boldsymbol{n}$ (see Section 2.2.1), therefore director angles of 0° equal those of 180° and 360°, and similarly those of 90° equal 270°. Each of these angles was substituted into Equation 3.4, repeated here in Equation 5.1 for clarity, for ϕ as a function of dimensionless height, $\frac{z}{h}$, in degrees,

$$\phi\left(\frac{z}{h}\right) = (\phi_{max} - 2°)\frac{z}{h} + 2°. \tag{5.1}$$

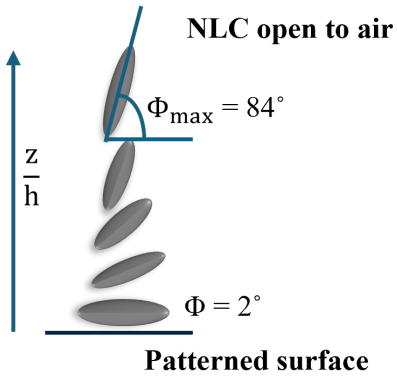

Figure 5.3: Schematic of the MLC 7023 semi-droplet director through the dimensionless height of the semi-droplet, $\frac{z}{h}$, from an approximately planar tilt angle ($\phi = 2°$) at the patterned surface, to a maximum tilt angle $\phi_{max} = 84°$ at the air/NLC interface. Not to scale. *Figure adapted from [1].*

Substitution of Equation 5.1 into Equations 3.6 and 3.7 (for $n_e(\frac{z}{h})$ and Δn_{eff}, as detailed in Section 3.3.5) calculates Δn_{eff} values using $n_e = 1.53$ and $n_o = 1.46$[2]. The smallest difference between these calculated Δn_{eff} and the expected

[1]Nissan Chemical Industries Ltd. Data sheet for 'Alignment Coatings for LCDs-SUNEVER Series'-1/2

[2]Merck data

$\Delta n_{\text{eff}} = 0.036$ deduces the tilt angle of $\phi_{\text{max}} = 84°$. The variations of $\phi(\frac{z}{h})$, $n_{\text{e}}(\frac{z}{h})$, and $n_{\text{e}}(\frac{z}{h})$ - n_{o} are shown in Figure A.10. This ϕ_{max} matches with the expected non-homeotropic air/NLC interface[15, 48], and has confirmed the potential of MLC 7023 in sensing devices for homeotropically-aligning analytes (see Section 2.5.1) since the switch from 84° to 90° at the air/NLC interface would likely give a clearly observable optical effect.

Figure 5.4 demonstrates the height variations across the width (a) and length (b) cross-sections marked with white lines in Figures 5.1a-e. Whilst the maximum measured and predicted heights are expected to match from averaging the calculated Δn_{eff}, the shape of the semi-droplet cross-section is based on the distance between the pink fringes in the x - axis, hence a different Δn_{eff} would simply scale the heights in the *height* - axis by a constant value. Therefore, the effect of gravity for these samples can still be analysed.

The capillary length is a factor considered in Chapter 4 for the effect of gravity vs. surface tension on the semi-droplets, and it was concluded that there are no significant effects given that the E7 semi-droplet height $\lesssim 50\mu$m[1]. Whilst the surface tension for MLC 7023 is much lower than E7 ($\gamma = 0.0242\text{Nm}^{-1}$ compared to $\gamma =$ 'low'[48]), the density and acceleration due to gravity are unchanged hence the capillary length, $L_{\text{c}} = \left(\frac{\gamma}{\rho g}\right)^{\frac{1}{2}}$[134], will be less than that for E7, i.e $L_{\text{c}} \lesssim 1.55$mm with $\frac{d}{L_{\text{c}}} \gtrsim 1.9$. Therefore, it is expected that gravity will have a greater effect on the shape of the MLC 7023 semi-droplets, with the models fitting less well to the measured heights at a lower height than for E7 (i.e. $\lesssim 50\mu$m). However, this is not the case as the model fits well for all heights measured, with the most significant deviations for predicted heights $\gtrsim 125\mu$m (magenta).

A potential explanation is that the much lower surface tension for MLC 7023[48] allows the NLC to spread more evenly across the surface resulting in more accurate d and L values used with the non-LC specific model. The quality of filling was discussed in Section 4.4.1,[1] to be a reason for a reduced agreement between the measured and predicted maximum heights. This more even filling is supported by qualitative observations that the concentric birefringent fringes are relatively well oriented around the approximate centre of the squares and by

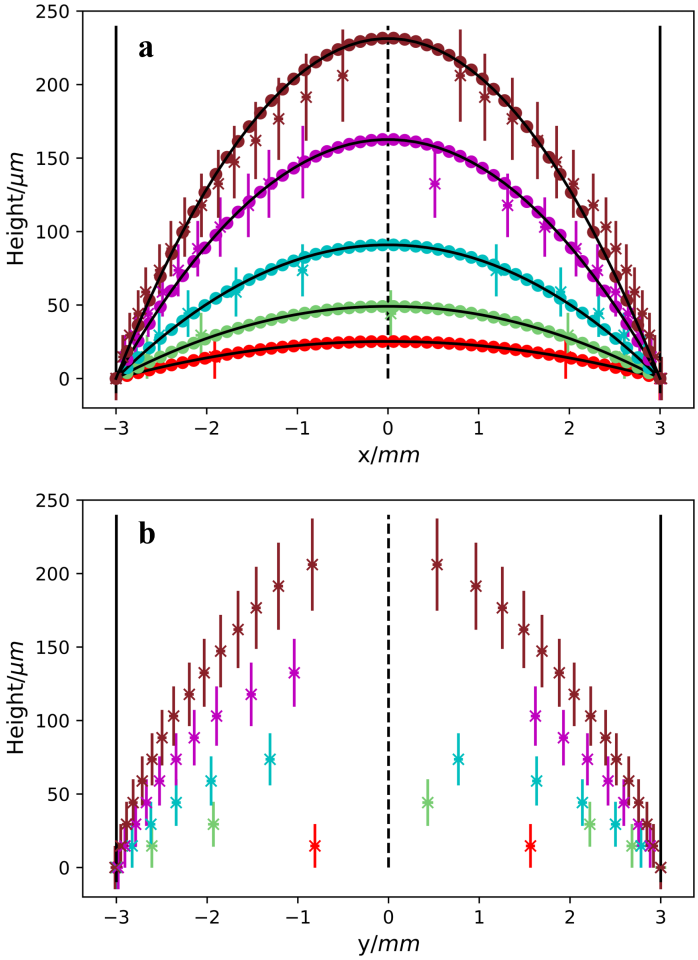

Figure 5.4: Height variation using the centre-to-centre distances of pink birefringent fringes for MLC 7023 semi-droplets confined in 6 x 6mm squares across the *a:* widths. The data is fitted to both Equation 4.6 (*black line*), or Equation 4.2 (*circles*). *b:* The centre-to-centre distances of the fringes along the lengths. Four different volumes are demonstrated including: $V = 0.5\mu$L (red), $V = 1\mu$L (light green), 1.8μL (light blue), $V = 3\mu$L (magenta), $V = 5\mu$L (brown). A dashed line is included at $x,y = 0$, as well as solid lines at the expected edges of the confinement shapes.

comparison to the $x,y = 0$ dashed lines in Figure 5.4. Qualitative analysis of the samples in Figure 5.1 leads to the conclusion that MLC 7023 semi-droplets fill better into the corners of the confinement than for E7 for the lower heights, i.e with predicted heights of 21 - 75μm (Figures 5.1a-c). As was discussed in Section

4.5.3, the experience of the person filling the samples must be considered for the filling quality, however it was found that an E7 semi-droplet with a predicted height of 21µm in a 6mm square shown in Figures 4.11a,b (with a V of 0.5µL) is still too small of a V for high quality filling. It is clear that the equivalent MLC 7023 semi-droplet (Figure 5.1a) has a high quality of filling, implying that the improved quality is at least in part to the reduced surface tension of MLC 7023. Another factor is the greater uncertainty in the measured heights for MLC 7023 than E7 due to the uncertainty in Δn_{eff} and therefore is it more likely that the models will fit within uncertainty.

Black solid lines at $\pm$ d of Figure 5.4a demonstrate the expected edge of the confinement and evidence that there is no significant under- or overfilling, which agrees with the results found for E7 confined within 6mm squares[1]. The definition of significant here is any measurement at the edges of the semi-droplet with an under- or overfill greater than the uncertainty in the measurement. Figure 5.4b presents the semi-droplet height variations along the length of the samples in Figures 5.1a-e. There is not a significant difference in the level of symmetry seen in the width (Figure 5.4) and length axes.

5.3.2 MLC 7023 Semi-Droplet Interface Angle

Interface angles for MLC 7023 semi-droplets with predicted heights of 21 - 208µm (corresponding to $V = 0.5$ - 5µL and Figures 5.1a-e) are presented in Figure 5.5a. The blue data points are calculated from $V = AL$, ϵ (Equation 4.2) and Equation 4.7 and are in agreement with those presented in Chapter 4,[1] for E7 as the model is non-LC specific. The red points are from a linear fit of the first few data points on the left-hand side of the corresponding samples in Figure 5.4a. The largest resultant angle from these methods is a θ_{I} of 10° which is small enough that an accurate direct measurement would likely result in a large percentage error, lending further evidence to the utility of the predictive models.

For $V \leq 1.8$µL, the values calculated from the predictive model and the linear fit agree within one error bar, demonstrating that both methods have almost equal validity given the semi-droplets are small. However, there is not a clear error bar

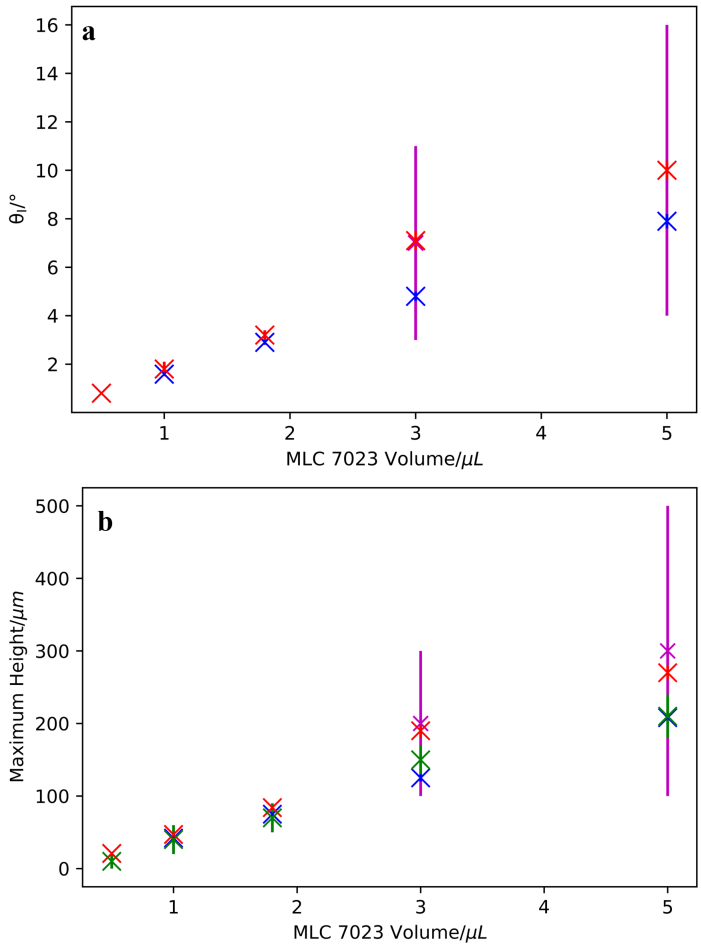

Figure 5.5: Two key properties identified through different methods of the MLC 7023 semi-droplets confined in 6mm squares. *a:* The predicted interface angle, θ_{I}, is derived from either calculating $V = AL$, estimating ϵ (Equation 4.2), and finally Equation 4.7 (blue), or measured from linear fits of the first few data points on the left-hand side of the height variation plots in Figure 5.4a using the small angle approximation ($\tan(\theta_{\mathrm{I}}) \approx \theta_{\mathrm{I}}$ for small θ_{I}) (red). These data points are also calculated for the larger semi-droplets without the small angle approximation (magenta). *b:* The maximum height is calculated from the θ_{I} in *a* using Equation 4.6. The measured heights from the birefringent fringes are also included (green).

for the linear fit method for the sample with a V of 0.5µL as there are not enough fringes ($m = 1$, Figure 5.1a). Therefore, the linear fit method is less favourable than the predictive model which provides an error bar of $\pm$ 0.03°. The linear fit and predicted data points begin to diverge for $V \geq 3$µL, specifically in agreement

within three error bars ($V = 5\mu L$) or greater than three error bars ($V = 3\mu L$) with each other. Therefore, the magenta data points are added as linear fits to measure θ_I without the small angle approximation, resulting in θ_I that agrees within one error bar with the prediction, but with a much larger uncertainty.

Figure 5.5b shows the heights calculated using Equation 4.6 with the interface angles from Figure 5.5a. The green data points are the measured maximum heights which, as previously detailed in Figures 5.1a-e, agrees within one error bar with the predicted maximum heights. The linear fit data points also agree with the measured heights within one error bar ($V = 1$ and $1.8\mu L$) or two error bars ($V = 0.5$ and 3 and $5\mu L$) although this is not surprising since the measured heights have relatively large uncertainties. There is less good agreement between the predicted and linear fit data points, i.e, whilst there is agreement within one error bar ($V = 0.5$ and $1\mu L$) and two error bars ($V = 1.8\mu L$), there are values that do not agree within three error bars or better ($V = 3$ and $5\mu L$). This lends further evidence that the linear fit method is not suitable for MLC 7023 $V \gtrsim 3\mu L$. Whilst the magenta data points do agree with all other data points within one error bar, the large corresponding uncertainty has been propagated through

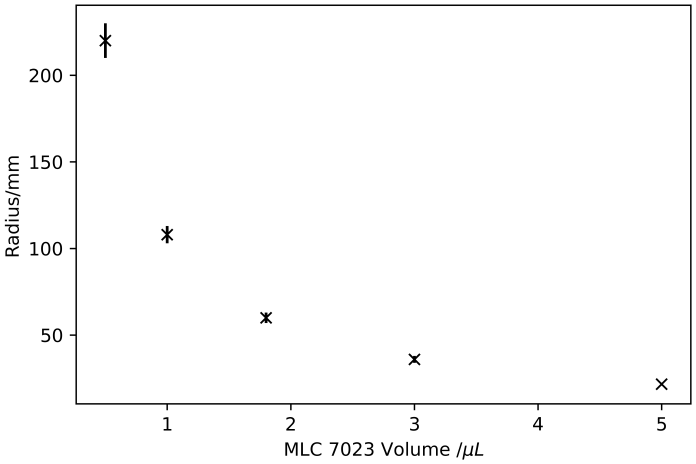

Figure 5.6: Plot of the radius with dispense volume of the MLC 7023 semi-droplets based on the simple geometric circle on which they are modelled (see Figure 4.2b). The values presented here correspond to those that would be seen for E7 as they are from the same, non LC-specific predictive model.

from the interface angle to the height calculation and therefore is still non-ideal.

The radius of the circle on which the semi-droplet cross-sections are modelled (see Figure 4.2b) is shown in Figure 5.6 which evidences that, as was shown for the E7 semi-droplets to verify the HAN director field in Section 4.5.1,[1], the radius is of the order of millimetres and much larger than the maximum height. This should be the same pattern that would be seen for all semi-droplets in the 6mm semi-droplets, as the predictive model for the semi-droplet is non LC-specific.

5.3.3 Defect Formation in MLC 7023 Semi-Droplets

As was discussed in Chapter 4, E7 semi-droplets generally had disclination lines that aligned perpendicular to the rubbing axis with the majority aligned along the approximate centre of the semi-droplets[1], however there is a greater variation of the position of the disclination line for the MLC 7023 semi-droplets. From qualitative evaluation of the approximate position of these lines within the semi-droplets in Figure 5.1, $\sim 44\%$ are closer to the left hand edge, $\sim 33\%$ are through the centre, $\sim 22\%$ are not easy to quantify and none are closer to the right hand edge.

The most common position for the disclination line is towards the left hand side of the semi-droplet seen for predicted heights of 75,208 - 330µm (Figures 5.1c,e-g, respectively), with none towards the right hand side. This implies that the positioning is not related to random movements of the semi-droplet caused by movement from the hot plate to the imaging stage after the heating and cooling cycle. As many of the heating cycles were completed on a hot plate placed onto a stage that can rotate, it is possible there was a small tilt in the stage towards the left.

Two-thirds of the semi-droplets with a disclination line oriented near the centre are the smallest semi-droplets, i.e. for predicted heights of 21,42µm, (including also 380µm in Figures 5.1a,b,h, respectively). This weighting towards smaller heights could be related to a greater effect of the surface and air/NLC interface anchoring on the NLC in-between these boundaries than for higher samples.

Additionally, a tilt in the stage would have less effect as there is less NLC and therefore less NLC movement possible.

One of the semi-droplets in the 22% that is less easy to quantify is the semi-droplet with a predicted height of 125µm (Figure 5.1d), where the disclination line is more random than the other samples. The other is the tallest measured semi-droplet with a predicted height of 420µm (Figure 5.1i) which has the disclination line aligned approximately parallel to the rubbing direction, likely due to the large amount of NLC within the surface area, therefore more possible director configurations.

Another consideration of less central disclination lines in the MLC 7023 semi-droplets compared to E7 is the comparative elastic constants of the two liquid crystals where for E7, $\frac{K_3}{K_1} = 1.54$[1] and for MLC 7023, $\frac{K_3}{K_1} = 1.20$ [48], therefore the director field will grow differently on cooling (see Section 2.2.3). Additionally, for E7 there was no tilt at the air/NLC interface, however the direction of the 84° tilt at the MLC 7023 air/NLC interface is likely to be asymmetric, therefore the disclination lines could originate from discontinuities of oppositely oriented tilts, as shown schematically in Figure 5.7.

When considering device configurations that would likely be most ideal for future MLC 7023-based sensing applications of those investigated here, a sensible condition is that $V \lesssim 5$µL (predicted height $\lesssim 208$µm) as samples taller than these (Figures 5.1f-i with predicted heights of 290 - 420µm) have dark regions at the edges which mean that the maximum height and/or the shape of a cross-section cannot be fully measured. Furthermore, results of the methods to calculate θ_I and the maximum height as presented in Figure 5.5 begin to diverge for $V \gtrsim 3$µL (predicted height of 125µm), therefore semi-droplets below this height would be preferred as there are more suitable methods to evaluate their cross-sectional properties. However, for the lowest semi-droplet with a V of 0.5µL (predicted height of 21µm), there is not a uncertainty gained from the linear fit to measure θ_I which, when combined with the fact that the quality of filling may be hard to

[1] Merck data sheets

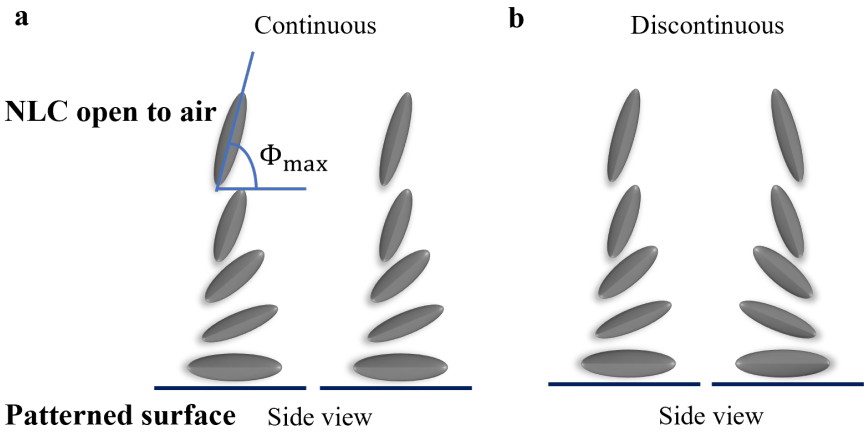

Figure 5.7: The tilt angle at the air/NLC interface for MLC 7023 semi-droplets, $\phi_{\max} = 84°$, can in theory either cause a *a:* continuous or *b:* discontinuous region of the director field, dependent on the direction of the tilt. The tilts may not be exactly opposite as in *b*. Not to scale. *Aspects of the figures adapted from [1].*

maintain for such a small volume for those less experienced in the process (see Section 4.5.3), implies that larger semi-droplets than this would be preferable.

In summary, a compelling range for future sensing devices is $0.5\mu L \lesssim V \lesssim 3\mu L$, corresponding to predicted heights of $21\mu m \lesssim h(0) \lesssim 125\mu m$. This is a positive conclusion as the small semi-droplet volume required would save material in future sensing devices.

5.3.4 MLC 7023 Semi-Droplet Director Fields under Varied Polarisation Conditions

Figure 5.8 provides examples of three key features observed in the MLC 7023 semi-droplets with predicted heights of 21, 208, 380µm (*a-c*, respectively) when crossed polarisers are rotated with respect to the rubbing direction between 0° (*i*) and 45° (*v*). The equivalent rotations for the other samples in Figure 5.1 are presented in Figure A.11.

Similar to the smallest E7 semi-droplets imaged in the 'dark' state (Figures 4.11a,b), the director field is largely dark for the equivalent MLC 7023 semi-

droplet with a predicted height of 21µm in Figure 5.8ai. There is a slight visible retardation colour as the director field will not act as if it were in a planar cell that is completely dark under these conditions due to the approximately homeotropic air/NLC interface anchoring and the disclination line evidencing director distortions. For greater heights, as was also seen for E7, there are brighter and darker regions in a single semi-droplet regions in the 'dark' state.

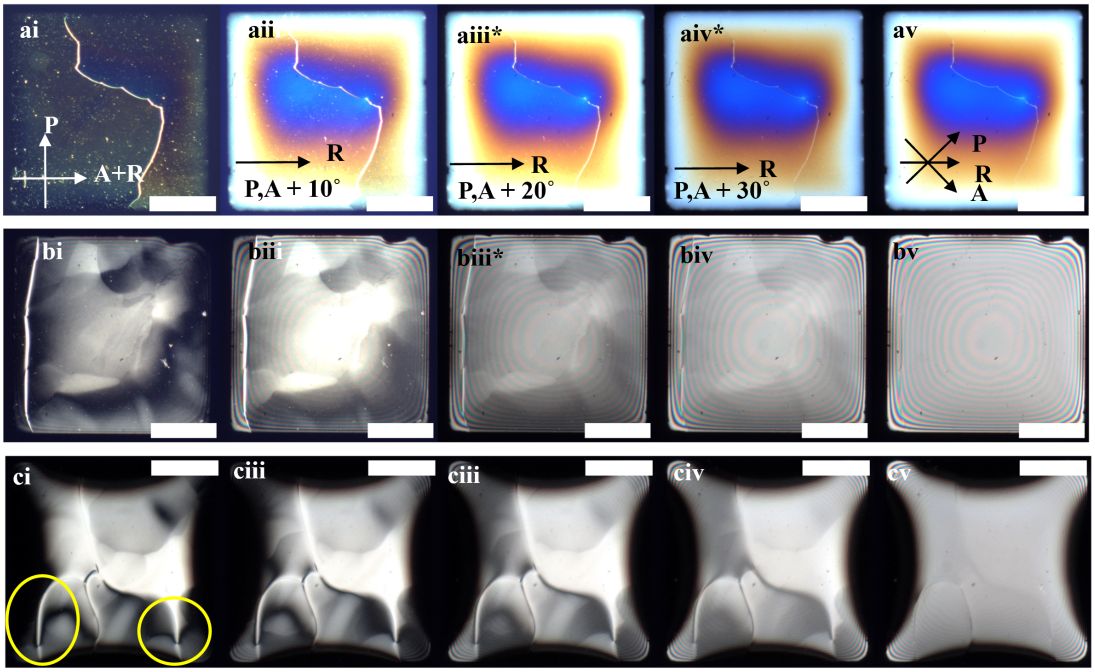

Figure 5.8: Rotation of crossed polarisers through 0° (i) - 45° (v) with respect to the rubbing direction of MLC 7023 semi-droplets with predicted heights: *a:* 21µm, *b:* 208µm, *c:* 380µm. The yellow circles indicate examples of potential origins of possible strength $= \pm\frac{1}{2}$ defects. P, A and R show the relative directions of the polariser, analyser and rubbing direction, respectively. The scale bars are 2mm. The * indicates where the imaging exposure was known to be adjusted to preserve the quality of the images.

An observation seen in these crossed polariser rotations (except for the predicted height of 21µm, Figure 5.8ai) are domains with different brightnesses on rotation. i.e., the semi-droplets do not become brighter homogeneously, as can be seen in e.g. Figures 5.8b,c. However, it is clear in the majority of the cases that when in

the 'bright' state the brightness is approximately homogeneous, except for semi-droplets such as those with predicted heights of 125, 330, 380µm (Figures A.11c,e and 5.8c, respectively) where there is still a small brightness inhomogeneity. This pattern of inhomogeneous brightening was also seen for the smallest E7 semi-droplet (predicted height of 21µm, Figure 4.11a,b), but not for taller samples e.g. the semi-droplet with a predicted height of 208µm in Figure 4.11c. For MLC 7023, the domains of different brightness are often not divided by such a clear domain wall as was observed for E7.

One possible explanation for these less well defined domains and the fact that the inhomogeneous brightening is observed over all volumes in the MLC 7023 semi-droplets is MLC 7023's much smaller surface tension than E7[48], hence a greater spreading of the NLC. Another consideration is the comparative elastic constants of the two liquid crystals where the bend deformation is less for MLC 7023 than E7, with $K_3 = 13.3$pN[48] vs. 17.1pN[1], respectively, and $K_1 = 11.1$pN for both[2][48]. There is an additional symmetry breaking in the MLC 7023 semi-droplets from the unknown direction of director tilt at the air/NLC interface. In contrast to the other MLC 7023 samples, the predicted height of 21µm sample (Figure 5.8a) appears to have homogeneous brightening on rotation from the dark to bright state, implying the expected higher level of order within the semi-droplet due to less NLC within the same surface area, as well as a greater anchoring effect from the bounding surfaces on the 'bulk' NLC in the centre of the semi-droplet height.

There is evidence of potential defects (see Section 3.3.3) with strengths of $\pm\frac{1}{2}$, although they are less trivial to identify than for the E7 semi-droplets, with the potential origin points of the two dark brushes that make up some of these defects circled in yellow in Figures 5.8ci, A.11c,d,f (predicted heights of 125, 290, 380, 420µm). These predicted heights are greater than or equal to the height where linear fits to calculate θ_I begin to agree less with the predictive models as was presented in Figure 5.5, i.e. ≥ 125µm. The presence of these defects is likely related to both the extra disorder possible from more NLC, but also the previously

[1] Merck data sheets
[2] Merck data sheets

discussed effect that the effect from anchoring conditions is only significant until approximately 100µm from any bounding surfaces (Section 2.2.3).

Low retardation colours near the centre of the semi-droplets are seen in MLC 7023 semi-droplets with predicted heights of 208, 330µm, as circled in yellow in Figures 5.9a,b, respectively. These colours are most clear in the dark state and are unexpected due to the grey retardation colour expected at the tall semi-droplet centres. Assuming that the height is not significantly varied in these regions, these colours imply a director variation that decreases Δn_{eff} ($\Gamma = height \cdot \Delta n_{\text{eff}}$, see Section 3.3.2). It is worth noting that the semi-droplet with a predicted height of 208µm is different to the equivalent sample in Figure 5.1e, with the rotation of the crossed polarisers with respect to the stationary semi-droplet shown in Figure A.12. The maximum measured height = 180 ± 30µm, although this is harder to measure as the birefringent fringes distort around the extra defect lines seen in this sample's director field.

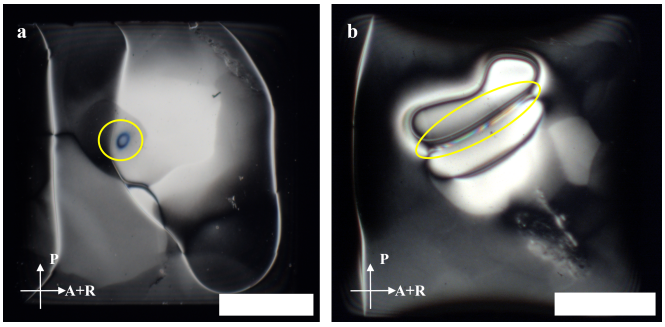

Figure 5.9: Polarised images with crossed polarisers aligned with the rubbing direction to demonstrate the low birefringence colour features (circled in yellow) in 'tall' MLC 7023 semi-droplets with predicted heights: *a:* 208µm and *b:* 330µm. P, A and R show the relative directions of the polariser, anaylser and rubbing, respectively. The scale bars are 2mm.

MLC 7023 semi-droplets with predicted heights of 21µm and 208µm are shown in Figures 5.10a,b, respectively, with three polarisation conditions including crossed polarisers at 45° to the rubbing direction (*i*) and addition of a lambda plate either perpendicular (*ii*) or parallel (*iii*) to the rubbing direction. The observations are very similar to the E7 semi-droplets (Figure 4.12), with an orange outer edge

in Figures 5.10aii,bii, and a blue edge for Figures 5.10aiii,ciii, implying that the director in those areas aligns parallel to the rubbing direction. It can be seen in the first birefringent fringe for the taller sample (b) that there is a retardation shift that matches the change seen for the one fringe on the smaller sample (a). It is again implied in Figure 5.10aii that there is a hard to see discontinuity, as the height of the semi-droplet is increasing towards the centre of the semi-droplet, therefore the retardation colour would be expected to increase along the Michel-Lévy chart (see Section 3.3.2). This could be related to a region where the almost HAN director field throughout the height (Figure 5.3) is likely to break down at the very corners, as was discussed in Section 4.2.3,[1]. This is less clear in Figures 5.10aiii,biii, where it does imply that there is a continuous increase in height towards the centre of the semi-droplet, related to the increase in retardation colour.

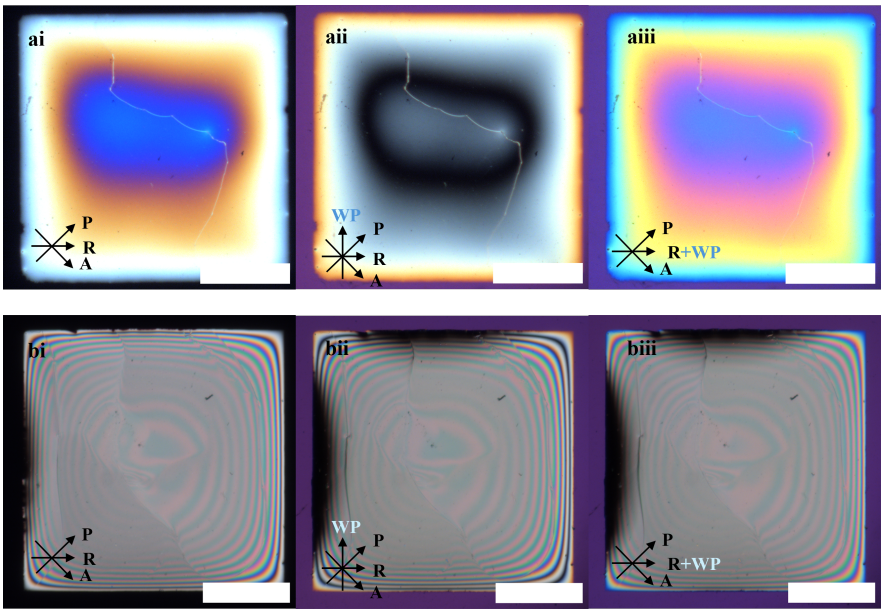

Figure 5.10: Polarised images of MLC 7023 semi-droplets with predicted heights = *a:* 21µm and *b:* 208µm. A lambda plate is *i:* not added or added *ii:* perpendicular or *iii:* parallel to the rubbing direction. P, A, R and WP show the relative directions of the polariser, analyser, rubbing direction, and lambda waveplate, respectively. The scale bars are 2mm.

5.4 Summary

This chapter investigated MLC 7023 semi-droplets confined in 6mm squares, with a description of their physical properties based on the predictive height model and measured height presented in Chapter 4,[1], as well as a discussion of the filling quality and identification of director field information under varying polarisation conditions. MLC 7023 was chosen as previous literature indicates that the anchoring at the air/NLC interface is not homeotropic[15, 48], therefore has potential suitability in sensing homeotropically-aligning analytes.

The predicted heights from the model were used with the number of birefringent fringes counted on polarised images of the MLC 7023 semi-droplets and the full wave equation to calculate an average $\Delta n_{\text{eff}} = 0.036 \pm 0.004$. The director field throughout the height of the semi-droplet is assumed to vary linearly from 2° at the substrate surface to a maximum tilt angle at the air/NLC interface of $\phi_{\text{max}} = 84°$, providing further evidence that MLC 7023 may be useful for homeotropically-aligning analytes.

It is concluded that the MLC 7023 semi-droplets can be measured to a greater height than E7 due to the measurement limits from the pink birefringent fringes, i.e. the maximum measurable predicted heights of 208µm and 125µm for MLC 7023 and E7[1], respectively. This increased limit was described by the much lower Δn for MLC 7023[1] compared to E7[49].

The effective birefringence was used to plot the cross-section of the MLC 7023 semi-droplets across their widths and was found to fit well to the predictive height models to a greater height than for E7 for heights $\lesssim$ 125µm compared to $\lesssim$ 50µm[1]. This was attributed to the much lower surface tension for MLC 7023 compared to E7[48], allowing for a better filling quality due to the increased ability to spread. This was a surprising result however as it was expected from the decreased surface tension that gravity should have a greater effect, i.e. $\frac{d}{L_c} > 1.9$, where 1.9 is the value of this ratio for E7[1].

[1] Merck data

The interface angle calculated from the predictive model was compared to the linear fit of the first few data points on the left hand side of the cross-section height plots. It was discussed that for $V \gtrsim 3\mu L$, there is a less good agreement between the two θ_I and hence a less accurate maximum height calculated when these values are substituted into Equation 4.6. The interface angles presented in this discussion were still $\lesssim 10°$, therefore supporting the need for the predictive model as direct interface angle measurements would likely have a large associated uncertainty.

Combining many conclusions provides the most preferable parameter space of those investigated for future sensing devices, including that for predicted heights $\gtrsim 290\mu m$ the semi-droplet cross-section cannot be measured due to the dark edges of NLC on imaging; the pink fringe measurement limit is for predicted heights $\lesssim 208\mu m$; for $V \gtrsim 3\mu L$ (predicted height of $125\mu m$) there is less good agreement in θ_I; the model starts to agree less well with the measured height cross-sections for predicted heights $\gtrsim 125\mu m$, and that there is not a clear uncertainty for θ_I from the linear fit for the $V = 0.5\mu L$ (predicted height of $21\mu m$) semi-droplet. The most preferable parameter space of those investigated for MLC 7023-based sensing devices is therefore $0.5\mu L \lesssim V \lesssim 3\mu L$, corresponding to $21\mu m \lesssim$ maximum predicted height $\lesssim 125\mu m$ which are low volumes and therefore will save material if this were to be used in industrial sensing devices.

A discussion of the director field images on rotation of crossed polarisers between 0° - 45° relative to the rubbing direction demonstrated the main observation of an inhomogeneous increase in the brightness for different regions of the semi-droplets throughout the rotation for most of the samples. This is seen for greater MLC 7023 semi-droplet heights than E7, which is attributed again to potentially the surface tension, the lower bend elastic constant for MLC 7023[48] compared to E7[1], and a symmetry breaking of the direction of the 84° tilt at the MLC 7023 air/NLC interface. For some of the higher MLC 7023 semi-droplets (predicted heights $\geq 125\mu m$), there is evidence of potential defects with strengths of $\pm\frac{1}{2}$, as is described in relation to increased disorder from a greater volume of NLC being

[1]Merck data sheets

confined within the same 6mm square confinement surface area, and the reduced effect of the anchoring surfaces in the centre of the 'bulk' NLC from the greater semi-droplet height.

The retardation shift seen in on addition of a waveplate demonstrates the same pattern as was seen for E7, where the outer edges are aligned with the rubbing axis, and there is evidence of a discontinuity before the main area of LC in the centre of the semi-droplets.

The next chapter investigates the director fields formed in E7 and MLC 7023 semi-droplets in 6mm squares with predicted heights of 21μm - 420μm, confined on chemically patterned surfaces made without the fabrication step of rubbing the alignment layer. The motivation is to determine if the resultant director fields have greater potential for sensing devices.

Chapter 6

Confinement of Liquid Crystals on Non-Rubbed Chemically Patterned Squares

6.1 Introduction

In the previous chapter, the confinement behaviours of MLC 7023 semi-droplets in chemically patterned rectangles were discussed beginning with the effective birefringence calculated as $\Delta n_{\text{eff}} = 0.036 \pm 0.04$, corresponding to a tilt angle of the director at the air/nematic liquid crystal (NLC) interface of $\phi_{\text{max}} = 84°$. This result evidenced that MLC 7023 could provide a large optical contrast pre- and post-analyte addition for homeotropically-aligning analytes in sensing applications, something that is unlikely for E7 due to its homeotropic air/NLC interface anchoring. It was identified that MLC 7023 semi-droplets can be characterised to a greater predicted height of 208µm compared to 125µm[1] for E7 due to the significantly lower birefringence[1][49]. Additionally, a better fit of the predictive height models across the width cross-sections was attributed to the much lower surface tension[48] hence greater ability to fill the confinement to a high quality,

[1]Merck data sheets

as well as the greater uncertainty on Δn_{eff} for MLC 7023 than E7. The parameter space for MLC 7023 semi-droplets that was identified as having the best potential for sensing devices was $0.5\mu L \lesssim V \lesssim 3\mu L$, corresponding to $21\mu m \lesssim$ *maximum predicted height* $\lesssim 125\mu m$.

This chapter discusses the confinement behaviours of both E7 and MLC 7023 in 6 x 6mm chemically patterned squares fabricated with the same method used in Chapters 4 and 5, but without rubbing of the alignment layer with predicted heights varying again over 21 - 420µm. This investigation is beneficial to the development of a commercial sensing system as removing the rubbing step would make the fabrication more efficient. In addition, rubbing the sample can add small uncertainties in the surface patterning if the substrate is not perfectly aligned with the desired direction of the rubbing machine, as well when ensuring the rubbing direction is aligned with the 6mm square on the photomask during photolithography (see Sections 3.2.4 and 3.2.5).

6.2 Experimental Methods

6.2.1 Patterned Surface Fabrication

The chemically patterned surfaces were fabricated as described in Section 3.2 to produce 6 x 6mm squares without rubbing of the polyimide layer, therefore there was no preferred alignment direction for the NLC director. Either E7 or MLC 7023 was confined within a hydrophobic monolayer denoting the square.

6.2.2 NLC Deposition

Both NLCs were pipetted using specifically measured volumes onto the confinement areas of the substrate at room temperature before being spread to the confinement edges using directional compressed air or gentle tilting as required. The samples were then exposed the temperature cycles in Table 4.1 or 5.1 for E7 or MLC 7023, respectively.

The surfaces were used multiple times, and between each new dispense of NLC

the 'old' NLC was removed from the surface with isopropanol (IPA) before drying with compressed air and/or evaporation on a hot plate. Polarised imaging was completed using the bespoke imaging device (see Section 3.3.1).

6.3 Results and Discussion

6.3.1 Semi-Droplet Height

Figures 6.1 and 6.2 present polarised images of E7 and MLC 7023 semi-droplets, respectively, on non-rubbed chemically patterned 6mm squares with semi-droplet predicted heights of 21 - 420µm, matching those in Chapters 4 and 5. The measured heights are calculated using the full wave equation, $h = \frac{m\lambda}{\Delta n_{\text{eff}}}$, with the same effective birefringences from Chapters 4 and 5 of $\Delta n_{\text{eff}} = 0.1$ for E7[1] and $\Delta n_{\text{eff}} = 0.036 \pm 0.04$ for MLC 7023.

The measured heights for the E7 semi-droplets agree within one error bar (Figures 6.1c) or three error bars (Figures 6.1a,b) to the semi-droplets with predicted heights of 75µm and 21µm, 42µm, respectively. This is slightly less good agreement than for the 6mm square rubbed samples in Section 4.4.1,[1] where the agreement was within two error bars or better. An explanation could be the decreased uniformity in the director field in the non-rubbed samples, hence it is harder to count the fringes. For the MLC 7023 semi-droplets there is good agreement within one error bar between the predicted and measured heights in Figure 6.2, providing further validity to the value of Δn_{eff} calculated in Chapter 5 as the heights agree well when using a different surface condition, but the same NLC. However, it should be noted that the uncertainties in the measured heights are greater for MLC 7023 than for E7 due to the increased uncertainty in Δn_{eff}.

The semi-droplets exhibiting the maximum measurable heights across the semi-droplet cross-section correspond to those with a predicted height of 125µm for both E7 and MLC 7023, based on either the limit of measurement related to the pink birefringent fringes (Figure 6.1d for E7) or distortion of these fringes due to disclination lines across the semi-droplet (Figure 6.2d for MLC 7023). This is consistent with the observation from Section 4.4.1,[1] for E7, however is lower

NLC Volume, V/µL	0.5 ± 0.01	1 ± 0.01	1.8 ± 0.01
Measured height, h/µm	37 ± 6	64 ± 7	85 ± 8
Predicted height, h/µm	21 ± 1	42 ± 2	75 ± 3
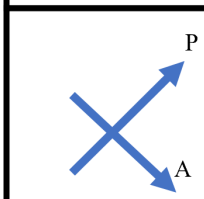	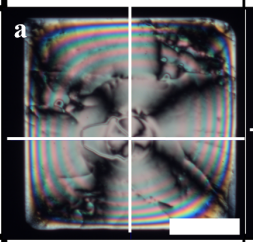	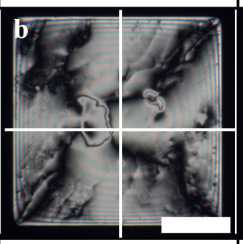	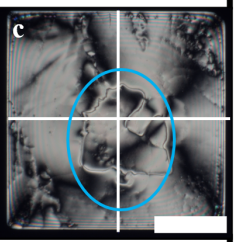
NLC Volume, V/µL	3 ± 0.01	5 ± 0.01	7 ± 0.01
Measured height, h/µm	-	-	-
Predicted height, h/µm	125 ± 5	208 ± 9	290 ± 10
	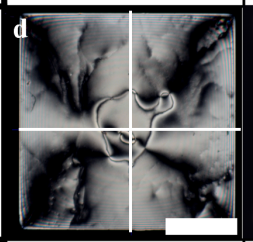	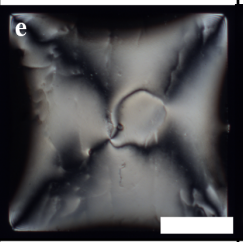	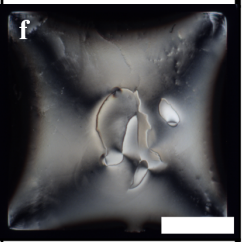
NLC Volume, V/µL	8 ± 0.01	9 ± 0.01	10 ± 0.1
Predicted height, h/µm	330 ± 10	380 ± 20	420 ± 20
	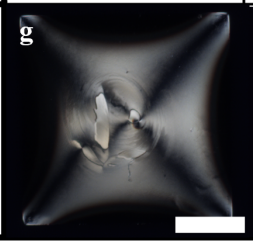	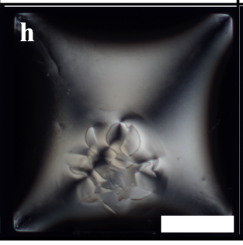	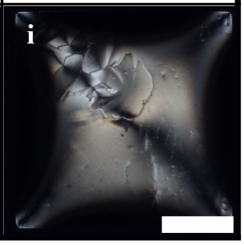

Figure 6.1: Polarised light imaging of varying E7 semi-droplet volumes confined in 6mm squares on chemically patterned surfaces without rubbing of the polyimide alignment layer. Maximum heights measured using pink birefringent fringes are compared to those predicted from calculation of the semi-droplet cross-sectional area ($V = AL$), leading to predictions of ϵ (Equation 4.2), interface angle (Equation 4.7) and finally, height (Equation 4.6). White lines show the cross-sections along which the centre-to-centre distances of the fringes have been measured to deduce the height variations across the semi-droplet width and length. P and A show the relative directions of the polariser and analyser, respectively. The scale bars are 2mm. The cropping of the images was varied to ensure that the field of view required to capture all information (e.g. any overflowing liquid crystal) is retained while maximising image visibility. The blue circle in *c* is an e.g of the least uniform region of the semi-droplets, generally near the semi-droplet centre.

NLC Volume, V/µL	0.5 ± 0.01	1 ± 0.01	1.8 ± 0.01
Measured height, h/µm	30 ± 20	40 ± 20	90 ± 20
Predicted height, h/µm	21 ± 1	42 ± 2	75 ± 3
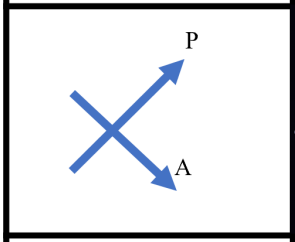	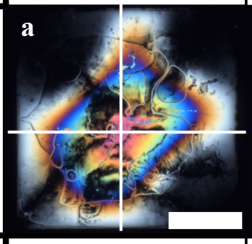	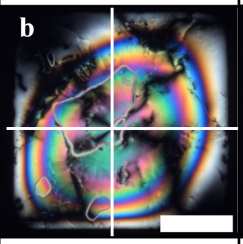	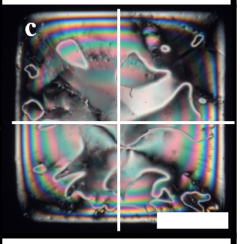
NLC Volume, V/µL	3 ± 0.01	5 ± 0.01	7 ± 0.01
Measured height, h/µm	100 ± 20	-	280 ± 30
Predicted height, h/µm	125 ± 5	208 ± 9	290 ± 10
	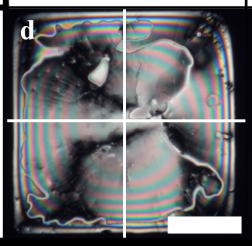	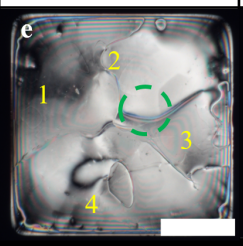	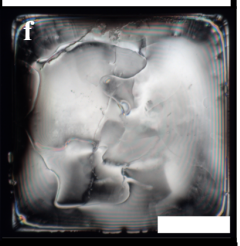
NLC Volume, V/µL	8 ± 0.01	9 ± 0.01	10 ± 0.1
Predicted height, h/µm	330 ± 10	380 ± 20	420 ± 20
	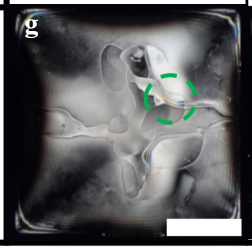	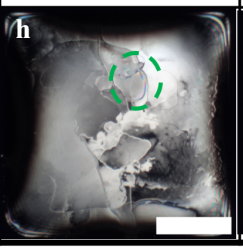	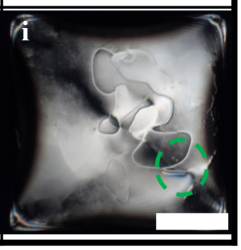

Figure 6.2: Polarised light imaging of varying MLC 7023 semi-droplet volumes confined in 6mm squares on chemically patterned surfaces without rubbing of the polyimide alignment layer. Maximum heights measured using pink birefringent fringes are compared to those predicted from calculation of the semi-droplet cross-sectional area ($V = AL$), leading to predictions of ϵ (Equation 4.2), interface angle (Equation 4.7) and finally, height (Equation 4.6). White lines show the cross-sections along which the centre-to-centre distances of the fringes have been measured to deduce the height variations across the semi-droplet width and length. P and A show the relative directions of the polariser and analyser, respectively. The scale bars are 2mm. The cropping of the images was varied to ensure that the field of view required to capture all information (e.g. any overflowing liquid crystal) is retained while maximising image visibility. The four regions denoted by disclination lines is shown in *e*. The green circles in *e*-*i* are exemplar regions of low birefringence colours near the tall semi-droplet centres.

than the predicted height of 208µm observed for MLC 7023 in Chapter 5. The non-rubbed MLC 7023 samples have a less uniform director field with a large distortion of the fringes, for example the four sections denoted by disclination lines highlighted in Figure 6.2e.

A feature observed in the director fields with increasing E7 semi-droplet height is the position on the semi-droplets where there is the greatest non-uniformity i.e., for all the semi-droplets presented in Figures 6.1a-g these domains are centered approximately at the middle of the semi-droplet with an example circled in blue in Figure 6.1c. This is likely where the antagonistic anchoring from the square borders meet, creating discontinuities in the director field. However, for the semi-droplets with predicted heights of 380µm and 420µm (Figures 6.1h,i, respectively) this region is not centered in the middle of the semi-droplet as is attributable to the larger amount of E7 confined in the same size square, hence greater motion of the confined NLC when the sample is moved e.g. on placement from the hot plate to the imaging stage.

There is a greater spread of the position of the main non-uniformity for the MLC 7023 semi-droplets. The region is centered either near the middle of the semi-droplet (Figure 6.2b), throughout the majority of the semi-droplet (Figures 6.2a,c,d), or the distortion aligns with the vertical and horizontal axes (Figures 6.2e,g), the vertical axis (Figures 6.2f,h), or a diagonal axis (Figure 6.2i). For the tall semi-droplets with predicted heights of 330 - 420µm there is a rotation in the direction of this non-uniformity and is again related to the increasing volume of MLC 7023 within the square. Semi-droplets with predicted heights of approximately 208µm likely represent a turning point where the effects of anchoring and surface tension meet a balance in the formation of the director field. This is evidenced by the majority of the MLC 7023 semi-droplets with predicted heights less than 208µm having less uniform domain structures and that the semi-droplets with predicted heights greater than 208µm have domains that align more parallel to a specific axis.

Whereas the disclination lines are localised close to the non-rubbed E7 semi-droplets centres, similar lines in the MLC 7023 semi-droplets occur over the ma-

jority of the surface area. This can again be described by symmetry breaking from the unknown tilt direction of the MLC 7023 director at the air/NLC interface that forms discontinuities in the director field, as was discussed in Section 5.3.3. The disclination lines are more circular over a greater proportion of the semi-droplet surface area for the non-rubbed MLC 7023 semi-droplets as the antagonistic tilt angles will occur along both the width and length axes due to the lack of a rubbing direction. A discussion of the director near the edges of the square confinements will be given in Section 6.3.2.

Figures 6.3a,b exhibit the height profiles of semi-droplet width cross-sections for E7 and MLC 7023, respectively, as marked by white lines in Figures 6.1a-d and 6.2a-d. The circle points represent the data fitted to Equation 4.2, the continuous curved black line is a fit to Equation 4.6, the dashed black lines show where $x = 0$, and the thick black lines indicate the expected edges of the semi-droplet confinement. The results match the conclusions from Chapter 4, where the E7 semi-droplets with height $\lesssim 50\mu m$ fit best with the models[1], with a decreasing fitting quality for the taller semi-droplets. Additionally, it was discussed in Chapter 5 that there is only significant loss of fitting quality for semi-droplets with predicted heights $\gtrsim 125\mu m$, with a high-quality fitting observed for the semi-droplet with a predicted height of 125µm in Figure 6.3b (magenta). Whilst there is no significant under- or overfilling in the four axes for both the E7 and MLC 7023 semi-droplets, where Figures 6.4a,b show the height variations along the length for E7 and MLC 7023, respectively, it is clear in Figures 6.3 and 6.4 that there are missing data points near the semi-droplet centres. This is a product of a large amount of defect and domain behaviour observable in the polarised images in Figures 6.1 and 6.2, and which impacts the accurate counting of the pink birefringent fringes.

As was similarly observed in Section 5.3.4, there is evidence of low birefringence colours for the non-rubbed E7 semi-droplets with predicted heights $\geq 208\mu m$ (Figures 6.1e-i) from the light brown/orange colour observed. As $\Gamma = height \cdot \Delta n_{eff}$ (see Section 3.3.2) and height is assumed constant, this again exhibits a variation in the director to decrease the Δn_{eff}. Compared to the rubbed samples

from Chapter 4 where there was no or minimal evidence of such colours near the tall semi-droplet centres, it can again be concluded that the non-rubbed samples exhibit much less uniformity. The lower birefringence colours are clearer in the non-rubbed MLC 7023 semi-droplets with predicted heights $\geq$ 208µm (Figures 6.2e-i) especially around the disclination lines, with some examples circled in green.

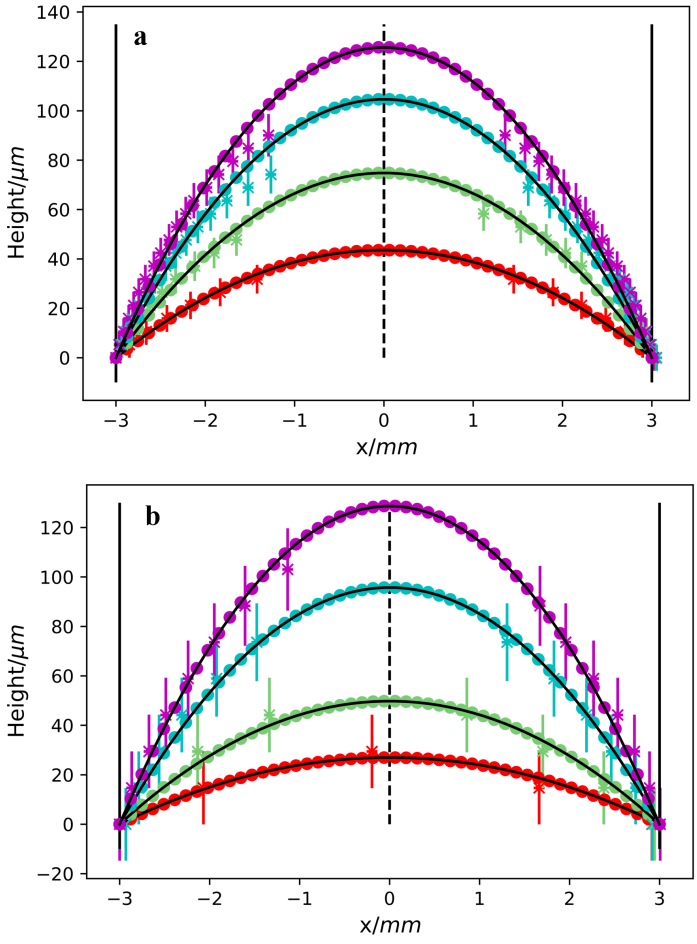

Figure 6.3: Height variation using the centre-to-centre distances of pink birefringent fringes across the widths of *a:* E7 and *b:* MLC 7023 semi-droplets confined in a 6 x 6mm square. The data is fitted to both Equation 4.6 (*black line*), or Equation 4.2 (*circles*). Three NLC dispense volumes are used with V = 0.5µL (red), 1µL (green), 1.8µL (blue), 3µL (magenta). A dashed line is included at x = 0, as well as solid lines at the expected edges of the confinement shapes.

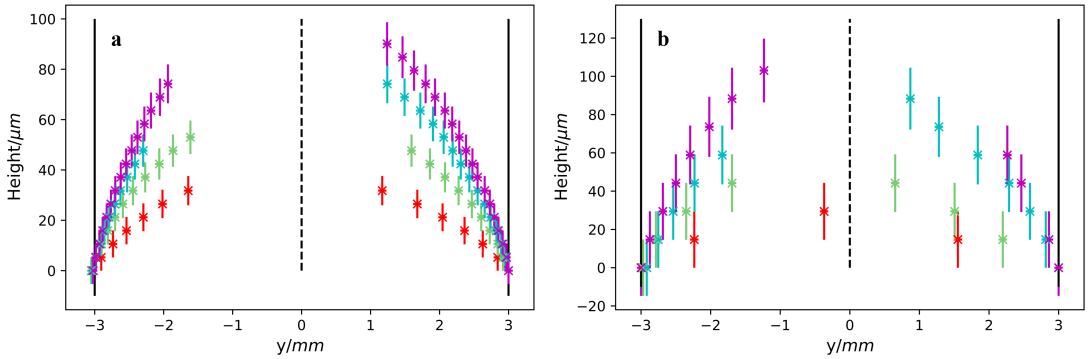

Figure 6.4: Height variation using the centre-to-centre distances of pink birefringent fringes across the lengths of *a:* E7 and *b:* MLC 7023 semi-droplets confined in a 6 x 6mm square. Three NLC dispense volumes are used with $V = 0.5\mu L$ (red), $1\mu L$ (green), $1.8\mu L$ (blue), $3\mu L$ (magenta). A dashed line is included at $y = 0$, as well as solid lines at the expected edges of the confinement shapes.

6.3.2 Semi-Droplet Director Fields under Varied Polarisation Conditions

Figures 6.5, 6.6, A.13 and A.14 demonstrate the rotation of crossed polarisers from aligned with the horizontal and vertical axes of the square semi-droplets (i) to aligned 45° to these axes (v). It is less correct to label the state in which the polarisers are aligned along the horizontal and vertical as the 'bright' state, and a 45° rotation as the 'dark' state as in Chapters 4 and 5 since there is not a preferred director orientation from rubbing, therefore in the following description they are labelled as the '0°' and '45°' states, respectively.

For the majority of the E7 and MLC 7023 semi-droplets there is evidence in the 0° state of four dark brushes approximately parallel to the polariser axes as highlighted by the yellow dashed lines in Figure 6.5ai, with the exceptions being the semi-droplets for both NLCs with predicted heights of 420μm (Figures 6.5c and 6.6d) and the MLC 7023 semi-droplet with a predicted height of 380μm (Figure 6.6c). The brushes for the majority of semi-droplets rotate clockwise with a clockwise rotation of the polarisers to the 45° state and hence suggest a potential strength = +1 defect (see Section 3.3.3, including a discussion of

another potential description for the dark regions[122]), as highlighted in Figure 6.5av. In the 45° state the brushes intersect the very corners of the semi-droplet suggesting that the director lies along the diagonal axes at the corners, with further potential exceptions being the MLC 7023 semi-droplets with predicted heights of 21µm and 42µm (Figures 6.6a,b, respectively) as the colours near the corners are too dark to validate this.

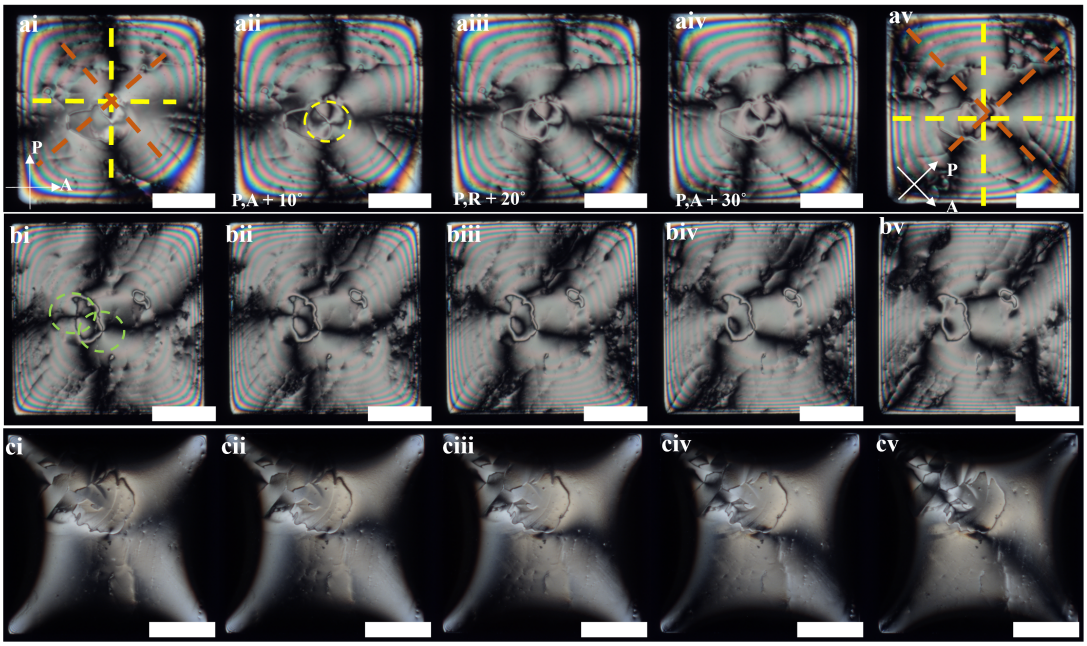

Figure 6.5: Rotation of crossed polarisers through 0° - 45° with respect to the horizontal/vertical axes of E7 semi-droplets with predicted heights: *a:* 21µm, *b:* 42µm, *c:* 420µm. P and A show the relative directions of the polariser and analyser, respectively. The scale bars are 2mm. The dashed lines in *ai,v* provide a guide to the shape of the potential strength = +1 defect, with the yellow lines demonstrating the dark brushes and the yellow circle in *aii* representing the origin of the potential strength = +1 defect. The green circles in *bi* represent the origins of potential strength = $\pm \frac{1}{2}$ defects.

However, some of the director fields are less simple than only a potential strength = +1 defect as can be explained for E7 by dividing the semi-droplets into three main categories. The simplest category includes semi-droplets with predicted heights of 21µm and 75µm (Figures 6.5a and A.13a, respectively) where the

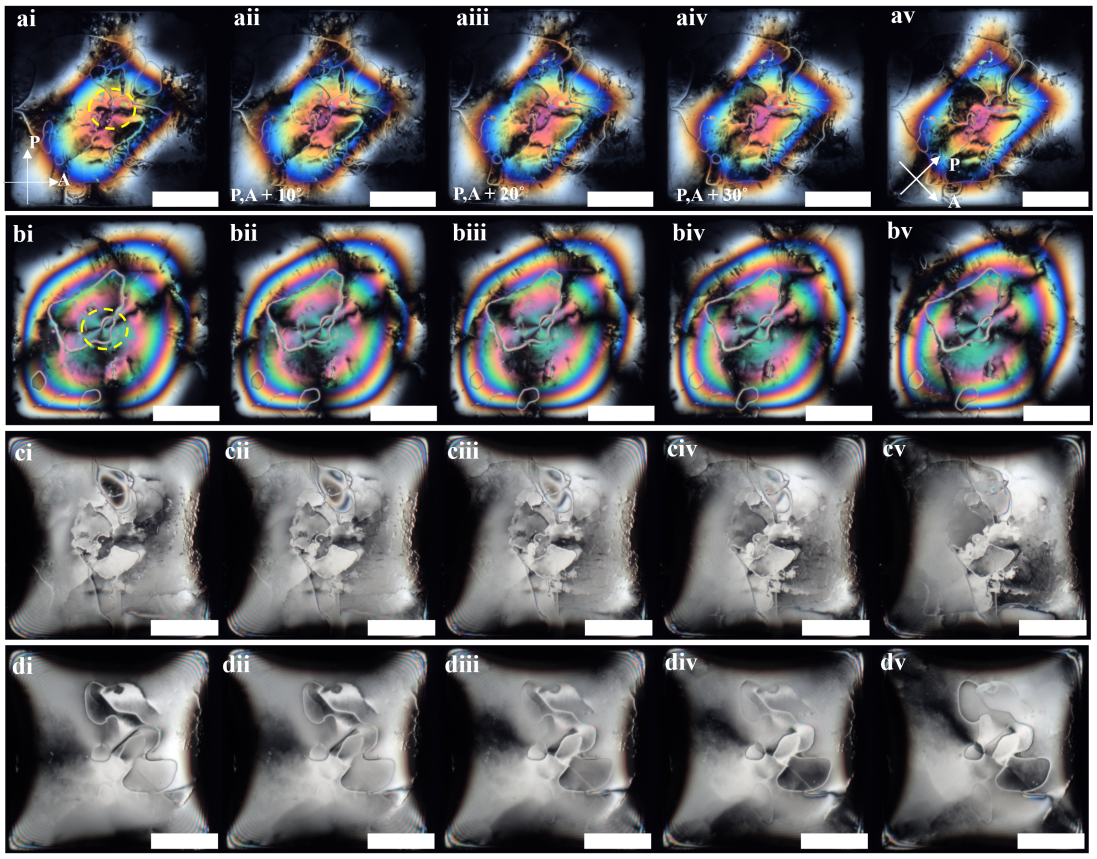

Figure 6.6: Rotation of crossed polarisers through 0° - 45° with respect to the horizontal of MLC 7023 semi-droplets with predicted heights: *a:* 21µm, *b:* 42µm, *c:* 380µm, *d:* 420µm. P and A show the relative directions of the polariser and analyser, respectively. The scale bars are 2mm. The yellow circles in *ai,bi* represent the origins of the potential strength = +1 defect.

brushes do indicate a potential strength = +1 defect as the clearest defect. There is a loosely circular structure on both of these samples from which the defect originates as circled in yellow. The second category consists of the semi-droplets with predicted heights of 42µm and 208µm (Figures 6.5b and A.13c, respectively) where the clearest defects are two potential strength = $\pm\frac{1}{2}$ defects, the origin of which are circled in green. Finally, the third category is comprised of the semi-droplets with predicted heights of 125µm and 290 - 420µm (Figures 6.5c and A.13b,d-f) with defects that are non-trivial to identify. This is the most common category as it is the least uniform director field of the three categories, therefore

the most energetically favourable.

The MLC 7023 semi-droplets are better categorised into a 'small' and 'tall' grouping with predicted heights $\leq$ 125µm and $>$ 125µm, respectively. The origins of the potential strength = +1 defects that are the clearest defect observed in the 'small' group are circled in yellow in Figures 6.6ai,bi and A.14a,b. For the 'tall' semi-droplets with predicted heights of 208 - 420µm (Figures 6.6c,d and A.14c-e), the evidence of the four dark brushes potentially indicating a strength = +1 defect is less clear or not observed as is a result of decreased uniformity allowed from a greater volume of MLC 7023.

Figure 6.7 presents crossed polarised images of E7 (*a,b*) and MLC 7023 (*c-e*) semi-droplets with a lambda plate added approximately along the length axis of the square. Semi-droplets with predicted heights of 208µm are included in Figures 6.7b,e to validate that the observations are consistent for greater heights, with the inset in *b* to improve the clarity of the birefringent colours at the corner. The blue colour observed at the very top and bottom edges for these samples is an increase in retardation relative to the first order magenta colour, implying that the director at those edges is parallel to the lambda plate axis (see Section 3.3.2). The decrease in retardation to orange relative to the magenta colour implies a director orientation perpendicular to the lambda plate axis. The inset in Figure 6.7a demonstrates the expected shape of the director field at the very edges based on this information and the observation that the dark brushes intersect the corners of the majority of semi-droplets in the 0° state. This is most likely a continuous transition from parallel with the width (horizontal) axis to parallel with the length (vertical) axis as there are no clear discontinuites between these orientations. This contrasts to the observation of the rubbed samples in Chapters 4 and 5 where the director aligned parallel to the width axis at the edges, i.e. along the rubbing direction.

Interestingly, for the MLC 7023 semi-droplet with a predicted height of 21µm shown in Figure 6.6a there are dark regions throughout the crossed polariser rotation which would imply that the director is homeotropic; that there is no NLC in those regions, or that there is a very small retardation that lies in the

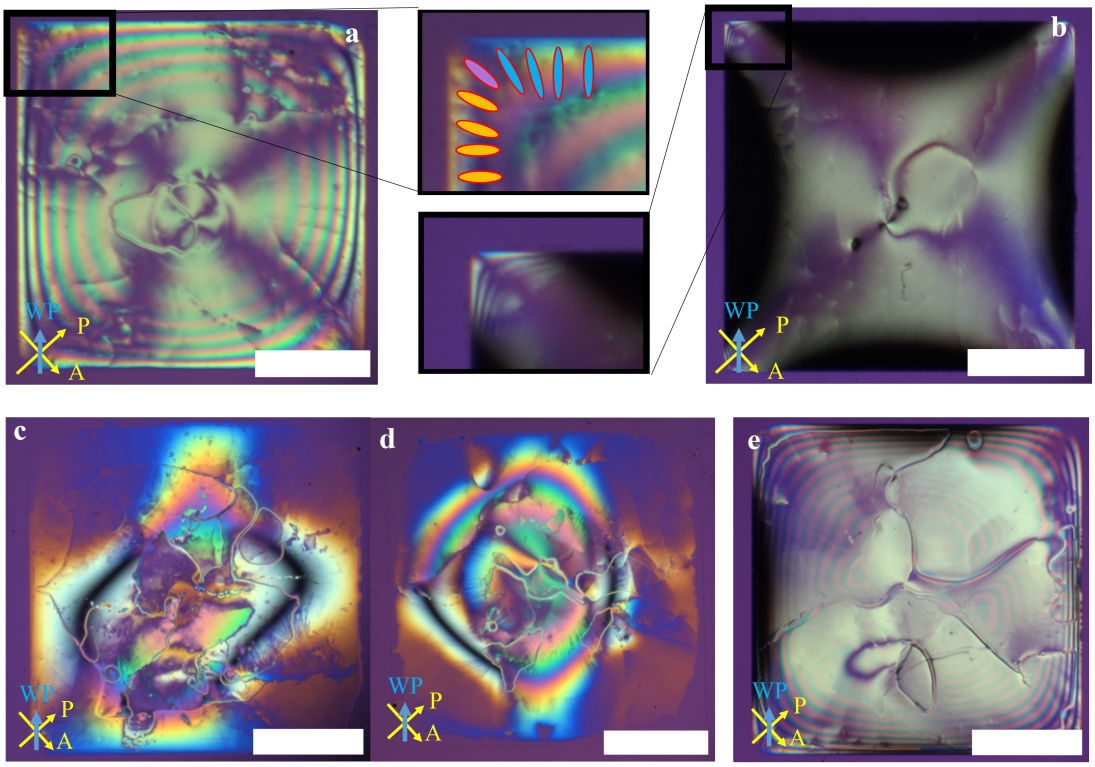

Figure 6.7: *a,b:* E7 or *c-e:* MLC 7023 semi-droplets with predicted heights *a,c,d:* 21µm, *b,e:* 208µm, with a lambda plate added along the length axis of the semi-droplet, at 45° to the crossed polarisers. Director representations are imposed onto the inset image for *a* to demonstrate what the waveplate implies about the director field near the corner of the semi-droplet (not to scale). The inset for *b* is to increase the clarity of the birefringent colours at the semi-droplet corner. P, A and WP to show the relative directions of the polariser, analyser and lambda waveplate, respectively. The scale bars are 2mm.

'black' region of the Michel-Lévy chart (see Figure 3.10). However, it is shown in Figure 6.7c,d for two different MLC 7023 semi-droplets with a predicted height of 21µm that these are in fact mostly low birefringent regions since they appear blue or orange as expected on addition of a lambda plate.

Figure 6.8 summarises the information of the director field at the substrate surface and air/NLC interface from Chapters 4 - 6. Using waveplate images, it has been demonstrated that the director aligns parallel to the rubbing direction at the edges of the confinement in the rubbed samples (Figures 4.12 and 5.10).

The assumed director field at the substrate surface for the rubbed samples is shown schematically in Figure 6.8ai. The centre of the schematic semi-droplet is left blank as analysis of the waveplate data focused on the edges, however the director is likely to align approximately along the rubbing axis at the substrate (see Section 2.2.3). Figure 6.8aii demonstrates the expected director orientation at the substrate for the non-rubbed samples, aligning parallel to the confinement walls as supported by the waveplate observations in Figure 6.7. These directors have not been extrapolated to the centre of the confinement as that is non-trivial, however it is clear that there would be discontinuities formed, therefore providing an explanation for the decreased uniformity in the director fields.

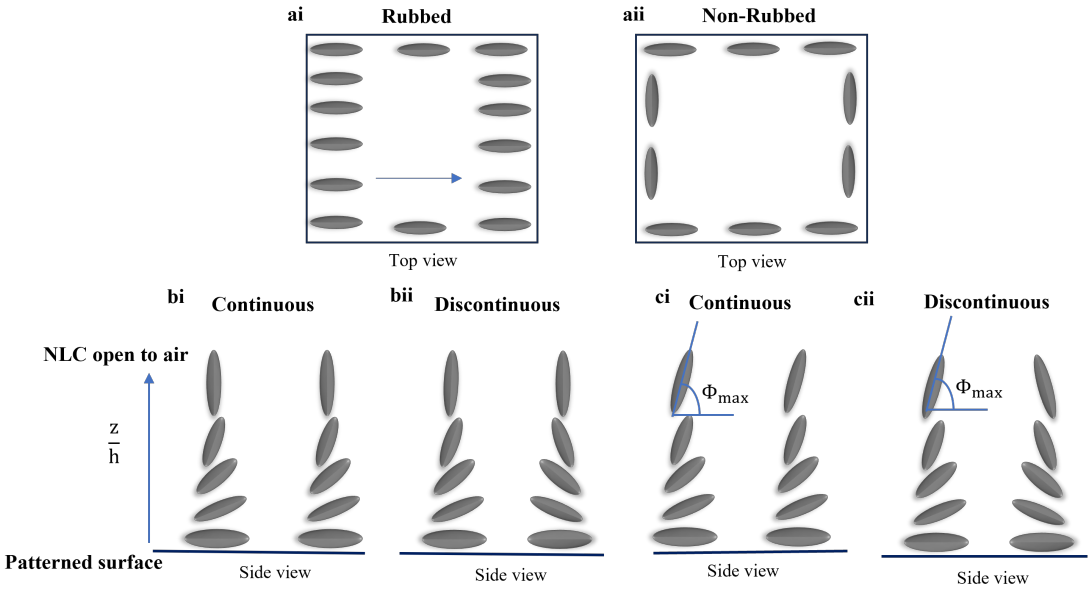

Figure 6.8: Schematic summary of the director at the *a:* substrate surfaces and *b:* air/ NLC interfaces based on the information from Chapters 4 - 5. *a:* In the rubbed samples, the director is expected to align approximately along the rubbing direction, marked with a blue arrow. *aii:* In the non-rubbed samples, waveplate data suggests the director is parallel to the confinement edges. *bi,ci*: If the director rotation is in the same direction, there will be no discontinuity, however *bii,biii:* there is potential for a discontinuity if the rotation is in opposite directions. It is clear that the non-rubbed samples have more degeneracy than the rubbed samples. Not to scale. *Some aspects of the figures adapted from [1].*

Figures 6.8b,c describe the director throughout the dimensionless height, $\frac{z}{h}$, with Figure 6.8c adapted from Figure 5.7 for clarity. For the E7 rubbed samples, $\phi_{\max}$ = 90°, therefore the region between $0 < \frac{z}{h} < 1$ for the dimensionless height is the only region that can be asymmetric, assuming a director field at the substrate that is entirely aligned with the rubbing direction as shown in Figure 6.8bii. As discussed previously, the $\phi_{\max} = 84°$ for the rubbed MLC 7023 semi-droplets could be oriented in multiple directions as shown in Figure 6.8c. The system is far more complicated in the non-rubbed samples, as the director at the substrate is not necessarily along the rubbing direction, therefore these tilts will likely face in more directions, explaining the reduced uniformity for the non-rubbed samples. It is clear that there is more degeneracy in the non-rubbed samples.

6.4 Summary

In this chapter E7 and MLC 7023 semi-droplets were confined within 6 x 6mm chemically patterned squares with non-rubbed polyimide and predicted heights of 21 - 420µm to ascertain if the director fields would be more suitable for future sensing devices compared to the rubbed samples in Chapters 4 and 5.

Using the effective birefringences calculated for E7 and MLC 7023 in the previous chapters, it was identified that the E7 semi-droplets had a slightly worse agreement between the maximum predicted and measured heights for the non rubbed samples compared with the rubbed samples, and for MLC 7023 there was good agreement within one error bar. It was concluded that the non-rubbed sample cross-sectional height variations behave similarly to those from the rubbed samples, including a good agreement between the measured and fitted models for heights $\lesssim$ 50µm for E7[1] and for $\lesssim$ 125µm for MLC 7023. However, it was far more difficult to accurately measure this variation in the non-rubbed vs. rubbed samples due to the additional defects and domains.

For the non-rubbed semi-droplets there were no clear central disclination lines in the director field and the main defect potentially observed was strength = +1. It was discussed that the semi-droplets can be divided into three or two

separate categories for E7 and MLC 7023, respectively, based on the behaviour of the dark brushes that imply different defect strengths on rotation of crossed polarisers with respect to a stationary semi-droplet sample. Addition of a lambda plate implies that the director aligns parallel to the borders of the square at the edges for the non-rubbed samples, whereas they aligned parallel to the rubbing axis at the edge for the rubbed samples. A summary of director orientations at the substrate surfaces and air/NLC interfaces for rubbed and non-rubbed samples using information gathered in Chapters 4 - 6 was presented.

It is clear that the semi-droplets formed on rubbed surfaces presented in Chapters 4 and 5 had more consistent and homogeneous director fields than the non-rubbed semi-droplets in the current chapter, therefore the rubbed samples are preferable for future sensing devices. As Chapters 4 - 6 have assumed that the chemically patterned surfaces are reusable from a lack of significant degradation observed in the polarised images, this reusability is quantitatively measured in the next chapter. Additionally, the shelf life of E7 and MLC 7023 semi-droplets confined on the surfaces is measured.

Chapter 7

Reusability of Chemically Patterned Surfaces and Shelf Life of Confined Semi-Droplets

7.1 Introduction

In Chapters 4 - 6, semi-droplets of both E7 and MLC 7023 were confined in 6 x 6mm chemically patterned squares both with rubbed and non-rubbed alignment layers. It was concluded that rubbed surfaces are favourable for potential future sensing devices due to the greater uniformity in the director field, and that MLC 7023 is slightly preferable over E7 due to its ability to form a higher quality filling of the confinement. In addition, the slight tilt angle at the air/nematic liquid crystal (NLC) interface for MLC 7023 semi-droplets would likely result in a sensing device with greater contrast pre- and post-analyte addition under polarised imaging.

In the previous chapters the surfaces were re-used after rinsing the 'old' NLC off the surface with isopropanol (IPA) as there was no significant qualitative evidence of surface degradation. The reusability is examined quantitatively in the current chapter by repeated filling of a single surface with E7 to confirm there

is no significant variation in the measured nematic to isotropic (N - I) transition temperatures on heating. The shelf life of NLC semi-droplets on the chemically patterned surfaces as well as their resistance to degradation whilst undergoing a temperature cycle is measured with respect to the transition temperatures. The transition temperatures are chosen as a measure of these quantities since a change of an LC sample composition can lead to a change in these temperatures. One example of this is by Allinson and Gleeson[49], where E7 transition temperatures vary with doping. The temperatures are both relatively trivial to measure and provide a route to quantitative evaluation of the properties. The implications of these investigations is discussed in relation to the sustainability of the reusable surfaces.

7.2 Experimental Methods

7.2.1 Sample Preparation

The chemically patterned surfaces were fabricated using the method described in Section 3.2 to produce 6 x 6mm squares. Either E7 or MLC 7023 was confined within a hydrophobic monolayer denoting these shapes, and sat atop a rubbed alignment layer.

7.2.2 NLC Deposition

The E7 or MLC 7023 semi-droplets were filled onto the substrates at room temperature and spread to the confinement edges using directional compressed air or gentle tilting as required. Depending on the NLC used to form the semi-droplets and the investigation being undertaken, different temperature cycles to heat and cool the samples were used as shown in Tables 4.1 (E7), 5.1, (MLC 7023) or 7.1 (E7 and MLC 7023).

Step No.	**Rate**/ °C min^{-1}	**End Temp.**/ °C	**Hold Time**/ min
1a: MLC 7023 on free surface			
1	5	75	0
2	0.5	87	0
3	2	90	10
4	2	87	0
5	0.5	75	0
6	5	<< I-N Transition	<120
1b: MLC 7023 on free surface			
1	5	80	0
2	0.5	90	10
2a: MLC 7023 in cover slips			
1	10	74	0
2	0.5	87	0
2b: MLC 7023 in cover slips			
1	10	78	0
2	0.5	88	0
3: E7 in cover slips			
1	10	57	0
2	0.5	63	0

Table 7.1: Temperature cycles applied to E7 and MLC 7023. Only the heating section of the cycle is included for 1b - 3.

7.2.3 Phase Transition Measurements

Both E7 and MLC 7023 are mixtures and experience a biphasic region over the N - I transition, therefore the beginning of this region on heating is denoted by $T_{\mathrm{N}\rightarrow\mathrm{I}}$ and the temperature at which the sample appears fully black under crossed polarisers is denoted as T_{NI}. Slight variations in the measured temperatures are likely related to the exact positioning of the sample in relation to the 2mm window of the hot plate during imaging of the temperature cycle, and difficulty in measuring the exact starting point for $T_{\mathrm{N}\rightarrow\mathrm{I}}$.

Patterned Surface Reusability

To quantitatively measure the reusability of the chemically patterned surfaces, an E7 semi-droplet with a predicted height of 208µm experienced the temperature cycle in Table 4.1 with $T_{\mathrm{N}\rightarrow\mathrm{I}}$ and T_{NI} measured on heating, before being washed off using IPA. Seven repeats of this process was completed to identify any potential significant variation in $T_{\mathrm{N}\rightarrow\mathrm{I}}$ or T_{NI} as well as to qualitatively evaluate

the director field after each heating and cooling cycle using polarised images.

Shelf-life of E7 Semi-Droplets

Measurements of $T_{N\rightarrow I}$ and T_{NI} for E7 and MLC 7023 semi-droplets with a predicted height of 208µm were used to assess if these NLCs are stable on the patterned surfaces over 14 or 16 days, respectively, alongside quantification of any degradation of the NLCs under temperature cycles. A single E7 semi-droplet was formed on the chemically patterned surface, left in a new plastic petri dish and experienced the temperature cycle in Table 4.1 on Day 0 twice, Day 1, Day 2, Day 7 and Day 14, where Day 0 is the day the semi-droplet was formed.

Shelf-life of MLC 7023 Semi-Droplets

Whilst the intention was to measure the shelf-life of the MLC 7023 semi-droplet using the same method as E7 (but with the sample instead left in a constant position on the hot plate between measurements) the values of $T_{N\rightarrow I}$ and T_{NI} did not remain constant after experiencing the temperature cycle in Table 7.1(1a). The error on the average of the temperatures are ± 2°C (as will be discussed in Section 7.3.3) which is much greater than the uncertainty from the hot plate of ± 0.1°C. Hence, only three measurements were taken including two on Day 0 and one on Day 1 using the cycles in Table 7.1(1a,1b), respectively, to account for the increased $T_{N\rightarrow I}$ and T_{NI}.

Due to this increase in $T_{N\rightarrow I}$ and T_{NI} for the MLC 7023 semi-droplet, four additional sets of measurements were undertaken. The first set investigated the shelf-life of separate MLC 7023 semi-droplets with a predicted height of 420µm kept on chemically patterned surfaces in new petri dishes for up to 16 days, without experiencing a temperature cycle. MLC 7023 from each semi-droplet was pipetted into untreated cover slips acting as a rudimentary cell for the measurement of $T_{N\rightarrow I}$ and T_{NI} with the temperature cycle in Table 7.1(2a) on heating. This method was used to remove the added complication of the free air/NLC interface.

The second additional measurement investigated the origins of a 'misting' effect that caused condensation on the inside of the hot plate lid upon heating the MLC 7023 semi-droplets, which appeared to be the main cause of the change in the measured temperatures. A hot plate cleaned with IPA was heated to 100°C at 10°Cmin^{-1} with nothing on it; three chemically patterned surfaces, or free surface MLC 7023 on untreated glass (other than a sample sticker to hold the NLC). The motivation was to observe if 'misting' occurs, as was identified by blurring of a pen mark on the glass window of the hot plate.

The third set of additional measurements quantified the effect of the 'misting', $\Delta T_{\mathrm{N\rightarrow I}}$ and ΔT_{NI}, by utilising a MLC 7023 semi-droplet with a predicted height of 420µm that experienced the temperature cycle in Table 5.1. The MLC 7023 was then pipetted off of the chemically patterned surface and placed between untreated cover slips to measure $T_{\mathrm{N\rightarrow I}}$ and T_{NI} with the temperature cycle in Table 7.1(2b). The final additional measurement is similar where three samples were placed on a single hot plate and experienced the temperature cycle in Table 5.1 to measure if having multiple samples creates a further significant effect on the change in temperature. The same process of measuring $\Delta T_{\mathrm{N\rightarrow I}}$ and ΔT_{NI} of MLC 7023 pipetted from a semi-droplet with a predicted height of 420µm in-between cover slips is used, with the temperature cycle in Table 7.1(2a).

7.3 Results and Discussion

7.3.1 Patterned Surface Reusability

Figure 7.1 presents polarised images of E7 semi-droplets with predicted heights of 208µm on a reused surface for each repeat of filling the chemically patterned square with E7, completing the temperature cycle in Table 4.1, and finally rinsing the E7 off the surface with IPA (see 'Patterned Surface Reusability' in Section 7.2.3). It is qualitatively demonstrated that the surfaces are reusable as there is no significant variation in the director field i.e. there is a consistent grey retardation colour, central defect line and good filling to the square corners.

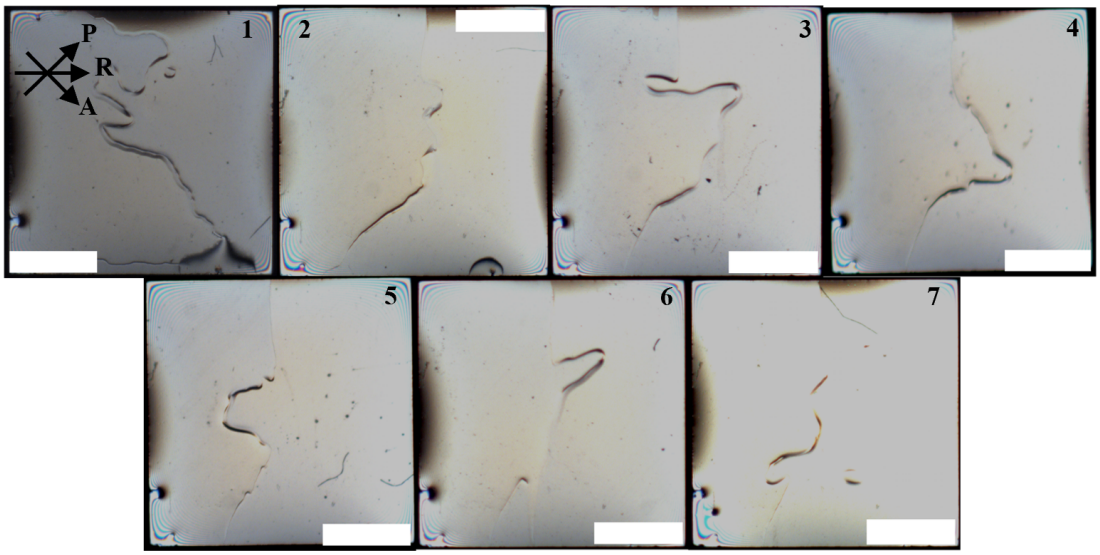

Figure 7.1: Polarised images of E7 semi-droplets with predicted height = 208µm. The 'old' NLC is rinsed off of the surface with IPA before refilling the same surface with E7, completing the temperature cycle in Table 4.1 and imaging, with this process repeated seven times. P,A, and R show the relative directions of the polariser, analyser and rubbing, respectively. The scale bars are 2mm.

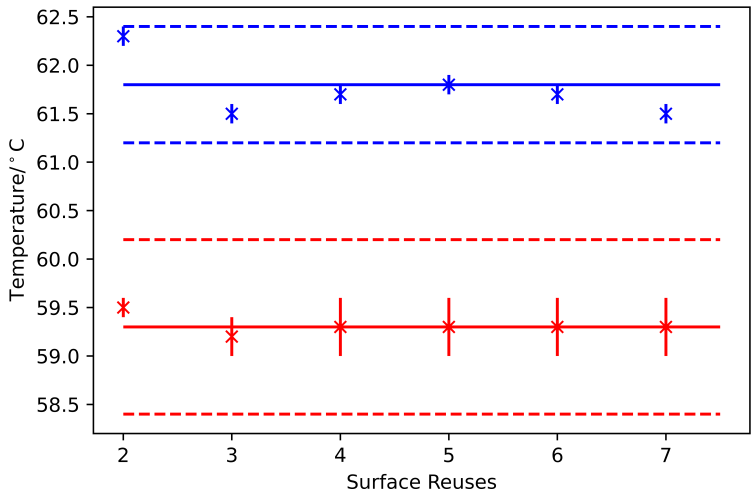

Figure 7.2: $T_{N\rightarrow I}$ (red) and T_{NI} (blue) upon heating E7 semi-droplets with predicted height = 208µm on six reuses of one chemically patterned 6 x 6mm square. The solid lines indicate the average $T_{N\rightarrow I}$ and T_{NI}, with the dashed lines ± three error bars.

$T_{N\rightarrow I}$ and T_{NI} are measured on heating for each of the repeats as presented in Figure 7.2[1] where the solid horizontal lines indicate the average temperatures, $\bar{T}_{N\rightarrow I} = 59.3 \pm 0.3$°C (red) and $\bar{T}_{NI} = 61.8 \pm 0.2$°C (blue), and the dashed lines indicate ± three error bars from the average. Each of the measurements agree within one error bar (or two error bars for T_{NI} for the second reuse) with the average and therefore it can be quantitatively concluded that the chemically patterned surface is stable for multiple uses for E7.

7.3.2 Shelf Life of E7 Semi-Droplets

Figure 7.3 presents $T_{N\rightarrow I}$ and T_{NI} for a single E7 semi-droplet with a predicted height of 208µm over 14 days as measured over six repeats of the temperature cycle in Table 4.1 (see 'Shelf Life of E7 Semi-Droplets' in Section 7.2.3). The solid lines denote the average temperatures of $\bar{T}_{N\rightarrow I} = 59.1 \pm 0.1$°C (red) and $\bar{T}_{NI} = 61.9 \pm 0.1$°C (blue), and the dashed lines indicate ± three error bars from these averages. Every data point agrees within one error bar with the average,

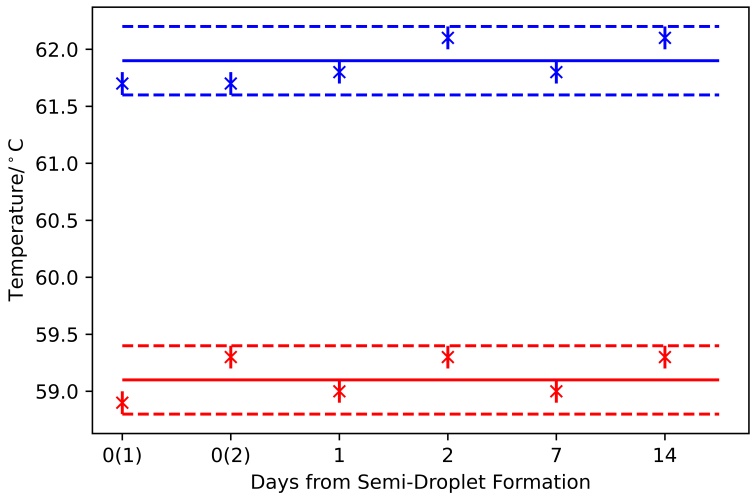

Figure 7.3: $T_{N\rightarrow I}$ (red) and T_{NI} (blue) upon heating of a single E7 semi-droplet with predicted height = 208µm over 14 days and six temperature cycles. The solid lines indicate the average $T_{N\rightarrow I}$ and T_{NI}, with the dashed lines ± three error bars.

[1]Six repeats presented in Figure 7.2 as hot plate lid closed for repeats 2-7, but open for 1.

therefore it can be concluded both that E7 semi-droplets on the chemically patterned surface have a shelf-life of at least 14 days and are resistant to degradation upon heating and cooling.

Figure A.15 presents polarised images of the first three temperature cycles of the E7 semi-droplet discussed in Figure 7.3, exhibiting most probably an air bubble that is retained after its deposition (Figure A.15a,b). The bubble is no longer present by the third temperature cycle (Figure A.15c) corresponding to Day 1 on Figure 7.3, likely due to the semi-droplet being allowed to 'settle' more overnight. However, this bubble does not have a significant effect on the temperature as the Day 0(1,2) measurements are not outliers.

Averaging the twelve measurements from Figures 7.2 and 7.3 results in $\bar{T}_{\mathrm{N\rightarrow I}} = 59.2 \pm 0.3$°C and $\bar{T}_{\mathrm{NI}} = 61.8 \pm 0.1$°C, in agreement within one error bar ($T_{\mathrm{N\rightarrow I}}$) or three error bars ($T_{\mathrm{NI}}$) when E7 is measured on heating between untreated cover slips with the temperature cycle in Table 7.1(3), $T_{\mathrm{N\rightarrow I}} = 59.0 \pm 0.1$°C and $T_{\mathrm{NI}} = 61.2 \pm 0.1$°C. A small difference in the temperatures between the E7 in cover slips versus as semi-droplets is unsurprising since the semi-droplets are open to the air in the hot plate, whereas the E7 in the cell is enclosed.

To measure the versatility of the E7 semi-droplets under different temperature cycle conditions, a semi-droplet with a predicted height of 208µm is heated using steps 1 and 2 in the temperature cycle in Table 4.1, without the hot plate lid over the sample and resulting in $T_{\mathrm{N\rightarrow I}} = 59.7 \pm 0.1$°C and $T_{\mathrm{NI}} = 62.2 \pm 0.1$°C. As these agree within two error bars with the value averaged over Figures 7.2 and 7.3, a lid over the heating implement is not necessarily essential and could lead to more efficient batch preparation.

7.3.3 Shelf Life of MLC 7023 Semi-Droplets

Measurements are taken of $T_{\mathrm{N\rightarrow I}}$ (red) and T_{NI} (blue) for an MLC 7023 semi-droplet with a predicted height of 208µm for three temperature cycles using either Table 7.1(1a) (Day 0) or Table 7.1(1b) (Day 1), as introduced in 'Shelf Life of MLC 7023 Semi-Droplets' in Section 7.2.3. The measurements are presented in

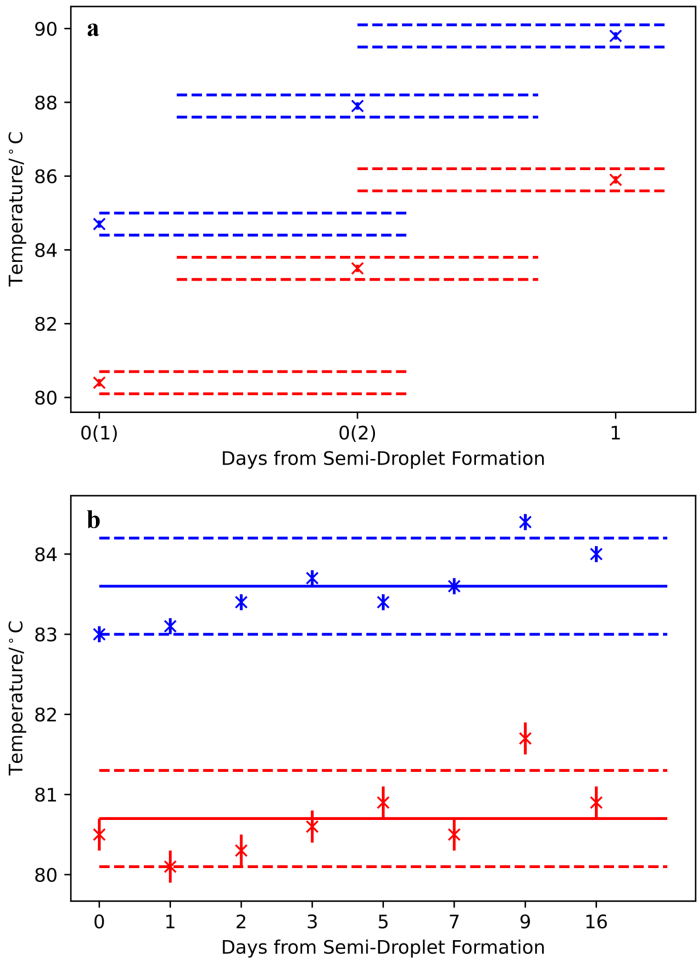

Figure 7.4: Measurements of $T_{\mathrm{N}\rightarrow\mathrm{I}}$ (red) and T_{NI} (blue) on heating to quantify the shelf life of MLC 7023 semi-droplets. *a:* A single semi-droplet with predicted height = 208µm, experiencing either the temperature cycle in Table 7.1(1a) (Day 0) or in Table 7.1(1b) (Day 1). *b:* MLC 7023 after experiencing the temperature cycle in Table 7.1(2a) as semi-droplets with predicted height = 420µm, and subsequently pipetted into untreated cover slips. The measurements are from MLC 7023 in untreated cover slips. The solid lines indicate the average $T_{\mathrm{N}\rightarrow\mathrm{I}}$ and T_{NI}, with the dashed lines ± three error bars.

Figure 7.4a, with the dashed lines denoting ± three error bars from each of the measurements. It is clearly exhibited that the temperatures do not remain stable between the different temperatures cycles as there is no agreement within three error bars or better between the data, and there is a large variation in the averages

of $\bar{T}_{N\rightarrow I} = 83 \pm 2°C$ and $\bar{T}_{NI} = 88 \pm 2°C$. The change in the temperature cycle for Day 1 is to account for the increased temperatures that are most likely a result of a 'mist' observed on the hot plate lid, as is discussed in more depth later in this section.

As is necessary from these observations, the shelf life of MLC 7023 semi-droplets is instead measured using semi-droplets with predicted heights of 420µm that are left for for 0 - 16 days without undergoing a temperature cycle. After the given time period, NLC from the semi-droplets is pipetted into cover slips with the subsequent measurements using the temperature cycle in Table 7.1(2a) shown in Figure 7.4b for $T_{N\rightarrow I}$ (red) and T_{NI} (blue). The solid horizontal lines denote the average $\bar{T}_{N\rightarrow I} = 80.7 \pm 0.2°C$ and $\bar{T}_{NI} = 83.6 \pm 0.2°C$ and the dashed lines show $\pm$ three error bars from this average, with the measurements in Figure 7.4b agreeing with this average within one error bar (Days 0, 2-7, 16 for $T_{N\rightarrow I}$ and Days 2-7 for T_{NI}), two error bars (Day 1 for $T_{N\rightarrow I}$ and Days 0,1,16 for T_{NI}) or three error bars (Day 9 for $T_{N\rightarrow I}$ and Day 9 for T_{NI}). A potential explanation for the slightly worse agreement for the T_{NI} measurements is from the 'misting' having a greater effect at higher temperatures. When comparing to 'fresh' MLC 7023 measured on heating between untreated cover slips using the temperature cycle in Table 7.1(2a), $\bar{T}_{N\rightarrow I} = 80.2 \pm 0.2°C$ and $\bar{T}_{NI} = 83.1 \pm 0.1°C$, the average transition temperatures from Figure 7.4b agree within two error bars. These measurements therefore evidence that MLC 7023 is stable on the chemically patterned surfaces for at least 16 days provided that they do not experience a temperature cycle.

To test the origin of the 'misting', a hot plate is cleaned with IPA before heating to 100°C with three different configurations on the hot plate including: no sample, three chemically patterned surfaces not filled with NLC, and MLC 7023 on untreated glass (held within a sample sticker). The window only shows signs of blurring with the MLC 7023 sample, as shown in Figure A.16. Whilst this could suggest degradation of the MLC 7023 on heating, thermogravimetric analysis (TGA, see Section 3.5) completed on MLC 7023[1] implies this may not be

[1]TGA data taken by Thomas Raistrick.

the case. As is shown in Figure A.17, there is only a 0.8% change in mass between 30°C and 100°C. A significant portion of the 'misting' appears to remain overnight, suggesting that it is not water vapour, therefore it is unclear what is causing this effect. Since it cannot be verified if this 'misting' is a contamination or a degradation, the effect that it has on the system is instead labelled as a change in the semi-droplet.

To quantify the impact of the 'misting', a MLC 7023 semi-droplet with a predicted height of 420µm is measured with the temperature cycle in Table 5.1 to obtain $T_{\mathrm{N\rightarrow I}} = 80.3 \pm 0.1$°C and $T_{\mathrm{NI}} = 86.4 \pm 0.1$°C. $T_{\mathrm{N\rightarrow I}}$ agrees within one error bar with the 'fresh' MLC 7023 measured between cover slips, but within much greater than three error bars with $\mathrm{T_{NI}}$, implying that the effect is most prominent near the isotropic phase. Relative to the 'fresh' MLC 7023 in cover slips, $\Delta T_{\mathrm{NI}} = 3.3 \pm 0.1$°C for the semi-droplet.

Following this, the same MLC 7023 semi-droplet with a predicted height of 420µm is pipetted between untreated cover slips, and experiences the temperature cycle in Table 7.1(2b). $T_{\mathrm{N\rightarrow I}} = 81.9 \pm 0.2$°C and $T_{\mathrm{NI}} = 84.8 \pm 0.1$°C are measured, with $\Delta T_{\mathrm{N\rightarrow I}} = 1.7 \pm 0.3$°C and $\Delta T_{\mathrm{NI}} = 1.7 \pm 0.1$°C when compared to the 'fresh' MLC 7023 between cover slips. $\Delta T_{\mathrm{N\rightarrow I}}$ and ΔT_{NI} are approximately two times less than $\Delta T_{\mathrm{NI}} = 3.3$°C measured from the semi-droplet. These results evidence two properties of the system. Firstly, there is a change that occurs during the temperature cycle of the semi-droplet which stays consistent on heating the MLC 7023 from the semi-droplet within the cover slips as $\Delta T_{\mathrm{N\rightarrow I}}$ equals ΔT_{NI}. Secondly, there is a change that occurs on heating the semi-droplet that does not remain when moved into the cover slips, as shown by the greater $\Delta T_{\mathrm{NI}} = 3.3$°C compared to $\Delta T_{\mathrm{NI}} = 1.7$°C for the measurement of the semi-droplet and cover slips, respectively. This is likely related to changing conditions within the closed hot plate that only occurs for the semi-droplet sample from the 'misting'.

For the majority of the temperature cycles run to produce the semi-droplets imaged for Chapters 4 - 6, up to three patterned surfaces filled with semi-droplets were placed on the hot plate at once. Therefore, to measure if there is a greater

effect from the 'misting' from more samples, MLC 7023 semi-droplets with predicted heights of 83µm, 208µm and 420µm were formed on three different patterned surfaces and experienced the temperature cycle in Table 5.1 together. MLC 7023 from the semi-droplet with the predicted height of 420µm was pipetted between untreated cover slips measuring $T_{\mathrm{N}\rightarrow\mathrm{I}} = 81.9 \pm 0.2$°C, and $T_{\mathrm{NI}} = 85 \pm 0.1$°C on heating with the temperature cycle in Table 7.1(2a), corresponding to $\Delta T_{\mathrm{N}\rightarrow\mathrm{I}} = 1.7 \pm 0.4$°C and $\Delta T_{\mathrm{NI}} = 1.9 \pm 0.1$°C relative to 'fresh' MLC 7023 between cover slips. These agree within one error bar with the $\Delta T_{\mathrm{N}\rightarrow\mathrm{I}}$ and ΔT_{NI} for the semi-droplet with a predicted height of 420µm experiencing the temperature cycle by itself, and measured with the semi-droplet MLC 7023 between cover slips as described in the previous paragraph. Therefore, it can be concluded that having multiple samples on the hot plate at once should not cause a significant additional effect.

The same process of moving MLC 7023 from the semi-droplet with a predicted height of 208µm after the temperature cycle with semi-droplets with predicted heights of 83µm and 420µm into cover slips is completed. $\Delta T_{\mathrm{N}\rightarrow\mathrm{I}} = 2.2 \pm 0.3$°C and $\Delta T_{\mathrm{NI}} = 2.6 \pm 0.1$°C compared to the 'fresh' MLC 7023 in cover slips again agree with each other within their error bars. However, $\Delta T_{\mathrm{N}\rightarrow\mathrm{I}}$ and ΔT_{NI} are slightly greater than was observed for the semi-droplets with predicted heights of 420µm, potentially due to the smaller droplets being proportionally more affected by the 'misting'. An in-depth examination of this is left for further work.

It is worth noting that sometimes T_{NI} occurred after the slow heating section (+0.5°C/min) as the prediction for a suitable temperature range based off of the temperatures for the 'fresh' MLC 7023 within cover slips was low compared to the contaminated MLC 7023 in the semi-droplet. This will increase the uncertainty in the measurement, both physically due to the thermal lag and in decreasing the potential imaging rate. However, $\Delta T_{\mathrm{N\text{-}I}}$ and ΔT_{NI} are an order of magnitude greater than the uncertainty in the measurement, therefore this change in heating rate is not significant.

As the effective birefringence, Δn_{eff}, was calculated in Chapters 5 using a predicted height, Δn_{eff} and hence the measured height will be correct for the resulting

MLC 7023 semi-droplets after undertaking a temperature cycle. Therefore, the 'misting' does not have an effect in that regard. However, there is a possible variation in the tilt angle at the air/NLC interface of the MLC 7023 semi-droplets as this is calculated assuming that the values of n_o and n_e are unchanged after the temperature cycle. It is very likely that this assumption is valid as the mechanisms through which the 'misting' could change the refractive indices would be negligible compared to uncertainties. It has been shown in e.g. Reis *et al.*[135] and Cooper *et al.*[136] that the refractive index of a system can be dependent on the composition, therefore if the 'misting' were related to some small amount of component leaving the semi-droplet the refractive indices could vary, however the loss is small as shown by the TGA data (Figure A.17).

The other possible variation is that a slightly different N - I temperature could show a slightly different n_e and n_o. However, it is shown by Allinson and Gleeson[49] that n_e and n_o have negligible difference near room temperature (within experimental error) for E7 compared to doped E7. The doped E7 samples and E7 have transition temperatures with variations of $T_{N\rightarrow I}$ and T_{NI} between 52.4°C - 59.3°C and 56.4°C and 61.5°C, respectively[49], which is a greater range than the $\Delta T_{N\rightarrow I}$ and ΔT_{NI} observed in this work. Therefore, this is not likely to have a significant impact on the MLC 7023 semi-droplets.

7.4 Summary

In this chapter, the reusability and shelf-life of chemically patterned squares confining NLC semi-droplets was both qualitatively and quantitatively measured. Specifically, the reusability of the surface was validated by filling a single surface with an E7 semi-droplet that had a predicted height of 208µm and measuring $T_{N\rightarrow I}$ and T_{NI} upon heating, before rinsing the 'old' E7 the surface with IPA and repeating the process. There was minimal variation across each repeat, with most data points agreeing within one uncertainty with the average $\bar{T}_{N\rightarrow I} = 59.3 \pm 0.3$°C and $\bar{T}_{NI} = 61.8 \pm 0.2$°C. The semi-droplets were imaged after each temperature cycle to qualitatively conclude that there was not a significant variation in the director field.

An E7 semi-droplet with a predicted height of 208μm was observed to have a shelf-life of at least 14 days and be resistant to degradation during six temperature cycles within this time. There was minimal variation in the measured $T_{\mathrm{N\rightarrow I}}$ and T_{NI}, where the data points agreed within one error bar with the average $\bar{T}_{\mathrm{N\rightarrow I}}$ = 59.1 ± 0.1°C and $\bar{T}_{\mathrm{NI}}$ = 61.9 ± 0.1°C. From averaging the data from both the reusability and shelf life measurements, $\bar{T}_{\mathrm{N\rightarrow I}}$ = 59.2 ± 0.3°C and $\bar{T}_{\mathrm{NI}}$ = 61.8 ± 0.1°C, as was found to agree well with the measurements for E7 measured between untreated cover slips, $T_{\mathrm{N\rightarrow I}}$ = 59.0 ± 0.1°C and T_{NI} = 61.2 ± 0.1°C, within one or three error bars, respectively.

For an E7 semi-droplet with a predicted height of 208μm with no hot plate lid, $T_{\mathrm{N\rightarrow I}}$ = 59.7 ± 0.1°C and T_{NI} = 62.2 ± 0.1°C was measured and agreed within two error bars with the average measurement for E7 semi-droplets. This has benefits for potential industrialisation of the semi-droplet system as sensors, as the heating cycle can be completed in larger batches that do not require a cover, although this will place the samples under a greater risk of contaminants such as dust.

It was concluded that MLC 7023 semi-droplets changed under a temperature cycle. Three consecutive measurements of the transition temperatures of a semi-droplet with a predicted height of 208μm did not agree within three error bars, resulting in averages of $\bar{T}_{\mathrm{N\rightarrow I}} = 83 \pm 2$°C and $\bar{T}_{\mathrm{NI}} = 88 \pm 2$°C. This was attributed to a 'misting' effect observed on the hot plate window, although the exact reason for the 'misting' was not identified.

To account for the change from the 'misting', the shelf-life of MLC 7023 semi-droplets was measured by forming semi-droplets with a predicted height of 420μm, leaving them on a chemically patterned surface for a certain number of days, depositing MLC 7023 from the semi-droplet between untreated cover slips and heating the cover slips. It was therefore concluded that the MLC 7023 semi-droplets have a shelf-life of at least 16 days given they do not undergo a temperature cycle as each measurement agreed within three error bars or better with the average $\bar{T}_{\mathrm{N\rightarrow I}}$ = 80.7 ± 0.2°C and $\bar{T}_{\mathrm{NI}}$ = 83.6 ± 0.2°C. These averages agree within two

error bars with the measurement of 'fresh' MLC 7023 in untreated cover slips of $T_{\mathrm{N}\rightarrow\mathrm{I}} = 80.2 \pm 0.2$°C and $T_{\mathrm{NI}} = 83.1 \pm 0.1$°C.

To quantify the impact of the 'misting', an MLC 7023 semi-droplet with a predicted height of 420µm experienced a temperature cycle, before being pipetted into untreated cover slips. The measured transition temperatures in the cover slips corresponded to $\Delta T_{\mathrm{N}\rightarrow\mathrm{I}} = 1.7 \pm 0.3$°C and $\Delta T_{\mathrm{NI}} = 1.7 \pm 0.1$°C compared to the 'fresh' MLC 7023 between cover slips. The fact that these differences have the same value was attributed to the lack of further change to the MLC 7023 between the cover slips. It was also verified that there is not a significant increase in the impact of the 'misting' if multiple samples experience a temperature cycle at the same time. This was measured by MLC 7023 pipetted from another semi-droplet with a predicted height of 420µm that experienced a temperature cycle at the same time and on the same hot plate as two other semi-droplets. The measured $\Delta T_{\mathrm{N}\rightarrow\mathrm{I}} = 1.7 \pm 0.4$°C and $\Delta T_{\mathrm{NI}} = 1.9 \pm 0.1$°C were in good agreement with the changes seen from the large semi-droplet undergoing a temperature cycle by itself. It was discussed that any effect that this 'misting' would have on the height measurements of the MLC 7023 semi-droplets presented in Chapters 5 and 6 would be negligible compared to measurement uncertainties.

This chapter has confirmed that the surfaces are reusable after washing with IPA as is a beneficial result economically, for sustainability, and for safety as IPA is safe and inexpensive compared to other solvents. In addition, this chapter has presented that E7 and MLC 7023 have a shelf-life of at least 14 days when left on the surface which is useful as they can therefore be batch filled before use. The next chapter explores the confinement behaviours of the ferroelectric nematic liquid crystal, FNLC-919, in 6 x 6mm chemically patterned squares.

Chapter 8

FNLC-919 Confined in Chemically Patterned Squares

8.1 Introduction

In Chapters 4 - 7, E7 and MLC 7023 semi-droplets were formed on chemically patterned squares with a polyimide layer that was either rubbed or non-rubbed, and the reusability of these surfaces alongside the shelf-life of the confined nematic liquid crystal (NLC) semi-droplets was measured. These samples were discussed in the context of potential future sensing devices and, although a proof of concept is a natural next step, instead a more novel investigation is discussed in this chapter with the relatively new class of LC, the ferroelectric nematic liquid crystal (FNLC).

FNLC-919 from Merck has been of interest in recent years due to its room temperature N_f phase with the first publication by Yu *et al.*[12] in 2023 confirming the transition temperatures of,

$$I \xleftrightarrow{80°C} N \xleftrightarrow{44°C} N_x \xleftrightarrow{32°C} N_f.$$

Due to this room temperature nature of FNLC-919 and the availability of the ma-

terial from Merck, experiments were able to be planned to probe the confinement behaviour of FNLC-919 within 6 x 6mm chemically patterned squares. Three FNLC-919 semi-droplets with predicted heights of 80µm, 210µm and 420µm are formed and investigated for their behaviours near the phase transitions. The semi-droplet height is assumed using the predictive models previously discussed to calculate the variation of Δn_{eff} as a function of temperature over the nematic (N) phase, and is compared to a calculated Δn_{eff} for a temperature comfortably into the N phase for one semi-droplet. Instabilities near the corners of the semi-droplets are discussed, as well as the shrinkage observed for the smallest FNLC semi-droplet from the confinement edges on cooling. Finally, the director field in the N_f phase after cooling to room temperature is discussed in relation to relevant literature. The varied air/FNLC interface anchoring over each phase is considered throughout this chapter. Whilst there is much more information that can be gathered from these systems, the properties presented here give a strong first insight into the FNLC semi-droplet system, with further discussion points introduced in the further work section (Section 9.2).

8.2 Experimental Methods

8.2.1 Patterned Surface Fabrication

The chemically patterned surfaces were fabricated using the methods described in Section 3.2 to produce 6 x 6mm squares. The FNLC-919 was confined within a hydrophobic monolayer denoting the square, and sat atop an alignment layer that is rubbed unless otherwise stated.

8.2.2 FNLC Deposition

To deposit the FNLC, the vial containing FNLC-919 was placed on a hot plate at approximately 90°C (above T_{NI}) with the patterned surface at room temperature. To spread the FNLC to the corners of the square, compressed directional air or gentle movement with a plastic pipette tip was used, with care taken to make minimal contact between the surfaces and the tip.

The surfaces were used multiple times, and between each new dispense of FNLC the 'old' FNLC was removed from the surface with isopropanol (IPA), before drying with compressed air and/or evaporation on a hot plate. Polarised imaging was completed using the bespoke imaging device (Section 3.3.1).

8.2.3 Measurement of Phase Behaviour

Two temperature cycles were completed for each semi-droplet, in reflection mode and followed by transmission mode, with the two modes of operation of the imaging system described in Figure 3.8b. The cycles consisted of heating at 1°Cmin^{-1} to 85/86°C before cooling at 1°Cmin^{-1} to approximately 27/28°C, with the cooling rate slowing at approximately 34°C due to limitations of the passive cooling of the hot stage. A copper plate coated in high temperature, matt black paint was added on top of the hot stage surface to allow more homogeneous thermal contact across the semi-droplet whilst covering the hole in the hotstage to improve the quality of reflection mode polarised imaging.

The analysis in the following sections is completed on the polarised images taken on cooling unless otherwise stated to ensure that the FNLC-919 has been taken to isotropic. The word 'bulk' in the following discussions refers to the FNLC in the semi-droplets that is relatively far from the pinning and anchoring surfaces, i.e far from the substrate surface or air/FNLC interface.

8.3 Results and Discussion

8.3.1 Phase Transitions

The phase transitions on cooling are denoted as $T_{\mathrm{I}\rightarrow\mathrm{N}}$, $T_{\mathrm{N\text{-}N_x}}$ and $T_{\mathrm{N_x\text{-}N_f}}$ for the start of the I - N transition as well as the N - N_x and N_x - N_f transitions, respectively. The temperatures at which these transitions occur for the FNLC-919 semi-droplets on cooling are presented in Figure 8.1 in blue, green and red bars, respectively for reflection (R) and transmission (T) mode. Grey horizontal lines show the expected values from the literature (see Section 8.1). 'small', 'medium' and 'large' refers to semi-droplets with volumes of 1.8µL, 5µL and 10µL,

corresponding to predicted heights of 80µm, 210µm and 420µm, respectively. Even though the FNLC should be in the isotropic phase when pulled into the pipette, it sometimes formed filaments similar to those seen in the N_f phase in previous literature e.g. by Jarosik *et al.*[137] and Máthé *et al.*[129]. This adds an uncertainty to the semi-droplet volume and is why the semi-droplets are labelled as small, medium and large in this chapter. The full data is included in Table A.1.

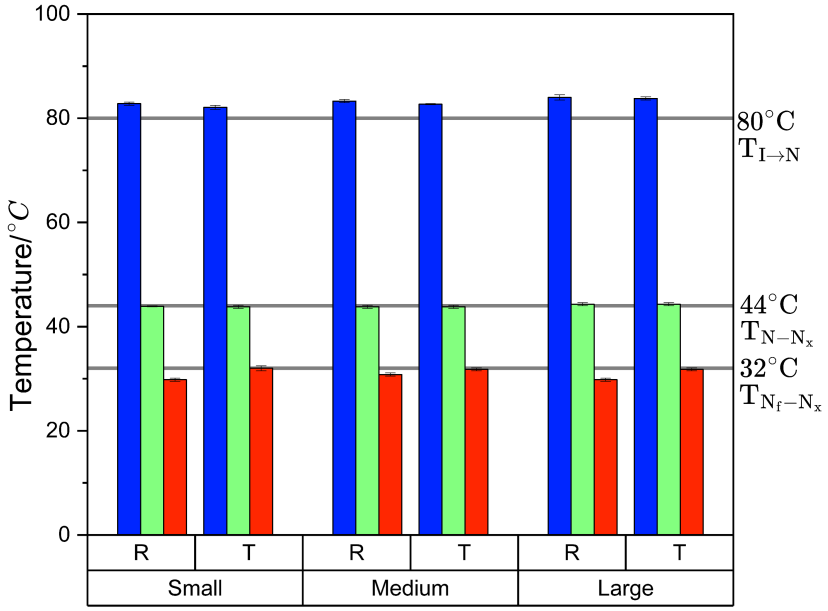

Figure 8.1: Transition temperatures on cooling for $T_{I\rightarrow N}$ (blue), $T_{N\text{-}N_x}$ (green) and $T_{N_x\text{-}N_f}$ (red) for the small, medium and large FNLC-919 semi-droplets measured in reflection (R) or transmission (T) imaging modes. The expected values from Merck are labelled with grey solid horizontal lines.

Any disparities between the reflection and transmission mode measurements in Figure 8.1 are likely a result of the added copper plate in reflection mode. Variations for the different semi-droplet heights could relate to the proportionally less pinning to the bounding surfaces (the substrate surface and the air/FNLC interface) in the 'bulk' for the taller semi-droplets (see Section 2.2.3). Additionally, the semi-droplets have an open air/FNLC interface and are therefore more greatly affected by laboratory conditions. The biphasic region for the I - N transition is

of the order of 6°C[1].

The overall average of $\bar{T}_{\mathrm{I}\rightarrow\mathrm{N}} = 83.1 \pm 0.5$°C is larger than the expected 80°C[2] which can be described by it being unclear whether 80°C was measured on heating or cooling or at the start or end of the biphasic region. The overall average of $\bar{T}_{\mathrm{N\text{-}N_x}} = 44.0 \pm 0.3$°C agrees excellently with the expected value of 44°C. For $\mathrm{T_{N_x\text{-}N_f}}$, the measurements between the reflection and transmission mode are in less good agreement with each other than for the other two transitions as it is difficult to identify the correct start of the phase transition in the reflection mode images. The overall average of $\bar{T}_{\mathrm{N_x\text{-}N_f}} = 31 \pm 1$°C is however in good agreement with the expected value of 32°C.

In the following sections, the director field over the phase transitions is discussed using both the reflection and transmission mode images, with a focus given to the small semi-droplet as the features are clearest. The difference in the images between reflection and transmission mode will arise from factors such as light travelling through the semi-droplet twice in reflection mode compared to once in transmission mode (see Section 3.3.1), and that it is difficult to get as high contrast in reflection compared to transmission. The temperatures presented in the figures are representative of some key observations and therefore the observations may not be first seen at exactly the temperature presented, however the full movies of the compiled images can be found in Movies 1-7 (see Section A.6.2). Whilst reflection mode images across the whole square, the transmission images field of view are limited by the 2mm imaging hole in the hot plate, therefore are circular.

Isotropic-to-Nematic Phase Transition

From the reflection mode images for the small semi-droplet in Figure 8.2a, it appears that the order over the I - N phase transition grows predominantly from the edges of the semi-droplet as evidenced by the birefringent fringes near the square edges compared to the centre at 82°C (Figure 8.2aiii). This could be

[1] Based off of differential scanning calorimetry data by Diana Nikolova.
[2] Expected transition temperatures from Merck.

attributed to a relatively strong pinning from the confinement edges compared to the bulk FNLC (see Section 2.2.3), or a cooler centre of the semi-droplet dependent on the temperature gradient from the hot stage. The presence of four dark brushes in the transmission mode images of Figures 8.2biii,biv could imply a defect with a strength of ± 1 with the likely origin highlighted with an orange circle. As discussed in Section 3.3.3, these dark brushes may not be related to defects, although defects is the explanation used in this chapter.

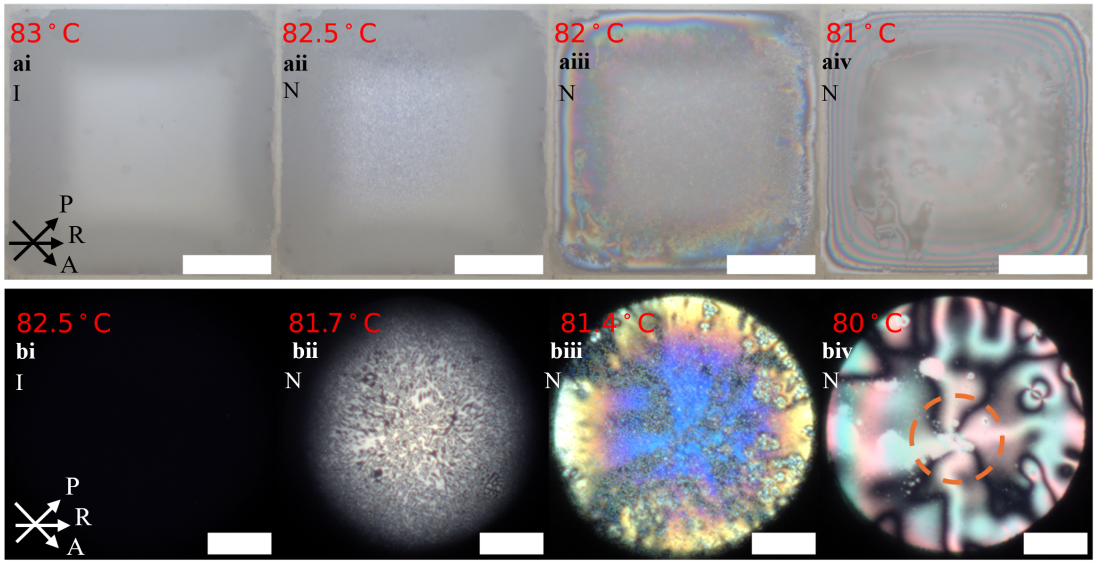

Figure 8.2: Cooling over the I - N phase transition of the small FNLC-919 semi-droplet in *a*: reflection and *b*: transmission mode polarised images. The potential centre of a possible strength = ± 1 defect is indicated in orange (*biv*). P, A and R show the relative directions of the polariser, analyser and rubbing, respectively. The reflection scale bars are 2mm, and for transmission are 0.5mm.

Figure 8.3 exhibits the small, medium and large semi-droplets (*a&b, c&d, e&f*, respectively) in reflection mode (*a,c,e*) or transmission mode (*b,d,f*), a few degrees after $T_{\mathrm{I}\rightarrow\mathrm{N}}$ (*i*) and near the N - $\mathrm{N_x}$ transition (*ii*). For the small semi-droplet (Figures 8.3a,b) there is a disclination line perpendicular to the rubbing direction. For the reflection mode images at 45°C for the medium and large semi-droplets (Figures 8.3cii,eii, respectively) there a subtle disclination line approximately parallel to the rubbing axis. All of these lines are indicated with blue arrows. The

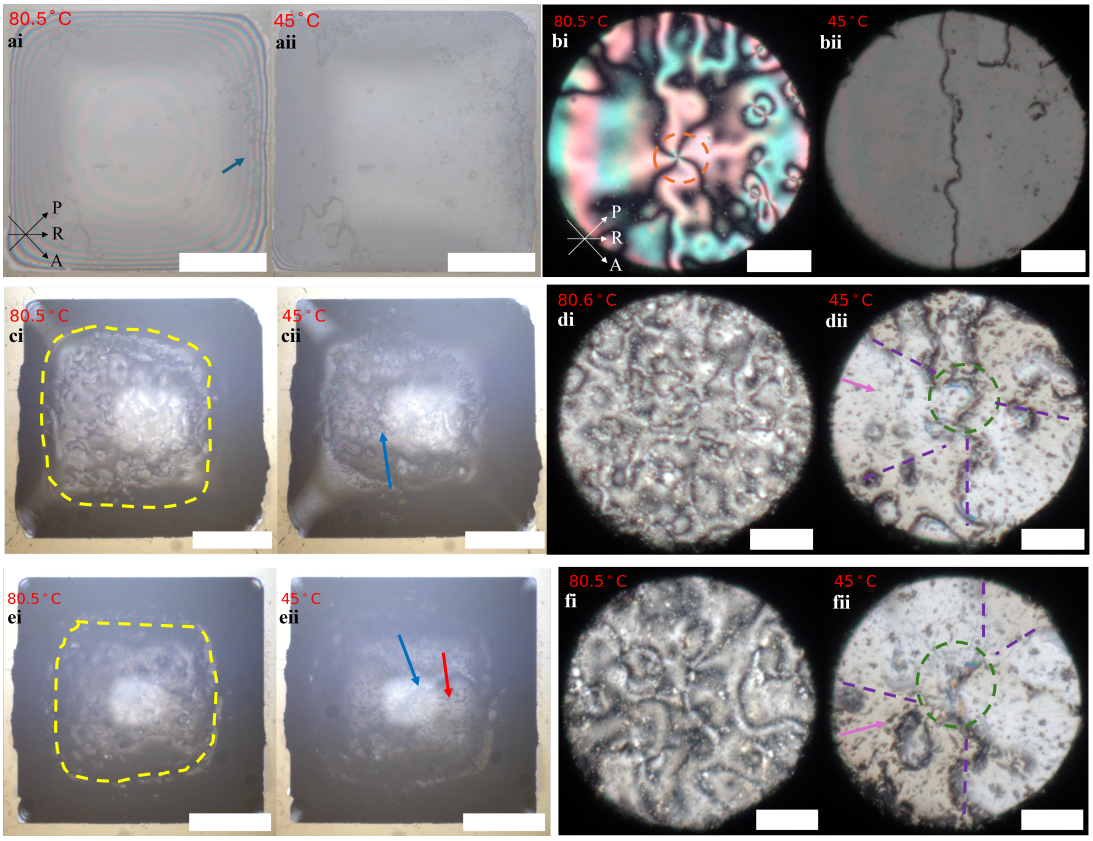

Figure 8.3: *a,c,e:* Reflection and *b,d,f:* transmission mode polarised images of the *a,b:* small, *c,d:* medium and *e,f:* large FNLC-919 semi-droplets at two temperatures in the N phase on cooling, *i:* a few degrees after $T_{\mathrm{I}\rightarrow\mathrm{N}}$ and *ii:* near the N - $\mathrm{N_x}$ transition. The blue arrows highlight some disclination lines (*ai,cii,eii*), the orange circle presents the origin of four dark brushes (*bi*), the yellow dashed line demonstrates an inner square (*ci,ei*), the purple dashes denote the edges of bright brushes (*dii,fii*), the green circles are low birefringence colour examples (*dii,fii*), the purple arrows indicate examples of brush-like textures (*dii,fii*), and the red arrow is an example of another brush-like texture (*eii*). P, A and R show the relative directions of the polariser, analyser and rubbing, respectively. The reflection scale bars are 2mm, and for transmission are 0.5mm.

perpendicular line for the small semi-droplet reflects the anchoring contributions from the bounding surfaces, similar to the E7 and MLC 7023 semi-droplets in Chapters 4 and 5, respectively. However, the parallel disclination for the medium and large semi-droplets is interesting as it was not generally seen for the rubbed E7 or MLC 7023 semi-droplets (with the potential exception of the MLC 7023 semi-

droplet with a predicted height of 420µm in Figure 5.1i). This will be related to an interplay between properties such as surface tension, anchoring energies and elastic constants (see Section 2.2.3) which are not well known for FNLC-919, although more properties of FNLC-919 have been very recently presented by Paul *et al.*[79].

In both the medium and large semi-droplets, an inner square-like shape is observed with examples circled in yellow in Figures 8.3ci,ei. Whilst this could be caused by a slightly more intense reflection of the light in the imaging system near the centre, if this were the case there would be a gradual change instead of a sharp border. Therefore, the area around the inner square could indicate better alignment than inside the square due to the lessened height at the edges, hence a greater contribution from the anchoring at the substrate surface and the air/FNLC interface on the bulk, as well as stronger relative pinning from the confinement edges. The inner square at 45°C for the large semi-droplet (Figure 8.3eii) appears more aligned compared to the medium (Figure 8.3cii). Additionally, this observation could relate to a transition in the alignment of the FNLC from a change in air/FNLC interface anchoring to homeotropic in the N phase[14]. Except for some MLC 7023 semi-droplets on non-rubbed surfaces such as Figure 6.2d, a similar square was not observed for the NLC semi-droplets. Near the centre of the large semi-droplet at this temperature there is also a brush-like texture that could indicate the director field direction, as highlighted by a red arrow in Figure 8.3eii.

For the equivalent temperatures imaged in transmission mode (Figures 8.3b,d,f), all three semi-droplets follow the expected pattern of greater disorder near the I - N phase transition temperature on cooling (see Section 2.2.1). Interestingly, all three semi-droplets also form a disclination line down the approximate centre the field of view at 45°C (Figures 8.3bii,dii,fii). The colours around this disclination line in the small semi-droplet are pink fringes that were utilised in Chapters 4 - 6, however for the medium and large semi-droplets there is a more nuanced director field. Firstly, there are a greater quantity of self-contained domains that are attributable to the greater volume of FNLC, hence proportionally less pinning

from the anchoring surfaces. Secondly, there are brush-like textures that appear to fan out radially from the approximate centre of the field of view, with examples highlighted using pink arrows. Thirdly, there are two lighter regions on opposite sides of the central disclination line that could be brushes indicating a possible strength = $\pm \frac{1}{2}$ defect, with examples outlined in purple.

Along the central disclination lines and some defects in the 45°C images for the medium and large semi-droplets (Figures 8.3dii,fii), there are low-birefringence colours with examples circled in green. Similar colours were observed for E7 and MLC 7023 semi-droplets in Chapters 5 and 6 that were related to varied director fields that change Δn_{eff} (see Section 3.3.2). The colours are not readily visible for the small semi-droplet however, as is likely again related the ratio of anchoring from the substrate surface and air/FNLC interface.

Nematic to Nematic 'x' Phase Transition

There is not a clear consensus on the exact properties of the N_x phase in the literature as was briefly discussed in Section 2.3. However, there are some interesting features to be observed on cooling over the N - N_x phase transition. The images for the small semi-droplet in Figure 8.4a imply that this transition is relatively subtle when imaged in reflection mode since key artefacts from the N phase (Figure 8.3a) remain in some form over the transition, such as the disclination line perpendicular to the rubbing axis.

At 43.8°C (Figure 8.4aii) there is a subtle texture that aligns approximately perpendicular to the rubbing direction with a slight curve, which then manifests in an s- like shape down the length of the semi-droplet at 43.5°C (Figure 8.4aiii), both of which are marked in blue as a guide to the eye[1]. In the transmission mode images, similar brush textures are observed at 43.5°C and 42°C (Figures 8.4bii,biii, respectively), and the disclination line observed in the N phase (Figure 8.4bii) becomes less well-defined. In addition, two dark brushes form that imply the potential presence of a strength = $\pm \frac{1}{2}$ defect, seemingly originating from this vertical disclination line as are highlighted in purple.

[1]These textures are difficult to see, even after contrast enhancement of the images.

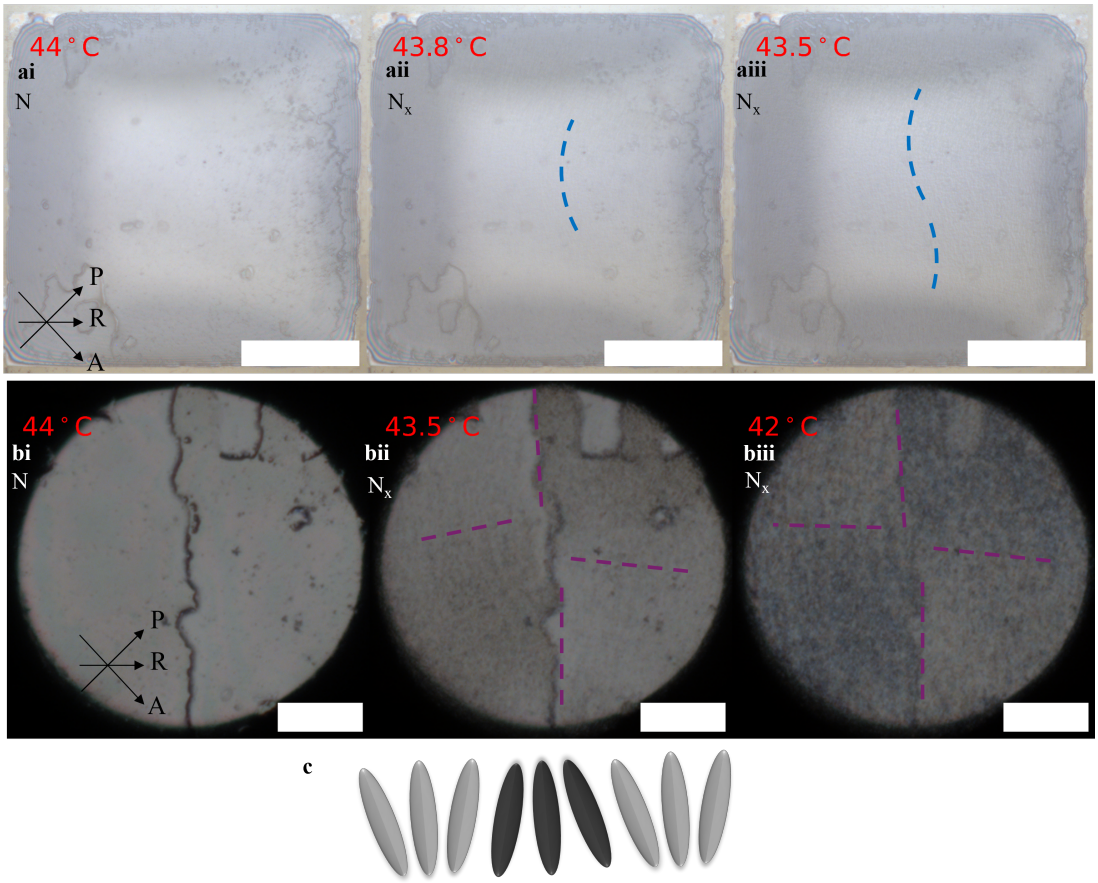

Figure 8.4: *a:* Reflection and *b:* transmission mode polarised images across the N - N_x phase transition on cooling for the small FNLC-919 semi-droplet. Blue lines show the approximate direction of the line textures (*ai,aii*) and purple lines indicate the edges of dark brushes (*biii*). P, A and R show the relative direction of the polariser, analyser and rubbing, respectively. The scale bars are 2mm for reflection, and for transmission are 0.5mm. *c:* Suggested splay stripe structure. Not to scale. *c based from [28, 29].* Note: The textures in *a* are difficult to resolve, even after contrast enhancement.

It has been demonstrated that FNLC-919 has a homeotropic air/FNLC interface in the N phase[14] and that FNLC anchoring at the air/FNLC interface is parallel to the interface in the N_f[13, 14] phase, therefore some reorientation of the FNLC is expected. A similar circular stripe texture centered on the middle of a free surface hexagonal confinement of FNLC-919 in the N_x phase is observed by Perera *et al.*[14], although in that work the width is 200µm and the confinement height is

20μm, therefore much smaller than the semi-droplets. A suggestion by Mertelj *et al.*[28] for RM 734 is that the FNLC forms a similar striped structure of splayed director pointing in opposite directions as demonstrated schematically in Figure 8.4c, as is supported by second harmonic generation to identify polarity in the structure[29]. However, planar cells with thicknesses of $\leq$ 20μm[28, 29] are used in those works with transitions observed for RM 734 as opposed to FNLC-919 on a free surface.

Figures 8.5a,c demonstrate the reflection mode images for the medium and large semi-droplets, respectively, in which it is observed that the inner square from the N phase (Figure 8.3c,e) becomes less well-defined with respect to the outer region of the semi-droplet. However, there is still a clear discrepancy between the director orientation within the square compared to outside of it.

For the medium semi-droplet, a black spot near the centre of the transmission mode images at 43.5°C and 42.5°C (Figures 8.5bii,biii, respectively) is circled in blue. It is not possible to identify a similar artefact in the reflection mode images (Figure 8.5a), which are taken on the first temperature cycle i.e. before the semi-droplet is imaged in transmission mode. This, alongside the fact that the spot appears larger at 42.5°C than 43.5°C, implies that it is not an air bubble caused from the FNLC deposition into the confinement and that it is unlikely to be dirt. A reasonable explanation could be a director field that is varied so that Δn_{eff} is greatly reduced, producing a low retardation colour (see Section 3.3.2). This could be related to the low birefringence colours observed near the disclination line and other domains in the transmission mode images for both the medium and large semi-droplets, with examples circled in green in Figures 8.5bi,di. Alternatively, the dark point could indicate a director field distorted to be locally isotropic or homeotropic.

Potentially analogous dark regions are observed in the N_f phase for free surface RM 734[13] and FNLC-919[14], described as a defect. Near the centre of the sample in [14] is the lowered region of FNLC-919 as discussed in Section 2.3 which is of a comparable size of approximately 100μm compared to a diameter of the dark spot in Figure 8.5biii of approximately 80μm.

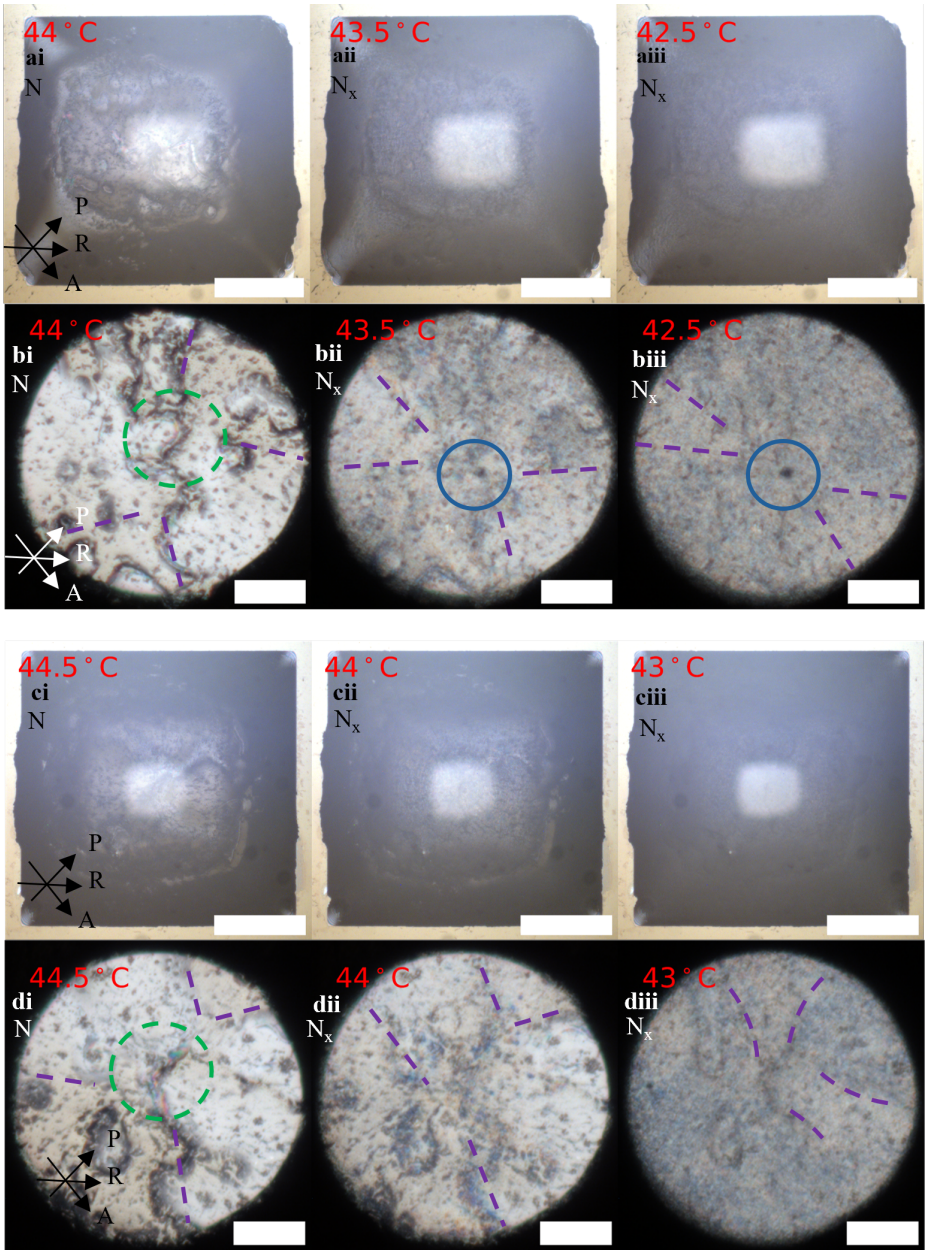

Figure 8.5: *a,c*: Reflection and *b,d*: transmission mode polarised images across the N - N_x phase transition for the *a,b*: medium and *c,d:* large FNLC-919 semi-droplets. The green circles highlight exemplar regions of low birefringence colour (*bi,di*), the blue circles highlight a small dark region (*bii,biii*), and the purple dashes indicate bright and dark fringes (*b,d*). P, A and R show the relative directions of the polariser, analyser and rubbing, respectively. The scale bars are 2mm for reflection, and for transmission are 0.5mm.

Also in the transmission mode images for the medium and large semi-droplets (Figure 8.5b,d, respectively) there are two light or dark brushes which could again imply the possible presence of a strength = $\pm\frac{1}{2}$ defect, as highlighted in purple. An interesting feature seen clearest in the dark brushes of all semi-droplets in transmission mode (Figures 8.4b and 8.5b,d) is a blue-shift in the birefringence colours which is a greater retardation colour on the Michel-Lévy chart (see Section 3.3.2). This could imply that the anchoring at the air/FNLC interface is tending towards planar (as is expected in the N_f phase[13]).

Nematic 'x' to Ferroelectric Nematic Phase Transition

Reflection mode polarised images for the small semi-droplet over the N_x - N_f phase transition are exhibited in Figure 8.6a, displaying a stripe texture similar to that discussed in the previous section. At 30°C (Figure 8.6ai) a reverse 's' shape texture is observed, similar to that seen in Figure 8.4aiii at 43.5°C but curved in the opposite direction as highlighted in blue. At 29.5°C, the texture lies perpendicular to the rubbing axis. At 29°C (Figure 8.6aiii), the texture has rotated to align approximately with the top left-to-bottom right diagonal axis. By 28.5°C (Figure 8.6aiv) the stripe textures are more pronounced and are mostly aligned with the rubbing axis, which is unsurprising as the anchoring from the rubbed planar polyimide is expected to cause a preferred director direction. This rotation implies that there has been some change in the anchoring at the air/FNLC interface, as discussed in the previous section.

Transmission mode images of the small semi-droplet in Figure 8.6b demonstrate that the blue shift previously observed at 42°C (Figure 8.4biii) is no longer apparent at 33.5°C (Figure 8.6bi), suggesting a reduction of Δn_{eff} assuming the height of the semi-droplet is constant. Also at 33.5°C, there is a slight directional orientation of the director field approximately towards the central disclination line as highlighted in yellow, emphasising the discontinuous nature of the line. The rotation of the stripe textures in the director field is again clear, where they align approximately along the top right-to-bottom left diagonal at 33°C and 32.5°C (Figures 8.6bii,biii, respectively), before rotation to lie approximately parallel to

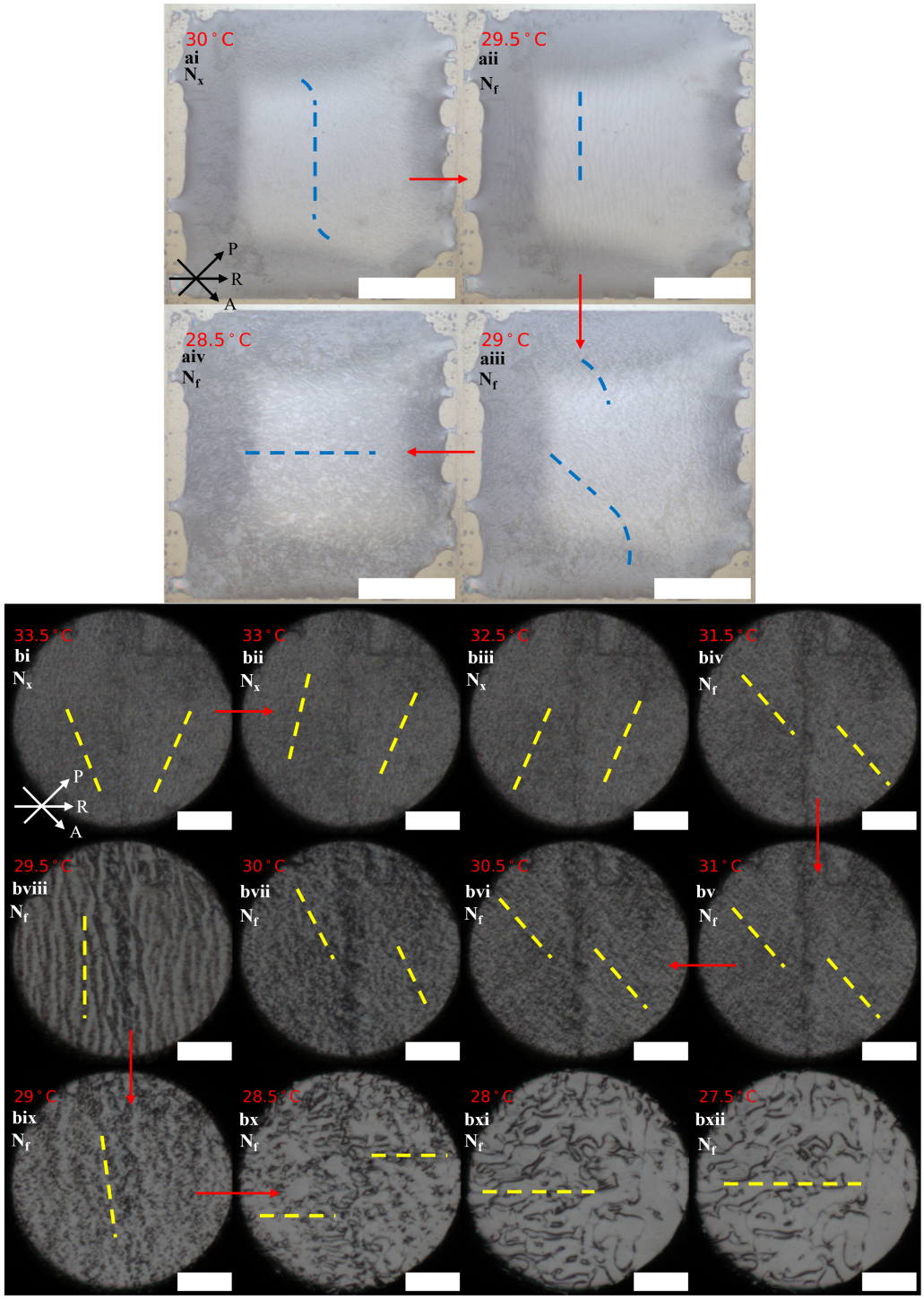

Figure 8.6: *a:* Reflection and *b:* transmission mode polarised images of the small FNLC-919 semi-droplet across the N_x - N_f phase transition. The blue and yellow dashes highlight the directions of the textures. P, A and R show the relative directions of the polariser, analyser and rubbing, respectively. The scale bars are 2mm for reflection, and for transmission are 0.5mm. Note: Especially in *a*, the textures are difficult to resolve due to contrast limitations.

the top left to bottom right diagonal at 31.5°C - 30°C, although this is noticeably less steep at 30°C (Figures 8.6biv-bvii). At 29.5°C, as was also observed for 29.5°C in the reflection mode images (Figures 8.6aii,bviii, respectively), the stripe textures and disclination line are oriented approximately perpendicular to the rubbing axis. At 29°C (Figure 8.6bix), this central disclination line is harder to identify, likely due to the relatively rapid re-anchoring to the director field at 28.5°C (Figure 8.6bx) where the stripe textures begin to align approximately parallel to the rubbing axis except for the central disclination line. By 28°C (Figure 8.6bxi), the majority of the stripe texture is approximately parallel to the rubbing direction.

It is clear in Figure 8.7 that there is a difference in periodicity of the stripe textures for temperatures a few degrees before and after the N_x - N_f transition, shown by 35°C (*a*) and 29.5°C (*b*) with periodicities of the order of magnitudes of 10µm and 100µm, respectively. The periods from this thesis are greater than FNLC-919 at 35°C in an approximately 10µm thick cell, with a periodicity of approximately 5µm by Perera *et al.*[14]. However, the periods in this thesis are of a similar size and direction (perpendicular to the rubbing axis) for the stripesobserved in FNLC-919 in a 2µm cell at 42°C by Paul *et al.*[79], with a period of approximately 10µm.

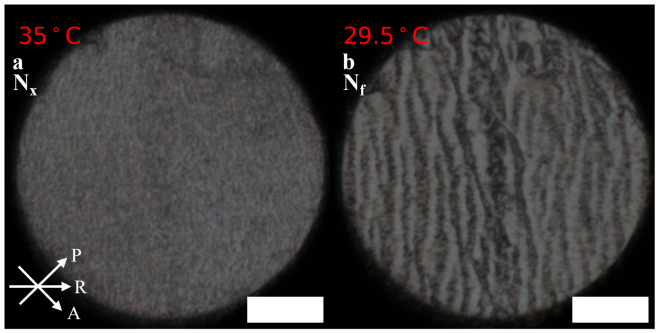

Figure 8.7: Transmission mode images of the small FNLC-919 semi-droplets a few °C *a:* before and *b:* after the N_x - N_f phase transition to highlight the approximately 10x difference in the stripe texture periodicity. P, A and R show the relative directions of the polariser, analyser and rubbing, respectively. The scale bars are 0.5mm.

For the medium semi-droplet transmission mode images (Figure 8.8a), instead of a texture near 29.5°C that aligns approximately perpendicular to the rubbing axis as observed for the small semi-droplet (Figures 8.6aii,bviii), the medium semi-droplet has a circular semi-symmetric director field at 29.4°C and 29°C (Figure 8.8avii,aviii, respectively) as highlighted in yellow. The dark spot as circled in Figures 8.5bii,biii and 8.8ai-vii is no longer distinguishable by 29.4°C, although it is difficult to identify by 30°C. At 28.8°C (Figure 8.8avix) there is a subtle, approximately central and vertical texture line that traces a similar path to the disclination line seen at 31°C (Figure 8.8aiv) as highlighted in green. This implies that the disclination line is still present at 29.4°C or 29°C (Figures 8.8avii, aviii, respectively) but unclear compared to the other textures, or that there are memory effects of the director. There are slightly visible brushes as highlighted in red at 30.5°C and 28.4°C (Figures 8.8av,axi, respectively) that could imply a potential strength $= \pm \frac{1}{2}$ defect.

In the transmission mode image for the large semi-droplet at 29.5°C as demonstrated by Figure 8.8bvi , there is a texture perpendicular to the rubbing direction reminiscent of the central disclination line clearly seen for the small semi-droplet (Figure 8.6bviii), as well as stripe-like textures that point towards the disclination-like texture in a different direction to the surrounding temperatures.

Máthé *et al.*[13] describe the behaviour of a RM 734 sessile droplet where the addition of particles can highlight a circular motion of the heated droplet. A similar effect could be the cause of the line textures as explained above, with the rotation clearer due to the increased millimetre wide semi-droplets compared to few 100 micrometer-scale sized droplets in their work.

Unlike for the small semi-droplet, there is no clearly good alignment of the texture with the rubbing axis for the medium and large semi-droplets at approximately 28°C (Figures 8.8axii,bviii), as is again related to the ratio of the effect of the anchoring from the substrate surface and air/FNLC on the bulk FNLC.

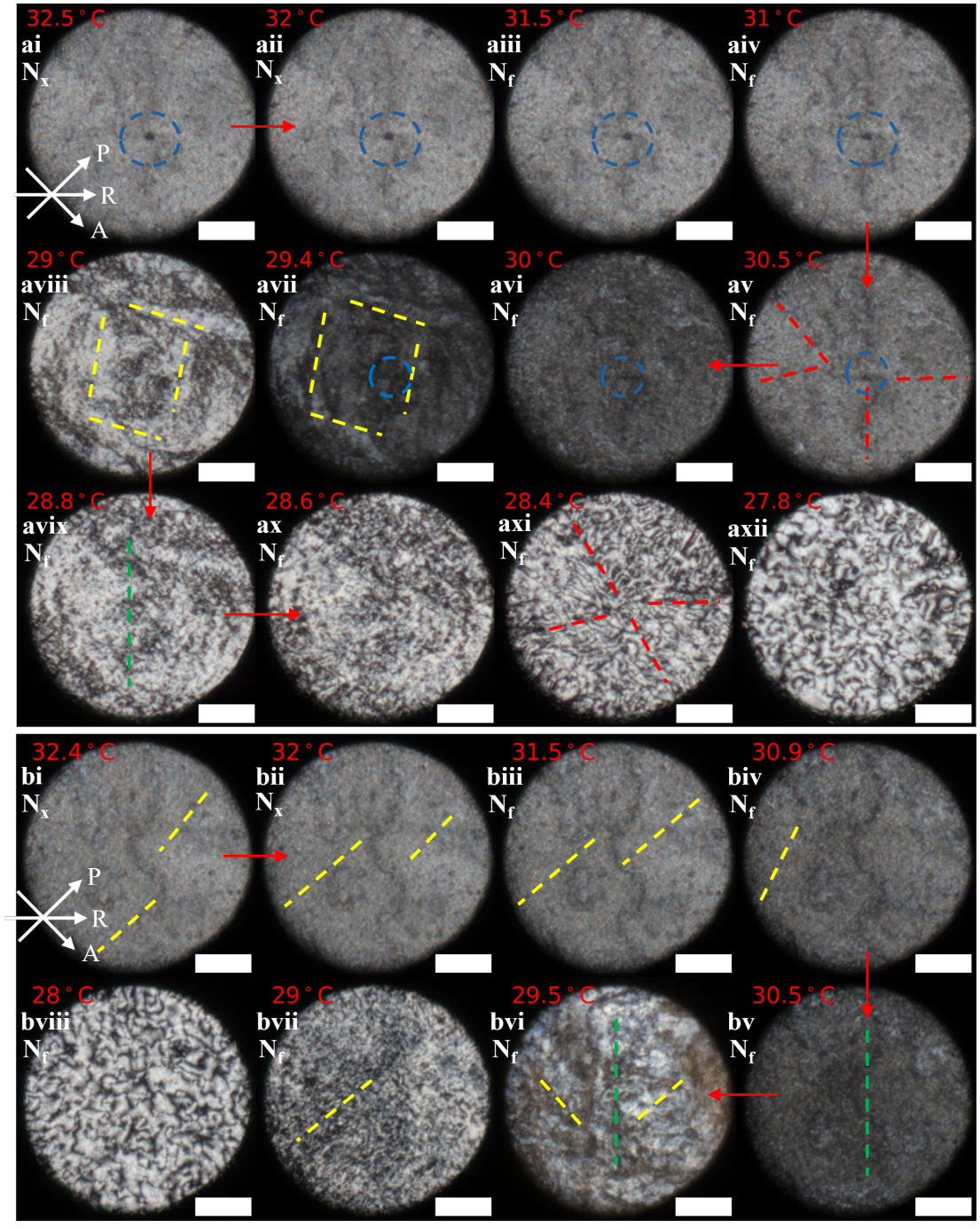

Figure 8.8: Transmission mode images of the *a:* medium and *b:* large FNLC-919 semi-droplets across the N_x - N_f phase transition. A dark spot is circled in blue (*ai-iv*), green represents disclination lines (*avix,bvi*), red highlights the outer borders of two very subtle, potential dark brushes suggesting a possible strength $= \pm \frac{1}{2}$ defect (*av,axi*), and yellow is a guide to the texture directions. P, A and R show the relative directions of the polariser, analyser and rubbing, respectively. The scale bars are 0.5mm.

8.3.2 Small Semi-Droplet Behaviour in the N Phase and the Effective Birefringence

Unlike for the NLC semi-droplets in Chapters 4 - 6, the measurement for the number of birefringent fringes using the full wave equation, $\Delta n_{\text{eff}} = \frac{m\lambda}{h}$, must be made on reflection mode images with the sample on a hotplate since the FNLC-919 N phase is above room temperature, expected at 44°C and above[1]. Therefore, for FNLC-919, the effective birefringence is evaluated assuming the height to be that predicted from Equation 4.6 (see Section 4.3,[1], with 80 ± 20µm in this case). Again the wavelength, λ, is taken to be 0.53 ± 0.04µm. The resulting values for Δn_{eff} as a function of temperature over the N phase is presented in Figure 8.9.

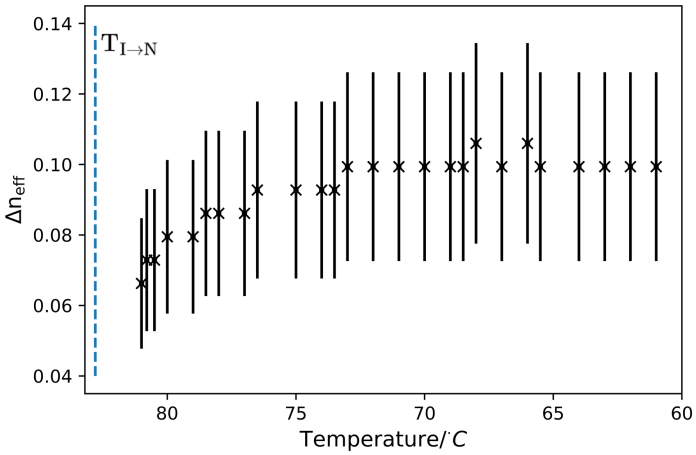

Figure 8.9: Variation of Δn_{eff} with temperature on cooling across the N phase of the small FNLC-919 semi-droplet.

It is well known that the order parameter of an NLC varies most rapidly near the N - I phase transition[57] which has an effect on Δn_{eff} (see Sections 2.2.1 and 3.3.5). Δn_{eff} in Figure 8.9 increases with decreasing temperature until approximately 73°C, where it remains constant within the error bars and within the measured temperature range. The reflection mode image at 45°C in Figure 8.3aii

[1]Merck

shows that the fringes are no longer clear enough to count near the the N - N_x transition.

It is worth noting the difference in the optics between reflection and transmission mode and the effect this has on Δn_{eff}. If the number of birefringent fringes in each mode is labelled as m_r and m_t, respectively, then $m_r = 2m_t$ as the light passes through the semi-droplet twice in reflection mode (see Figure 3.8b). Therefore, in reflection mode the light passes through two times the height, where $h_r = 2h_t$. When this is substituted into the full wave equation for the $\Delta n_{\text{eff,r}}$ for reflection mode,

$$\Delta n_{\text{eff,r}} = \frac{m_r \lambda}{h_r} = \frac{2m_t \lambda}{2h_t} = \Delta n_{\text{eff,t}},$$

the result is equivalent to the $\Delta n_{\text{eff,t}}$ for transmission mode.

To confirm that the air/FNLC interface is homeotropic for the semi-droplet in the N phase, as previously shown for FNLC-919[14], the approximate values of $n_e = 1.71$ and $n_o = 1.48$ at a wavelength of approximately 0.53µm, read from Figure 9 by Abe *et al.*[128], are substituted into Equation 3.5, repeated here in Equation 8.1 for clarity. Equation 8.1 describes a linear rotation of the director from planar at the substrate surface to homeotropic at the air/FNLC interface through the dimensionless height, $\frac{z}{h}$ in degrees,

$$\phi\left(\frac{z}{h}\right) = 90° \frac{z}{h}, \tag{8.1}$$

as previously described in Section 3.3.5. The shape is provided schematically in Figure 8.10. After substitution of Equation 8.1 in Equations 3.6 and 3.7, Δn_{eff} = 0.1 is calculated, with the estimated uncertainty from reading n_e and n_o from Figure 9 in [128] being ± 0.05. The variations of $\phi\left(\frac{z}{h}\right)$, $n_e\left(\frac{z}{h}\right)$ and $n_e\left(\frac{z}{h}\right)$ - n_o are shown in Figure A.18. At 64°C, which is chosen as it is comfortably into the plateau region of the N phase Figure 8.9, $\Delta n_{\text{eff}} = 0.10 \pm 0.03$. The two Δn_{eff} values are in agreement assuming the air/FNLC interface is homeotropic.

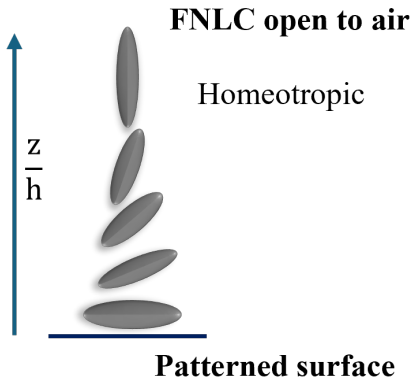

Figure 8.10: Schematic of the hybrid-aligned ferroelectric nematic director of FNLC semi-droplets through the dimensionless height of the semi-droplet, $\frac{z}{h}$, from planar at the patterned surface, to homeotropic at the air/FNLC interface in the N phase. *Figure adapted from [1].*

8.3.3 Instabilities at Semi-droplet Corners

Branch-like structures are highlighted in yellow in Figures 8.11a,b for the large and small semi-droplets, respectively. The small semi-droplet in Figure 8.11a is presented in reflection mode to provide a clearer image of the constituent branches in the structures whereas the large semi-droplet in Figure 8.11b is presented in transmission mode to demonstrate the birefringence of the offshoots.

Similar observations are presented in the FNLC literature, where FNLC is deposited on or near a free surface of the ferroelectric lithium niobate (LN), and the LN is charged using either light (photovoltaic), e.g.[83, 85, 87] or temperature (pyroelectric), e.g.[30, 82, 84]. Examples have also been shown to produce the instabilities using an electric field with glass substrates, e.g.[88, 138]. The increase in polarisation of the LN (pyroelectric) and FNLC on cooling further into the N_f builds large and repellent charges that overcome the surface tension to cause FNLC to be ejected, as explained by Rayleigh[82, 139]. It is not clear in what phase the instabilities observed in this thesis are formed. The increase of polarisation for FNLC-919 is reported by Paul *et al.*[79] to be approximately 6000μCm^{-2} between approximately 24°C and 30°C.

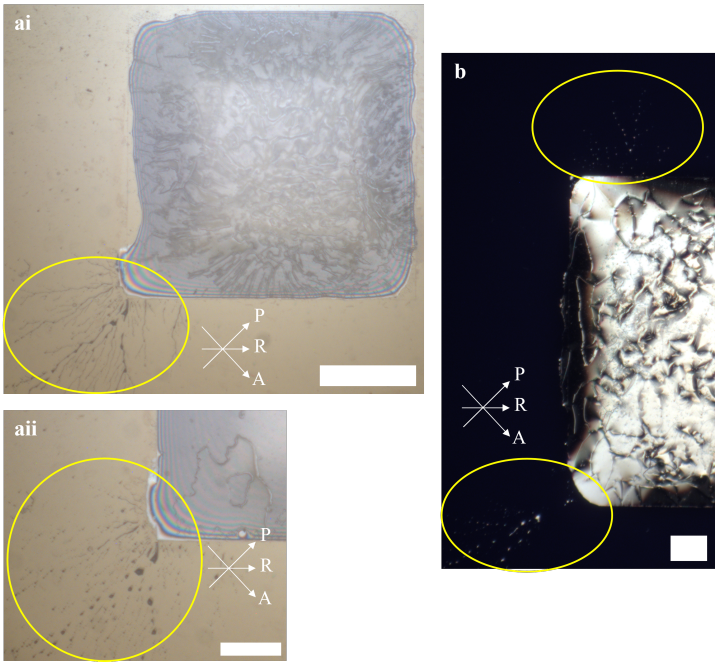

Figure 8.11: *ai:* Reflection mode image of the small FNLC-919 semi-droplet at 51.2°C on heating. The scale bar is 2mm. *aii* The same region at 51°C on cooling. The scale bar is 1mm. *b:* Transmission mode image after the second temperature cycle of the large FNLC-919 semi-droplet. The scale bar is 1mm. The instability features are highlighted by the yellow circles. P, A and R show the relative directions of the polariser, analyser and rubbing, respectively.

The origin of these instabilities from the semi-droplets is less clear as the patterned surface is not a ferroelectric material like LN, nor is there an applied electric field. However, the majority of the jets originate from or near the corners of the semi-droplets, which is unsurprising as filling a liquid into a corner is likely to be energetically unfavourable. Therefore, a build up of charge or a spontaneous charge on the semi-droplet has an increased probability of the charge build up overcoming the surface tension. Máthé *et al.*[13] discuss an electric field generated on cooling an RM 734 droplet, which could have an effect here.

A similar branching effect as can be seen clearly in Figure 8.11a was reported by e.g. Barboza *et al.*[82] from repellent charges. In the small and large semi-droplets, there are branches that occur out of more positions after the second temperature cycle compared to the first cycle, which could be indicative of a

relatively random and spontaneous nature of the instabilities. In some cases, it is observed that small droplets form from the previously ejected FNLC as circled in Figure 8.11aii, with a similar effect previously discussed in the literature by e.g. Barboza *et al.*[82].

8.3.4 Semi-Droplet Shrinkage and Growth

Figure 8.12a demonstrates a shrinkage that occurs on cooling over the N_x phase for the small semi-droplet, where a majority of the unpinning of the FNLC from the confinement edges occurs along the rubbing axis. Figure 8.12b plots the shrinkage with temperature along the axis corresponding to the white lines marked on the reflection images in Figure 8.12a, normalised to the width at 50°C. There is a proportional shrinkage of 0.09 ± 0.01 over the 50°C to 28°C temperature range. This shrinkage behaviour is not seen for the E7 or MLC 7023 semi-droplets, which implies this behaviour is related to the specific properties of the FNLC, specifically the N_x.

This shrinkage is not likely to be associated with a significant change in density when comparing to the FNLC M5 measured by Parton-Barr *et al.*[131], whose density was found to change by only approximately 0.015gcm^{-3} over the N_x phase. Therefore, the volume must be approximately consistent so the shrinkage in one axis would correspond to a growth in another, most likely the height since there is no obvious overflow of the FNLC from the top or bottom of the square.

The shrinkage behaviour is likely a complicated interplay between different properties of the FNLC-919 in the N_x phase. Approximate values read from plots in the recent publication by Paul *et al.*[79] are summarised in the rest of this paragraph. The polarisation of FNLC-919 shows a sharp increase over the N - N_x transition from 0 - 28000μCm^{-2}, before a general increase on cooling to 40000μCm^{-2} at the N_x - N_f transition. A general trend of increasing splay, twist and bend (see Section 2.2.3) is seen over the N_x phase with decreasing temperature. A sharp dip in the viscosity starting at the N - N_x phase transition from 100mPa·s to 75mPa·s is reported the first 2.5°C of the phase could be a key descriptor as to why the shrinkage is observed mostly over the N_x phase (see Figure

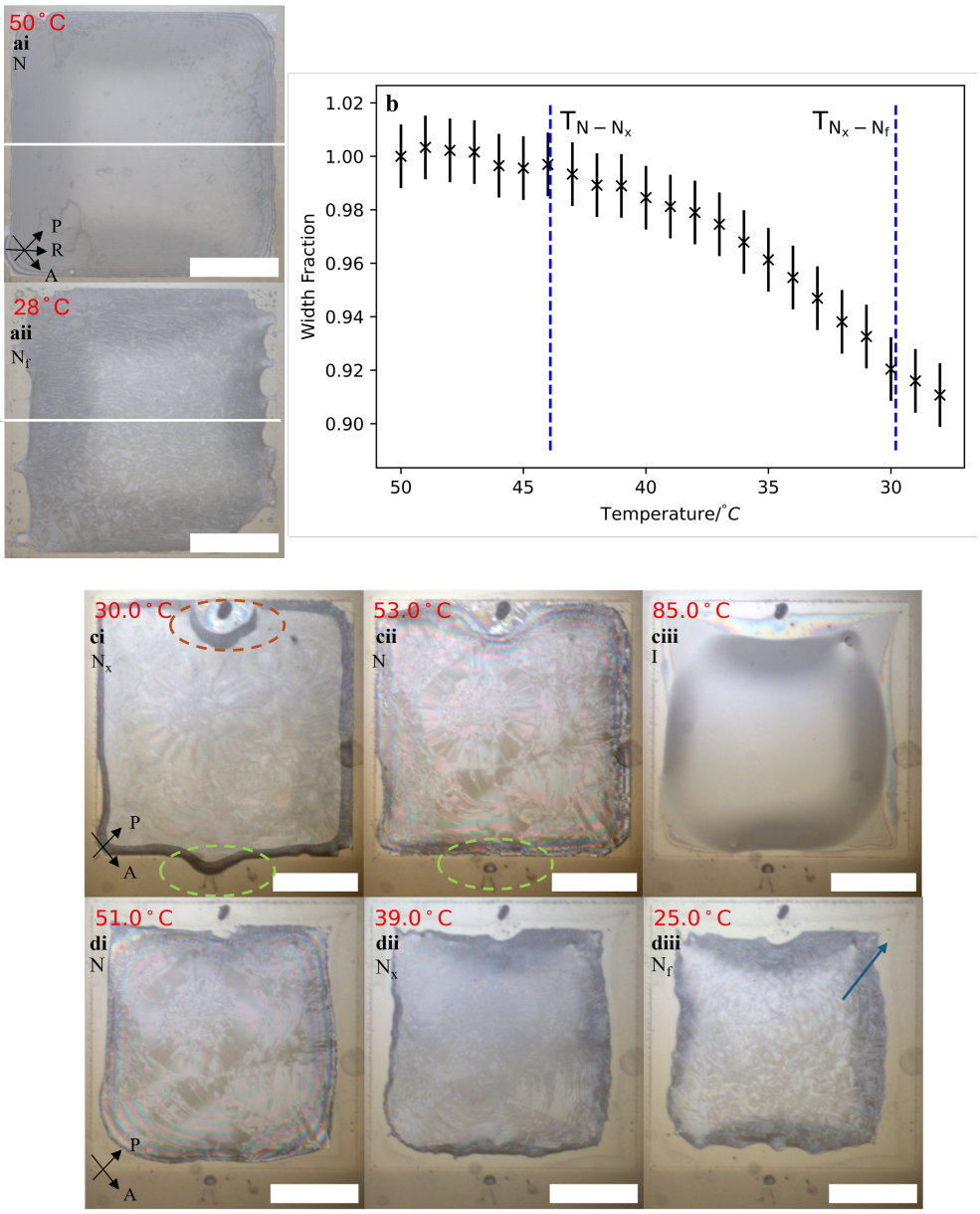

Figure 8.12: Reflection mode polarised images of the shrinkage behaviour of small FNLC-919 semi-droplets for *a:* rubbed and *c,d:* non-rubbed surfaces. *b:* Plot of the shrinkage with temperature along the axis marked in white in *a*, normalised to the width at 50°C. For the non-rubbed semi-droplet, images are presented on *c:* heating and *d:* cooling. The orange circle indicates the impurity on the sample (*ci*), the green circle highlights the shrinkage forming an instability (*cii*), and the blue arrow shows the 'shadow' remaining near the end of the temperature cycle (*diii*). P, A and R show the relative directions of the polariser, analyser and rubbing, respectively. The scale bars are 2mm.

8.12a) as the FNLC-919 can flow easier. This dip is followed by a general increase to the N_x - N_f phase transition, where it reaches 120mPa·s[79].

A different potential explanation for the shrinkage is a change in contact angle with temperature. An example from the literature is by Gvozdovskyy *et al.*[140] who present a decrease in the contact angle of an NLC on glass with an approximate change of 5° in 60°C. However, NLCs are not polar (see Section 2.2.1). The shrinkage could also be caused by evaporation from the LC droplet, however shrinkage would have likely been observed also on heating.

To validate that the shrinkage along the rubbing axis has some dependence on the rubbing, a second small FNLC-919 semi-droplet on a non-rubbed surface with an equivalent predicted height of 80µm is presented in Figures 8.12c,d on heating and cooling, respectively. The temperature cycle for this semi-droplet can be found in Movie 7 (see Section A.6.2). The FNLC-919 in the non-rubbed sample shrinks in all four axes which points towards the importance of the rubbing step, however it is shown by Figure 8.12c that some shrinkage effects also occur on heating, suggesting the reorganisation of the droplet is not simply contraction on cooling. It is worth considering that the time that the FNLC has to reorganise is dependent on the heating and cooling rate.

There are some further interesting observations from this non-rubbed sample. The first is highlighted in orange in Figure 8.12ci where there is a imperfection in the sample. It is unclear if this is a droplet of FNLC-919 with a low birefringence colour, or if it is an impurity on the surface. However, it is clear that this does not have a significant effect on the images in Figure 8.12d as the FNLC is always spatially below this imperfection.

A second observation is circled in green in Figures 8.12ci,cii where the slight overfilling of the FNLC-919 shrinks to form a better square shape, likely due to the hydrophobic monolayer (see Section 3.2.6) repelling the FNLC. There is a droplet remaining in Figure 8.12cii that has a similar shape to the instabilities discussed in Section 8.3.3. It is worth noting that in some samples there is also a small growth of the FNLC to fill to the edges of the confinement better, however

this is a less dramatic effect than the shrinkage and is therefore left for future work. This also supports the assertion that the shrinkage is not due to evaporation.

A third observation is the 'shadow' that remains after the cooling, as highlighted by a blue arrow in Figure 8.12diii. This could indicate that the surfaces are less reusable with FNLC-919 than was measured in Chapter 7 for E7, potentially related to stronger electrostatic interactions from the ferroelectric properties of the FNLC (see Section 2.3) causing more damage to the surfaces. Further investigation of the reusability of the surfaces is beyond the scope of this thesis, however it is worth noting that the same surface was used to investigate the small, medium and large semi-droplets.

Finally, to obtain some assurance that use of FNLC-919 does not damage the reusability of a surface, the 6 x 6mm square was filled with an E7 semi-droplet with a predicted height of 210µm after the data collection for the first FNLC-919 semi-droplet investigated, i.e. the large semi-droplet. Qualitatively, the director field was compared to previous director fields obtained with this E7 volume to validate that there was no significant change (Figure A.19). Quantitatively, the key transition temperatures were measured where $T_{\mathrm{N}\rightarrow\mathrm{I}} = 58.9 \pm 0.2$°C and $T_{\mathrm{NI}} = 61.6 \pm 0.1$ °C, which agree within one error bar with the averages for E7 semi-droplets presented in Chapter 7 of $T_{\mathrm{N}\rightarrow\mathrm{I}} = 59.2 \pm 0.3$°C and $T_{\mathrm{NI}} = 61.8 \pm 0.1$ °C.

8.3.5 $\mathrm{N_f}$ Phase Director Field After Cooling

The following discussion compares the director field of the FNLC-919 semi-droplets in the $\mathrm{N_f}$ phase after cooling with a focus on the small semi-droplet. The discussion draws on related published research wherever possible. Figure 8.13 exhibits transmission mode polarised images of the small semi-droplet after the first (a) and second (b) temperature cycles. It is important to note that the anchoring at the air/FNLC interface is parallel to the interface[13, 14] in the $\mathrm{N_f}$ phase.

The most prominent feature of the small semi-droplet director field are the

domain-like structures, an example of which is highlighted in yellow in Figure 8.13a, and focused on in Figure 8.14. Domain-like structures in the literature are commonly aligned approximately parallel to the rubbing axis and observed in cells, e.g.[11, 30, 31, 78, 79, 80, 123, 125]. They are reporting on DIO[31, 125], RM734[11, 30, 80, 123], and FNLC-919[78, 79].

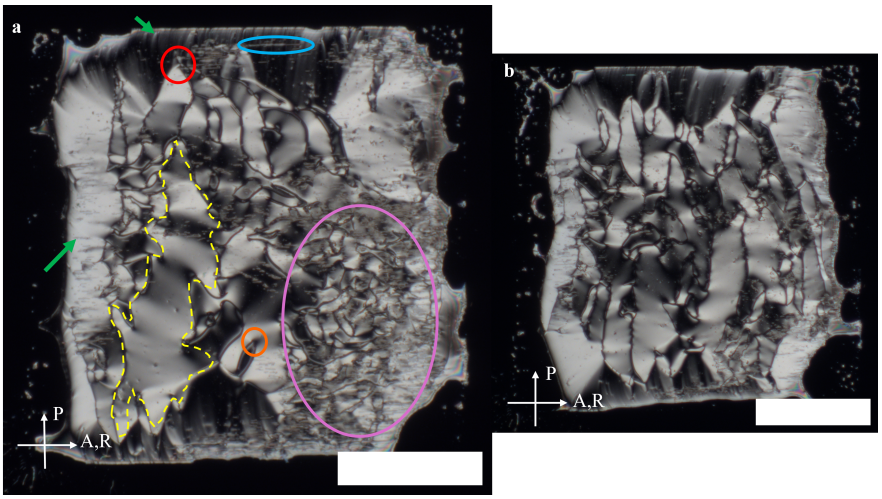

Figure 8.13: Transmission mode polarised images of the small semi-droplet after the *a:* first and *b:* second temperature cycles. The annotations in *ai* demonstrate features of the director field: *yellow*: large domain aligning approximately perpendicular to the rubbing axis, *purple*: domains aligning approximately parallel to the rubbing axis, *orange*: dark point, *red*: triangular end points of domains, *blue*: small textures approximately parallel to the rubbing axis, *green*: brush-like textures. P, A and R show the relative directions of the polariser, analyser and rubbing, respectively. The scale bars are 2mm.

Fewer examples of domain structures in the literature are aligned perpendicular to the rubbing axis, e.g.[12, 27, 123]. References [12, 27] have some key aspects that make them similar to this work, including Kumari *et al.*[27] who investigate DIO with a height of approximately 10µm placed on a rubbed glass (with polyimide) surface with a free air/FNLC interface. Yu *et al.*[12] utilise FNLC-919-filled cells between approximately 2 - 10µm in thickness, with the perpendicular domains observed in cells with anti-parallel rubbing. If we focus on the latter example[12], the description for the domains in cells with 4.2µm and 10.2µm cell gaps is related

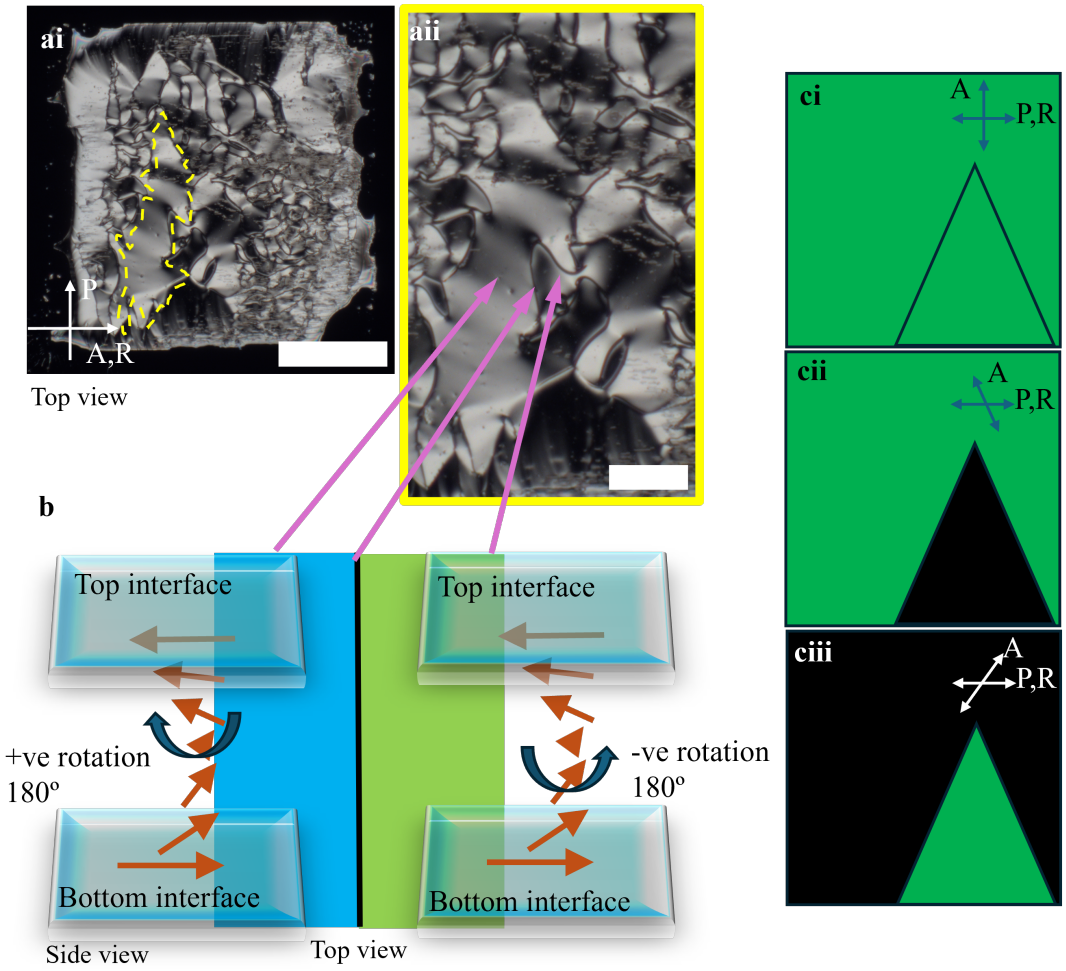

Figure 8.14: Description of twist in FNLC systems. *a:* Reproduction of Figure 8.13a to highlight the domains perpendicular to the rubbing axis. The scale bar is 2mm in *ai* and 1mm in *aii*. *b:* π-twist of the director throughout the height of an FNLC sample observed for domain-like structures in the literature that lie perpendicular to the rubbing axis. *c:* The sharper domain structures observed in some works that demonstrate twist. (*cii, ciii*). P, A and R demonstrate the relative directions of the polariser, analyser and rubbing, respectively. Not to scale. *b,c redrawn and/or adapted from information in [12].*

to a twist of the director throughout approximately 180° in opposite directions, as demonstrated schematically in Figure 8.14b (see also Section 3.3.4). However, some of the domain structures in their work[12] have more of a triangular shape than observed in Figure 8.13, as demonstrated schematically in Figure 8.14c.

Similar triangular structures are seen in earlier and later works, such as [123] and [78], respectively.

To confirm that these domains are indeed twisted in the small semi-droplet, a third 'small' (predicted height of 80μm) FNLC-919 semi-droplet was formed on a new surface from the original small, medium and large semi-droplets. The new semi-droplet experienced a single temperature cycle which, as can be seen in Figure 8.15ai, has a similar domain structure to that observed in Figure 8.13

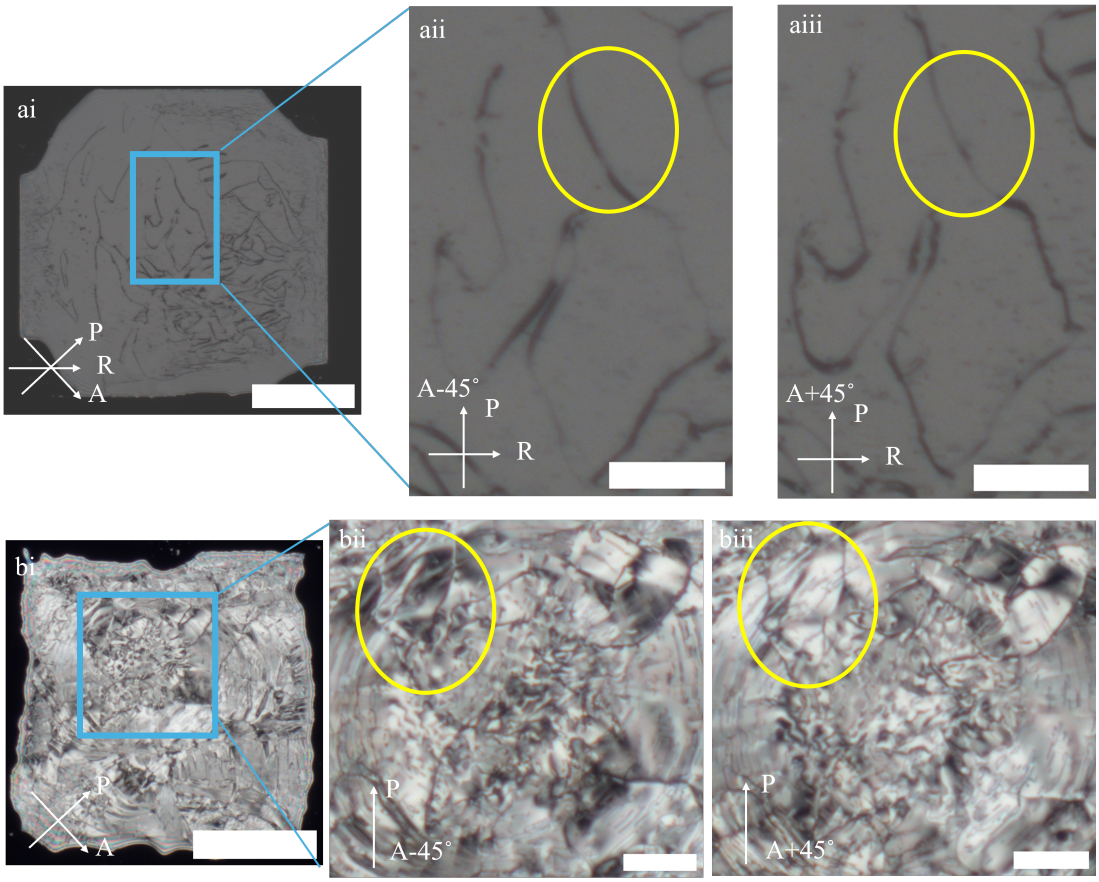

Figure 8.15: Transmission mode images of a second and third small FNLC-919 semi-droplet on *a:* rubbed or *b:* non rubbed surfaces. The analyser is untwisted with respect to crossed with a second polariser in *aii,aiii,bi,biii*, with different optical regions observed in the different conditions as circled in yellow as an example. P, A and R show the relative directions of the polariser, analyser and rubbing, respectively. The scale bars on *i* are 2mm, and on *ii,iii* are 0.5mm.

(Figure 8.14ai). The non-rubbed second small semi-droplet that was discussed in Section 8.3.4 is also imaged in the N_f phase as shown in Figure 8.15bi. In Figure 8.15, the analyser is untwisted from the crossed position with the other polariser. In one polarisation condition, regions of the walls appear dark which correspond to light areas in the alternate polariser condition i.e. between Figures 8.15aii vs. aiii and 8.15bii vs. biii, with examples circled in yellow. This implies the presence of twist, as explained in Section 3.3.4.

It is worth considering that the twist angle throughout the height of the semi-droplet may be different than the close to 180° in the FNLC-919, perpendicular domain example by Yu *et al.*[12]. A similar twisting effect is seen in other literature such as [27, 78, 80, 123, 124, 125] (although this is likely not an exhaustive list). Yu *et al.*[12] also discuss a cell with rubbing axes at 90° to each other, with a twist angle of 80° and no domains in the N_f phase. Discussion at the recent 19th Annual Conference on Ferroelectric Liquid Crystals 2025 implied that there is potential for rotations greater than 180°. Due to the large height of the small semi-droplets, predicted to be 80µm (compared to $\lesssim$ 20µm in the literature [12, 27, 78, 123, 125]), the small semi-droplet may support a larger twist throughout the height.

Qualitatively, if the director experiences a twist of 0° or 180°, the director in two adjacent twisted regions will align with each other at the air/FNLC interface, but antiparallel to the substrate, as is the case in Figure 8.14b. If the twist is 360°, the directors will align in both regions, and be parallel at both the substrate and air/FNLC interface. This is unlikely as it would require more twist so would be energetically unfavourable, as shown in Figure 8.16a (see Section 2.2.3). In either case, the aligned director means an aligned polarisation direction (see Section 2.3), therefore does not require a large energy cost. If the director experiences a twist of 90° or 270°, the directors (and hence polarisations, see Section 2.3) will be opposite to each other as shown schematically in Figure 8.16bi (assuming the twist is in opposite rotation directions). Regions of opposite polarisations are seen in some literature such as [11, 30, 31] (again likely not an exhaustive list). The regions would therefore likely be connected by a director that rotates

similarly to that shown in Figure 8.16bii. However, this is speculative and does not consider all of the intermediary twist angles, with further investigation into the exact twist left for future work.

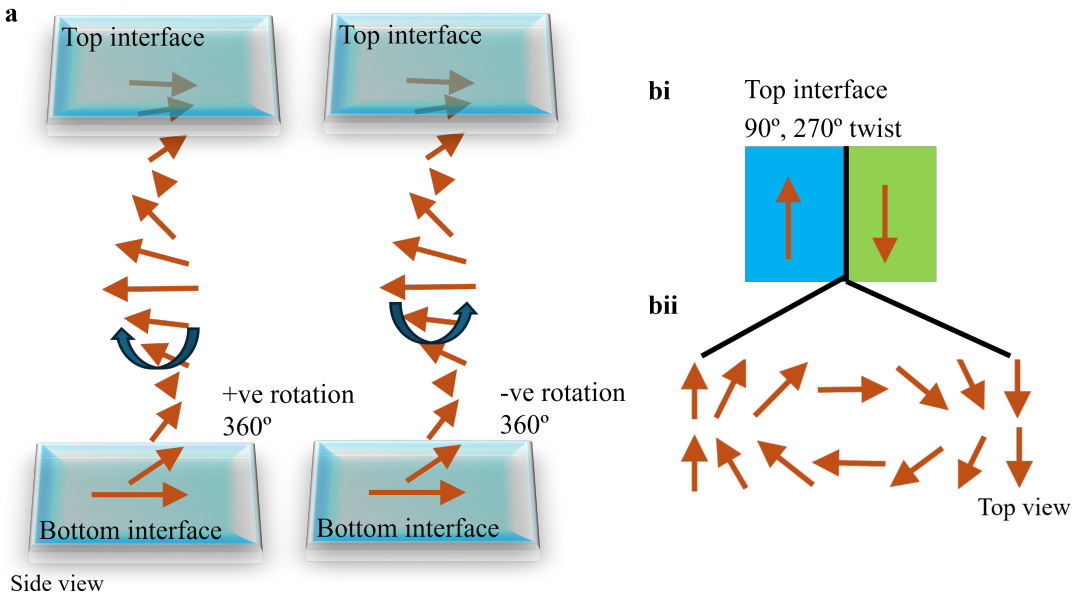

Figure 8.16: Schematics of different twist angles. *a:* A twist angle of 360° would be less energetically favourable than a 180° due to the added director distortion. *bi:* If the twist angle is 90° or 270°, and the directors rotate in opposite directions, the director (and hence polarisations, see Section 2.3) will be opposite to each other, with the domain wall director rotating in one of the ways as shown in *bii. bi and bii redrawn/ adapted from information in [11, 30, 31] and [30, 31], respectively.*

A reason for the perpendicularity of these domains with respect to the rubbing axis could also be tentatively described based off of the work by Máthé *et al.*[13]. It is discussed that on cooling for an RM 734 droplet, there are electric fields generated from both a flexoelectric and ferroelectric polarisation[13]. This, paired with the literature that observed domains perpendicular to the rubbing axis on addition of an electric field e.g.[11, 80], implies that the resultant director field could be related to an internal electric field. Fields in the semi-droplets could have a larger magnitude than seen by Máthé *et al.*[13], as larger height will induce a greater thermal gradient between the top and bottom of the semi-droplet

meaning there may be a greater magnitude of electric field (compared to the thermal gradient of approximately 23mK/μm[13]). The comparison to the work by Máthé *et al.*[13] comes with the caveat that RM 734 was dicussed in their work relative to a transition of N - N_f, not FNLC-919 over N - N_x - N_f.

An artefact circled in Figure 8.13a and reproduced in Figures 8.17ai,b demonstrates that the perpendicular domains end at an arrow-like point near the top and bottom edges of the small semi-droplets, but without intersection with the edge. This is similar to an artefact discussed by Marni *et al.*[30] for an RM734 sample, and are described as having 180° twist. Whilst some of these arrow-like points do contact with the sample edges in Marni *et al.*[30], this is not the case in this current work. For the director field in the current work after the first temperature cycle (Figure 8.13a, reproduced in Figure 8.17ai), the perpendicular domains terminate further from the edges in the y - axis ($y = \pm\frac{L}{2}$) the closer to the right-hand edge of the semi-droplet in the x - axis ($x = +d$) is approached, and end approximately halfway across the x - axis ($x \sim 0$) of the semi-droplet. This could provide evidence for inconsistent height in the N_f phase and/or a different twist angle.

There are two pieces of evidence implying that the height and/or twist angle of the small semi-droplet after the second temperature cycle is more consistent than after the first cycle (Figures 8.13b,a, reproduced in Figures 8.17aii,ai, respectively). Firstly, for the second cycle the arrow textures at the end of the domains continue over the majority of the semi-droplet width. Secondly, most of the domains align approximately perpendicular to the rubbing axis across the majority of the semi-droplet width for the second cycle instead of having a region equivalent to the purple circled area in Figure 8.13a, highlighted in Figure 8.17c. The purple region could have some other twist angle to those in the perpendicular domains, indicated as β in the schematic related to Figure 8.17c, as previously discussed (see Figure 8.16). The purple region could also indicate that the semi-droplet is thinner on the right hand side. A similar observation is presented for the free surface of AUUQU-2-N (from Merck)/DIO by Hedlund *et al.*[141], where on cooling one region of the sample has a height of approximately 100nm, com-

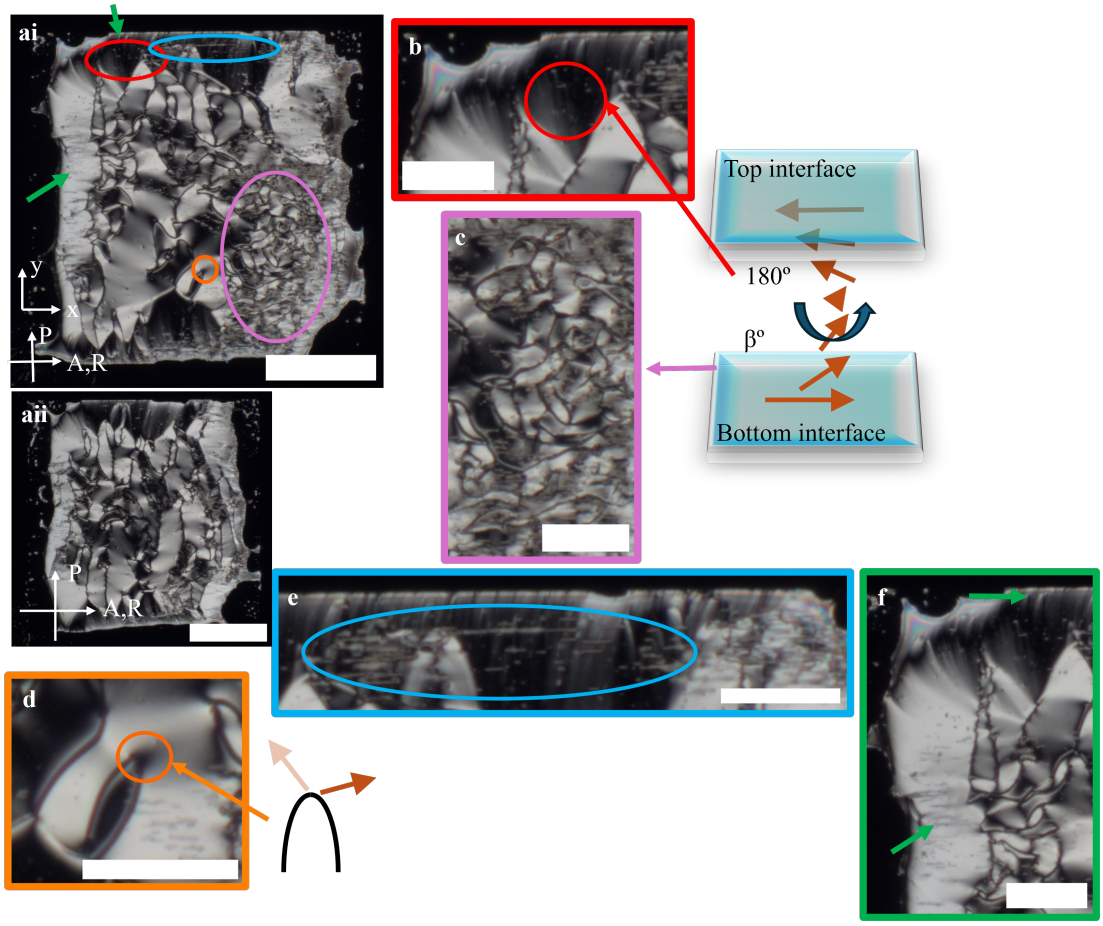

Figure 8.17: Highlighted regions of the *ai:* reproduced Figure 8.13a. *aii:* Reproduced Figure 8.13b for reference. P, A and R show the relative directions of the polariser, analyser and rubbing, respectively. The scale bar is 2mm. *b:* At the end of the perpendicular domains there are triangular points, likely approximately 180° twist regions. *c:* The domains that align approximately parallel to the rubbing axis could be from a β° twist angle. *d:* Dark regions are observed at the combination of the domain lines. *e:* Textures parallel to the rubbing axis. *f*: Brush-like textures parallel to the rubbing axis at the edge and perpendicular to it at the top of the semi-droplet. Schematics not to scale. The scale bars are 1mm. *b,c as well as d schematics redrawn and/or adapted from information in [12, 30] and [30]([31]), respectively.*

pared to another region at approximately 800nm in the N_f phase. A difference in height is also observed for FNLC-919 with a free air/FNLC interface by Perera *et al.*[14], as previously discussed in Section 2.3 (see Figure 2.7c).

A texture that is similarly observed in e.g.[30, 31] is circled in orange in Figure 8.13a and reproduced in Figure 8.17d, where the domain lines join. As expected, some evidence of a partially disrupted director field is observed[30] as highlighted by the arrows on the schematic.

Another interesting observation is the small lines at the top and bottom edges of the small semi-droplet, with an example circled in blue in Figure 8.13a and highlighted in Figure 8.17e. These align parallel to the rubbing axis as can likely be attributed to the greater proportion of anchoring on the bulk FNLC from the bounding surfaces, since it would be expected (assuming a similar shape to the NLC semi-droplets in Chapters 4 - 6) that the semi-droplet is less tall near the edge. However, this description is somewhat contradictory to the brush-like textures highlighted with green arrows at the top of the semi-droplet in Figure 8.13a and reproduced in 8.17f. These could also indicate the direction of the director throughout the height of the semi-droplet, however are generally instead approximately perpendicular to the rubbing axis near the top of the semi-droplet, and parallel near the edge.

Evidence of rotation of the observed director field textures with height is exhibited in the medium and large semi-droplets in Figures 8.18a,b, respectively. In the medium semi-droplet[1], the domains loosely align perpendicular to the rubbing axis, but with a slight curve in a reverse 'c'-shape. The texture of the large semi-droplet has fewer large domains, but more defect lines or small domains that have greater alignment with the rubbing axis than the small or medium semi-droplets, with guides to the eye marked in red. This could again be related to the magnitude of the induced internal electric fields on cooling as discussed earlier in this section with respect to the work by Máthé *et al.*[13] with a greater thermal

[1]It is worth noting that the medium semi-droplet was tilted more than usual after the first temperature cycle on movement to the imaging stage, however this should have minimal impact on the director field shown in Figure 8.18a.

gradient. Additionally, the effect of the anchoring from the substrate surface and air/FNLC interface will have less of an effect on the bulk FNLC for these larger semi-droplets. The uncertain rate of cooling near the N - N_f phase transition will also have an impact on how these director fields manifest. As discussed earlier in this section (see Figures 8.16 and 8.17c), there could be a different twist angle of the director, β, throughout the semi-droplet height. A similar rotation in the director field with height was also observed in the taller MLC 7023 semi-droplets in the non-rubbed samples from Chapter 6.

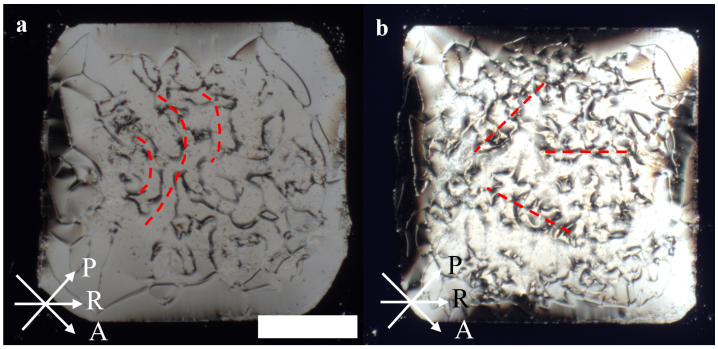

Figure 8.18: Transmission mode polarised images of the *a*: medium and *b*: large FNLC-919 semi-droplets after the second temperature cycle. The red dashed lines show an approximate shape of the domain structures. P, A, and R show the relative directions of the polariser, analyser and rubbing, respectively. The scale bars are 2mm.

8.4 Summary

The behaviour of FNLC-919 semi-droplets confined in chemically patterned 6 x 6mm squares has been discussed in this chapter, mostly in relation to a small semi-droplet with a predicted height of 80µm as it gave the clearest features during imaging. These investigations were taken as first attempt of confining FNLCs in millimetre-sized confinement structures as the majority of FNLC investigations are currently completed in cells or on ferroelectric surfaces. Therefore, the main focus of this chapter was not on future sensing devices as was the case for Chapters 4 - 7.

Firstly, the phase transition temperatures of the small, medium and large semi-droplets were measured. $\bar{T}_{\text{N-I}} = 83.1 \pm 0.5$°C was an overestimation of the expected 80°C[1], although it was unclear if the expected value was measured at the beginning or end of the biphasic transition region, and on heating or cooling. $\bar{T}_{\text{N-N}_\text{x}} = 44.0 \pm 0.3$°C and $\bar{T}_{\text{N}_\text{x}\text{-N}_\text{f}} = 31 \pm 1$°C were found to be in good agreement with the expected values of 44°C and 32°C, respectively.

The semi-droplet director fields were discussed over the phase transitions, with a main observations for the I - N transition the evidence of a disclination line similar to that observed in the N phase for the NLCs in Chapters 4 and 5. For the small semi-droplet, there is evidence of a potential defect with a strength of $\pm$ 1, and in the medium and large semi-droplets there is evidence of potential defects with strengths of $\pm \frac{1}{2}$. Over the N - N_x transition, there is a blue shift in the colours observed and possible evidence of strength = $\pm \frac{1}{2}$ defects, and the periodicity of the stripe textures were compared to the literature[14, 79]. Near the N_x - N_f transition, there are rotating stripe textures.

Some interesting observations were discussed, the first of which was the variation of Δn_{eff} over the N-phase on cooling, using the predicted height. This acted as expected[57], with a low order parameter (therefore lower Δn_{eff}) a few degrees after $T_{\text{I}\rightarrow\text{N}}$ (see Sections 2.2.1 and 3.3.5), before Δn_{eff} increasing and then becoming mostly constant at approximately 73°C. This was found to agree well with $\Delta n_{\text{eff}} = 0.1$, calculated for a temperature comfortably into the N phase, assuming a HAN director, and using n_{o} and n_{e} values from the literature[128]. Second, instabilities near the corners of the semi-droplet were attributed to the principle by Rayleigh[139], described also by e.g. Barboza *et al.*[82], based on a competition between surface tension and a build up of charge at the energetically unfavourable pointed corners. Thirdly, a discussion of the shrinkage behaviour of the small semi-droplet was presented where it was demonstrated graphically that there is a decrease in the width fraction over 50°C to 28°C of 0.09 $\pm$ 0.01. To verify that the shrinkage along the rubbing axis was related to the rubbing

[1]Expected FNLC-919 transition temperatures from Merck.

step of the surface fabrication, a small semi-droplet was formed on a non-rubbed surface and was found to shrink in all four axes.

Finally, a discussion of the N_f phase director field after cooling for the small semi-droplet in relation to a range of relevant literature was discussed, with the main observation being twisted domains that align approximately perpendicular to the rubbing axis, in contrast to what is most regularly observed in the literature of parallel domains. Height effects were observed where the main domain structures within the director fields were aligned in different directions with increasing semi-droplet height.

It is clear that this investigation was fruitful and has many more avenues of investigation as will be discussed in Section 9.2. However, this is a novel and exciting look into millimetre-sized confinement of FNLC-919 on a free surface, on a substrate different to those regularly used in the literature. It is clear that the NLC samples would be preferable for any sensing devices as they have far simpler director fields at room temperature, and their material properties are much better understood.

Chapter 9

Conclusions and Further Work

9.1 Conclusions

The primary motivation of this thesis has been to develop systems of millimetre-sized liquid crystal (LC) confinements with a free air/LC interface for LC-based sensing devices. These devices are expected to be able to detect analytes over a greater area, changes to the director field on addition of an analyte would be observable without polarised imaging, the surfaces would be reusable, and the confined LC samples would have a reasonable shelf life.

In Chapter 4[1], the well-known nematic liquid crystal (NLC), E7, was filled into chemically patterned rectangles with aspect ratios between 0.5 - 1, widths and lengths between 6 - 13mm and 6 - 20mm, respectively, and with maximum semi-droplet heights between approximately 20 - 420μm. A model to describe the semi-droplet cross-section was derived and validated by measurements using polarised imaging. An effective birefringence for the semi-droplets, $\Delta n_{\text{eff}} = 0.1$, was derived from assuming a hybrid aligned nematic (HAN) geometry of the NLC director from planar at the solid substrate to homeotropic at the air/NLC interface. The model and measurements agreed over the cross-sections provided that the semi-droplet had a height $\lesssim$ 50μm, regardless of the aspect ratio. The 6 x 6mm

[1] A significant portion of Chapter 4 is published in [1].

square filled with semi-droplets of heights between 125 - 290µm had the clearest director field for potential sensing devices and were the most symmetric across their width, therefore the following chapters focused on the 6 x 6mm squares. The main potential defects visible in the 6mm square semi-droplets had strengths of $+\frac{1}{2}$, with waveplate imaging suggesting an alignment of the director at the confinement edges parallel to the rubbing axis.

The homeotropic air/NLC interface for E7 is potentially non-ideal for providing a large contrast pre- and post-analyte addition in a sensing device, and would likely not be suitable for homeotropically-aligning analytes. Therefore, in Chapter 5 the NLC, MLC 7023, was filled into the squares as a non-homeotropic air/NLC interface had previously been indicated[15, 48]. Indeed, the measured tilt angle at the air/NLC interface was $\phi_{\text{max}} = 84°$, deduced from the measured $\Delta n_{\text{eff}} = 0.036 \pm 0.004$. Due to the much lower birefringence[1][49] and surface tension of MLC 7023 compared to E7[48], the MLC 7023 semi-droplets were measurable to a greater height (208µm compared to 125µm[1]), filled the confinements to a higher quality, and had symmetric width cross-sections to greater heights of $\lesssim$ 125µm compared to $\lesssim$ 50µm for E7. MLC 7023 semi-droplets with predicted heights between 21 - 125µm were identified as the preferable size of those measured for future sensing devices. For some taller MLC 7023 semi-droplets, potential defects with strengths of $\pm \frac{1}{2}$ were evidenced, and the waveplate imaging provided the same information as for the rubbed E7 semi-droplets, where the director is parallel to the rubbing axis near the confinement edges.

The chemically patterned surfaces investigated in Chapters 4 and 5 had a rubbed alignment layer, and were generally characterised by a disclination line approximately perpendicular to the rubbing direction. It was of interest in Chapter 6 to investigate E7 and MLC 7023 semi-droplets on non-rubbed planar substrates as in a real world application, removing the rubbing step would simplify fabrication. However, it was concluded that the non-rubbed surfaces result in far less simple director fields, including an increased difficulty in measuring the height of the cross-sections with polarised imaging. Common defects potentially observed had

[1]Merck data

strengths of +1, with the E7 and MLC 7023 semi-droplets divided into three and two categories, respectively, based on their director fields. Unlike for the rubbed samples, addition of a waveplate highlighted that the director at the edges of the squares was parallel to the confinement edges.

Throughout Chapters 4 - 6, the chemically patterned surfaces were reused by cleaning off the 'old' NLC using the relatively inexpensive and safe isopropanol, before refilling with 'new' NLC. In Chapter 7, this reusability and the shelf-life were quantified and compared to the N - I phase transition temperatures measured on heating for both NLCs confined within two untreated coverslips. It was concluded that the surfaces were reusable with E7 semi-droplets, and that E7 semi-droplets had a shelf-life of at least 14 days with resistance to changes under temperature cycles. The overall average transition temperatures, $\bar{T}_{\mathrm{N}\rightarrow\mathrm{I}} = 59.2 \pm 0.3$°C and $\bar{T}_{\mathrm{NI}} = 61.8 \pm 0.1$°C, were in good agreement with the measurements between coverslips. Additionally, a good agreement was found between this average and the transition temperatures measured for an E7 semi-droplet heated on a hot plate with no lid, which may be beneficial for batch producing samples.

For MLC 7023 semi-droplets undergoing three consecutive temperature cycles, a large uncertainty in the average of ± 2° was measured. However, the shelf-life was at least 16 days provided the sample did not undergo a temperature cycle with the average, $\bar{T}_{\mathrm{N}\rightarrow\mathrm{I}} = 80.7 \pm 0.2$°C and $\bar{T}_{\mathrm{NI}} = 83.6 \pm 0.2$°C, in good agreement with the coverslip measurements. The change to the samples observed on the MLC 7023 temperature cycles (where $\Delta T_{\mathrm{N}\rightarrow\mathrm{I}}$ and ΔT_{NI} was approximately 2°C) was discussed to be unlikely to have a significant impact on the MLC 7023 semi-droplets measured in Chapters 5 and 6, and to not have a greater effect when multiple semi-droplet samples experienced a temperature cycle on a single hot plate.

The availability of the relatively new ferroelectric nematic liquid crystal (FNLC) material, FNLC-919, provided an exciting opportunity to observe its confinement behaviours for three semi-droplet heights, labelled 'small', 'medium' and 'large', in the 6 x 6mm squares. The average transition temperatures on cooling for the N - $\mathrm{N_x}$ and $\mathrm{N_x}$ - $\mathrm{N_f}$ phase transitions, $\bar{T}_{\mathrm{N\text{-}N_x}} = 44.0 \pm 0.3$°C and $\bar{T}_{\mathrm{N_x\text{-}N_f}} = 31 \pm$

1°C, were in good agreement with their expected values of $T_{\text{N-N}_\text{x}} = 44°\text{C}$[1] and $T_{\text{N}_\text{x}\text{-N}_\text{f}} = 32°\text{C}$, respectively. There was less good agreement with the expected $\text{T}_{\text{I}\rightarrow\text{N}} = 80°\text{C}$ of $\bar{T}_{\text{N}\rightarrow\text{I}} = 83.1 \pm 0.5°\text{C}$, attributed to the quoted temperature in the literature potentially being at the end of the I - N transition on cooling (T_{IN}), or measured on heating. The textures near the phase transitions of the semi-droplets were discussed with a focus on the small semi-droplet, including the main visible possible defects, disclination lines in the N phase similar to those observed for the NLCs in Chapters 4,[1] and 5, and the stripe textures.

Other features were discussed for the small FNLC-919 semi-droplet including that at 64°C, when the semi-droplet was comfortably into the N phase (18.8°C from $T_{\text{I}\rightarrow\text{N}}$), $\Delta n_{\text{eff}} = 0.10 \pm 0.03$. This was validated using n_e and n_o values from the literature[128], and assuming a HAN director field to also result in $\Delta n_{\text{eff}} = 0.1$. The branched textures at the semi-droplet corners were attributed to a competition between charge and surface tension[82, 139]. The shrinkage behaviour of the small semi-droplet predominantly over the N_x phase was quantified as a 0.09 ± 0.01 fractional shrinkage between 50°C - 28°C, and was found to relate to the rubbing axis. Finally, the director field of the small semi-droplet in the N_f phase was compared to relevant literature, with the main feature being the twisted domains perpendicular to the rubbing axis.

The investigations summarised here have greatly developed the understanding of confinement of LCs in millimetre-sized chemically patterned surfaces with an air/LC interface. There are many further avenues of research that could be taken with some examples briefly discussed in Section 9.2.

9.2 Further Work

It is clear that there are multiple research directions in which further interesting and novel research could be completed on the topics discussed throughout this thesis. This section will present some ideas and how they relate to potential sensing devices or the understanding of LC confinement behaviours in general.

[1] Expected FNLC-919 transition temperatures from Merck.

Further characterisation of the chemically patterned surfaces could be undertaken to refine the resulting surface. For example, ellipsometry[142] could be completed on the thin film layers of the surface as it can be used to measure the layer height and homogeneity. Contact angle measurements of E7, MLC 7023 and FNLC-919 on each of the layers would benefit the understanding of the patterned surface also.

A potential extension from Chapter 4 is to optimise the device configurations further by obtaining a more optimal square size around the 6 x 6mm used throughout this thesis, especially as there is a large difference between the 6 x 6mm and 11 x 11mm sizes.

To further develop Chapter 5, MLC 7023 semi-droplets could be formed in the other confinement sizes from Chapter 4 including the 11 x 11mm square as well as the 16 x 13mm and 10 x 20mm rectangles. This would be motivated by the generally improved filling quality of MLC 7023 semi-droplets compared to E7 semi-droplets observed in Chapter 5, which suggest there may be a more optimum confinement size for MLC 7023. Additionally, it was shown for MLC 7023 semi-droplets with predicted heights $\gtrsim 208\mu m$ that the predicted interface angle was likely $\gtrsim 10^{\circ}$, hence it may be possible to measure the angles directly without large uncertainties for the tall semi-droplets. Therefore, it may also be the case for the tall E7 semi-droplets that the angles could be directly measured.

Whilst it is clear in Chapter 6 that the non-rubbed 6 x 6mm squares are less ideal than the rubbed samples for potential future sensing devices, it is possible that confinement shapes with a different aspect ratio could form a disclination line closer to what was observed for the rubbed samples. In Bao *et al.*[15] there is no rubbing, however approximately central defect patterns were observed for their E7 and MLC 7023 stripes with a much greater length than width. For example, rectangles with a lower aspect ratio than the 0.5 minimum measured in this thesis may allow for the removal of the rubbing step without compromising on the simplicity of the director field, however Chapter 4,[1] concluded that rectangular confinements are less preferable to square ones.

An alternative origin for the dark brushes under the crossed polariser rotation in Chapters 4 - 6 was discussed in relation to work by Tsakonas *et al.*. A next step to validate if the dark brushes are from defects or not is to form squares with the same geometry as in this work, but without rubbing and within a cell, to allow a more direct comparison to their work.

A natural next step for Chapter 7 would be to validate the reusability of the surface with MLC 7023 and FNLC-919 semi-droplets. Whilst there is no significant evidence of the degradation of the surfaces with MLC 7023, there was some evidence that the surfaces are less reusable with FNLC-919. For example, to produce a second 'small' FNLC-919 semi-droplet with a similar director field to the one discussed most in Chapter 8, a newly fabricated surface was required.

Further investigations to identify the origin and effect of the 'misting' observed on the temperature cycles for the MLC 7023 semi-droplets as discussed in Chapter 7 would be beneficial. Such investigations might include comparing the results in Chapters 5 - 7 to a fresh batch of MLC 7023, or quantifying the change in the phase transition temperatures over the whole semi-droplet height range investigated.

Chapter 8 has left more unanswered questions than can be suggested here, as research into ferroelectric nematic liquid crystals (FNLCs) is a relatively new topic within the LC community. A very recent publication in December 2025 by Paul *et al.*[79] has characterised many properties about FNLC-919, and therefore it would be interesting to further link some of the properties in that work[79] to the semi-droplet behaviour. Further research into the branched structures observed at the edges of the semi-droplets would aid understanding of the associated electrostatic properties and the surface tension behaviours of FNLC-919. For example, different curvatures at the square confinement corners could be fabricated to evaluate if this has any effect on the instabilities. A more in-depth study of the semi-droplet shrinkage behaviour for both the rubbed and non-rubbed surfaces over more repeats would build a clearer image of the mechanisms that cause the shrinkage. In some cases, mostly observed on heating, the FNLC-919 semi-droplets grew to form a more perfectly filled square, which was an interesting

observation that could be investigated further.

Development of the imaging system to allow transmission mode images to be able to be taken over a greater than 2mm field of view whilst also heating or cooling the semi-droplet would develop the information gained from the FNLC-919 semi-droplets further.

A key next step in the development of the semi-droplets is to test them as sensors, beginning with readily available analytes such as sodium dodecyl sulphate (SDS), demonstrated in references such as [17] to promote radial (perpendicular to the interface) anchoring on LC-droplets. This would be completed using the MLC 7023 semi-droplets due to their non-homeotropic air/NLC interface, with the systems analysed for their stability and detection limit as are common metrics in LC-based sensing literature.

Of the examples discussed in Section 2.5.2, the most stable example had a shelf-life of upwards of four months by stabilisation of the droplets using a polyacrylamide hydrogel[109]. The semi-droplets in this work have potential to have a shelf-life of greater than 14 or 16 days as the measurements in Chapter 7 for E7 and MLC 7023 did not show significant signs of change over this time period. Therefore, a next step could be to measure the shelf-life of the E7, MLC 7023 and FNLC-919 semi-droplets for greater than 14 and 16 days, to evaluate if a shelf life greater than or equal to four months is achievable. The free surface NLC semi-droplets are sensitive to dust and tilting, therefore similar structures with a greater mechanical stability could be developed using techniques such as polymer stabilisation of the NLC[143] within the chemically patterned surface. Some preliminary work has been completed on polymer stabilisation as is discussed briefly in Figure A.20, although this can be challenging to get a good coverage of the polymer network over the millimetre-sized free surfaces.

In Section 2.5.3, a range of LC-based sensing systems and related sensitivities were briefly summarised, including choosing a hydrogel[112], use of microgels[17], surfactants[108], and droplet doping[113]. Similar techniques could be adapted into the semi-droplet system presented here to improve upon the sensitivity.

It is expected that the large surface area of the semi-droplets means that it is more likely for an analyte to come into contact with it, however it could also result in less effective LC-based sensor systems. For example, changes in the director field could be slower or require more analyte due to the increased amount of NLC that a change initiated by an analyte has to propagate through. Therefore, further optimisation of the confinement sizes and NLC dispense volumes with this in mind would be beneficial.

There are many other aspects of the semi-droplet systems that could be considered with respect to sensing applications. However, it is clear that the systems discussed in this work have shown good potential as LC-based sensing devices, with clear director fields pre-analyte addition, and parameters starting to be optimised. These semi-droplets have aspects that lend themselves to sustainability as well as time and money efficiency. Examples include the reusability with the relatively cheap isopropanol, the ability to have multiple semi-droplets undergo a temperature cycle at once, and that an E7 semi-droplet can undergo a temperature cycle without a hot plate lid. The fabrication process could also easily be made more efficient, for example designing a photomask with the chosen confinement size repeated across it to allow for batch patterning of the surfaces during photolithography. In addition to this potential for sensing, more doors have been opened into research on general LC confinement research, in particular with FNLCs.

Appendix A

Supplementary Information

Please note some of this chapter is published in A. Bond *et al.* (2025). The behaviour of nematic liquid crystals in chemically patterned millimetre-sized rectangular surfaces. *Liquid Crystals*. pp 1-15. https://doi.org/10.1080/02678292.2025.2489426[1]. Figures that have been taken or adapted from [1] are marked in the relevant captions.

A.1 Appendix for Chapter 3

A.1.1 Bespoke Photomask

The shapes and sizes of the bespoke photomask (Figure 3.5) is presented in the list below, with L the length of the rectangles and $2d$ the width. There is a minimum 2.8mm of empty space around a shape to ensure that LC does not enter an adjacent region of patterning.

Rectangles: L = 60mm with 2d between 0.005mm - 16mm (9 sizes)
L = 20mm with $2d$ between 2.5mm - 16mm (6 sizes)
L = 16 mm with $2d$ of 11mm & 13mm (2 sizes)
$2d$ = 1.2mm with L between 0.005mm - 60mm (16 sizes)

Squares: L,$2d$ = 0.01mm - 16mm (6 sizes)

Circles: Diameter = 0.01mm - 15mm (12 sizes)

A.1.2 Code to Align Images for Figures

```
#Temperatures to include in the figure
numbers_include=[83,82.5,82,81]

#Extension of the images to be included
image_extension='.png'

#How many columns of images to form in the figure
number_columns=4

#Name of the resulting figure
filename="Demonstrate the code.png"

#Quality and transparency of the figure
quality=1200
transparent_choice=True

#Labelling information
label_colour='red'
label_fontsize=8
unit='$^\circ$C'
label_position=(25,200)

#Spacing of the images to remove white spaces/overlaps
width_spacing=0
height_spacing=0
```

Figure A.1: Annotated options for the code written to efficiently align images measured under increasing height. The user saves the images as the corresponding temperature and includes them in a list in the code. The code inserts the images, aligns them, and labels them. This could easily be adapted for use in, for example, increasing voltage. The whole code is not included here.

A.2 Appendix for Chapter 4

A.2.1 Contact Angle

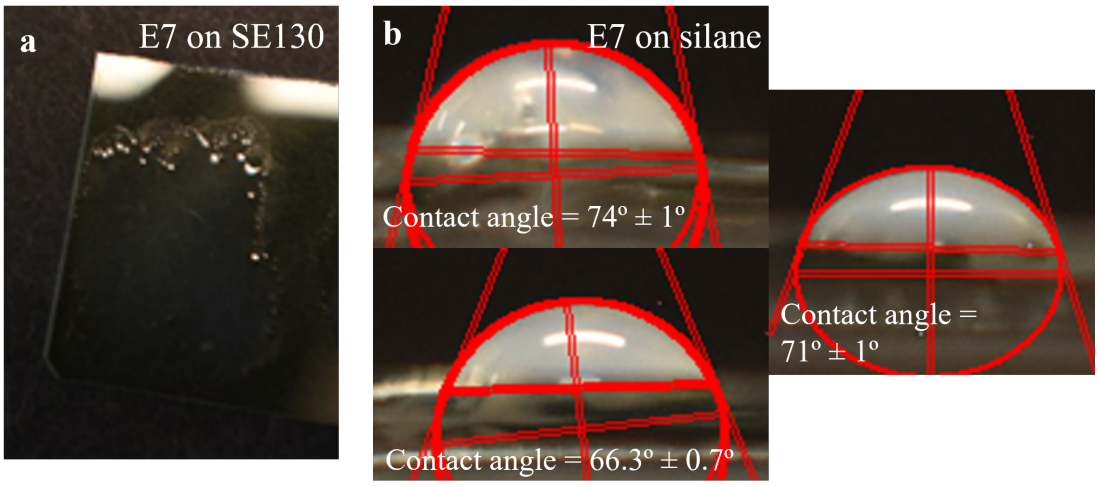

Figure A.2: Droplet of E7 on homogeneous SE130 polyimide or silane to measure the contact angle. *Images included in DOI of [1].*

A.2.2 Additional Polarised Images

NLC Volume, V/µL	7 ± 0.01*	9 ± 0.01*	13 ± 0.1*
Measured height, h/µm	80 ± 8	101 ± 9	-
Predicted height, h/µm	87 ± 3	112 ± 4	161 ± 6
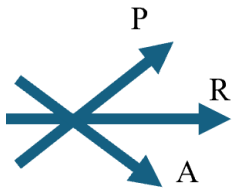	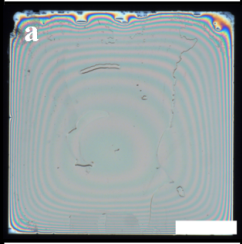	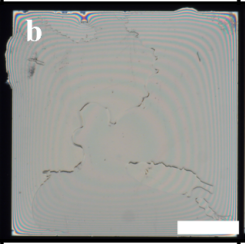	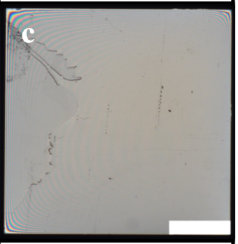
NLC Volume, V/µL	15 ± 0.1*	20 ± 0.1*	25 ± 0.1*
Measured height, h/µm	-	-	-
Predicted height, h/µm	186 ± 6	248 ± 7	310 ± 10
	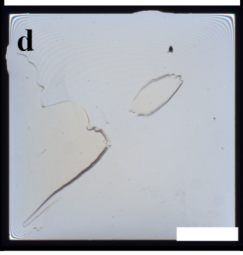	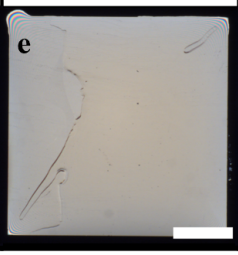	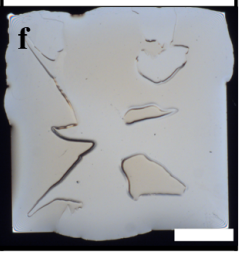

Figure A.3: Varying NLC 'semi-droplet' volumes confined in 11 x 11 mm squares on chemically patterned surfaces with a rubbed alignment layer on a solid substrate and an NLC/air interface. Maximum heights measured using pink birefringent fringes are compared to those predicted heights from the presented models from calculation of the semi-droplet cross-sectional area ($V = AL$), leading to predictions of ϵ (Equation 4.2), interface angle (Equation 4.7) and finally, height (Equation 4.6). The rubbing direction is at 45° to the crossed polarisers, with arrows marked P, A and R to show the relative directions of the polariser, analyser and rubbing respectively. The scale bars are 3mm. (*): Only rubbing axis known, but number of fringes counted to measure the height if clear fringes are present. The cropping of the images was varied to ensure that the field of view required to capture all the information (e.g any overflowing liquid crystal) is retained while maximising the image visibility. *Image adapted from supplementary information in [1].*

NLC Volume, V/µL	11 ± 0.1	15 ± 0.1*	20 ± 0.1*	25 ± 0.1
Measured height, h/µm	80 ± 8	101 ± 9	-	-
Predicted height, h/µm	79 ± 3	108 ± 4	144 ± 6	180 ± 6
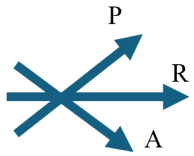	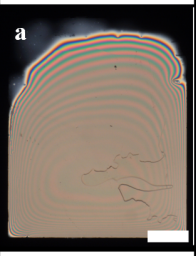	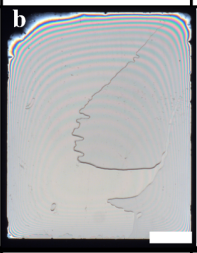		
NLC Volume, V/µL	10 ± 0.1	12.5 ± 0.1		
Measured height, h/µm	-	-		
Predicted height, h/µm	75 ± 5	94 ± 6		
				

Figure A.4: Varying NLC 'semi-droplet' volumes confined in rectangles of *a-d:* 16 x 13mm; *e,f* 20 x 10mm, on chemically patterned surfaces with a rubbed alignment layer on a solid substrate and an NLC/air interface. Maximum heights measured using pink birefringent fringes are compared to those predicted heights from the presented models from calculation of the semi-droplet cross-sectional area ($V = AL$), leading to predictions of ϵ (Equation 4.2), interface angle (Equation 4.7) and finally, height (Equation 4.6). The rubbing direction is at 45° to the crossed polarisers, with arrows marked P, A and R to show the relative directions of the polariser, analyser and rubbing respectively. The scale bars are 3mm. (*): Only rubbing axis known, but number of fringes counted to measure the height if clear fringes are present. The cropping of the images was varied to ensure that the field of view required to capture all the information (e.g any overflowing liquid crystal) is retained while maximising the image visibility. *Image adapted from supplementary information in [1].*

A.2.3 Code to Fit to Measured Heights

```
#Import required modules
import numpy as np
import matplotlib.pyplot as plt
from scipy.optimize import curve_fit

#d = 3000um
def cousins(x,area):
    return (((3*area)*((3000**2)-x**2))/(4*(3000**3))) #Equ. 4.1
def ab(x,angle):
    eta=(1-(((x*np.sin(angle))/3000)**2))**(-1/2) #Inverse of alpha in Equ. 4.5
    return 3000*((1/(np.sin(angle)*eta))-(1/np.tan(angle))) #Equ. 4.5
x_model=np.linspace(-3000,3000,50) #50 data points between -d to d

#Call in the data
def get_data_x(filename):
    distance=np.genfromtxt(filename,skip_header=1,usecols=0)
    distance_uc=np.genfromtxt(filename,skip_header=1,usecols=1)
    height=np.genfromtxt(filename,skip_header=1,usecols=2)
    height_uc=np.genfromtxt(filename,skip_header=1,usecols=3)
    return np.array([distance,distance_uc,height,height_uc])

#Plot the data
#Fit the models to the data and plot the models
def plot_data(data,style1,style2,colour,label1,label2,label3):
    plt.errorbar(data[0],data[2],xerr=data[1],yerr=data[3],
                 fmt=style1,color=colour,label=label1)
    x_model=np.linspace(-3000,3000,50)
    popt1,pcov1=curve_fit(cousins,(data[0]*10**3),data[2],sigma=data[3])
    popt2,pcov2=curve_fit(ab,(data[0]*10**3),data[2],sigma=data[3])
    plt.errorbar((x_model*10**(-3)),cousins(x_model,popt1[0]),xerr=0,yerr=0,
                 fmt=style2,color=colour,label=label2)
    plt.errorbar((x_model*10**(-3)),ab(x_model,popt2[0]),xerr=0,yerr=0,
                 fmt='k-',label=label3)


#Form the plot skeleton
plt.figure(dpi=2400)
plt.xlabel("x/$mm$",fontsize='large')
plt.ylabel("Height/$\mu m$",fontsize='large')

#Plot the data with optional labels
sample1_data_x=get_data_x('sample1x.txt')
plot_data(sample1_data_x,'x','o','r','Fringes: V1$\mu L$','Cousins Model','AB Model')

sample2_data_x=get_data_x('sample2x.txt')
plot_data(sample2_data_x,'x','o','#78cd72','Fringes: V2$\mu L$','Cousins Model','AB Model')

sample3_data_x=get_data_x('sample3x.txt')
plot_data(sample3_data_x,'x','o','c','Fringes: V3$\mu L$','Cousins Model','AB Model')

#Add guide lines at x=0 and edges
plt.vlines(0,0,75,linestyles='dashed',colors='k')
plt.vlines(-3,-10,75,colors='k')
plt.vlines(3,-10,75,colors='k')
#plt.legend(fontsize='xx-small')
```

Figure A.5: Annotated code to fit the measured height across the semi-droplet cross-section widths.

A.2.4 Additional Crossed Polariser Rotation

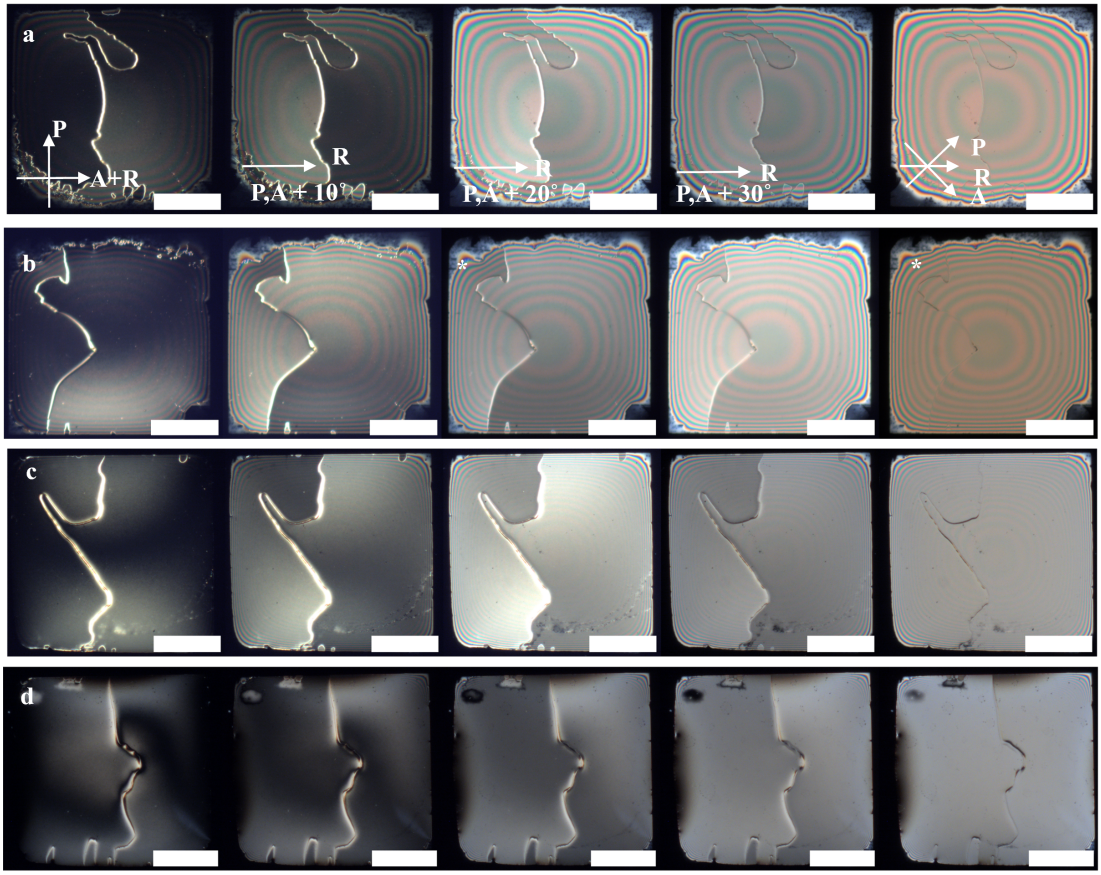

Figure A.6: Rotation of crossed polarisers through 0° - 45° with respect to the rubbing direction of E7 semi-droplets with predicted heights: *a:* 42µm, *b:* 75µm, *c:* 125µm, *d:* 208µm. P, A and R show the relative directions of the polariser, analyser and rubbing direction, respectively. The scale bars are 2mm. The * indicates where the imaging exposure was known to be adjusted to preserve the quality of the images.

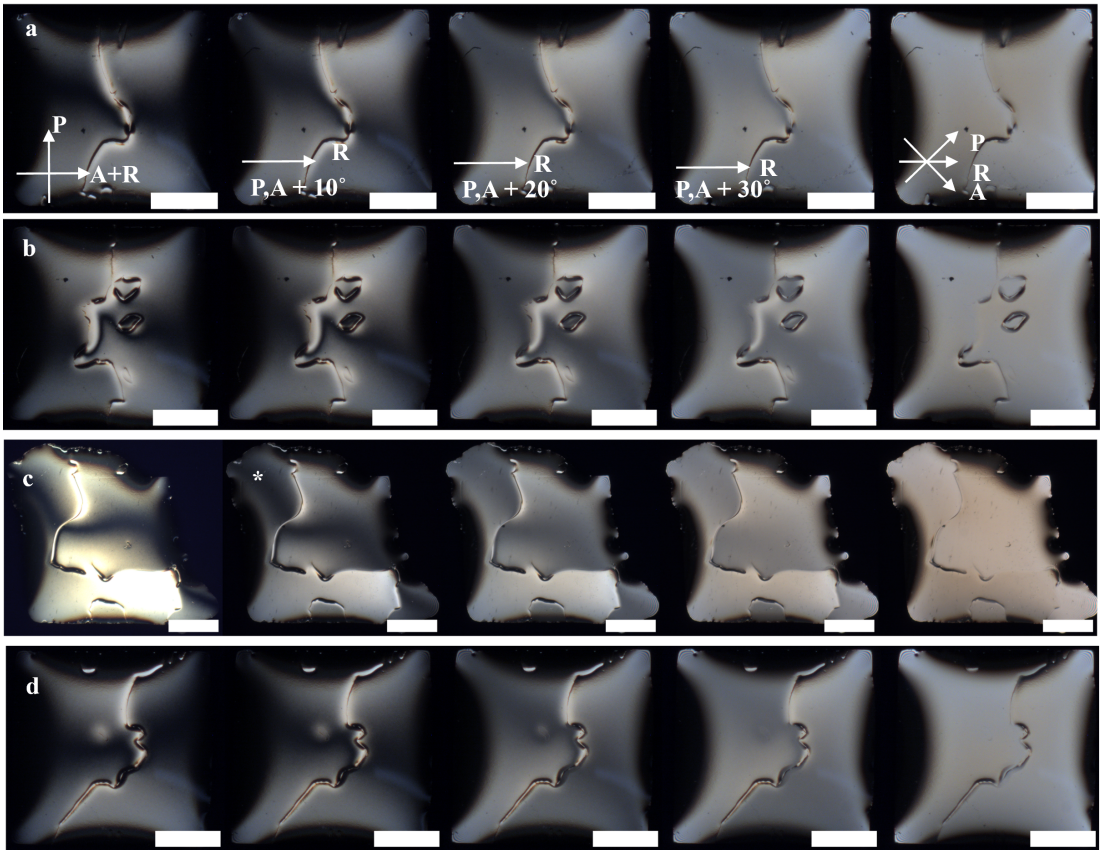

Figure A.7: Rotation of crossed polarisers through 0° - 45° with respect to the rubbing direction of E7 semi-droplets with predicted heights: *a:* 290µm, *b:* 330µm, *c:* 380µm, *d:* 420µm. P, A and R show the relative directions of the polariser, analyser and rubbing direction, respectively. The scale bars are 2mm. The * indicates where the imaging exposure was known to be adjusted to preserve the quality of the images.

A.3 Appendix for Chapter 5

A.3.1 Additional Polarised Images

NLC Volume, V/µL	1.5 ± 0.01	2 ± 0.01	4 ± 0.01	6 ± 0.01
Measured height, h/µm	60 ± 20	90 ± 20	180 ± 30	265 ± 40
Predicted height, h/µm	63 ± 3	83 ± 3	167 ± 7	250 ± 10

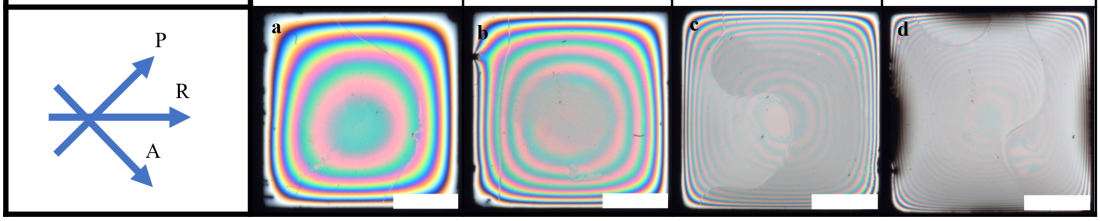

Figure A.8: Polarised light imaging of varying MLC 7023 semi-droplet volumes confined in 6mm chemically patterned squares with a rubbed alignment layer on a solid substrate and an air/NLC interface. Maximum heights measured using pink birefringent fringes are compared to the those predicted from calculation of the semi-droplet cross-sectional area ($V = AL$), leading to predictions of ϵ (Equation 4.2), interface angle (Equation 4.7) and finally, height (Equation 4.6). P, A and R show the relative directions of the polariser, analyser and rubbing, respectively. The scale bars are 2mm. The cropping of the images was varied to ensure that the field of view required to capture all the information (e.g. any overflowing liquid crystal) is retained while maximising the image visibility).

A.3.2 Code for Tilt Angle

```
#Import necessary functions
import numpy as np
import matplotlib.pyplot as plt
from scipy.integrate import quad


#Define ne and no
no=1.46
ne=1.53
#Define a function to calculate effective birefringence
def neff_integration(x):
    angle_rad=np.radians(((theta_max_single-2)*x)+2) #Equ. 5.1
    return ((ne*no)/((((ne*np.sin(angle_rad))**2)+
                     ((no*np.cos(angle_rad))**2))**(1/2)))-no #Equ. 3.6 & 3.7

#Changing air/LC interface angle between 2-90 degrees in 10000 steps
theta_max=np.linspace(2,90,10000)
integral_list=[]
#integrate over the 10000 maximum air/LC interface angles
for theta_max_single in theta_max:
    integral_list.append(quad(neff_integration,0,1)[0])

integral_array=np.array(integral_list)
#Find absolute difference between expected and calculated neff
integral_difference=abs(integral_array-0.036)
integral_diff_list=integral_difference.tolist()
#Identifying the calculated neff closest to expected
lowest=integral_diff_list.index(min(integral_diff_list))
print('theta_max that agrees most with neff=0.036: ',
      theta_max[lowest],'degrees, with an neff= ',integral_list[lowest])
```

Figure A.9: Annotated code to calculate the air/NLC interface tilt angle of the MLC 7023 semi-droplets, based on a comparison of Δn_{eff} calculated for 10000 air/NLC angles with the expected $\Delta n_{\text{eff}} = 0.036$.

A.3.3 Effective Birefringence

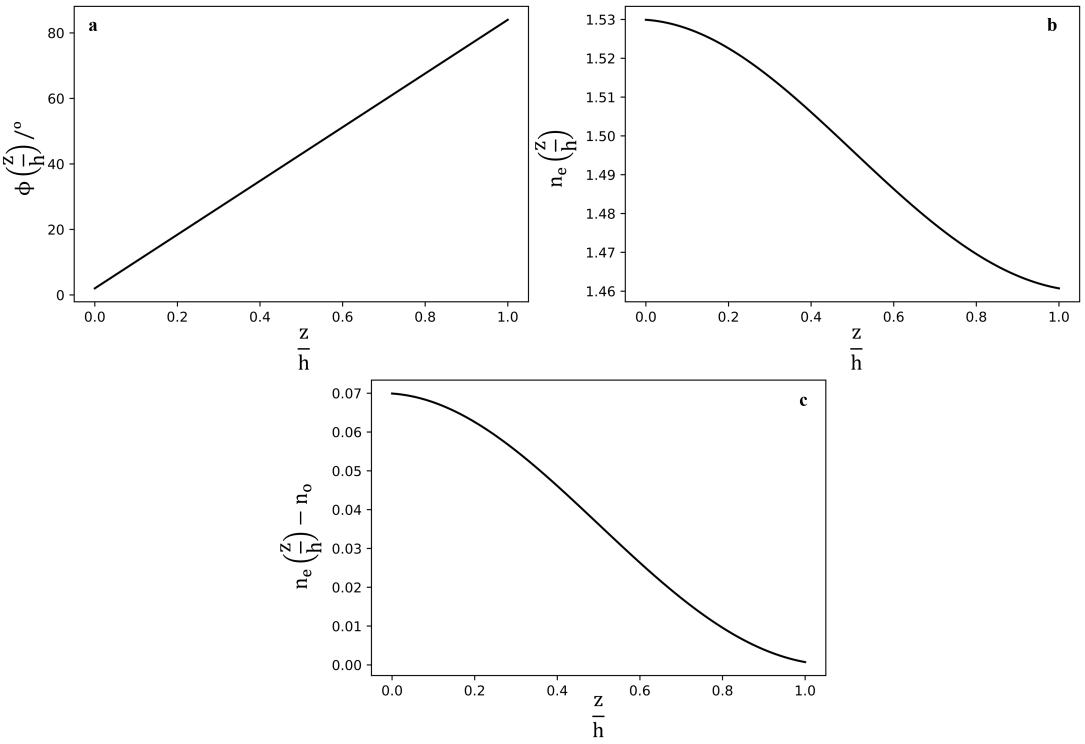

Figure A.10: Plots through the dimensionless height of the MLC 7023 semi-droplet, $\frac{z}{h}$, of *a:* director angle, ϕ, *b:* extraordinary refractive index, n_e, and *c:* $n_e(\frac{z}{h}) - n_o$, where n_o is the ordinary refractive index. *Image adapted from supplementary information in [1].*

A.3.4 Additional Crossed Polariser Rotations

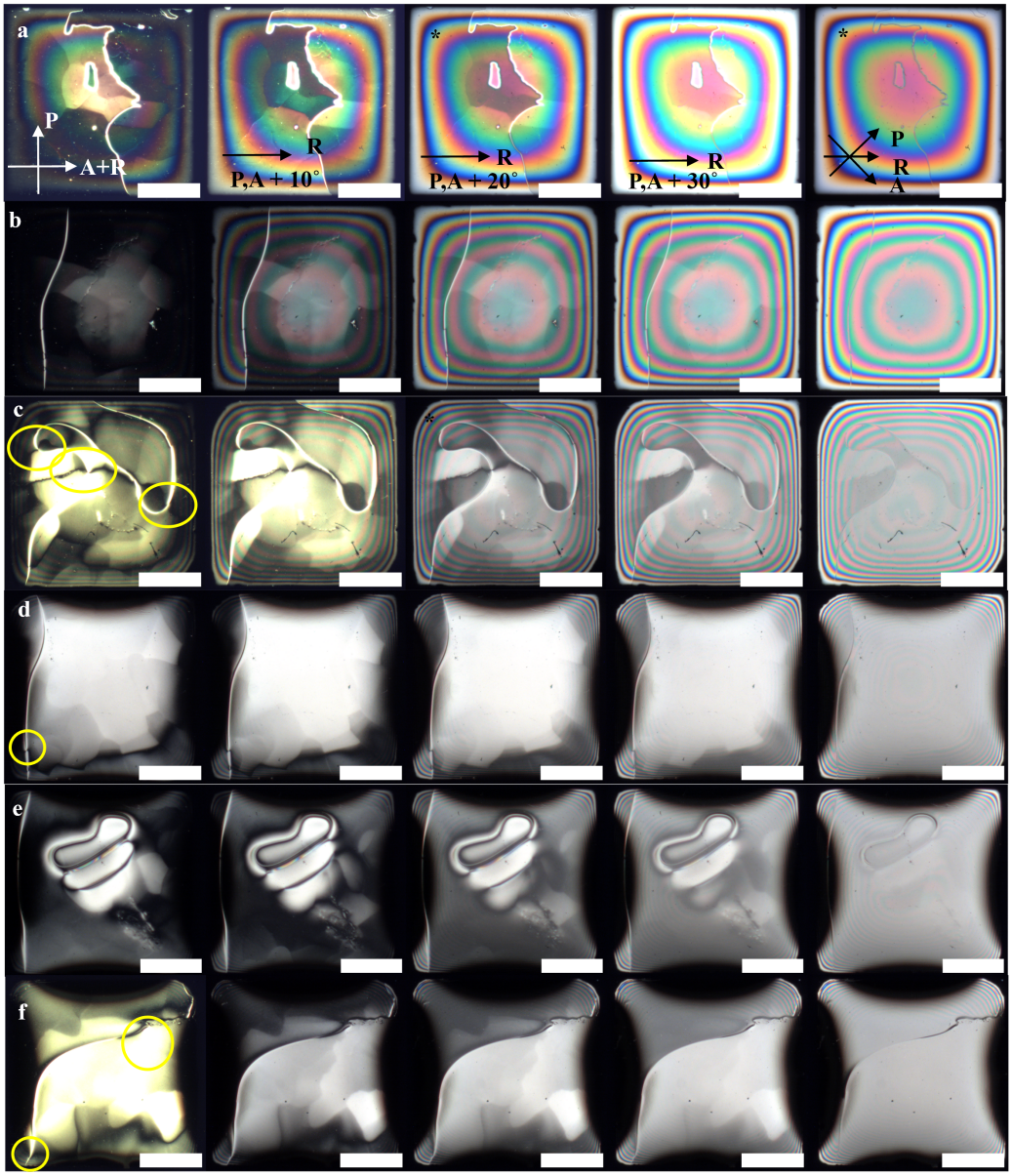

Figure A.11: Rotation of crossed polarisers through 0° - 45° with respect to the rubbing direction of MLC 7023 semi-droplets with predicted heights: *a:* 42µm, *b:* 75µm, *c:* 125µm, *d:* 290µm, *e:* 330µm, *f:* 420µm. P, A and R show the relative directions of the polariser, analyser and rubbing direction, respectively. The scale bars are 2mm. The * indicates where the imaging exposure was known to be adjusted to preserve the quality of the images. The yellow circles in *c,d,f* indicate examples of potential origins of possible strength $= \pm\frac{1}{2}$ defects.

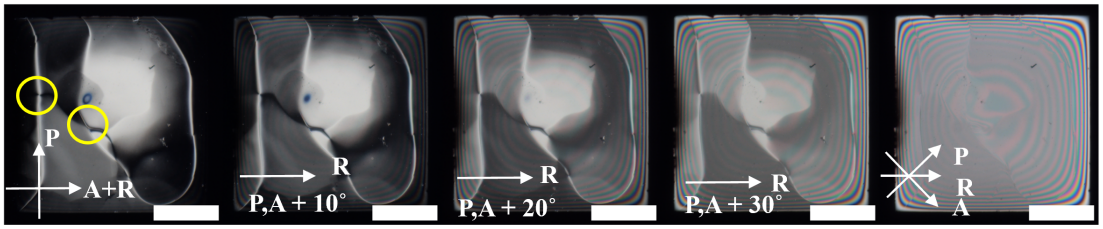

Figure A.12: Rotation of crossed polarisers through 0° - 45° with respect to the rubbing direction of a MLC 7023 semi-droplet with a predicted height = 208μm. P, A and R show the relative directions of the polariser, analyser and rubbing direction, respectively. The scale bars are 2mm. The yellow circles indicate examples of potential origins of possible strength = $\pm\frac{1}{2}$ defects.

A.4 Appendix for Chapter 6

A.4.1 Additional Crossed Polarisers Rotation

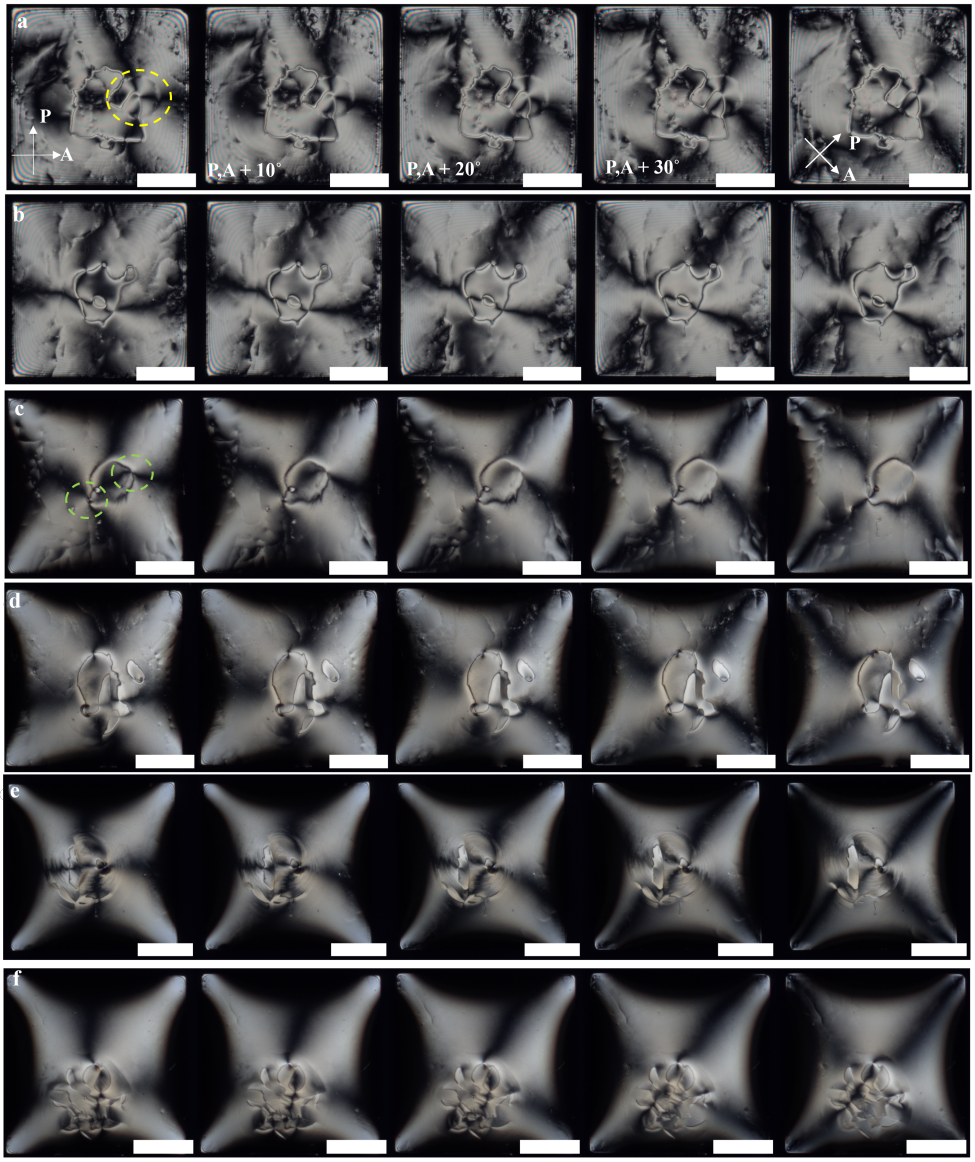

Figure A.13: Rotation of crossed polarisers through 0° - 45° with respect to the rubbing direction of E7 semi-droplets with predicted heights: *a:* 75µm, *b:* 125µm, *c:* 208µm, *d:* 290µm, *e:* 330µm, *f:* 380µm. P and R show the relative directions of the polariser and analyser, respectively. The scale bars are 2mm. The yellow circle in *a* represents the origin of the potential strength = +1 defect. The green circles in *c* represent the origins of possible strength = $\pm \frac{1}{2}$ defects.

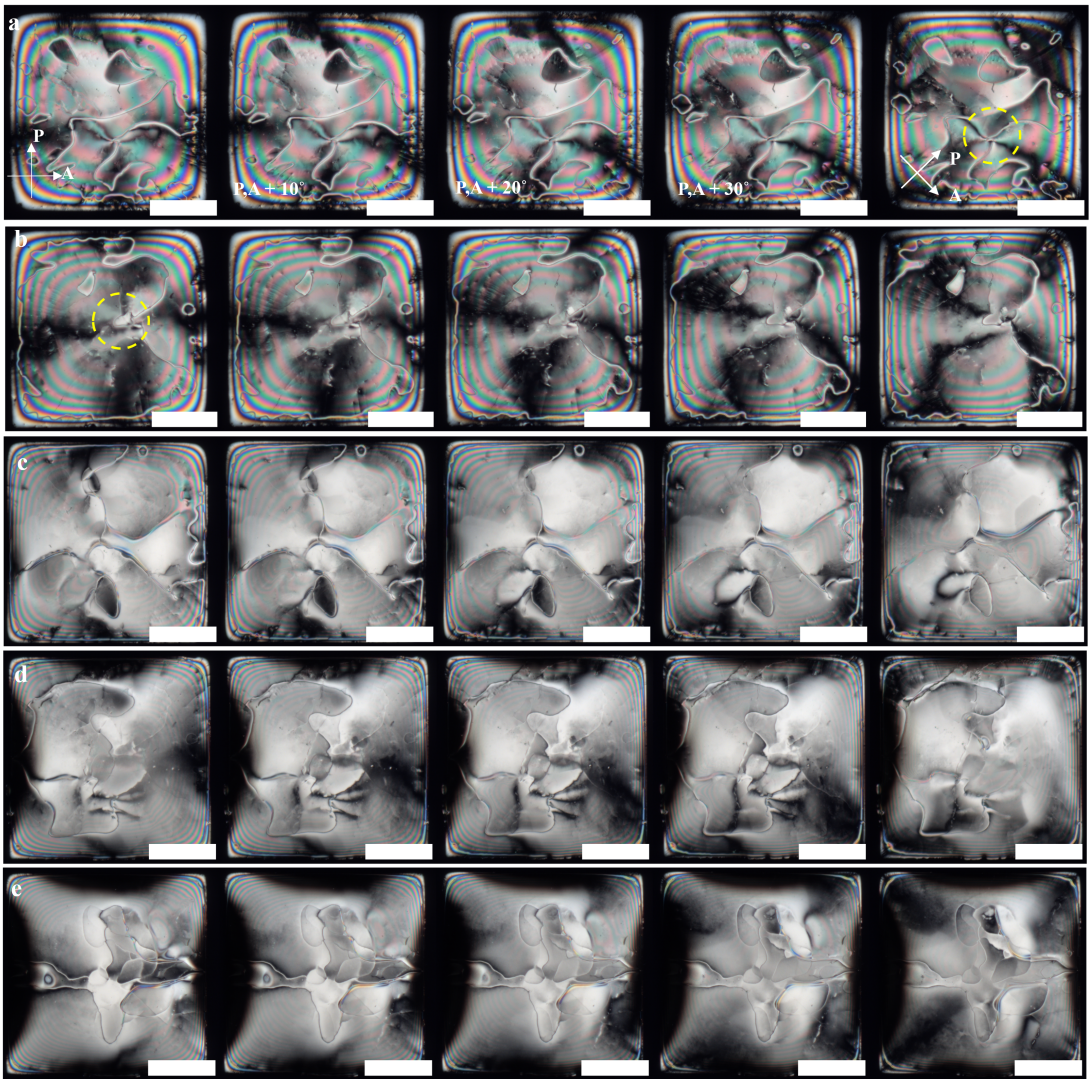

Figure A.14: Rotation of crossed polarisers through 0° - 45° with respect to the rubbing direction of MLC 7023 semi-droplets with predicted heights: *a:* 75µm, *b:* 125µm, *c:* 208µm, *d:* 290µm, *e:* 330µm. P and R show the relative directions of the polariser and analyser, respectively. The scale bars are 2mm. The yellow circles in *a,b* represent the origins of the possible strength = +1 defect.

A.5 Appendix for Chapter 7

A.5.1 E7 Semi-Droplet Heating

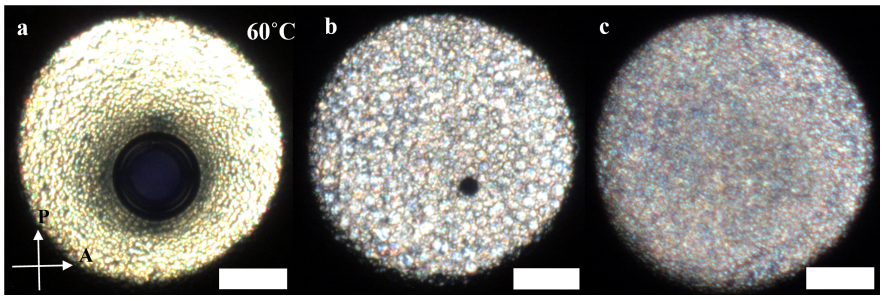

Figure A.15: Polarised images of a single E7 semi-droplet with predicted height = 208μm for three heating and cooling cycles, imaged at 60°C on heating. P and A show the relative positions of the polariser and analyser, respectively. The scale bars are 0.5mm.

A.5.2 MLC 7023 'Misting' Investigations

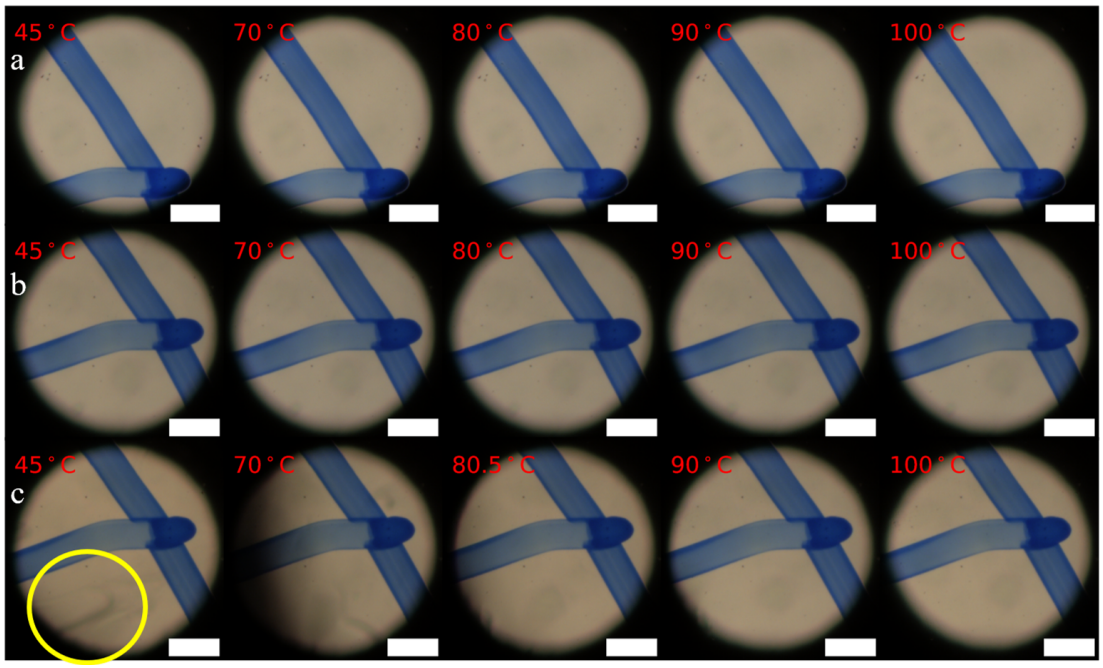

Figure A.16: Images of a hot plate heated to 100°C at 10°Cmin^{-1}. The hot plate was cleaned with IPA and a shape was drawn onto the window prior to heating with *a:* no sample, *b:* three chemically patterned surfaces or a *c:* MLC 7023 sample with a free surface, on the hot plate. The images in *c* shown most sign of additional blurriness, with an example circled in yellow. The scale bars are 0.5mm. The movement of the image drawn onto the window is a result of the exact positioning of the window over the imaging hole in the hot plate. Imaged with no polarisers. Improvement of this investigation to further understand the effect of the 'misting' is saved for future work.

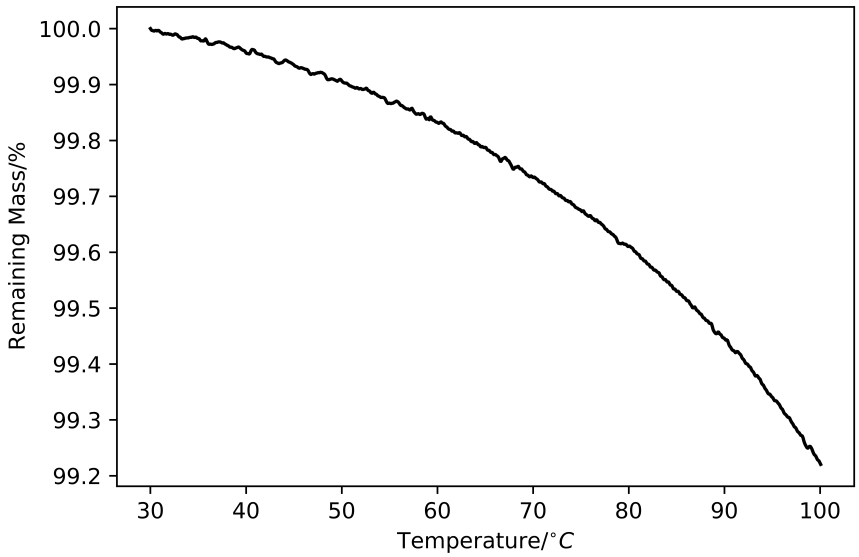

Figure A.17: Thermogravimetric analysis of MLC 7023 between 30°C and 100°C, normalised to the mass at 30°C. The heating rate was 10°Cmin^{-1}. There is a minimal change over this temperature range of 0.8%. *Data taken by Thomas Raistrick.*

A.6 Appendix for Chapter 8

A.6.1 Transition Temperatures

(a)			
Semi-droplet	$\mathbf{T_{I\rightarrow N}}$/°C Reflection	$\mathbf{T_{I\rightarrow N}}$/°C Tranmission	**Average** $\mathbf{T_{I\rightarrow\ N}}$/°C
Small	82.8 ± 0.3	82.1 ± 0.4	82.5 ± 0.4
Medium	83.3 ± 0.3	82.7 ± 0.1	83.0 ± 0.3
Large	84.0 ± 0.5	83.8 ± 0.3	83.9 ± 0.5
Average			**83.1 ± 0.5**

(b)			
Semi-droplet	$\mathbf{T_{N\text{-}N_x}}$/°C Reflection	$\mathbf{T_{N\text{-}N_x}}$/°C Tranmission	**Average** $\mathbf{T_{N\text{-}\ N_x}}$/°C
Small	43.9 ± 0.1	43.8 ± 0.3	43.9 ± 0.3
Medium	43.8 ±0.3	43.8 ± 0.3	43.8 ± 0.3
Large	44.3 ± 0.3	44.3 ± 0.3	44.3 ± 0.3
Average			**44.0 ± 0.3**

(c)			
Semi-droplet	$\mathbf{T_{N_x\text{-}N_f}}$/°C Reflection	$\mathbf{T_{N_x\text{-}N_f}}$/°C Tranmission	**Average** $\mathbf{T_{N_x\text{-}\ N_f}}$/°C
Small	29.8 ± 0.3	32 ± 0.5	31 ± 1
Medium	30.8 ± 0.3	31.8 ± 0.3	31.3 ± 0.5
Large	29.8 ± 0.3	31.8 ± 0.3	31 ± 1
Average			**31 ± 1**

Table A.1: Transition temperatures of small, medium and large FNLC-919 semi-droplets measured on cooling, imaged in reflection and transmission mode. The third column is the average of the two imaging modes, with the number in bold the overall average. *a:* $T_{\mathrm{I\rightarrow N}}$. *b:* $T_{\mathrm{N\text{-}N_x}}$. *c:* $T_{\mathrm{N_f\text{-}N_x}}$

A.6.2 Semi-Droplet Movies

The movies for the FNLC-919 semi-droplets can be obtained on request from the author. The names are as follows:

Movie 1	Small semi-droplet heat and cool. Reflection.
Movie 2	Small semi-droplet heat and cool. Transmission.
Movie 3	Medium semi-droplet heat and cool. Reflection.
Movie 4	Medium semi-droplet heat and cool. Transmission.
Movie 5	Large semi-droplet heat and cool. Reflection.
Movie 6	Large semi-droplet heat and cool. Transmission.
Movie 7	Non- rubbed small semi-droplet heat and cool. Reflection.

A.6.3 Effective Birefringence

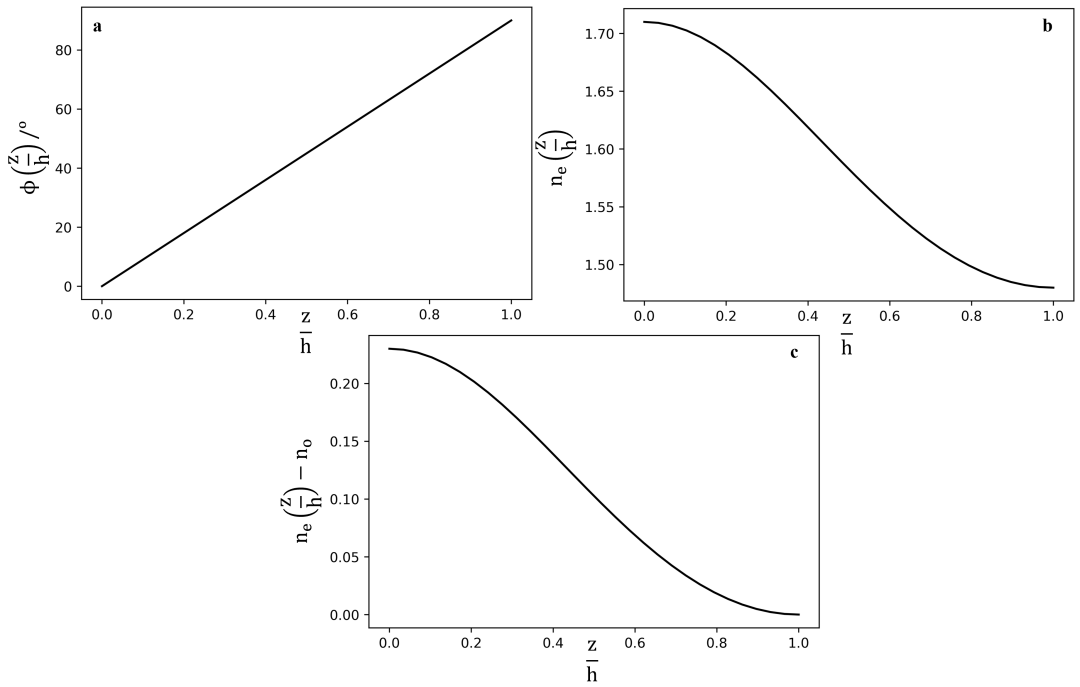

Figure A.18: Plots through the dimensionless height of the FNLC-919 semi-droplet, $\frac{z}{h}$, of *a:* director angle, ϕ, *b:* extraordinary refractive index, n_{e}, and *c:* $n_{\mathrm{e}}(\frac{z}{h}) - n_{\mathrm{o}}$, where n_{o} is the ordinary refractive index. *Image adapted from supplementary information in [1].*

A.6.4 E7 Semi-Droplet

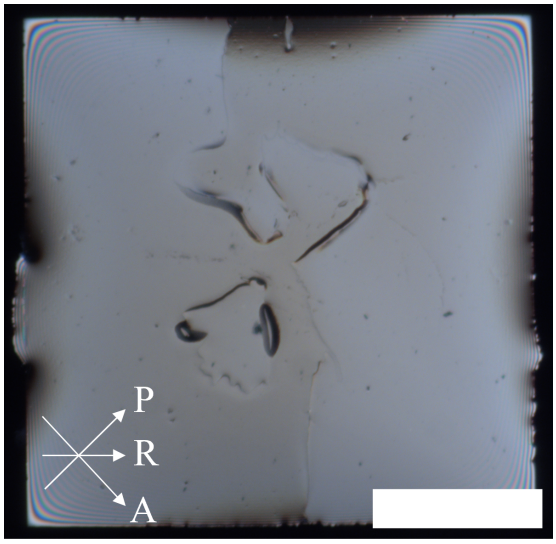

Figure A.19: Polarised image of an E7 semi-droplet with predicted height = 208µm to qualitatively evaluate the reusability of the patterned surfaces after use with FNLC-919. P, A and R show the relative directions of the polariser, analyser and rubbing, respectively. The scale bar is 2mm.

A.7 Appendix for Chapter 9

A.7.1 Polymer Stabilisation

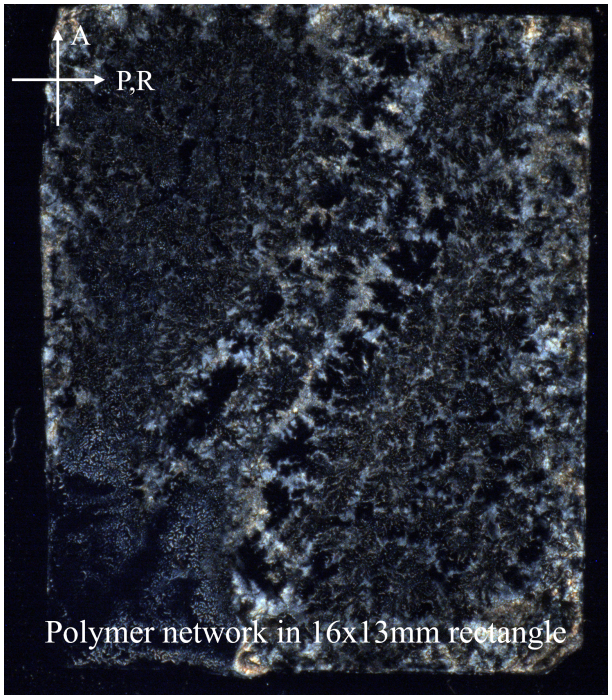

Figure A.20: Polymer network in a 16 x 13mm rectangle with a free surface. A sample of E7 was polymer stabilised before the E7 was washed out of the network with IPA. Further details are beyond the scope of this thesis, and are left for future work. P, A and R show the relative direction of the polariser, analyser and rubbing, respectively.

References

[1] A. Bond, T. Moorhouse, S.A. Peyman, and H.F. Gleeson. The behaviour of nematic liquid crystals in chemically patterned millimetre-sized rectangular surfaces. *Liquid Crystals*, pages 1–15, 2025. https://doi.org/10.1080/02678292.2025.2489426. ii, xxi, xxii, xxiv, xxv, xxvi, xxvii, xxviii, xxix, xxxi, xxxii, xxxvi, xxxix, xlii, xliii, xliv, xlvi, 2, 5, 15, 21, 22, 23, 25, 26, 31, 39, 40, 41, 45, 48, 51, 54, 55, 56, 57, 59, 60, 77, 82, 83, 84, 86, 89, 91, 95, 96, 99, 101, 105, 112, 113, 148, 150, 167, 168, 170, 171, 175, 177, 178, 179, 185, 194

[2] D. Dunmur, (Handbook eds)J.W. Goodby, P.J. Collings, T. Kato, C. Tschierske, H.F. Gleeson, and P. Raynes. *Volume 2 (Physical Properties and Phase Behavior of Liquid Crystals), Chapter 3 (Optical properties of liquid crystals)*. Handbook of Liquid Crystals. Boschstr. 12, 69469 Weinheim, Germany: Wiley-VCH Verlag & Co. KGaA, Second edition, 2014. xix, 6, 7

[3] P.J. Collings and J.W. Goodby. *Introduction to Liquid Crystals. Chemistry and Physics. Chapter 1 (Welcome to a delicate and special phase of matter)*. Boca Raton, Florida: CRC Press, Second edition, 2019. xix, xx, 6, 7, 10

[4] D-K. Yang and S-T. Wu. *Fundamentals of Liquid Crystal Devices. Chapter 1 (Liquid crystal physics)*. Wiley-SID Series in Display Technology. The Atrium, Southern Gate, Chichester, West Sussex, PO19 8SQ, England: John Wiley & Sons Ltd, 2006. xix, xx, 6, 9, 10, 25

[5] E. Hecht. *Optics. Chapter 8 (Polarization).* Global edition. Fifth edition, 2017. Edinburgh Gate, Harlow, Essex, CM20 2JE, England: Pearson Education. xix, xxii, 7, 8, 32, 34, 41

[6] P.J. Collings and J.W. Goodby. *Introduction to Liquid Crystals. Chemistry and Physics, Chapter 3 (Nature's anistropic fluids - it's all about direction).* Boca Raton, Florida: CRC Press, Second edition, 2019. xix, xx, 9, 11, 18, 34

[7] B. Broughton, (Handbook eds)J.W. Goodby, P.J. Collings, T. Kato, C. Tschierske, H.F. Gleeson, and P. Raynes. *Volume 2 (Physical Properties and Phase Behavior of Liquid Crystals), Chapter 9 (Surface alignment of liquid crystals).* Handbook of Liquid Crystals. Boschstr. 12, 69469 Weinheim, Germany: Wiley-VCH Verlag & Co. KGaA, Second edition, 2014. xx, 10

[8] D-K. Yang and S-T. Wu. *Fundamentals of Liquid Crystal Devices. Chapter 12 (Tunable liquid crystal photonic devices).* Wiley-SID Series in Display Technology. The Atrium, Southern Gate, Chichester, West Sussex, PO19 8SQ, England: John Wiley & Sons Ltd, 2006. xx, 10

[9] J.E. Lydon, H. Gleeson, and E.I.L. Jull. The identification of the sign and strength of disclinations in the schlieren (nucleated domain) texture of the nematic phase, by optical microscopy. *Liquid Crystals*, 44(12-13):1775–1786, 2017. xx, xxiii, 11, 34, 35, 36

[10] Q. Liao, S. Aya, and M. Huang. Review of emergent polar liquid crystals from material aspects. *Liquid Crystals Reviews*, 12(2):149–194, 2024. xx, 12

[11] X. Chen, E. Korblova, D. Dong, X. Wei, R. Shao, L. Radzihovsky, M.A. Glaser, J.E. Maclennan, D. Bedrov, D.M. Walba, and N.A. Clark. First-principles experimental demonstration of ferroelectricity in a thermotropic nematic liquid crystal: polar domains and striking electro-optics. *Proceedings of the National Academy of Sciences of the United States of America*, 117(25):14021–14031, 2020. xx, xli, 12, 156, 159, 160

[12] J-S. Yu, J.H. Lee, J-Y. Lee, and J-H. Kim. Alignment properties of a ferroelectric nematic liquid crystal on the rubbed substrates. *Soft Matter*, 19(13):2446–2453, 2023. xx, xxiv, xl, xli, 12, 13, 14, 37, 38, 42, 131, 156, 157, 159, 162

[13] M.T. Máthé, Á. Buka, A. Jákli, and P. Salamon. Ferroelectric nematic liquid crystal thermomotor. *Physical Review E*, 105(5):L052701, 2022. xx, 13, 14, 140, 141, 143, 146, 151, 155, 160, 161, 163

[14] K. Perera, A. Alyami, A. Adaka, M.S.H. Himel, N. Haputhanthrige, O.D. Lavrentovich, E. Mann, and A. Jákli. Self-assembled biconvex microlens array using chiral ferroelectric nematic liquid crystals. *Advanced Optical Materials*, 12(32):2401507, 2024. xx, 13, 14, 38, 42, 138, 140, 141, 145, 149, 155, 163, 165

[15] P. Bao, D.A. Paterson, S.A. Peyman, J.C. Jones, J.A.T. Sandoe, R.J. Bushby, S.D. Evans, and H.F. Gleeson. Textures of nematic liquid crystal cylindric-section droplets confined by chemically patterned surfaces. *Crystals*, 11(1):65, 2021. xx, 3, 15, 16, 17, 38, 42, 45, 62, 64, 78, 81, 84, 96, 168, 171

[16] X. Zhan, Y. Liu, K-L. Yang, and D. Luo. State-of-the-art development in liquid crystal biochemical sensors. *Biosensors*, 12(8):577, 2022. xx, 1, 11, 17, 18

[17] S. Aery, A. Parry, A. Araiza-Calahorra, S.D. Evans, H.F. Gleeson, A. Dan, and A. Sarkar. Ultra-stable liquid crystal droplets coated by sustainable plant-based materials for optical sensing of chemical and biological analytes. *Journal of Materials Chemistry. C*, 11(17):5831–5845, 2023. xx, 18, 19, 173

[18] W-M. Munief, F. Heib, F. Hempel, X. Lu, M. Schwartz, V. Pachauri, R. Hempelmann, M. Schmitt, and S. Ingebrandt. Silane deposition via gas-phase evaporation and high-resolution surface characterization of the ultrathin siloxane coatings. *Langmuir*, 34(35):10217–10229, 2018. xxi, xxii, 22, 28, 29

[19] G. Nabil, W.F. Ho, and H.P. Chan. Experimental study on the performance of a variable optical attenuator using polymer dispersed liquid crystal. *Applied Optics*, 52(22):E15–E21, 2013. xxi, 22

[20] D.J. Lipomi and R.S. Ramji. *Introduction to Nanoengineering. Chapter 12 (Generation of nanostructures 1: top-down approaches)*. Burlington House, Piccadilly, London, W1J 0BA, UK: The Royal Society of Chemistry, 2024. xxi, 23, 24

[21] A.C. Mendhe, (Book eds)B.R. Sankapal, A. Ennaoui, R.B. Gupta, and C.D. Lokhande. *Simple Chemical Methods for Thin Film Deposition. Synthesis and Applications. Chapter 9 (Spin coating: easy technique for thin films)*. 2023. 152 Beach Road, #21-01/04 Gateway East, Singapore 189721, Singapore: Singer Nature Singaport Pte Ltd. xxi, 23, 24

[22] D.J. Lipomi and R.S. Ramji. *Introduction to Nanoengineering. Chapter 7 (Advanced functional polymers: photoresists, semiconductors, actuators, and biomaterials)*. Burlington House, Piccadilly, London, W1J 0BA, UK: The Royal Society of Chemistry, 2024. xxi, 25, 26

[23] Thermo Fisher Scientific Inc. 1H,1H,2H,2H-perfluorooctyltrichlorosilane, 97%, 2006-2026. [Online]. Last accessed 18 January 2026. Available from: https://www.thermofisher.com/order/catalog/product/L16606.09. xxii, 28

[24] A.P. Amalathas, M.M. Alkaisi, and (Book ed)J. Thirumalai. *Micro/Nanolithography - A Heuristic Aspect on the Enduring Technology. Chapter 2 (Fabrication and replication of periodic nanopyramid structures by laser interference lithography and UV nanoimprint lithography for solar cells applications)*. The Shard, 25th floor, 32 London Bridge Street, London, SE19SG-United Kingdom: IntechOpen, 2018. xxii, 28, 29

[25] T. Scharf. *Polarized Light in Liquid Crystals and Polymers. Chapter 7 (Practical polarization optics with the microscope)*. Hoboken, New Jersey & Canada: John Wiley & Sons, Inc., 2007. xxii, xxiii, 8, 30, 32, 33, 34

[26] B. Sørensen. A revised Michel-Lévy interference colour chart based on first-principles calculations. *European Journal of Mineralogy*, 1, 2013. xxiii, 33, 34

[27] P. Kumari, B. Basnet, M.O. Lavrentovich, and O.D. Lavrentovich. Chiral ground states of ferroelectric liquid crystals. *Science*, 383(6689):1364–1368, 2024. xxiv, 13, 37, 38, 156, 159

[28] A. Mertelj, L. Cmok, N. Sebastián, R.J. Mandle, R.R. Parker, A.C. Whitwood, J.W. Goodby, and M. Čopič. Splay nematic phase. *Physical Review X*, 8(4):041025, 2018. xxxviii, 140, 141

[29] N. Sebastián, L. Cmok, R.J. Mandle, M.R. de la Fuente, I.D. Olenik, M. Čopič, and A. Mertelj. Ferroelectric-ferroelastic phase transition in a nematic liquid crystal. *Physical Review Letters*, 124(3):037801, 2020. xxxviii, 140, 141

[30] S. Marni, F. Caimi, R. Barboza, N. Clark, T. Bellini, and L. Lucchetti. Fluid jets and polar domains, on the relationship between electromechanical instability and topology in ferroelectric nematic liquid crystal droplets. *Soft Matter*, 20(25):4878–4885, 2024. xli, 150, 156, 159, 160, 161, 162, 163

[31] B. Basnet, M. Rajabi, H. Wang, P. Kumari, K. Thapa, S. Paul, M.O. Lavrentovich, and O.D. Lavrentovich. Soliton walls paired by polar surface interactions in a ferroelectric nematic liquid crystal. *Nature Communications*, 13:3932, 2022. xli, 38, 156, 159, 160, 162, 163

[32] B. Bahadur. Liquid crystal displays. *Molecular Crystals and Liquid Crystals*, 109(1):3–93, 1984. 1

[33] M. Schadt. Liquid crystal materials and liquid crystal displays. *Annual Review of Materials Research*, 27:305–379, 1997. 1

[34] H. Kawamoto. The history of liquid-crystal displays. *Proceedings of the IEEE*, 90(4):460–500, 2002. 1

[35] R.H. Chen. *Liquid Crystal Displays: Fundamental Physics and Technology*. Wiley-SID Series in Display Technology. Hoboken, New Jersey and Canada: John Wiley & Sons, Inc., 2011. 1

[36] S. Kobayashi, T. Miyama, H. Akiyama, A. Ikemura, and M. Kitamura. Development of liquid crystal displays and related improvements to their performances. *Proceedings of the Japan Academy, Series B, Physics and Biological Sciences*, 98(9):493–516, 2022. 1

[37] Y-J. Wang, P-J. Chen, X. Liang, and Y-H. Lin. Augmented reality with image registration, vision correction and sunlight readability via liquid crystal devices. *Scientific Reports*, 7:433, 2017. 1

[38] J.R. Talukder, Y. Huang, and S-T. Wu. High performance LCD for augmented reality and virtual reality displays. *Liquid Crystals*, 46(6):920–929, 2019. 1

[39] K. Yin, E-L. Hsiang, J. Zou, Y. Li, Z. Yang, Q. Yang, P-C. Lai, C-L. Lin, and S-T. Wu. Advanced liquid crystal devices for augmented reality and virtual reality displays: principles and applications. *Light: Science & Applications*, 11:161, 2022. 1

[40] A. Zia, S. Saeed, T. Man, H. Liu, C.X. Chen, and Y. Wan. Next-generation interfaces: integrating liquid crystal technologies in augmented and virtual reality – a review. *Liquid Crystals Reviews*, 12(1):30–56, 2024. 1

[41] S-H. Lee, S-G. Park, J-S. Ma, W-S. Kim, and S-W. Oh. High-performance switchable visor for augmented reality using low-voltage, fast-response cholesteric liquid crystals. *Dyes and Pigments*, 243:113068, 2025. 1

[42] H. Wang, T. Xu, Y. Fu, Z. Wang, M.S. Leeson, J. Jiang, and T. Liu. Liquid crystal biosensors: principles, structure and applications. *Biosensors*, 12(8):639, 2022. 1

[43] (eds)A.P.H.J. Schenning, G.P. Crawford, and D.J. Broer. *Liquid Crystal Sensors*. The Liquid Crystals Book Series. Boca Raton, Fl: CRC Press, 2017. 1, 17

[44] S.A. Oladepo. Development and application of liquid crystals as stimuli-responsive sensors. *Molecules*, 27(4):1453, 2022. 1

[45] I. Pani, S. Sil, and S.K. Pal. Liquid crystal biosensors: a new therapeutic window to point-of-care diagnostics. *Langmuir*, 39(3):909–917, 2023. 1

[46] V.K. Gupta, J.J. Skaife, T.B. Dubrovsky, and N.L. Abbott. Optical amplification of ligand-receptor binding using liquid-crystals. *Science*, 279(5359):2077–2080, 1998. 1, 7, 17

[47] A.A. Parry. *The Design of Novel Liquid Crystal Droplets for Biosensing Devices*. PhD thesis, University of Leeds, 2023. 1, 18

[48] D.A. Paterson, P. Bao, R.H. Abou-Saleh, S.A. Peyman, J.C. Jones, J.A.T. Sandoe, S.D. Evans, H.F. Gleeson, and R.J. Bushby. Control of director fields in phospholipid-coated liquid crystal droplets. *Langmuir*, 36(23):6436–6446, 2020. 3, 38, 42, 50, 78, 81, 84, 90, 93, 96, 97, 99, 168

[49] H. Allinson and H.F. Gleeson. Physical properties of mixtures of low molar mass nematic liquid crystals with photochromic fulgide guest dyes. *Liquid Crystals*, 14(5):1469–1478, 1993. 3, 39, 42, 47, 82, 96, 99, 116, 127, 168

[50] (Handbook eds)J.W. Goodby, P.J. Collings, T. Kato, C. Tschierske, H.F. Gleeson, and P. Raynes. *Volume 1- 8*. Handbook of Liquid Crystals. Boschstr. 12, 69469 Weinheim, Germany: Wiley-VCH Verlag & Co. KGaA, Second edition, 2014. 5

[51] P.J. Collings and J.W. Goodby. *Introduction to Liquid Crystals. Chemistry and Physics*. Boca Raton, Florida: CRC Press, Second edition, 2019. 5

[52] D-K. Yang and S-T. Wu. *Fundamentals of Liquid Crystal Devices*. Wiley-SID Series in Display Technology. The Atrium, Southern Gate, Chichester, West Sussex, PO19 8SQ, England: John Wiley & Sons Ltd, 2006. 5

[53] E. Hecht. *Optics*. Global edition. Fifth edition, 2017. Edinburgh Gate, Harlow, Essex, CM20 2JE, England: Pearson Education. 5

[54] T. Scharf. *Polarized Light in Liquid Crystals and Polymers*. Hoboken, New Jersey & Canada: John Wiley & Sons, Inc., 2007. 5

[55] R.J. Mandle, E. Bevis, J.W. Goodby, (Handbook eds)J.W. Goodby, P.J. Collings, T. Kato, C. Tschierske, H.F. Gleeson, and P. Raynes. *Volume 3 (Nematic and Chiral Nematic Liquid Crystals), Chapter 1 (Phase structures of nematic liquid crystals)*. Handbook of Liquid Crystals. Boschstr. 12, 69469 Weinheim, Germany: Wiley-VCH Verlag & Co. KGaA, Second edition, 2014. 7

[56] D. Guillon, (Handbook eds)J.W. Goodby, P.J. Collings, T. Kato, C. Tschierske, H.F. Gleeson, and P. Raynes. *Volume 3 (Nematic and Chiral Nematic Liquid Crystals), Chapter 2 (Phase transitions in rod-like liquid crystals)*. Handbook of Liquid Crystals. Boschstr. 12, 69469 Weinheim, Germany: Wiley-VCH Verlag & Co. KGaA, Second edition, 2014. 7

[57] H.F. Gleeson, C.D. Southern, P.D. Brimicombe, J.W. Goodby, and V. Görtz. Optical measurements of orientational order in uniaxial and biaxial nematic liquid crystals. *Liquid Crystals*, 37(6-7):949–959, 2010. 7, 148, 165

[58] P.J. Collings and J.W. Goodby. *Introduction to Liquid Crystals. Chemistry and Physics. Chapter 13 (Light and liquid crystals - a panoply of color)*. Boca Raton, Florida: CRC Press, Second edition, 2019. 7

[59] Y. Yang. *Optical Trapping of Nematic and Chiral Nematic Liquid Crystalline Droplets*. PhD thesis, University of Manchester, 2009. 9

[60] G. Barbero and L.R. Evangelista. *Adsorption Phenomena and Anchoring Energy in Nematic Liquid Crystals. Chapter 1 (Nematic liquid crystals: fundamentals and bulk properties)*. The Liquid Crystals Book Series. 6000 Broken Sound Parkway NW, Suite 300. Boca Raton, FL 33487-2742: CRC Press. Taylor & Francis Group, LLC, 2006. 9

[61] F.C. Frank. I. Liquid crystals. On the theory of liquid crystals. *Discussions of the Faraday Society*, 25(0):19–28, 1958. 9

[62] I.W. Stewart, (Handbook eds)J.W. Goodby, P.J. Collings, T. Kato, C. Tschierske, H.F. Gleeson, and P. Raynes. *Volume 1 (Fundamentals of Liquid Crystals), Chapter 4 (Continuum theory for liquid crystals).* Handbook of Liquid Crystals. Boschstr. 12, 69469 Weinheim, Germany: Wiley-VCH Verlag & Co. KGaA, Second edition, 2014. 9

[63] G. Barbero and L.R. Evangelista. *Adsorption Phenomena and Anchoring Energy in Nematic Liquid Crystals. Chapter 2 (Nematic liquid crystals: surface properties).* The Liquid Crystals Book Series. 6000 Broken Sound Parkway NW, Suite 300. Boca Raton, FL 33487-2742: CRC Press. Taylor & Francis Group, LLC, 2006. 9

[64] S.H. Ryu and D.K. Yoon. Liquid crystal phases in confined geometries. *Liquid Crystals*, 43(13-15):1951–1972, 2016. 10

[65] M.J. Shin and D.K. Yoon. Role of stimuli on liquid crystalline defects: from defect engineering to switchable functional materials. *Materials*, 13(23):5466, 2020. 10

[66] S.J. Cowling, (Handbook eds)J.W. Goodby, P.J. Collings, T. Kato, C. Tschierske, H.F. Gleeson, and P. Raynes. *Volume 1 (Fundamentals of Liquid Crystals), Chapter 9 (Optical microscopy studies of liquid crystals).* Handbook of Liquid Crystals. Boschstr. 12, 69469 Weinheim, Germany: Wiley-VCH Verlag & Co. KGaA, Second edition, 2014. 11, 34

[67] M. Born. *Ueber anisotrope Flüssigkeiten: Versuch einer Theorie der flüssigen Kristalle und des elektrischen Kerr-Effekts in Flüssigkeiten.* 1916. 30,614-650. 11, 12

[68] R.J. Mandle, S.J. Cowling, and J.W. Goodby. A nematic to nematic transformation exhibited by a rod-like liquid crystal. *Physical Chemistry Chemical Physics*, 19(18):11429–11435, 2017. 11

[69] R.J. Mandle, S.J. Cowling, and J.W. Goodby. Rational design of rod-like liquid crystals exhibiting two nematic phases. *Chemistry – A European Journal*, 23(58):14554–14562, 2017. 11

[70] H. Nishikawa, K. Shiroshita, H. Higuchi, Y. Okumura, Y. Haseba, S. Yamamoto, K. Sago, and H. Kikuchi. A fluid liquid-crystal material with highly polar order. *Advanced Materials*, 29(43):1702354, 2017. 11, 12

[71] O.D. Lavrentovich. Ferroelectric nematic liquid crystal, a century in waiting. *Proceedings of the National Academy of Sciences of the United States of America*, 117(26):14629–14631, 2020. 12

[72] N. Sebastián, M. Čopič, and A. Mertelj. Ferroelectric nematic liquid-crystalline phases. *Physical Review E*, 106(2):021001, 2022. 12

[73] S. Brown, E. Cruickshank, J.M.D. Storey, C.T. Imrie, D. Pociecha, M. Majewska, A. Makal, and E. Gorecka. Multiple polar and non-polar nematic phases. *ChemPhysChem*, 22(24):2506–2510, 2021. 12

[74] D. Nikolova, R. Tuffin, H.F. Gleeson, and M. Osipov. Thermodynamic potential of ferroelectric nematic liquid crystals and consequences for polarization switching. *Physical Review E*, 112(1):015415, 2025. 12

[75] P.M. Rupnik, E. Hanžel, M. Lovšin, N. Osterman, C.J. Gibb, R.J. Mandle, N. Sebastián, and A. Mertelj. Antiferroelectric order in nematic liquids: flexoelectricity versus electrostatics. *Advanced Science*, 12(9):2414818, 2025. 12

[76] X. Chen, V. Martinez, E. Korblova, G. Freychet, M. Zhernenkov, M.A. Glaser, C. Wang, C. Zhu, L. Radzihovsky, J.E. Maclennan, D.M. Walba, and N.A. Clark. The smectic Z_a phase: antiferroelectric smectic order as a prelude to the ferroelectric nematic. *Proceedings of the National Academy of Sciences of the United States of America*, 120(8):e2217150120, 2023. 12

[77] A. Ghimire, B. Basnet, H. Wang, P. Guragain, A. Baldwin, R. Twieg, O.D. Lavrentovich, J. Gleeson, A. Jakli, and S. Sprunt. Dynamics of the antiferroelectric smectic-Z_a phase in a ferroelectric nematic liquid crystal. *Soft Matter*, 21(44):8510–8522, 2025. 13

[78] S. Abe, Y. Shibata, M. Kimura, and T. Akahane. Self-consistent explanation of the untwist alignment of ferroelectric nematic liquid crystals with decreasing cell thickness and deviation of the surface easy axis experimented upon using the brewster angle reflection method. *Crystals*, 14(2):157, 2024. 13, 37, 156, 158, 159

[79] A. Paul, M. Paul, M. Badu, A. Ghimire, N.P. Dhakal, S. Sprunt, A. Jákli, and J.T. Gleeson. Comprehensive characterization of a reference ferroelectric nematic liquid crystal material. *Materials*, 18(24):5496, 2025. 13, 38, 138, 145, 150, 152, 154, 156, 165, 172

[80] F. Caimi, G. Nava, R. Barboza, N.A. Clark, E. Korblova, D.M. Walba, T. Bellini, and L. Lucchetti. Surface alignment of ferroelectric nematic liquid crystals. *Soft Matter*, 17(35):8130–8139, 2021. 13, 37, 156, 159, 160

[81] P. Kumari, B. Basnet, H. Wang, and O.D. Lavrentovich. Ferroelectric nematic liquids with conics. *Nature Communications*, 14:748, 2023. 13

[82] R. Barboza, S. Marni, F. Ciciulla, F.A. Mir, G. Nava, F. Caimi, A. Zaltron, N.A. Clark, T. Bellini, and L. Lucchetti. Explosive electrostatic instability of ferroelectric liquid droplets on ferroelectric solid surfaces. *Proceedings of the National Academy of Sciences of the United States of America*, 119(32):e2207858119, 2022. 13, 71, 150, 151, 152, 165, 170

[83] S. Marni, G. Nava, R. Barboza, T.G. Bellini, and L. Lucchetti. Walking ferroelectric liquid droplets with light. *Advanced Materials*, 35(22):2212067, 2023. 13, 150

[84] R. Barboza, S. Bahwi, S. Marni, and L. Lucchetti. On the behavior of ferroelectric liquid droplets in the vicinity of a ferroelectric solid. *Crystals*, 13(5):750, 2023. 13, 150

[85] S. Marni, R. Barboza, A. Zaltron, and L. Lucchetti. Optical control of mass ejection from ferroelectric liquid droplets: a possible tool for the actuation of complex fluids. *Journal of Molecular Liquids*, 384:122287, 2023. 13, 150

[86] L. Cmok, V. Coda, N. Sebastian, A. Mertelj, M. Zgonik, S. Aya, M. Huang, G. Montemezzani, and I. Drevensek-Olenik. Running streams of a ferroelectric nematic liquid crystal on a lithium niobate surface. *Liquid Crystals*, 50(7-10):1478–1485, 2023. 13

[87] A. Sterle, L. Cmok, N. Sebastián, A. Mertelj, Y. Kong, X. Zhang, and I. Drevenšek-Olenik. Light-induced dynamics of liquid-crystalline droplets on the surface of iron-doped lithium niobate crystals. *Optical Materials Express*, 13(1):282–294, 2023. 13, 150

[88] M.T. Máthé, B. Farkas, L. Péter, Á. Buka, A. Jákli, and P. Salamon. Electric field-induced interfacial instability in a ferroelectric nematic liquid crystal. *Scientific Reports*, 13:6981, 2023. 13, 150

[89] O.D. Lavrentovich. Deformed states in paraelectric and ferroelectric nematic liquid crystals. *Annual Review of Condensed Matter Physics*, 17, 2025. 13

[90] J.P. Bramble, S.D. Evans, J.R. Henderson, C. Anquetil, D.J. Cleaver, and N.J. Smith. Nematic liquid crystal alignment on chemical patterns. *Liquid Crystals*, 34(9):1059–1069, 2007. 15

[91] T. Ohzono, H. Monobe, K. Shiokawa, M. Fujiwara, and Y. Shimizu. Shaping liquid on a micrometre scale using microwrinkles as deformable open channel capillaries. *Soft Matter*, 5(23):4658–4664, 2009. 15

[92] C. Anquetil-Deck and D.J. Cleaver. Nematic liquid-crystal alignment on stripe-patterned substrates. *Physical Review E*, 82(3):031709, 2010. 15

[93] T. Ohzono and J-i. Fukuda. Transition of frustrated nematic order and fluctuation of topological defects in microwrinkle grooves. *Soft Matter*, 8(45):11552–11556, 2012. 15

[94] T. Ohzono and J-i. Fukada. Zigzag line defects and manipulation of colloids in a nematic liquid crystal in microwrinkle grooves. *Nature Communications*, 3:701, 2012. 15

[95] Y. Choi, H. Yokoyama, and J.S. Gwag. Determination of surface nematic liquid crystal anchoring strength using nano-scale surface grooves. *Optics Express*, 21(10):12135–12144, 2013. 15

[96] A.H. Lewis, I. Garlea, J. Alvarado, O.J. Dammone, P.D. Howell, A. Majumdar, B.M. Mulder, M.P. Lettinga, G.H. Koenderink, and D.G.A.L. Aarts. Colloidal liquid crystals in rectangular confinement: theory and experiment. *Soft Matter*, 10(39):7865–7873, 2014. 15

[97] J. Walton, N.J. Mottram, and G. McKay. Nematic liquid crystal director structures in rectangular regions. *Physical Review E*, 97(2):022702, 2018. 15

[98] L. Fang, A. Majumdar, and L. Zhang. Surface, size and topological effects for some nematic equilibria on rectangular domains. *Mathematics and Mechanics of Solids*, 25(5):1101–1123, 2020. 15

[99] B. Shi, Y. Han, and L. Zhang. Nematic liquid crystals in a rectangular confinement: solution landscape, and bifurcation. *SIAM Journal on Applied Mathematics*, 82(5):1808–1828, 2022. 15

[100] J.R.L. Cousins, A.S. Bhadwal, L.T. Corson, B.R. Duffy, I.C. Sage, C.V. Brown, N.J. Mottram, and S.K. Wilson. Weak-anchoring effects in a thin pinned ridge of nematic liquid crystal. *Physical Review E*, 107(3):034702, 2023. 15, 16, 17, 45, 46, 48, 49, 50, 52, 62, 63, 74

[101] T. Pawale, J. Swain, M.R. Hashemi, G. Tierra, and X. Li. Dynamic motions of topological defects in nematic liquid crystals under spatial confinement. *Advanced Materials Interfaces*, 10(15):2300136, 2023. 15

[102] X-J. Zhang, Y-W. Sun, Z-W. Li, and Z-Y. Sun. Relative kinetic stability of defect patterns in two-dimensional nematic liquid crystals with rectangular confinement. *The Journal of Chemical Physics*, 161(7):074904, 2024. 15

[103] J. Tang, Z. Li, M. Xie, Y. Luo, J. Yu, G. Chen, and Z. Chen. Liquid crystal based label-free optical sensors for biochemical application. 14:240203, 2024. 17

[104] S. Sil, K. Mishra, and S.K. Pal. Liquid crystal biosensors: an overview of techniques to monitor enzyme activity. *Langmuir*, 41(8):4959–4975, 2025. 17

[105] S. Chattha, P.K. Chan, and S.R. Upreti. The use of artificial intelligence in liquid crystal applications: A review. *The Canadian Journal of Chemical Engineering*, 103(3):1060–1082, 2025. 18

[106] S.U. Pickering. CXCVI.-Emulsions. *Journal of the Chemical Society, Transactions*, 91(0):2001–2021, 1907. 18

[107] O.H. Piñeres-Quiñones, D.M. Lynn, and C. Acevedo-Vélez. Environmentally responsive emulsions of thermotropic liquid crystals with exceptional long-term stability and enhanced sensitivity to aqueous amphiphiles. *Langmuir*, 38(3):957–967, 2022. 18

[108] S. Aery, J.J. Crassous, and A. Dan. Optical detection of proteins using microgel-stabilized pickering liquid crystal-in-water emulsions. *Langmuir*, 41(1):392–402, 2025. 18, 19, 173

[109] G. Zhang, A. Zhu, S. Wang, Q. Chen, B. Liu, J. Zhou, and Z. Wu. Stabilizing liquid crystal droplets with hydrogel films and its application in monitoring adenosine triphosphate. *Colloids and Surfaces A: Physicochemical and Engineering Aspects*, 654:130122, 2022. 18, 173

[110] Y. Su, Z. Lan, J. Wang, L. Zeng, D. Zhou, Z. Peng, W. Sun, and Y. Liu. Optical fiber sensor for determination of methanol ratio in methanol-doped ethanol based on two cholesteric liquid crystal droplets embedded in chitosan. *Journal of Lightwave Technology*, 39(15):5170–5176, 2021. 19

[111] P. Ma, P. Li, Y. Wang, D. Chang, W-W. Gao, and C. Gao. Liquid crystalline microdroplets of graphene oxide *via* microfluidics. *Chinese Journal of Polymer Science*, 39:1657–1664, 2021. 19

[112] J. Deng, W. Liang, S. Rhodes, and J. Fang. Influence of polymer networks on the sensor properties of hydrogel dispersed liquid crystal droplets. *Colloids and Surfaces A: Physicochemical and Engineering Aspects*, 570:438–443, 2019. 19, 173

[113] S. Xie, R. He, Q. Zhu, M. Jin, R. Yang, S. Shen, J. Cui, Y. Zou, M. Zhang, and L. Shui. Label-free optical sensor based on liquid crystal sessile droplet array for penicillin G determination. *Colloids and Surfaces A: Physicochemical and Engineering Aspects*, 644:128728, 2022. 19, 173

[114] S.B. Awad, R. Nagarajan, (Book eds)R. Kohli, and K.L. Mittal. *Developments in Surface Contamination and Cleaning. Chapter 6 (Ultrasonic cleaning)*. The Boulevard, Langfrod Lane, Kidlington, Oxford, OX5 1GB, UK: William Andrew Publishing, 2010. 22

[115] F.J. Fuchs, (Book eds)J.A. Gallego-Juárez, and K.F. Graff. *Power Ultrasonics. Applications of High-Intensity Ultrasound. Chapter 19 (Ultrasonic cleaning and washing of surfaces)*. Woodhead Publishing Series in Electronic and Optical Materials. Langford Lane, Kidlington, OX5 1GB, UK:Woodhead Publishing, 2015. 22

[116] J.R. Vig. UV/ozone cleaning of surfaces. *Journal of Vacuum Science & Technology A*, 3(3):1027–1034, 1985. 22

[117] J.M. Gorham, A.K. Stover, and D.H. Fairbrother. Modification of 1H,1H,2H,2H-perfluorooctyltrichlorosilane self-assembled monolayers by atomic hydrogen. *The Journal of Physical Chemistry C*, 111(50):18663–18671, 2007. 28

[118] M. Psarski, J. Marczak, G. Celichowski, G.B. Sobieraj, K. Gumowski, F. Zhou, and W. Liu. Hydrophobization of epoxy nanocomposite surface with 1H,1H,2H,2H-perfluorooctyltrichlorosilane for superhydrophobic properties. *Central European Journal of Physics*, 10:1197–1201, 2012. 28

[119] G. Chang, L. Chen, and Z. Li. Preparation of tetrafluoro-λ^6-sulfanyl bridged-bonding perfluoroalkyl phenylethyltrichlorosilane and its application on fabric finishing. *Materials Research Express*, 7(7):075305, 2020. 28

[120] Ximea GmbH. MC050CG-SY, 2010-2026. [Online]. Last accessed 19 January 2026. Available from: https://www.ximea.com/products/usb-vision-industrial/xic-sony-cmos-pregius-usb3-cameras/sony-imx250-usb3-color-industrial-camera. 30

[121] Thorlabs Inc. High-Magnification Zoom Lens Systems for Machine Vision, 1999-2026. [Online]. Last accessed 19 January 2026. Available from: https://www.thorlabs.com/high-magnification-zoom-lens-systems-for-machine-vision?tabName=Field%2520of%2520View. 30

[122] C. Tsakonas, A.J. Davidson, C.V. Brown, and N.J. Mottram. Multistable alignment states in nematic liquid crystal filled wells. *Applied Physics Letters*, 90(11):111913, 2007. 36, 37, 82, 108

[123] N. Sebastián, R.J. Mandle, A. Petelin, A. Eremin, and A. Mertelj. Electrooptics of mm-scale polar domains in the ferroelectric nematic phase. *Liquid Crystals*, 48(14):2055–2071, 2021. 37, 156, 158, 159

[124] X. Chen, E. Korblova, M.A. Glaser, J.E. Maclennan, D.M. Walba, and N.A. Clark. Polar in-plane surface orientation of a ferroelectric nematic liquid crystal: polar monodomains and twisted state electro-optics. *Proceedings of the National Academy of Sciences of the United States of America*, 118(22):e2104092118, 2021. 37, 38, 159

[125] M.O. Lavrentovich, P. Kumari, and O.D. Lavrentovich. Twist, splay, and uniform domains in ferroelectric nematic liquid crystals. *Nature Communications*, 16:6516, 2025. 37, 156, 159

[126] T. Scharf. *Polarized Light in Liquid Crystals and Polymers. Chapter 8 (Optics of liquid crystal textures)*. Hoboken, New Jersey & Canada: John Wiley & Sons, Inc., 2007. 39

[127] Synthon Chemicals. Liquid crystal mixture E7, 2022. [Online]. Last accessed 18 January 2026. Available from: https://shop.synthon-chemicals.com/en/LIQUID-CRYSTALS/LIQUID-CRYSTALS-MIXTURES/Liquid-crystal-mixture-E7.html. 42

[128] S. Abe, Y. Shibata, M. Kimura, and T. Akahane. Determining the anisotropic refractive indices of ferroelectric nematic liquid crystals by renormalized ellipsometry. *The Journal of The Institute of Image Information and Television Engineers*, 78(6):677–682, 2024. 42, 149, 165, 170

[129] M.T. Máthé, K. Perera, Á. Buka, P. Salamon, and A. Jákli. Fluid ferroelectric filaments. *Advanced Science*, 11(9):2305950, 2024. 42, 134

[130] Anton Paar GmbH. *Instruction Manual. DMA^{TM} 4100M. DMA^{TM} 4500M. DMA^{TM} 5000M.* Austria, 2017. 43

[131] C. Parton-Barr, H.F. Gleeson, and R.J. Mandle. Room-temperature ferroelectric nematic liquid crystal showing a large and diverging density. *Soft Matter*, 20(3):672–680, 2024. 43, 152

[132] R. Bottom and (Book ed)P. Gabbott. *Principles and Applications of Thermal Analysis. Chapter 3 (Thermogravimetric analysis).* 2008. 9600 Garsington Road, Oxford OC4 2DQ, UK: Blackwell Publishing Ltd. 44

[133] J.R.L. Cousins, B.R. Duffy, S.K. Wilson, and N.J. Mottram. Young and young–laplace equations for a static ridge of nematic liquid crystal, and transitions between equilibrium states. *Proceedings of the Royal Society A: Mathematical, Physical and Engineering Sciences*, 478(2259):20210849, 2022. 48

[134] P.G. de Gennes. Wetting: statics and dynamics. *Reviews of Modern Physics*, 57(3):827–863, 1985. 49, 84

[135] J.C.R. Reis, I.M.S. Lampreia, Â.F.S. Santos, M.L.C.J. Moita, and G. Douhéret. Refractive index of liquid mixtures: theory and experiment. *ChemPhysChem*, 11(17):3722–3733, 2010. 127

[136] E.J. Cooper, M. Reynolds, T. Raistrick, S.R. Berrow, E.I.L. Jull, V. Reshetnyak, D. Mistry, and H.F. Gleeson. Controlling the optical properties of transparent auxetic liquid crystal elastomers. *Macromolecules*, 57(5):2030–2038, 2024. 127

[137] A. Jarosik, H. Nádasi, M. Schwidder, A. Manabe, M. Bremer, M. Klasen-Memmer, and A. Eremin. Fluid fibers in true 3D ferroelectric liquids. *Proceedings of the National Academy of Sciences of the United States of America*, 121(13):e2313629121, 2024. 134

[138] M.T. Máthé, H. Nishikawa, F. Araoka, A. Jákli, and P. Salamon. Ramification and labyrinth instabilities in a ferroelectric nematic fluid exposed to electric fields. *Journal of Molecular Liquids*, 413:126047, 2024. 150

[139] Lord Rayleigh. On the equilibrium of liquid conducting masses charged with electricity. *The London, Edinburgh, and Dublin Philosophical Magazine and Journal of Science*, 14(87):184–186, 1882. 150, 165, 170

[140] I. Gvozdovskyy, Y. Kurioz, and Y. Reznikov. Exposure and temperature dependences of contact angle of liquid crystals on photoaligning surface. *Opto-Electronics Review*, 17(2):116–119, 2009. 154

[141] K.G. Hedlund, V. Martinez, X. Chen, C.S. Park, J.E. Maclennan, M.A. Glaser, and N.A. Clark. Freely suspended nematic and smectic films and free-standing smectic filaments in the ferroelectric nematic realm. *Physical Chemistry Chemical Physics*, 27(1):119–128, 2025. 161

[142] (Book eds.)H.G. Tompkins and E.A. Irene. *Handbook of Ellipsometry*. 2005. 13 Eaton Avenue, Norwich, NY 13815: William Andrew Publising and Tiergartenstrasse 17, D-69129 Heidelberg, Germany: Springer-Verlag GmbH & Co. KG. 171

[143] I. Dierking and (Book ed)I. Dierking. *Polymer-modified Liquid Crystals. Chapter 6 (Introduction to polymer stabilized liquid crystals)*. Soft Matter Series, No. 8. Burling House, Piccadilly, London, W1J 0BA, UK: The Royal Society of Chemistry, 2019. 173